

Developing multi-modal imaging agents for stem cell tracking

May Zaw Thin

September 2018

For the degree of Doctor of Philosophy

University College London (UCL), UK

Supervisors: Dr Tammy Kalber & Prof Mark Lythgoe

Centre for Advanced Biomedical Imaging (CABI)

Paul O'Gorman Building

72 Huntley Street

London, WC1E 6DD

Declaration

I, May Zaw Thin, confirm that the work presented in this thesis is my own. Where information has been derived from other sources, I confirm that this been indicated in the thesis.

May Zaw Thin

20th September 2018

Abstract

Clinical trials using stem cells as a regenerative therapy or a delivery vehicle for anti-cancer agents have been increasing but the outcomes are highly variable. *In vivo* imaging of stem cell delivery to target organs will help improve their therapeutic efficacy. However, a single imaging modality cannot provide the complete answer. The work in this thesis aims to develop a multi-modal imaging approach to overcome the limitations of each modality.

To understand the distribution pattern of transplanted stem cells *in vivo*, luciferase expressing adipocyte derived mesenchymal stem cells (ADSCs) were labelled with novel bimodal (nuclear/magnetic resonance imaging) nanoparticles and the following hypotheses were tested; 1) that the distribution pattern of transplanted ADSCs would be different between venous and arterial routes, 2) that the arterial route would provide a more efficient way of delivering ADSC to tumours. In addition, ultrasound-guided renal artery injection was developed to improve stem cell delivery to kidney and the efficiency of this injection was assessed using photoacoustic and bioluminescence imaging. Moreover, the applicability of gold nanoparticles (GNP) as cell tracking agents was explored using multi-modal imaging.

Results demonstrated the advantages of multi-modal imaging in assessing different cell distribution patterns after two systemic injections and confirmed that the arterial route was more efficient in delivering ADSCs to tumours. The assessment of cell localisation and viability in the kidney suggests that the level of cell engraftment improved after ultrasound-guided renal artery injection. Multi-modal imaging results indicated that GNPs are a promising cell tracking agent for computed tomography but further studies are required to define their specific applications.

In conclusion, this work has demonstrated the successful application of multi-modal imaging for stem cell tracking in different organs. The findings from this thesis proved that combining the strengths of each modality can provide greater insight into cell migration and distribution.

Impact statement

Stem cell therapies have been extensively studied to provide regenerative therapies for a variety of diseases as well as treatments for cancer. Although they are increasingly applied in ongoing clinical trials, there is a major problem in evaluating their effectiveness. Therefore, the ability to track healthy transplanted cells will allow us to study the delivery, survival and integration into diseased organs, which is of key importance when predicting the potential benefit of cell therapies.

However, there is no single imaging modality that can address all the issues facing stem cell therapies. For these reasons, in this thesis, a novel multi-modal imaging approach has been developed by combining different imaging modalities into a single agent using advanced molecular biology and nanochemistry. This imaging strategy has been successfully applied to track stem cells over time and at a high resolution to investigate their fate. In addition, different stem cell delivery routes have been assessed to optimise tumour delivery. Not only the efficiency in delivering cell to target organs but also the safety of the administration routes has been compared and assessed with multi-modal imaging.

The knowledge and information obtained from this thesis will be valuable to the cell therapy community as a whole in answering a number of questions such as cell dose, timings and intervals of delivery and homing of cells, which are major hindrances in translational process. More importantly, the safety of administering stem cell therapies have been addressed in this thesis which is a priority for clinical translation. In addition, the results from this thesis have provided a greater understanding of the behaviour of the stem cells after transplantation, which will be beneficial for the area of stem cell research.

Acknowledgements

This research project would not have been possible without the support of many people.

I am eternally grateful to Dr Tammy Kalber for her incredible supervision and allowing me to do part-time PhD. Her love and support inspired me greatly to work hard in this project. I would like to thank Prof Mark Lythgoe for training me to think outside the box and be creative in tackling difficult research questions. My special thanks to Dr Daniel Stuckey for being there for me whenever I need help and never hesitant to point out my mistakes.

I would like to thank Dr John Connell for guiding me through my early years in PhD and listening to my endless complaints. Dr Stephen Patrick for his insightful knowledge in everything. Dr Ollie Ogunlade for his help in photoacoustic imaging. Dr Ma Da, Dr Bernard Siow, Dr Tim Witney and Dr Elizabeth Sage for providing valuable advices. Ana Gomez and Morium Ali for helping me with all types of technical problems and giving me homemade food. Dr Tom Roberts for being the most annoying desk buddy I could have asked for.

I would like to thank all my external collaborators especially Dr Robin Bofinger for being the best chemist I have ever worked with (and the only one). Finally, I would like to thank the whole of CABI for just being CABI, a place which make me feel like home.

Publications and awards arising from this PhD

Peer-reviewed journal articles

Published

Abdollah M & Carter T, Jones C, Kalber T, Rajkumar V, Tolner B, Gruettner C, **Zaw Thin M**, Bagaña Torres J, Ellis M, Robson M, Pedley B, Mulholland P, de Rosales R.T.M and Chester K. Fucoidan Prolongs the Circulation Time of Dextran-Coated Iron Oxide Nanoparticles. ACS Nano. 2018. DOI: 10.1021/acsnano.7b06734.

Castillo SD, Tzouanacou E, **Zaw Thin M**, Berenjano IM, Parker VE, Chivite I, Milà-Guasch M, Pearce W, Solomon I, Angulo-Urarte A, Figueiredo AM, Dewhurst RE, Knox RG, Clark GR, Scudamore CL, Badar A, Kalber TL, Foster J, Stuckey DJ, David AL, Phillips WA, Lythgoe MF, Wilson V, Semple RK, Sebire NJ, Kinsler VA, Graupera M, Vanhaesebroeck B. Somatic activating mutations in Pik3ca cause sporadic venous malformations in mice and humans. Sci Transl Med. 2016; 8(332):332ra43.

Pending

Zaw Thin M, Bofinger R, Connell J, Patrick S, Stuckey D, Helen H, Tabor A, Lythgoe M, Kalber T. Multi-modal imaging of stem cell delivery to breast tumours. Under review.

Zaw Thin M, Ogunlade O, Comenge J, Patrick S, Stuckey D, David A, Levy R, Lythgoe M, Beard P, Kalber T. Ultrasound-guided renal artery injection for stem cell delivery to kidney. Under review.

Bofinger R, **Zaw Thin M**, Mitchell N, Patrick S, Stowe C, Gomez AR, Hailes H, Kalber T and Tabor A. Development of lipopolyplexes for gene delivery and optical imaging: a comparison of the effects of differing modes of targeting peptide display on the structure and transfection activities of lipopolyplexes. Under review.

Published abstracts

2016

Zaw Thin May, Bofinger Robin, Connell John, Patrick Stephen, Hailes Helen, Tabor Alethea, Lythgoe Mark and Kalber Tammy. Novel multimodal imaging agent for stem cell tracking. European Molecular Imaging Meeting (2016).

Zaw Thin May, Connell John, Patrick Stephen, Lythgoe Mark and Kalber Tammy. Gold nanoparticles as a long term stem cell tracking agent for Computed Tomography. European Molecular Imaging Meeting (2016).

Zaw Thin May, Bofinger Robin, Connell John, Patrick Stephen, Hailes Helen, Tabor Alethea, Lythgoe Mark and Kalber Tammy. Novel multimodal imaging agent for stem cell tracking. Division of Medicine Research Retreat (2016).

Zaw Thin May, Bofinger Robin, Connell John, Patrick Stephen, Hailes Helen, Tabor Alethea, Lythgoe Mark and Kalber Tammy. Novel multimodal imaging agent for stem cell tracking. World Molecular Imaging Conference (2016).

2017

Zaw Thin M, Stuckey DJ, Castillo SD, Tzouanacou E, Pearce W, Dewhurst RE, Badar A, Kalber TL, David AL, Lythgoe MF, Wilson V, Sebire NJ, Graupera M and Vanhaesebroeck B. Doppler Ultrasound imaging of venous malformation. International Centre for Genetic Engineering & Biotechnology Ultrasound meeting (2017).

2018

Zaw Thin May, Bofinger Robin, Connell John, Patrick Stephen, Stuckey Daniel, Hailes Helen, Tabor Alethea, Lythgoe Mark and Kalber Tammy. Generation of Trimodal Imaging Stem Cells for Quantification and Optimization of Stem Cell Cancer Therapy. European Molecular Imaging Meeting (2018).

Zaw Thin May, Bofinger Robin, Connell John, Patrick Stephen, Stuckey Daniel, Hailes Helen, Tabor Alethea, Lythgoe Mark and Kalber Tammy. Multi-modal imaging of stem cell homing to breast tumour. London Stem Cell Network Symposium (2018).

Awards

- 2017 Best oral presentation - US imaging in cardiac and vascular medicine, International Centre for Genetic Engineering and Biotechnology
- 2016 Best 3 minutes PhD oral presentation – Division of Medicine Research Retreat, UCL
- 2015 The Old Student's Association (OSA) Scholarship - UCL

Table of contents

Declaration	2
Abstract	3
Impact statement	4
Acknowledgements	5
Publications and awards arising from this PhD	6
Table of contents	9
List of figures	16
List of tables	24
Abbreviations	25
Chapter 1 Introduction – Stem cell therapy and <i>in vivo</i> cell tracking	29
1.1 Overview of stem cell therapy	30
1.2 Cell types	31
Haematopoietic stem cell (HSC)	31
Embryonic stem cells (ESCs) and induced pluripotent stem cells (iPSCs)	31
Neural stem cells (NSCs)	32
Mesenchymal stem cells (MSCs)	32
1.3 The properties of MSCs and their applications	32
Paracrine and endocrine signalling	32
Immunomodulation	33
Tumour homing	33
1.4 Monitoring cell therapies <i>in vivo</i>	36
1.5 Direct cell labelling	36
Fluorescence imaging (FLI)	37
Magnetic resonance imaging (MRI)	38
Nuclear imaging	38
Photoacoustic (PA) imaging	40
Computed tomography (CT) imaging	42
1.6 Reporter gene imaging	43
Fluorescent reporter gene imaging	43
Bioluminescence imaging (BLI)	43
Nuclear reporter gene imaging	44
MRI reporter gene imaging	45
PA reporter gene imaging	46

1.7 Stem cells delivery	47
Intravenous (IV) injection	47
Intra-arterial (IA) injection	48
Local injection routes	49
1.8 Assessment of therapeutic response	50
1.9 Which imaging techniques should we use?	51
1.10 Limitation of in vivo imaging	52
1.11 Summary and research aims	52
Chapter 2 – General methods	54
2.1 Materials	55
2.2 Cell culture	55
2.2.1 Isolation and characterisation of ADSCs	55
2.2.2 Transduction of ADSCs	55
2.2.3 Differentiation assay	56
Adipogenic differentiation	56
Chondrogenic differentiation	56
Osteogenic differentiation	56
2.3 Transmission Electron Microscopy (TEM)	57
2.4 <i>In vivo</i> studies	57
2.4.1 Ultrasound-guided intracardiac injection	58
2.4.2 BLI	58
2.4.3 SPECT/CT	58
2.4.4 MRI	58
2.5 <i>Ex vivo</i> BLI and biodistribution study	60
2.6 Histology and immunohistochemistry (IHC)	60
Chapter 3 – Synthesis and characterisation of a SPECT/MRI dual imaging probe	62
3.1 Abstract	63
3.2 Introduction	64
3.2.1 Design of multi-modal imaging probes	64
3.2.2 Types of radioisotopes and applications	65
3.2.3 Experimental approach	67
3.2.4 Research objectives	67
3.3 Methods	68
3.3.1 Synthesis and characterisation of DOTA-SPIONs	68
3.3.2 Radiolabelling DOTA-SPION with Indium-111 Chloride ($^{111}\text{InCl}_3$)	69

3.3.3 <i>In vitro</i> assessment of ¹¹¹ In-DOTA-SPION chelation	70
3.3.4 <i>In vivo</i> studies	71
3.3.5 <i>In vivo</i> assessment of ¹¹¹ In-DOTA-SPION chelation	71
3.3.6 SPECT/CT	71
3.3.7 Statistical analysis	71
3.4 Results	72
3.4.1 Characterisation of DOTA-SPIONs	72
3.4.2 Optimisation of DOTA-SPION radiolabeling	73
3.4.3 <i>In vitro</i> validation of ¹¹¹ In-DOTA-SPION chelation	74
3.4.4 <i>In vivo</i> validation of ¹¹¹ In-DOTA-SPION chelation	76
3.5 Discussion	78
3.6 Conclusion	79
Chapter 4 – Multi-modal imaging of stem cell distribution after systemic injections	80
4.1 Abstract	81
4.2 Introduction	82
4.2.1 The role of multi-modal imaging in cell tracking	82
4.2.2 Challenges	82
4.2.3 Experimental approach	83
4.2.4 Research Objectives	84
4.3 Methods	85
4.3.1 Cell culture	85
4.3.2 Intracellular iron uptake	85
Ferrozine assay	85
Perl's Prussian blue staining	86
Transmission Electron Microscopy (TEM)	86
Retention of ¹¹¹ In-DOTA-SPIONs after intracellular uptake	86
4.3.3 The effect of ¹¹¹ In-DOTA-SPION labelling on cell function	87
Migration assay	87
Differentiation assay	87
4.3.4 The effect of radiolabelling on cell proliferation and cell death	88
ADSC labelling with ¹¹¹ In-oxine	88
<i>In vitro</i> luciferase assay	88
<i>In vitro</i> cell death assay	88
4.3.5 <i>In vivo</i> studies	89
4.3.6 <i>In vivo</i> cell and particle injections	89
<i>In vivo</i> evaluation of particle release from dead cells	89

ADSCs labelling with ¹¹¹ In-DOTA-SPIONs for <i>in vivo</i> experiment	89
<i>In vivo</i> biodistribution studies in healthy animals	90
<i>In vivo</i> cell viability assessment of radiolabelled ADSCs	91
4.3.7 <i>In vivo</i> imaging	91
BLI	91
SPECT/CT	91
MRI	91
4.3.8 <i>Ex vivo</i> BLI and biodistribution study	91
4.3.9 Histology and immunohistochemistry (IHC)	91
4.3.10 Statistical analysis	92
4.4 Results	93
4.4.1 Intracellular uptake and retention of ¹¹¹ In-DOTA-SPION in ADSCs	93
4.4.2 The effect of ¹¹¹ In-DOTA-SPION labelling on cell function	95
4.4.3 The effect of radiolabelling on cell proliferation and cell death	97
4.4.4 <i>In vivo</i> cell viability study of radiolabelled ADSCs using BLI	98
4.4.5 <i>In vitro</i> and <i>in vivo</i> assessment of particles release from dead cells	99
4.4.6 Assessment of ¹¹¹ In-DOTA-SPION labelled ADSCs distribution following IV or IC injection	101
4.4.7 Histological analysis	105
4.4.8 General assessment of the animals after multi-modal imaging	108
4.5 Discussion	109
4.6 Conclusion	113
Chapter 5 – Multi-modal imaging of stem cell delivery to tumours	114
5.1 Abstract	115
5.2 Introduction	116
5.2.1 Mesenchymal stem cell therapy for cancer	116
5.2.2 The role of non-invasive <i>in vivo</i> imaging in MSC-based cancer therapy	116
5.2.3 Experimental approach	117
5.2.4 Research Objectives	117
5.3 Methods	118
5.3.1 Cell culture	118
5.3.2 <i>In vivo</i> studies	118
5.3.3 <i>In vivo</i> cell and particle injection	118
Orthotopic breast tumour implantation using a non-surgical method	118
<i>In vivo</i> biodistribution studies in tumour bearing animals	119
5.3.4 <i>In vivo</i> imaging	120
BLI	120

SPECT/CT	120
MRI	120
Ultrasound	120
5.3.5 <i>Ex vivo</i> BLI and <i>ex vivo</i> biodistribution study	121
5.3.6 <i>Ex vivo</i> MRI	121
5.3.7 Histology and immunohistochemistry (IHC)	121
5.3.8 Statistical analysis	121
5.4 Results	122
5.4.1 Assessment of ¹¹¹ In-DOTA-SPION labelled ADSCs delivery to tumor following IV or IC	122
5.4.2 Assessment of non-specific background ¹¹¹ In-DOTA-SPION particle uptake in tumour following IV or IC	125
5.4.3 <i>Ex vivo</i> MRI	126
5.4.4 Assessment of non-radiolabelled ADSCs delivery to tumour following IV or IC	127
5.4.5 Measurement of tumour growth	128
5.4.6 Assessment of blood supply to tumour	128
5.5 Discussion	130
5.6 Conclusion	132
Chapter 6 – Multi-modal imaging of stem cell delivery to kidney	133
6.1 Abstract	134
6.2 Introduction	135
6.2.1 Stem cell therapy for kidney diseases	135
6.2.2 Photoacoustic imaging for stem cell tracking to kidney	136
6.2.3 Experimental approach	137
6.2.4 Research objectives	138
6.3 Material	139
6.3.1 Gold nanorods (GNRs)	139
6.4 Methods	140
6.4.1 Cell culture	140
6.4.2 ADSC labelling with GNRs	140
6.4.3 Internalisation of GNRs by ADSCs	140
Silver enhancement staining	140
6.4.4 The effect of GNR labelling on cell proliferation	140
<i>In vitro</i> luciferase assay	140
6.4.5 The effect of GNR labelling on differentiation potential	141
Differentiation assay	141
6.4.6 <i>In vivo</i> studies	141

6.4.7 <i>In vivo</i> cell and particle injections	141
6.4.8 <i>In vivo</i> imaging	142
BLI	142
PA imaging	142
SPECT/CT	142
MRI	142
6.4.9 <i>Ex vivo</i> BLI imaging	143
6.4.10 Histology and immunohistochemistry (IHC)	143
6.4.11 Statistical analysis	143
6.5 Results	144
6.5.1 Intracellular uptake of GNRs and their effect on cell proliferation and differentiation potential	144
6.5.2 Stem cell delivery to kidney via ultrasound-guided renal artery injection	145
6.5.3 Quantitative assessment of ultrasound-guided renal artery injection using ¹¹¹ In-DOTA-SPION particles	147
6.5.4 Assessment of the cell viability and cell localisation following renal artery injection	148
6.5.5 Histological analysis	150
6.6 Discussion	152
6.7 Conclusion	154
Chapter 7 – Developing gold nanoparticles as a stem cell tracking agent for computed tomography	155
7.1 Abstract	156
7.2 Introduction	157
7.2.1 Gold nanoparticles as CT contrast agents	157
7.2.2 Gold nanoparticles as CT stem cell tracking agents	157
7.2.3 Experimental approach	158
7.2.4 Research objectives	159
7.3 Materials	160
7.3.1 Gold nanoparticles	160
7.4 Methods	160
7.4.1 Cell culture	160
7.4.2 Internalisation of GNPs by ADSCs	160
ADSC labelling with GNPs	160
TEM	160
7.4.3 <i>In vitro</i> CT imaging	160
7.4.4 ADSC labelling with Zirconium-89 (⁸⁹ Zr)-oxine	161
7.4.5 <i>In vivo</i> studies	161

7.4.6 <i>In vivo</i> cells injection	161
7.4.7 <i>In vivo</i> imaging	162
BLI	162
PET/CT	162
7.5 Results	164
7.5.1 Internalisation of GNPs in ADSCs	164
7.5.2 <i>In vitro</i> CT contrast of GNP labelled ADSCs	165
7.5.3 <i>In vivo</i> CT contrast of GNP labelled ADSCs	166
7.5.4 Tracking GNP labelled ADSCs in lungs	167
7.5.5 Tracking GNP labelled ADSCs in kidney	168
7.6 Discussion	169
7.7 Conclusion	170
Chapter 8 – Final discussion	171
References	176
Appendix 1 – Staining solution	199
Appendix 2 – <i>In vivo</i> stability assessment of ¹¹¹ In-DOTA-SPION	200
Appendix 3 – ¹¹¹ In-DOTA-SPION labelled cell distribution in healthy animals after systemic injections	201
Appendix 4 – ¹¹¹ In-DOTA-SPION labelled cell distribution in tumour bearing animals after systemic injections	203

List of figures

- Figure 1.1 Schematic representations of possible mechanism behind MSCs homing to tumour and using them as a carrier for anti-cancer therapy (adapted from *Levy et al., 2013*). 35
- Figure 2.1 Ultrasound-guided intracardiac injection through left ventricular cavity. (a) The animal was positioned in supine position on the platform (i) with the ultrasound transducer (ii) on the chest and the syringe in injection mount (iii) facing towards the apex of the heart. (b) The needle was pierced through the skin, the chest wall and left ventricular wall. (c) The successful injection was visualised by the presence of hyperechogenic contrast. 58
- Figure 3.1 Schematic representation of the structure of ^{111}In -DOTA complex. 65
- Figure 3.2 Schematic representation of the surface of FluidMAG-CT functionalised with carboxyl group 67
- Figure 3.3 Schematic representation of the synthesis of DOTA-SPION showing a peptide bond formation between the carboxyl group and amine group. 69
- Figure 3.4 Procedure for measuring DOTA-SPION radiolabelling yield with TLC. (a) Radioactive particles were placed at the base of TLC strip. (b) TLC strip was submerged in DTPA solution. (c) The base and top part of TLC strip were cut and put into gamma counter measuring tubes. (d) Radioactivity was measured with gamma counter. 70
- Figure 3.5 TEM micrograph of SPION and DOTA-SPION showing a similar morphological appearance. 72
- Figure 3.6 Buffer optimisation study showing the percentage of radioactivity on DOTA-SPION after 4 hours incubation with HEPES buffer pH 5.5, pH 7 or ammonium acetate buffer pH 6. 73
- Figure 3.7 Labelling kinetic of DOTA-SPIONs after incubation with ^{111}In for 6 hours at 70 °C. 74
- Figure 3.8 *In vitro* validation of ^{111}In -DOTA-SPION chelation (a) Schematic representation of static binding of In^{3+} to negative carboxyl groups or to DOTA chelator (b) The radiolabelling yield from TLC data after 4 hours incubation with ^{111}In at 70 °C. (c) The percentage of radioactivity on DOTA-SPION and SPION 75

from the chelation stability study after 18 hours incubation in culture media at 37°C.	
Figure 3.9 <i>In vivo</i> validation of ^{111}In -DOTA-SPION chelation. (a, c, e) SPECT/CT images at 1 hour, days 1, 3 and 7 after IV injection of ^{111}In -DOTA-SPION, ^{111}In -SPION and free $^{111}\text{InCl}_3$. (b, d, f) 3D ROI quantification of SPECT signal in liver and kidney as calculated as %ID/mm ³ .	76
Figure 3.10 3D ROI quantification of SPECT signal in liver and kidney at 1 hour after IV injection as calculated as %ID/mm ³ .	77
Figure 4.1 Schematic representation of a tri-modal (BLI, SPECT/CT & MRI) imaging agent for stem cell tracking.	83
Figure 4.2 Assessment of migration capability using IBIDI culture inserts (adapted from IBIDI's supporting material: instructions for culture inserts). (a) Cells were seeded in 4-well silicone inserts. (b) The insert was removed the next day. (c) Cell migration between a defined gaps of 500 μm was monitored.	87
Figure 4.3 Schematic representations of ADSCs labelling with ^{111}In -DOTA-SPIONs.	90
Figure 4.4 Schematic outlines of the whole body ADSCs distribution studies using multimodal imaging.	90
Figure 4.6 Intracellular uptake of ^{111}In -DOTA-SPIONs in ADSCs. (a) ADSCs were incubated for 16 hours with ^{111}In -DOTA-SPIONs at the concentration indicated and intracellular iron uptake was measured using Ferrozine assay. (b) Prussian blue staining of ADSCs treated with ^{111}In -DOTA-SPION showing blue aggregates compared to untreated control. (c) TEM images showing SPION aggregates in lysosomes compared to untreated control.	93
Figure 4.7 The retention of ^{111}In -DOTA-SPION in ADSCs showing the percentage of radioactivity retained in ADSCs up to 7 days after labelling with ^{111}In -DOTA-SPION.	94
Figure 4.8 The effect of ^{111}In -DOTA-SPION labelling on ADSC migration. (a) The control cells and (b) ^{111}In -DOTA-SPION labelled ADSCs were stained with Hoechst 33342 for image analysis. (c) The number of cells between the gaps showed no significant difference between the control group and ^{111}In -DOTA-	95

SPION labelled group.

- Figure 4.9 Tri-lineage differentiation of control ADSCs and ^{111}In -DOTA-SPION labelled ADSCs. (a) Oil red o staining for adipogenic differentiation which displays the red coloured oil droplets. (b) Alcian blue staining for chondrogenic differentiation which displays the blue coloured proteoglycans. (c) Alizarin red s staining for osteogenic differentiation which displays the red coloured calcium deposits. 96
- Figure 4.10 The effect of ^{111}In -DOTA-SPION labelling on cell proliferation and cell viability. (a) Luciferase-based cell proliferation assay at different time points showing BLI signals (photons/s in log scale) of three non-radiolabelled samples: control cells, cells incubated with DMSO (control vehicle for ^{111}In -oxine) and DOTA-SPION labelled cells and two radiolabelled samples: cells labelled with ^{111}In -oxine and ^{111}In -DOTA-SPIONs. (b) Cell death assay at different time points showing the percentage cell death of five different samples as described in (a). 97
- Figure 4.11 *In vivo* cell viability assessments of radiolabelled ADSCs. (a) BLI images of ^{111}In -oxine labelled ADSC at 1 hour, days 1, 3 and 7 after IV showing the signal in the chest decreased over time. (b) BLI signal in the whole body decreased over time (photon/s in log scale). 98
- Figure 4.12 *In vitro* assessment of particles release from dead cells. The time-lapse microscopic images of H_2O_2 treated ^{111}In -DOTA-SPION labelled ADSCs showing the particles inside cell aggregates. 99
- Figure 4.13 SPECT/CT images showing biodistribution of (a) $^{111}\text{InCl}_3$ only, (b) ^{111}In -DOTA-SPIONs only, (c) ^{111}In -DOTA-SPIONs labelled cells and (d) labelled cell lysates at 1 hour after intravenous injection. Representative images were presented using %ID/ mm^3 as colour scale after correction for ^{111}In decay. 100
- Figure 4.14 Whole body distribution of ^{111}In -DOTA-SPION labelled ADSCs following IV or IC injection at different time points. (a, b) BLI signal was mainly seen in the chest after IV injection, whereas IC presented a wider BLI distribution. (c) BLI signal from the whole body decreased similarly over time (photons/s in log scale). (d & e) Decay corrected SPECT-CT images of dual labelled ADSCs uptake in organs after IV and IC injection. (f) 3D ROI quantification of SPECT signal in lungs, liver, brain and kidney at day 0 after IV 101

- or IC injection calculated as %ID/mm³ after decay correction.
- Figure 4.15 *Ex vivo* BLI images of lungs, liver, spleen, brain and kidney at 1 hour, days 1, 3 and 7 after (a) IV and (b) IC injection. 102
- Figure 4.16 *In vivo* and *ex vivo* quantification of ¹¹¹In-DOTA-SPION labelled cells uptake in lungs, liver, spleen, brain and kidney following IV or IC injection at different time points. (a & b) 3D ROI quantification of *in vivo* SPECT signal in organs after IV & IC injection calculated as %ID/mm³ after decay correction (c & d) *Ex vivo* quantification of radioactivity distribution in organs after IV and IC injection calculated as %ID/g after decay correction. 103
- Figure 4.17 BLI images of non-radiolabelled ADSC at 1 hour, days 1, 3 and 7 following IV or IC injection. (a, c) BLI signal in the chest and the whole body decreased over time. (b, c) BLI signal in the whole body decreased over time (photons/s in log scale). 103
- Figure 4.18 MRI images of ¹¹¹In-DOTA-SPION labelled ADSCs at 1 day following IV or IC injection. (a & b) T₂*-weighted MR images of the liver and the brain in control and dual labelled cells injected animals with SPECT data co-registered. (c) T₂*-weighted MR images of the kidney in a control mouse and mice injected with dual labelled cells intravenously and intracardially. 104
- Figure 4.19 Histological analysis of ¹¹¹In-DOTA-SPION labelled cells uptake in lungs at 7 days after IV injection. (a, c) Positive Prussian blue (SPION) and (b, d) vimentin staining (ADSC) of adjacent lung tissue sections confirmed the presence of dual labelled cells within lungs parenchyma. (e) The dual labelled cells did not express Iba1. (f) The macrophages did not contain iron. 105
- Figure 4.20 Histological analysis of ¹¹¹In-DOTA-SPION labelled cells uptake in brain at day 3 after IC injection. Positive Prussian blue (SPION) and vimentin (ADSC) staining of adjacent brain tissue sections confirmed the presence of dual labelled cells within the cerebral capillary bed. 106
- Figure 4.21 Histological analysis of brain sections at day 3 after IC injection. (a) The obstruction of cerebral blood vessels due to iron labelled cells was detected by positive Prussian blue (SPION) staining. (b) H & E staining of adjacent brain section showing a small area of cerebral infarct (c) in higher magnification. 107
- Figure 4.22 Ejection fraction analysis before and after IC injection showing the 108

cardiac function was not impaired.	
Figure 5.1 Schematic representations of mammary glands in a mouse and the mammary fat pad where 4T1 breast cancer cells were implanted.	118
Figure 5.2 Schematic outlines of imaging ADSCs delivery to tumour using BLI, SPECT/CT and MRI.	119
Figure 5.3. Multi-modal imaging of ¹¹¹ In-DOTA-SPION labelled ADSCs engraftment in tumour following IV or IC injection. (a & b) BLI signal in tumour at day 3 after IV injection and 1 hour after IC injection. (c) <i>Ex vivo</i> BLI images of tumour at day 3 after IV & IC injection. (d) The percentage of BLI signal in tumour relative to whole body after IV and IC injection. (e) BLI signal from the tumour and the whole body decreased over time (photons/sec in log scale). (f) SPECT/CT images of dual labelled ADSCs at day 0 after IV and IC injection showing the tumour uptake in a mouse with IC injection. (g) 3D ROI quantification of SPECT signal in tumour at days 0, 1 & 3 after IV & IC injection calculated as %ID/mm ³ after decay correction. (h) T ₂ [*] -weighted MR images of tumour acquired at pre-injection and day 1 after IC injection of dual labelled ADSCs showing the presence of focal hypointensity within the tumour.	122
Figure 5.4 Histological analysis of ¹¹¹ In-DOTA-SPION labelled cells uptake in tumour at 3 days after IC injection showing positive vimentin (ADSC) staining in tumour tissue section.	124
Figure 5.5 SPECT/CT images of dead tumour bearing mouse immediately after IC injection of 2.5 x 10 ⁵ ¹¹¹ In-DOTA-SPION labelled cells showing cell aggregates in heart, lungs, carotid artery and common iliac arteries. Representative images were presented using %ID/ml as colour scale after correction for ¹¹¹ In decay.	124
Figure 5.6 Assessment of the background particles uptake in tumour. <i>Ex vivo</i> quantification of radioactivity distribution in tumour at (a) day 0 and (b) day 3 after IV and IC injection of ¹¹¹ In-DOTA-SPION labelled cells and particles only calculated at %ID/g after decay correction	125
Figure 5.7 <i>Ex vivo</i> MRI assessment of the cells uptake in tumour at day 3 after IV and IC injection. T ₂ [*] -weighted images of (a) a control tumour injected with ADSCs only (b & c) tumours injected with ¹¹¹ In-DOTA-SPION labelled ADSCs intravenously and intracardially showing areas of focal hypointensity.	126

Figure 5.8 Assessment of non-radiolabelled ADSCs engraftment in tumour following IV or IC injection. (a) BLI signal in tumour at day 3 after IV injection and 1 hour after IC injection. (b) <i>Ex vivo</i> BLI images of tumour at day 3 after IV and IC injection. (c) BLI signal from the tumour and the whole body decreased over time (photons/sec in log scale). (d) The percentage of BLI signal in tumour relative to whole body after IV and IC injection. (e & f) Histological analysis of non-radiolabelled cells uptake in tumour at 3 days after IV and IC injection showing positive vimentin (ADSC) staining in tumour tissue sections.	127
Figure 5.9 MRI measurement of the rate of tumour growth showing no significant difference between ADSC injected and particle only injected groups.	128
Figure 5.10 Assessment of tumour blood supply using Doppler ultrasound. (a) 3D power Doppler image of tumour showing the total blood supply. (b - d) Colour Doppler and pulsed wave Doppler image of the tumour showing the venous and arterial blood supply.	128
Figure 6.1 Characterisation of GNRs. (a) TEM images of GNRs coated with 34 nm silica shell. (b) Ultraviolet-visible spectrum of silica coated GNRs in ethanol. (c) Optical absorption spectrum of GNRs and haemoglobin showing the absorption band of GNR is in the near-infrared window where the absorption of oxyhaemoglobin (HbO ₂) and deoxyhaemoglobin (HHb) is minimal.	139
Figure 6.2 Schematic outlines of multi-modal imaging of stem cell delivery to kidney following ultrasound-guided renal artery injection.	141
Figure 6.3 Intracellular uptakes of GNRs in ADSCs and the effect on cell proliferation. (a & b) Silver enhancement staining of ADSCs treated with GNRs showing the dark aggregates inside the cytoplasm compared to untreated control. (c) Luciferase-based cell proliferation assay at different time points showing no significant difference between luminescence signals of control and GNR labelled ADSCs.	144
Figure 6.4 Tri-lineage differentiation of control ADSCs and GNR labelled ADSCs. (a) Oil red o staining for adipogenic differentiation which displays the red coloured oil droplets. (b) Alcian blue staining for chondrogenic differentiation which displays the blue coloured proteoglycans. (c) Alizarin red s staining for osteogenic differentiation which displays the red coloured calcium deposits.	145
Figure 6.5 Less invasive ultrasound-guided renal artery injection. (a) The animal was positioned in left lateral position on the platform (i) with the ultrasound	146

transducer (ii) on the right lower quadrant of the abdomen and the syringe in injection mount (iii) facing towards the paravertebral muscle of the animal. (b) Colour Doppler image of the kidney showing renal blood supply (c & d) Pulsed wave Doppler images identifying the venous and arterial flow velocity pattern. (e) The needle was pierced through the skin and the vertebral muscle of the animal to penetrate into the right renal artery. (f) The successful injection was visualised by the presence of hyperechogenic contrast around renal cortex.

Figure 6.6 Quantitative assessment of ultrasound-guided right renal artery injection at different time points. (a) Decay corrected SPECT/CT images showing the retention of ^{111}In -DOTA-SPION particles in the right kidney for 7 days after injection. (b) 3D ROI quantification of SPECT signal in lungs, liver, brain, right and left kidney at 1 hour, days 1, 3 and 7 after injection calculated as $\%ID/mm^3$ after decay correction. (c) T_2^* -weighted MR images of both kidneys at day 1 after injection showing a large area of signal hypointensity in the right kidney compared to left kidney. 147

Figure 6.7 BLI and PA images of GNR labelled ADSCs in right kidney at different time points after right renal artery injection. (a) BLI images at 1 hour, days 1, 3 and 7 after injection showing the majority of signal within the right kidney and some signal from the lungs. (b) BLI signal from the whole body decreased over time (photons/s in log scale). (c) *Ex vivo* BLI images of both kidneys at 1 hour and day 8 after injection showing BLI signal from the right kidney. (d) PA images acquired at different wavelengths showing the higher PA contrast in right kidney than the surrounding renal blood vessels at 730 nm using the spleen as anatomical landmark (images are presented as MIP). (e-g) 3D volume-rendered PA images at days 0, 3 and 7 after injection showing the widespread PA contrast in right kidney including cortex (C) and medulla (M), compared to left kidney (the kidneys are manually segment and false coloured). 149

Figure 6.8 Histological analysis of GNR labelled ADSCs uptake in kidney at day 8 after right renal artery injection. (a & b) Vimentin (ADSC) staining of control (left kidney) and injected right kidney sections showing the widespread red staining in the cortex and medulla of right kidney compared to the control. Positive vimentin (ADSC) and silver enhancement staining of right kidney tissue sections showing the presence of dual labelled cells within the renal (c) capillary bed and (d) parenchyma compared to control. 150

Figure 7.1 Assessment of the efficiency of CT components from PET/CT scanner. 3D rendered CT image of a mouse model of vascular malformation after GNP-based vascular contrast agent injection.	158
Figure 7.2 Schematic outlines of investigating the applicability of GNP as a stem cell tracking agent for CT following different delivery methods.	162
Figure 7.3 Intracellular uptakes of GNPs in ADSCs. (a & b) Phase contrast microscopic image of ADSCs treated with GNPs showing the dark aggregates inside the cytoplasm compared to untreated control. (c) TEM image of GNP labelled ADSCs showing the entrapment of GNPs inside endosomes.	164
Figure 7.4 Assessing the CT contrast of GNP labelled ADSCs <i>in vitro</i> . 0.5×10^5 cell pellets incubated with (a) 0.04 mg/ml (b) 0.08 mg/ml and (c) 0.2 mg/ml of GNPs showing the positive CT contrast compared to water.	165
Figure 7.5 BLI and CT images of GNP labelled ADSCs which acquired serially up to 2 months after subcutaneous injection into the left side of the flank. (a) BLI images showing the presence of GNP labelled cells at the injection site. (b) CT images showing the positive contrast from GNP labelled cells at the same location. (c) BLI signal from the injection site decreased over time (photons/s in log scale). (d) Quantification of CT signal at the injection site remained stable (presented as the relative Hounsfield unit from the opposite side of the flank).	166
Figure 7.6 CT and BLI images of the control (PBS) and GNP labelled ADSCs in the lungs at 1 day after intratracheal intubation. Cross section and 3D model CT lung images of (a) the control showing absence of positive contrast in the lungs and (b) GNP labelled ADSCs showing the widespread positive contrast in both right and left lobes of the lungs. (c) BLI images of GNP labelled ADSCs showing the presence of cells in the trachea and both lobes of the lungs.	167
Figure 7.7 BLI and PET/CT images of GNP labelled ADSCs in kidney at 3 hours after renal artery injection. (a) BLI image showing the signal appeared to be coming from the right kidney. (b) CT image showing the positive contrast at the right renal pelvis. (c) Co-registered PET/CT image showing the radioactive signal at the same location.	168

List of tables

Table 1.1 Summary of strengths and drawbacks of currently available in vivo imaging technologies for cell tracking (Adapted from <i>Zheng et al., 2017</i>).	51
Table 3.1 Hydrodynamic diameter and zeta potential of SPION with no DOTA and DOTA-SPION with 1 mM, 5 mM and 10 mM DOTA-amine concentration in PBS at 25°C. Data are shown as means ± SD (n = 3).	72
Table A2.1 <i>In vivo</i> 3D ROI quantification of SPECT signal (%ID/mm ³) in liver of ¹¹¹ InCl ₃ , ¹¹¹ In-SPION and ¹¹¹ In-DOTA-SPION at 1 hour, days 1, 3 & 7 after injection (n = 3 in each group).	200
Table A2.2 <i>In vivo</i> 3D ROI quantification of SPECT signal (%ID/mm ³) in kidney of ¹¹¹ InCl ₃ , ¹¹¹ In-SPION and ¹¹¹ In-DOTA-SPION at 1 hour, days 1, 3 & 7 after injection (n = 3 in each group).	200
Table A3.1 <i>Ex vivo</i> quantification of radioactivity distribution (%ID/g) in all organs at 1 hour, days 1, 3 & 7 after IV and IC injection (n = 3 in each group).	201
Table A4.1 <i>Ex vivo</i> quantification of radioactivity distribution (%ID/g) in all organs at 1 hour and day 3 after IV and IC injection in tumour bearing mice (n = 3 in each group).	203

Abbreviations

%ID	% injected dose
¹¹¹In	Indium-111
¹¹¹InCl₃	Indium-111 Chloride
¹²⁴I	Iodine-124
¹²⁴I-MIBG	¹²⁴ I-metaiodobenzylguanidine
¹²⁵I	Iodine-125
¹⁸F	Fluorine-18
¹⁸F-5-FPN	¹⁸ F-5-fluoro-N-(2-[diethylamino] ethyl) picolinamide
¹⁸F-FDG	¹⁸ F-fluorodeoxyglucose
¹⁸F-FESP	¹⁸ F-fluoroethyl spiperone
¹⁸F-FHBG	9-(4-[¹⁸ F]Fluoro-3-hydroxymethylbutyl)guanine
¹⁹F	Fluorine-19
3D	Three dimensional
⁶⁴Cu	Copper-64
⁸⁹Zr	Zirconium-89
^{99m}Tc	Technetium-99m
ADSCs	Adipose derived mesenchymal stem cells
AKI	Acute kidney injury
Bcl-2	B-cell lymphoma 2
BLI	Bioluminescence imaging
CABI	Centre for advanced biomedical imaging
CCD	Charged couple device
CCL5	Chemokine ligand 5
CD	Cluster of differentiation
CdSe	Cadmium selenide
CT	Computed Tomography
CXCR4	Chemokine receptor type 4
D2R	Dopamine 2-like receptor
DLS	Dynamic light scattering
DMEM	Dulbecco's modified Eagle's medium
DMEM-F12	Dulbecco's modified Eagle's medium nutrient mixture F12 Ham
DMSO	Dimethyl sulfoxide
DOTA	1,4,7,10-tetraazacyclododecane-1,4,7,10-tetraacetic acid

DTPA	Diethylenetriaminepentaacetic acid
EC	Endothelial cells
EDC/sulfo-NHS	1-Ethyl-3-[3-dimethylaminopropyl]carbodiimide-hydrochloride/(N-hydroxysulfosuccinimide)
EDTA	Ethylenediaminetetraacetic acid
EF	Ejection fraction
ESC	Embryonic stem cells
FCS	Fetal calf serum
FDA	Food and drug administration
FLI	Fluorescence imaging
FMT	Fluorescence molecular tomography
Gd³⁺	Gadolinium-III
GFP	Green fluorescent protein
GNP	Gold nanoparticles
GNR	Gold nanorods
H & E	Haematoxylin and eosin
HCl	Hydrochloric acid
HEPES	4-(2-hydroxyethyl)-1-piperazineethanesulfonic acid
hFTH	human ferritin heavy chain
HMPAO	Hexamethylpropylene amine oxime
HPLC	High-performance liquid chromatography
HSC	Haematopoietic stem cell
HSV1-tk	Herpes Simplex Virus type 1 thymidine kinase
HU	Hounsfield Units
IA	Intra-arterial
IC	Intracardiac
IFN-β	Interferon β
IGF-1	Insulin-like factor 1
IHC	Immunohistochemistry
IL6	Interleukin 6
IL8	Interleukin 8
iPSC	induced pluripotent stem cells
IV	Intravenous
keV	kilo electron Volt
kVp	kilo volt peak

LUC	Firefly luciferase enzyme
MBq	Megabecquerel
MCP-1	Monocyte chemoattractant protein-1
MES	2-(N-morpholino)ethanesulfonic acid
MIP	Maximum intensity projection
MRI	Magnetic resonance imaging
MSC	Mesenchymal stem cell
NET	Norepinephrine transporter
NIR	Near infra-red
NIS	Sodium-iodide symporter
NSC	Neural stem cells
NSG	Non-obese diabetic/severe combined immunodeficiency/gamma
Oatp1a1	Organic anion transporting polypeptides
oxine	Oxyquinolone
PA	Photoacoustic
PBS	Phosphate buffered saline
PEG	Polyethylene glycol
PET	Positron emission tomography
PFA	Paraformaldehyde
PFC	Perfluorocarbon
QD	Quantum dots
RARE	Rapid acquisition with relaxation enhancement
ROI	Region of interest
SD	Standard deviation
SDF-1	Stromal-cell derived factor 1
SPECT	Single photon emission computed tomography
SPION	Superparamagnetic iron oxide nanoparticle
Sr	Steradian
TAF	Tumour associated fibroblast
TE	Echo time
TEM	Transmission Electron microscopy
TGFβ1	Transforming growth factor β1
TLC	Thin layer chromatography
TR	Repetition time
TRAIL	Tumour necrosis factor-related apoptosis inducing ligand

UCL	University College London
VCAM-1	Vascular cell adhesion molecules 1
VEGF	Vascular endothelial growth factor
ZnS	Zinc sulphide

Chapter 1

Introduction

1.1 Overview of stem cell therapy

Stem cell transplantation has become the future of clinical medicine as it could potentially solve the problem of organ donor shortage, the failure of standard medications to treat cancer and the inability to halt the progression of terminal diseases. Clinical trials using stem cell products have been expanding over the years to develop adjuvant therapies for cancer as well as to provide regenerative treatment for cardiovascular diseases, multiple sclerosis, stroke and many other diseases. To date, a total of 1052 novel stem cell therapies have been registered as clinical trials and 393 trials have been completed in 2017 (*Fung et al., 2017*). According to the 2017 report for cell therapy in clinical trials (*Fung et al., 2017*), 75% of the clinical trials were financed by public funding which includes academic institutions and charities and 25% by industry such as pharmaceutical companies. Although there has been substantial investment and growing research in stem cells therapies, the majority of trials are still in early phase. There are a few cell therapies which have been shown to be beneficial in treating patients with advanced diseases, such as cancer but most have reported highly variable outcomes and many more have failed to show therapeutic efficacy (*Fisher et al., 2014; Marks et al., 2016*).

Many randomised clinical trials using stem cells for haematological malignancy and breast cancer reported improved disease-free survival rates, shorter hospital stays and overall survival rate (*Fernand et al., 2005; Nitz et al., 2005; Balduzzi et al., 2005*), but others have reported no statistically significant difference in these parameters (*Peters et al., 2005; Breems et al., 2005*). The same scenario has been reported in the use of stem cells as regenerative therapy. Although stem cell therapies have been shown to increase cardiac function in chronic ischaemic heart disease (*Assmus et al., 2013; Honold et al., 2012; Nguyen et al., 2016*), no evidence of functional improvement has been found in other studies (*Clifford et al., 2012; Jeevanantham et al., 2012; Nguyen et al., 2016*). However, there is no clear explanation for these discrepancies due to a lack of sufficient information on the fate of stem cells after transplantation. In addition, further studies are required to focus on the safety of stem cell-based therapies. Therefore, new imaging techniques for monitoring and evaluating the effectiveness and safety of stem cell therapy are urgently needed to acquire the location of viable stem cells in target organs alongside their therapeutic responses.

1.2 Cell types

Selecting the suitable stem cell type is one of the inconsistencies which has been reported by many preclinical and clinical studies. Stem cells are found within most organs of the body and are responsible for repairing and the regeneration of tissues throughout life. Stem cells are able to both self-renew, and differentiate into more than one cell type, making them ideal for regenerative therapy. The majority of cell therapy studies have used autologously derived cells, isolated from the patient own tissues, but it is also possible to utilise allogeneically derived stem cells which could offer a more realistic “off-the-shelf” approach for wide reaching cell therapies (*Fang et al., 2004*). However, presence of stem cells in adult heart and kidney is still controversial because there is no strong evidence for their existence and their regenerative capacity has been shown to be limited (<https://www.statnews.com/2018/10/14/harvard-brigham-retractions-stem-cell/>; *Humphreys 2014; Santeramo et al., 2017*)

Haematopoietic stem cell (HSC)

Among the different types of stem cell therapies, HSC transplantation is the earliest, most established and widely available cell therapy in the clinic. One of the main characteristics of HSCs is the ability to restore all haemopoietic cell lineages after bone marrow suppression (*Shizuru et al., 2005*). HSCs are routinely isolated from bone marrow, but pure HSC populations are rare and difficult to identify due to the heterogeneity of bone marrow cells (*Rector et al., 2013*). Therefore, HSCs are increasingly isolated from umbilical cord blood for clinical applications (*Ng et al., 2009*). The successful application of HSCs in haematological malignancies has changed the field of stem cell transplantation. Since the first therapy of HSC bone marrow transplantation in 1956 (*Thomas et al., 1957*), the development of stem cell research has increased tremendously due to advances in immunology and molecular biology.

Embryonic stem cells (ESCs) and induced pluripotent stem cells (iPSCs)

In addition to adult stem cells, researchers has found ESCs within the inner cell mass of mammalian blastocysts and they can be isolated during early embryonic development, typically 4-5 days in humans (*Rippon et al., 2004*). ESCs are pluripotent which means they have the ability to transform into any adult cell type derived from the three germ layers (ectoderm, mesoderm and endoderm, *Thomson et al., 1998*). Human ESC derived adult cells such as retinal pigmented epithelial cells have been used to treat macular degeneration diseases where the regeneration capabilities of other adult stem cells are limited (*Schwartz et al., 2012, 2015*). Due to ethical issues and the difficulty in obtaining sufficient cell doses from human sources, their use has been greatly restricted. As an alternative solution for

ESCs, iPSCs have been generated from adult cells by genetic reprogramming to achieve pluripotency (*Pengfei et al., 2016*). Although, iPSCs closely resemble ESCs and display the possibilities for replacing ESCs in regenerative medicine, various safety concerns including tumorigenicity remain unsolved (*Ben-David et al., 2011*).

Neural stem cells (NSCs)

NSCs are multipotent progenitor cells which have the ability to generate all neural lineages: neurons and all types of neuroglia cells (*Johe et al., 1996*). NSCs can be derived from neural tissue or extracted from embryonic brain tissue (*Johe et al., 1996*). Due to promising preclinical study results, NSCs have rapidly gained interest within the field of regenerative medicine to treat various neurodegenerative diseases including Parkinson's (*Ryu et al., 2005; Freed et al., 2001*) and Huntington's diseases (*McBride et al., 2004; Lindvall et al., 2012*). Nonetheless, their clinical translation is still in the early phases due to limited availability and lack of extensive knowledge in the basic biology of NSCs.

Mesenchymal stem cells (MSCs)

MSCs are non-haematopoietic adult stem cells which have the ability to differentiate into multiple lineages (*Dominici et al., 2006*). They can be readily isolated from different sources including bone marrow, adipose tissue, umbilical cord and amniotic fluid. Since MSCs are highly accessible and easily expandable *in vitro* with few ethical issues, they have become the favoured cell type for clinical trials. In addition, they have immunomodulatory properties and the ability to home to and incorporate into areas of inflammation such as tumours. Currently, MSC-based cell therapies make up approximately 14% of all cell therapy trials within the UK (*Sage et al., 2016*).

1.3 The properties of MSCs and their applications

Paracrine and endocrine signalling

MSCs have the capacity to differentiate into mesodermal lineages such as adipocytes, chondrocytes and osteocytes and have been used in cartilage and bone repair (*Oshima et al., 2004; Vilquin et al., 2006*). In addition, MSCs have been successfully differentiated into cardiomyocytes *in vitro* (*Noort et al., 2010; Ramkisoensing et al., 2011*) and applied in cardiac regeneration after myocardial infarct. Although there is no strong evidence of *in vivo* transformation of MSCs into cardiomyocytes, some studies have reported the improvement in cardiac function after MSC transplantation (*Nagaya et al., 2005; Berry et al., 2006*). Similar findings have been published using MSC-based cell therapies for end stage liver diseases (*Shi et al., 2012; Meier et al., 2013*), ischemic stroke (*Bakondi et al., 2009, Muir et al., 2017*) and chronic kidney diseases (*Choi et al., 2009; Eirin et al., 2014*). The results from

these studies indicate that the primary mechanism behind the regenerative capacity of MSCs is likely to be paracrine or endocrine signalling. Therefore, MSCs should be regarded as mesenchymal stromal cells rather than stem cells to more accurately reflect their ability to secrete trophic factors (*Caplan 2017*; <https://www.nature.com/articles/d41586-018-06756-9>)

MSCs secrete a number of active biological factors which are involved in different signalling processes: 1) growth factors, such as vascular endothelial growth factor (VEGF, *Yuan et al., 2011*); 2) immune system signalling, such as monocyte chemoattractant protein-1 (MCP-1, *Gnecchi et al., 2009*); 3) apoptosis regulator protein, such as B-cell lymphoma 2 (Bcl-2, *He et al., 2009*). Through these signalling molecules, MSCs have been shown to increase epithelial proliferation, promote angiogenesis and aid in cellular repair after tissue injury (*Gnecchi et al., 2009*). Conditioned medium derived from bone marrow MSCs, concentrated with different types of growth factors and chemokines (cell free), has been shown to increase healing in mice indicating the importance of MSC paracrine signalling within the wound repair mechanism (*Chen et al., 2008*). In addition, MSCs have the ability to respond to tissue repair signals by interacting with different types of immune modulators. In a mouse model of liver fibrosis, MSCs were shown to be able to migrate to the site of injury via stromal cell derived factor 1 (SDF1)/CXCR4 axis (*Zhang et al., 2015*). A number of cytokines including MCP-1 are secreted by MSCs and this has been reported to be involved in vascular remodelling and reduction of fibrosis in a mouse model of hind limb ischaemia (*Kinnaird et al., 2004*).

Immunomodulation

MSCs have the ability to migrate to sites of inflammation and decrease pro-inflammatory responses by reprogramming monocytes and macrophages (*Yi et al., 2012*), suppressing cytokine production by T cell (*Yi et al., 2012*) and secreting anti-inflammatory cytokines such as prostaglandin E2 (*Bouffi et al., 2010*). Due to these immunosuppressive properties, MSCs have been successfully applied in clinical trials to treat graft versus host disease (*Herrmann et al., 2011*; *Introna et al., 2013*), and implemented in many autoimmune diseases including rheumatoid arthritis (*Augello et al., 2007*) and type 1 diabetes (*Unsal et al., 2015*). Moreover, transplanted MSCs in an animal model of myocarditis were shown to reduce inflammation via the MCP-1 signalling pathway (*Ohnishi et al., 2007*).

Tumour homing

One of the unique properties of MSCs is their ability to home to and incorporate into tumours. Hence, they are being developed as delivery vehicles for therapeutic cancer agents. However, the detailed mechanisms and signalling pathways which initiate the homing process have not been fully elucidated. It is known that endogenous MSCs are able

to recognise inflammatory signals secreted during tissue injury and have the ability to migrate to injury sites and repair wounds (*Shah 2014*). Since tumours are regarded as wounds that do not heal, the tumour micro-environment secretes many inflammatory mediators which are believed to stimulate MSC homing to tumour tissue. Different types of cytokines such as interleukin 6 (IL6, *Shi et al., 2007*), chemokines such as interleukin 8 (IL8, *Kim et al., 2009*), growth factors such as platelet-derived growth factor-BB (*Klopp et al., 2007*) and MCP-1 mediated immune response (*Dwyer et al., 2007*) have been shown to be involved in attracting MSCs. Among them, the SDF1/CXCR4 signalling pathway plays a significant role in MSC migration. SDF1 is known to be secreted by many types of tumour and interacts with its receptor CXCR4 which is expressed on the surface of MSCs (*Lourenco et al., 2015*). In addition, the homing and integration of MSCs into tumour tissue requires interaction with endothelial cells (ECs), in a process called transendothelial migration. However, the exact mechanism used by MSCs is still unclear. It is broadly assumed that MSCs have a similar mechanism as leukocytes homing to infection and inflammation by tethering and rolling as a prelude to extravasation into tissues. A number of cell adhesion molecules such as P-selectin (*Lo et al., 2013*) and vascular cell adhesion protein 1 (VCAM-1, *Rüster et al., 2006*) have been shown to be involved in interaction with ECs to aid MSC transendothelial migration.

Due to their inherent tumour homing property (Figure 1.1), MSC-based cancer therapies have been extensively studied as adjuvant therapies to conventional therapies such as chemotherapy and radiotherapy in order to improve specificity to target cancer cells (*Kauer et al., 2011; Sage et al., 2016*). Many studies have explored MSCs as a delivery vector to carry anti-cancer agents for targeted cancer therapy. Human MSCs have been modified to express pro-apoptotic proteins such as tumour necrosis factor-related apoptosis inducing ligand (TRAIL) and have been successfully applied to induce tumour cell apoptosis in a mouse model of glioblastoma after surgical debulking (*Kauer et al., 2011*) and in mouse models of lung tumours (*Sage et al., 2014; Loebinger et al., 2009*). Other anti-cancer agents transported by MSCs include: drug-loaded nanoparticles such as doxorubicin-containing silica nanorattles (*Li et al., 2011*); viral mediated transfer of tumour-suppressed genes, for example, interferon β (IFN- β , *Ling et al., 2010*); and oncolytic virus such as the oncolytic measles virus (*Ong et al., 2013*). Although MSCs have been shown to travel to sites of tumour after systemic infusion, the homing mechanism has been shown to be transient and inefficient (*De Becker et al., 2016*). Various strategies have been explored to increase the homing efficiency, for example, by overexpressing chemokine receptors on MSCs via genetic modification (*Bobis-Wozowicz et al., 2011*) or by priming MSCs with conditioned medium obtained from tumour cells (*Gao et al., 2009*). Another study also reported an

increase in the levels of MSCs within tumour after irradiation due to increased expression of the cytokines and growth factors such as VEGF in tumour (Klopp *et al.*, 2007).

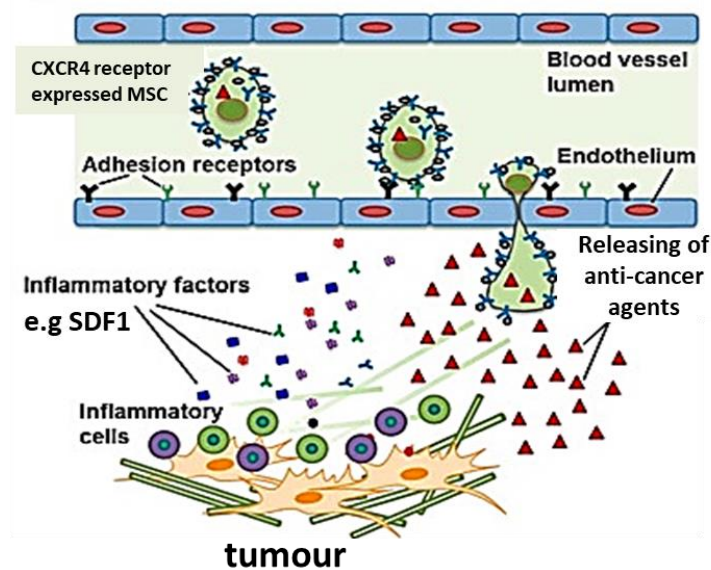


Figure 1.1 Schematic representations of possible mechanisms behind MSC homing to tumour and their use as carriers for anti-cancer therapy (adapted from Levy *et al.*, 2013).

Although many research groups have shown the therapeutic benefit of MSC-based therapies in various tumour studies (Loebinger *et al.*, 2009; Stuckey *et al.*, 2013; Sage *et al.*, 2014), others have reported the hazardous nature of MSCs, such as enhancing tumour progression and metastasis (Karnoub *et al.*, 2007). The complex mechanisms driving the pro-tumorigenic effect of MSCs are believed to be based on interactions between MSCs and tumour associated fibroblasts (TAF, Mishra *et al.*, 2008), the differentiation of MSCs into TAF (Jeon *et al.*, 2008) and the subsequent release of large amounts of chemokines such as chemokine ligand 5 (CCL5) (Jotzu *et al.*, 2010). In a mouse model of mammary breast tumour, the rate of tumour growth was shown to be significantly increased after co-injection of adipose tissue derived MSCs and breast tumour cells when compared to breast tumour cells alone (Muehlberg *et al.*, 2009). In addition to preclinical studies, clinical data has also reported the increase incidence of relapse in patients with leukaemia after co-transplantation of MSCs and HSCs (Ning *et al.*, 2008). Therefore, further studies are required to investigate the safety of MSC-based cancer therapies and therefore imaging tools are urgently needed to monitor their potential adverse effect.

1.4 Monitoring cell therapies *in vivo*

Although MSC-based therapies have been used in many diseases, their clinical translation is still within the early phases of clinical translation due to significant variabilities in their therapeutic efficacy. The potential effectiveness of a cell therapy is based on many factors:

1) the successful delivery of cells to the target organ using optimal route of administration, 2) the number of viable cells retained after transplantation to initiate their effect and 3) the length of cell survival at the engraftment site (*Perin et al., 2003*). However, there are some evidence suggesting that therapeutic efficacy is not always related to cell engraftment at the target organ. One study has reported improved renal function in mouse model of acute kidney injury although human kidney derived CD133+ cells failed to engraft in damaged kidney (*Santeramo et al., 2017*). In mouse model of graft-versus-host disease, MSC apoptosis in lungs has been reported to be important for immunomodulation (*Galleu et al., 2017*). These studies suggest that the requirement for cell survival and engraftment in target organ is not always compulsory and probably dependent on the cell types and disease models. For example, the engraftment of pluripotent stem cells in the diseased eye is necessary to repair and replacement of retinal neurons in degenerative eye disease (*Singh et al., 2018*).

Non-invasive *in vivo* imaging technologies play a vital role in visualizing transplanted cells in various diseased organs and assessing early response to therapy. The ideal imaging method should provide sufficiently high sensitivity and specificity to locate the transplanted cells within disease organs and monitor their fate and survival. Also, the technique should be able to quantify the numbers of viable implanted cells and should permit longitudinal long-term tracking of the cells. Currently, there is no single imaging modality that can fulfil all of these needs but there are various *in vivo* imaging methods that can be used to track cells. There are two general approaches in cell labelling: direct cell labelling and reporter gene imaging. Several important criteria's need to be considered for all cell labelling methods, which are biocompatibility, toxicity and safety not only to the stem cell but also to the target organ.

1.5 Direct cell labelling

In order to detect the location of the transplanted cells after delivery, stem cell can be directly labelled with various imaging probes depending on the imaging modality used. Direct labelling is one of the most widely used methods for stem cell labelling (*Guzman et al., 2007*) because it is relatively simple and there is no need to genetically modify the cells. Labelling is readily achieved by introducing labelling agents, for example, nanoparticles. These labelling agents are internalised by cells and serve as a surrogate measurement for cell imaging. Advances in imaging technologies have resulted in the development of next generation labelling agents which have superior quality over conventional agents. However, the effect of labelling agents on cell viability and functionality must be carefully considered before applying to *in vivo* studies.

Fluorescence imaging (FLI)

FLI is one of the most commonly used molecular imaging techniques in cellular imaging. In order to track the cells with FLI, the cells need to be labelled with fluorescent contrast agents which are known as fluorophores. The principle of FLI is based on the excitation of a fluorophore by a light source resulting in the emission of light signal which is detected by a highly sensitive charged couple device (CCD) camera. The electrons in a fluorophore absorb light energy from photons at a specific wavelength. Electrons in an excited state interact with surrounding molecules and the absorbed energy is released by fluorescence emission before they return to ground state. The electrons in the outermost orbital are important in determining the excitation and emission wavelength of a fluorophore, thereby influencing the duration and strength of fluorescence signal.

The desirable features of fluorophores for *in vivo* cell tracking applications are: small in size; non-cytotoxic; biocompatible; and that they can produce a bright signal with low background fluorescence. Fluorophores with lower emission wavelengths are not suitable for *in vivo* FLI due to the absorption of light by endogenous compounds such as haemoglobin and lipids. Therefore, near infra-red (NIR) dyes which have an emission spectra range from 700-1000 nm are the preferred choice for *in vivo* FLI and many NIR dyes such as DiD, Dil and Dio have already been used to track MSCs in small animal models (*Sutton et al., 2008; Progatzy et al., 2013*). However, some NIR lipophilic dyes, for example, Dil have been shown to be unsuitable for *in vivo* cell tracking due to intracellular transfer of the dye to the neighbouring cells (*Lassailly et al., 2010*). Moreover, a study focusing on tracking T helper cells in a mouse model of pancreatic tumour has demonstrated that mouse fur and skin pigmentation drastically reduced fluorescence signal and increased background autofluorescence, both major limitations of *in vivo* FLI. (*Bergers et al., 1999*).

Quantum dots (QD), also known as fluorescent semiconductor nanocrystals, can provide narrow emission ranges with a broad excitation spectrum resulting in reduction of autofluorescence. In addition, QDs possess many advantages over traditional fluorophores such as brighter signal, better photostability and size-tunable optical properties. QDs are comprised of semiconductor cores such as gold and cadmium. QDs with a cadmium selenide (CdSe) core surrounded by a zinc sulphide (ZnS) shell are the most commercially available QDs composition and have been used to track ES cells *in vivo* (*Lin et al., 2007*). However, the prospect of QDs in cell tracking is hindered by their cytotoxic effect on cells (*Muller-Borer et al., 2007*).

The advantages of FLI imaging in cell tracking is that it is reasonably inexpensive, widely available, and the labelling procedure is simple and quick as many can be performed under

5 minutes. Although FLI can provide single cell sensitivity *in vitro*, poor spatial resolution and signal quantification are the main drawbacks *in vivo* due to tissue absorption and light scattering. Over the last few years, some progress has been made to resolve these problems. Fluorescence molecular tomography (FMT) has been developed with the ability to acquire a 3D quantitative diffusion pattern of NIR dyes in mouse models (*Ntziachristos et al., 2008*). However, it is unlikely that FLI will be applied in the clinic due to limited tissue penetration.

Photoacoustic (PA) imaging

Due to the recent advances in medical physics, the development of PA imaging has emerged as a molecular imaging modality which can overcome the inherent limitations of optical imaging. The principle of PA is based on laser illumination of either endogenous or exogenous optical chromophores which absorb optical energy, this is then converted into heat followed by thermoelastic expansion and the production of acoustic waves. Because of its ability to excite endogenous optical chromophores such as haemoglobin and melanin, the applications of PA have been mainly utilised for imaging vascular structures (*Oladipupo et al., 2011*), tumour angiogenesis (*Siphanto et al., 2005*) and skin melanoma (*Oh et al., 2006*). Moreover, PA has previously been implemented in cell tracking by directly labelling the cells with exogenous contrast agents including NIR dyes (*Berninger et al., 2017*), gold nanorods (*Comenge et al., 2016*) and carbon nanotubes (*Bhattacharya et al., 2014*). Although PA imaging is a relatively new technique within the field of cell tracking, the main strengths of PA is that it can offer better penetration depth and higher spatial resolution than optical imaging due to the reduced scattering of acoustic waves in tissue. However, the imaging depth is still limited in PA due to light attenuation, thereby it is only suitable for cell tracking within superficial organs such as skin and musculoskeletal in humans (*Xu et al., 2016; Jo et al., 2018*). Furthermore, due to the difficulty in determining local light distribution in tissues, PA signal cannot be used to reliably measure and quantify cell number.

Magnetic resonance imaging (MRI)

MRI has become an important imaging tool for non-invasive stem cell tracking in living subjects as it can provide excellent spatial resolution of cell localisation. MRI has been routinely used in the clinic to acquire real time information from diseased organs due to its superior ability to delineate between different tissue contrasts within the same anatomical organ by controlling the sequence-dependent parameters. The principle of MRI is based on using radiofrequency pulses to excite hydrogen nuclei (protons) within a sample that has been placed in a strong static magnetic field. This causes the protons to spin and generate an electrical signal which can be detected by the MRI scanner. After proton excitation, two

main types of signal relaxation processes occur; longitudinal (T_1) relaxation; and transverse (T_2) relaxation. In general, T_1 relaxation is the transfer of energy from the excited nuclei to its surroundings and T_2 relaxation is the loss of magnetisation due to the change in random orientations of excited nuclei in transverse plane. The human body contains an abundance of protons leading to strong MRI signals, whilst the different environments in which protons reside leads to different T_1 and T_2 relaxation times and hence endogenous image contrast.

To further increase image contrast, exogenous contrast agents can be used. MRI contrast agents which are mainly used in medical imaging are based on paramagnetic gadolinium-III (Gd^{3+}) chelates or superparamagnetic iron oxide nanoparticles (SPIONs). Gd^{3+} -based contrast agents are known as positive contrast agents because they predominantly shorten T_1 relaxation times and propagate signal hyperintensity. Although Gd^{3+} -based agents have been used in clinical MRI since the 1980s, they are less commonly used as cell tracking agents due to inefficient cell internalisation and cell toxicity due to the high concentrations needed for cell based MR contrast (*Rudelius et al., 2003*).

Due to their high sensitivity in MRI and high cell labelling efficiency, SPIONs have become the preferred labelling agents for MRI cell tracking techniques. SPIONs have been extensively used to monitor stem cell therapies in animal models of myocardial infarct (*Stuckey et al., 2006*), ischemic strokes (*Walczak et al., 2008*) and cancer (*Ruan et al., 2012*). Since the success of tracking dendritic cells in melanoma patients (*de Varries et al., 2005*) and NSCs in patients with traumatic brain injury (*Zhu et al., 2006*), the use of SPIONs in clinical trials for stem cell therapies has increased rapidly. The main concept of SPION-based MR imaging is that highly magnetic iron oxides create local magnetic field inhomogeneities, dephasing the excited protons and causing shortening of T_2 and the related T_2^* relaxation time (*Sosnovik et al., 2008*). T_2^* is more sensitive to iron induced proton dephasing than T_2 and thus SPIONs generate hypointense regions of reduced signal on MR images when T_2^* weighted sequences are applied. The negative contrast from SPION labelled cells is thus representative of cell localization allowing their detection *in vivo*.

However, signal quantification has proven to be challenging due to the effect of SPIONs on the surrounding tissue leading to overestimation of the signal. In addition, the negative contrast can be difficult to differentiate from normal tissue with high iron content or within an air filled organ like lungs. A wide variety of mathematical calculations have been published to resolve this issue but there is still a huge scepticism over the correlation between cell number and SPION signal. Although SPIONs are known to be biocompatible and have no adverse effect on cell viability and cell function, some studies have reported that SPION labelled MSCs lose some aspect of differentiation capacity in a concentration-dependent

manner (*Andreas et al., 2012*). This problem can be potentially resolved by changing the coatings of the SPIONs or reducing the SPION concentration depending on the cell type.

To overcome the disadvantages of SPION, some studies have reported the use of perfluorocarbon (PFC) nano-emulsions in cell tracking with fluorine-19 (^{19}F) MRI. The advantages of ^{19}F -based cell tracking is the number of accumulated ^{19}F is directly proportional to the amount of signal intensity, which allows reliable quantification of ^{19}F labelled cells *in vivo* (*Srinivas et al., 2010*). ^{19}F -based cell tracking has been applied to the tracking of different stem cell types including NSCs (*Boehm-Sturm et al., 2011*) and MSCs (*Gaudet et al., 2015*) in various types of disease models, such as stroke (*Bible et al., 2012*) and lung metastases (*Makela et al., 2018*). However, compared to SPION imaging, the ^{19}F imaging set up is technically challenging, less sensitive and cell labelling with PFC can be complex.

As described above, MRI-based cell tracking techniques can provide high spatial resolution of cell localisation with superb soft tissue contrast, but the problem of reliable quantification of the number of transplanted cells within a target organ remains unsolved.

Nuclear imaging

Nuclear imaging has been used to detect stem cell localisation by labelling cells with radionuclides and imaging with either positron emission tomography (PET) imaging or single photon emission computed tomography (SPECT). The principle of PET imaging is based on positron emitting radionuclides with different half-lives such as Fluorine-18 (^{18}F): 110 minutes or Zirconium-89 (^{89}Zr): 3.3 days. When a low energy positron collides with a low energy electron within the body, an annihilation event occurs resulting in the generation of two high energy gamma ray photons (511 kilo electron Volt- keV) which travel in exact opposite directions (180 degrees). These photons are detected by a ring of scintillation crystals within the PET scanner and reconstructed into three dimensional (3D) images. The principle of SPECT imaging is similar to PET, the main difference being that the SPECT scanner detects a single gamma ray emitted from gamma emitters such as Technetium-99m ($^{99\text{m}}\text{Tc}$): 6 hours and Indium-111 (^{111}In): 2.8 days. As the level of energy emitted is proportional to the amount of photons detected, the SPECT scanner utilises pinhole collimators to determine the direction of the photons and filter them onto the gamma camera (scintillation crystal bed). Depending on the size and shape of the collimators, the sensitivity and the spatial resolution of SPECT images can be modified. Therefore, compared to SPECT, PET imaging can provide better sensitivity and resolution.

Food and drug administration (FDA) approved radiotracers such as ^{111}In -oxyquinolone (oxine) and $^{99\text{m}}\text{Tc}$ -hexamethylpropylene amine oxime (HMPAO) have been used to track

stem cells in different animal models including cerebral ischemia (*Detante et al., 2009*) and myocardial infarct (*Kraitchman et al., 2005*). ^{111}In -oxine cell labelling is one of the most established techniques in cell tracking which has been used in the clinic since the 1970s to track white blood cells to areas of inflammation (*Thakur et al., 1977*). This method has been successfully applied to track human MSCs in a mouse model of neuroblastoma (*Cussó et al., 2014*). Moreover, a clinical study using ^{111}In -oxine has reported the tracking of transplanted MSCs in patients with advanced liver cirrhosis (*Gholamrezaezhad et al., 2011*). However, the main drawback of ^{111}In -oxine labelling is its cytotoxic effect on cell proliferation and function. By using the oxine, a lipophilic chelator, radiotracers can cross the cell membrane where they subsequently dissociate and bind to intracellular proteins and DNA causing cell toxicity and ultimately leakage of the tracer. Although a labelling efficiency of over 80% is achievable, both the labelling efficacy and cell toxicity is highly dependent on the labelling method and cell type used. As an alternative to ^{111}In -oxine, $^{99\text{m}}\text{Tc}$ -HMPAO has been shown to have fewer adverse effects (*Botti et al., 1997*) due to its lower gamma energy (140 keV) compared to ^{111}In (171 and 245 keV), and it has previously been used to track different stem cell types (*Gleave et al., 2011*; *Detante et al., 2009*). However, due to its shorter half-life of 6 hours, $^{99\text{m}}\text{Tc}$ -HMPAO cannot be used for longitudinal cell tracking.

Owing to its enhanced resolution and sensitivity, PET radiotracers are expected to be more useful and efficient than SPECT. ^{18}F -fluorodeoxyglucose (^{18}F -FDG) is the most common PET radiotracer which is routinely used in clinic to detect many types of tumour. ^{18}F -FDG has also been used in the monitoring of cell migration to areas of myocardial infarct (*Doyle et al., 2007*) as well as tracking NSCs *in vivo* (*Stojanov et al., 2012*). However, the major drawback of this tracer is poor cell labelling efficiency and its short half-life of 110 minutes. Recently, in preclinical studies, ^{89}Zr -based cell labelling has been shown to be a better method for cell tracking with PET due to its long half-life: 3.3 days (*Bansal et al., 2015*; *Charoenphun et al., 2015*) but further evaluations are still required to progress into clinical translation.

Despite the dose dependent cytotoxic effect and poor spatial resolution of nuclear imaging, it is the only modality that can provide reliable quantification of the amount of cells in target organs. By using $^{99\text{m}}\text{Tc}$ -HMPAO labelling, the distribution of rat and human MSCs in different organs has been quantified and compared to investigate the clearance mechanism of MSCs from the body (*Khabbal et al., 2015*). In addition, nuclear imaging can provide superior cell detection sensitivity than MRI. In a canine model of myocardial infarct, both ^{111}In -oxine and SPION were used to track MSCs and the results showed nuclear imaging to be more sensitive than MRI in detecting low numbers of cell engraftment within the infarct area (*Kraitchman et al., 2005*). However, unlike MRI which does not use ionizing radiation,

nuclear imaging is less suitable for repeated imaging due to the risk of accumulated radiation dose.

Computed tomography (CT) imaging

CT imaging is one of the most widely available imaging modalities in diagnostic radiology, being used more frequently than MRI as it is less expensive, faster and easier to operate. The principle of CT imaging is based on the detection of X-ray energy, generated from a source that rotates around the patient. When X-rays pass through the body, they are deflected or absorbed to different degrees resulting in different levels of X-ray attenuation which is detected by the camera in the CT scanner and converted into 3D tomographic images. Since the difference between the electron density of bone and the surrounding soft tissue is vast, CT can easily detect the pathology of bone structures but has limited distinction between tissues with similar densities. Therefore, materials with high atomic numbers (Z) can provide good contrast in CT images. For example, iodine (Z = 53), barium (Z = 56) and gold (Z = 79) have been used as CT contrast agents for various medical applications such as the detection of blood vessels and imaging gastrointestinal tract to diagnose the abnormalities (*Clark et al., 2013; Wathen et al., 2013*).

Compared to other conventional cell tracking techniques, CT is not widely regarded as a molecular imaging technology and cell tracking with CT is a relatively new concept but has gained attention over the last few years. Since gold can provide good CT contrast and is known to be non-toxic, gold nanoparticles (GNP) have become an attractive labelling agent for cell tracking with CT. One study has explored the potential application of GNP labelling to monitor the distribution of implanted tumour cells in rat brain (*Menk et al., 2011*) and another study has been able to track GNP labelled immune cells to subcutaneous tumours (*Meir et al., 2015*). *Betzer et al.*, have also demonstrated the feasibility of monitoring GNP labelled MSCs in a mouse brain after direct injection (*Betzer et al., 2014*). Although CT imaging can offer the possibility of tracking cells with a more affordable clinical imaging modality, its progress is greatly hindered by the low sensitivity of CT imaging to the concentration of labelling agent. For example, in MRI, SPIONs can influence the T_2 relaxation time of the surrounding tissues with micromolar concentrations. Whereas, due to the lack of signal intensifying ability in CT, millimolar concentration of labelling agent is required to achieve adequate sensitivity.

In summary, direct cell labelling with different imaging probes is an effective method for imaging cell localisation after delivery. The main advantages of direct cell labelling is that it provides good signal-to-noise due to very little background. Direct cell labelling is also mostly suited to the detection of cells shortly after administration rather than long term imaging due

to dilution of the tracer with cell division. However, the main disadvantage is that the quantitative assessment of cell viability is not achievable with direct labelling, this is because signal from the imaging probe may remain after cell death or incorporate into resident phagocytic cells. For example, the leakage of radiotracers from cellular debris or the release of nanoparticles from dead cells which are subsequently engulfed by macrophages.

1.6 Reporter gene imaging

Reporter gene imaging can be achieved by incorporating the desired reporter gene into the DNA of the stem cell before transplantation. Among different gene transfer methods, lentiviruses are the most commonly used viral vectors to transfer genes (*De et al., 2003*). Generally, reporter genes are translated into transmembrane pumps or symporters, enzymes or cell surface receptors. When an appropriate exogenous substrate is administered to the body, they interact with the reporter gene products and a signal is generated. In the case of cell death, there will be no expression of the reporter gene products, hence, no signal will be produced. Since the reporter gene is passed down to all daughter cells, there is no issue with signal loss or dilution after cell division. Therefore, this imaging approach is suitable for long term cell monitoring. Many studies suggest that the insertion of reporter gene does not change cell phenotype or the differentiation potential of stem cells (*Cao et al., 2008; Mader et al., 2013*). However, concerns over possible toxic effects on cells and the unknown implications of genetically modified gene products in the human body cannot be neglected. Reporter genes have been developed for optical, nuclear, MRI and PA imaging platforms with a range of success.

Fluorescent reporter gene imaging

Fluorescent imaging using green fluorescent protein (GFP) is one of the earliest examples of the application of reporter gene imaging for *in vivo* cell tracking (*Kaneko et al., 2001*). Although most fluorescent proteins can provide adequate sensitivity with strong light signal, their *use in vivo* is mainly for *ex vivo* validation of the presence of stem cells in target organs due to the significant light scatter and limited depth information discussed earlier in FLI (*Cao et al., 2008; Massoud et al., 2003*).

Bioluminescence imaging (BLI)

BLI is the most frequently used reporter gene imaging for stem cell tracking in small animal studies. It has been used heavily for imaging different types of stem cells (*Chen et al., 2008; Wu et al., 2003; Cao et al., 2007*) and monitoring cell viability in various animal models such as acute renal injury (Tögel et al., 2008), liver fibrosis (*Di Rocco et al., 2012*) and breast tumour (*Klopp et al., 2007*). As firefly (*Photinus pyralis*) luciferase is the brightest of the

luciferase genes available, it is the most commonly used in cell tracking with BLI. The concept is based on the oxidation of the D-luciferin substrate by the luciferase enzyme in the presence of oxygen, magnesium and ATP which results in light emission (wavelength: 550-570nm) (*Thorne et al., 2010*). Since firefly luciferase is a non-mammalian gene, BLI can provide a high signal to background ratio resulting in high sensitivity cell detection. In addition, the gene and substrate are well tolerated with minimal toxicity (*Tiffen et al, 2010; Kim et al., 2015*). Although there is a strong relationship between the photons of light emitted in BLI and the number of cells, quantitative imaging cannot be achieved with BLI due to the requirement of various cofactors such as oxygen during the light production. In addition, due to light scattering, BLI has a maximum penetration of 1 cm in depth and poor spatial resolution (*Zheng et al., 2017*). In order to improve this issue a mutant form of luciferase, which is thermostable and red-shifted with a maximum emission wavelength of 612 nm, has been created and has been shown to perform better than wild type luciferase (*Branchini et al., 2010*). In order to achieve a better anatomical localisation of viable cells, the integration of an optional X-ray or CT component is available for most commercial BLI machines. Nonetheless, BLI is only suitable for imaging small animals and will never ethically or practically translate to the clinic.

PA reporter gene imaging

Although PA imaging is a relatively new technique within the medical imaging field, encouraging results from PA reporter gene imaging has demonstrated that it is a promising modality for cell tracking applications. Since PA imaging can provide enhanced penetration depth and higher resolution than FLI, fluorescent proteins such as the far-red fluorescent protein E2-Crimson (*Liu et al., 2013*) and NIR fluorescent proteins derived from bacterial phytochrome (*Filonov et al., 2012*) have been shown to be feasible for tracking cells using PA imaging. However, the main limitations of these proteins are low photostability and transient absorption effects which make them not appropriate for long term imaging (*Brunker et al., 2017*).

The LacZ gene, a common chromogenic reporter gene has also been explored as a PA reporter gene. LacZ expresses β -galactosidase, an enzyme which is responsible for lactose metabolism. β -galactosidase can cleave the glycosidic linkage in X gal, a colourless lactose analogue, leading to the production of a blue chromogenic agent which can be detected by PA. Although the lacZ gene has been used in PA imaging to monitor subcutaneous tumour growth in mice (*Cai et al., 2012*), the inefficient delivery of X-gal systemically has hindered its widespread use in PA imaging (*Li et al., 2007*).

Melanin, an endogenous chromophore, can provide good PA contrast due to its high photostability and broad optical absorption spectrum, which extends beyond the background haemoglobin signal between 600 and 700 nm (*Paproski et al., 2011*). Therefore, tyrosinase which is the key enzyme involved in the synthesis of melanin has been implemented as a reporter gene for PA imaging. Several studies have reported the use of the tyrosinase-based reporter gene for monitoring tumour growth up to 52 days (*Jathoul et al., 2015*) and imaging MSCs in preclinical studies (*Märk et al., 2014*). Since melanin has high affinity for iron and the ability to bind the PET reporter probe, ^{18}F -5-fluoro-N-(2-[diethylamino] ethyl) picolinamide (^{18}F -5-FPN), the tyrosinase reporter gene has been used to track MSCs in a rat model of myocardial infarction using multimodal imaging (PA, MRI and PET) (*Liu et al., 2018*). However, the potential toxic effect of melanin on cells is still highly questionable and further evaluation studies with various cell types are required before it can be applied in stem cell therapy monitoring.

Nuclear reporter gene imaging

Many SPECT/PET genetic reporter systems such as the Herpes Simplex Virus type 1 thymidine kinase (HSV1-tk), dopamine 2-like receptor (D2R) and sodium-iodide symporter (NIS) have been successfully applied within the cell tracking field. One of the advantages of SPECT/PET genetic reporters is that they can provide tomographic information of cell localisation, quantitative information of cell viability and is clinically translatable.

HSV1-tk is the most commonly used genetic reporter for SPECT/PET imaging. It is an intracellular enzyme that phosphorylates an exogenously injected radiotracer such as 9-(4-[^{18}F]Fluoro-3-hydroxymethylbutyl)guanine (^{18}F -FHBG) resulting in the retention of the radiotracer within viable cells. This imaging method has been successfully utilized to monitor stem cell engraftment in a mouse model of subcutaneous tumour (*Hung et al., 2005*) and to track MSC viability in a swine model of myocardial infarction serially for 10 days (*Gyöngyösi et al., 2008*). Moreover, the first clinical use of HSV1-tk has been demonstrated in the tracking of cytolytic T lymphocytes in patients with glioma (*Yaghoubi et al., 2009*). The desirable feature of this imaging strategy is the signal amplification due to the phosphorylation of many molecules of radionuclides resulting in increased signal to background ratio. However, the interaction between the tracer and enzyme may be limited if the tracer is unable to cross the cell membrane which will lead to reduction of signal (*Kircher et al., 2011*). Another major limitation of HSV1-tk imaging is that it has been shown to initiate an immune response (*Mercier-Letondal, et al., 2008*). Therefore, work has focused on the development of non-immunogenic human reporter genes but their main disadvantage is that

there is always a degree of native background uptake which can lead to poor specificity and sensitivity.

Another approach for PET reporter gene imaging is based on the binding of radiotracers to cell surface receptors, such as D2R. Hence, it is not necessary for the radiotracer to cross the cell membrane. D2R imaging has been used to monitor human muscle precursor cells in mice for potential application in various muscle disease (*Haralampieva et al., 2016*). In addition, this method could be useful tracking cells within the brain because ¹⁸F-fluoroethyl spiperone (¹⁸F-FESP) which has an affinity for D2R can cross the blood brain barrier (*Barrio et al., 1989*). However, the radioactive signal production may not be sufficient enough to detect cells because of the one to one relationship between radiotracer and D2R receptor.

Genes which encode cell membrane transporters or symporters, actively transports radiotracers into the cell. NIS is a widely utilized SPECT/PET genetic reporter for stem cell use. NIS transports radioactive iodine into the cell in exchange for sodium and it has been used to track cardiac stem cells in rats using Iodine-124 (¹²⁴I) for PET and ^{99m}Tc for SPECT imaging (*Terrovitis et al., 2008*). However, the main drawback of NIS is the high background uptake in the stomach and thyroid due to the presence of endogenous transporters. Another transporter gene imaging is the norepinephrine transporter (NET) which transports norepinephrine analogues such as ¹⁸F-metaiodobenzylguanidine (¹²⁴I-MIBG) into cells and it has been used track human T cells in mice (*Moroz et al., 2015; Badar et al., 2015*). Due to the lower background uptake, this imaging strategy could be a better option for stem cell detection. However, PET/SPECT reporter gene imaging still suffers from poor sensitivity and spatial resolution due to the fundamental limitations of the imaging techniques.

MRI reporter gene imaging

Over the past few years, a number of studies have been published using MRI reporter gene imaging. Reporter genes resulting in the increased expression of the iron carrier proteins transferrin or ferritin in cells, leads to the intracellular accumulation of iron and initiates T_2/T_2^* relaxation changes which can be detected by MRI. Overexpression of the human ferritin heavy chain (hFTH) has been used to track porcine cardiac stem cells within the myocardium using an iron sensitive MRI sequence (*Campan et al., 2011*). However, when compared to direct cell labelling with SPIONs, this technique has limited sensitivity for *in vivo* applications. Other limitations of this imaging strategy include potential toxicity, persistence of signal from dead cells and subsequent transferal to macrophages after phagocytosis (*Gilad et al., 2007*). Whereas, the MR reporter gene that results in expression of the transporter protein organic anion transporting polypeptides (Oatp1a1) facilitates the uptake of Gd³⁺-based contrast agents, which provide positive contrast on MR images. This method

has been shown to provide greater signal enhancement than traditional MRI reporter genes (*Patrick et al., 2014*) but it is still not as sensitive as nuclear or BLI reporter genes and the potential adverse effect on stem cell proliferation and function is unknown. In addition, this protein cannot be used for cell tracking in certain organs like liver and kidney because *oatp1a1* is endogenously expressed in these organs. Although MRI can provide deep tissue imaging, high spatial resolution with clinical applicability, MRI reporter genes are less commonly used to monitor cell viability due to low sensitivity of MR reporter genes.

In summary, the main advantage of reporter gene imaging is that it provides information on cell viability and is able to monitor cell behaviour and fate long-term, which cannot be obtained with direct cell labelling. In order to overcome the limitations of each imaging modality, various bicistronic and tricistronic reporter genes such as BLI/PET (*Love et al., 2007*), BLI/FLI/PET (*Ray et al., 2007*) and MRI/PET (*Lewis et al., 2015*) have been developed for multi-modal reporter gene imaging. However, signal production is lower than that achieved by direct labelling because it depends on the degree of transduction, expression and other biological factors, such as the strength of the gene promoter as well as the uptake and clearance of the imaging probe (*Li et al., 2018*). In addition, endogenous expression of the gene used as the reporter within the body also limits its use for assessing widespread whole body distribution.

1.7 Stem cells delivery

In addition to cell localisation and viability, non-invasive imaging has been shown to be a vital tool in assessing the optimal route of stem cell delivery to evaluate the distribution of transplanted cells and the safety of different injection routes.

Intravenous (IV) injection

IV injection is the most common route of MSC transplantation in both preclinical and clinical studies. Although IV injection is the most convenient and relatively safe injection route, very low number of cells engraft in target organs due to the entrapment of cells within the lungs.

BLI imaging has been extensively used in several animal models including in tumour (*Sasportas et al., 2009*), hind limb ischemia (*Hoffmann et al., 2010*) and acute renal injury (*Tögel et al., 2008*) to monitor the whole body distribution of MSCs after tail vein injection. In addition, BLI imaging has been shown to be able to detect low numbers of MSC engraftment within subcutaneous tumours after IV injection and has also been useful for monitoring MSC migration to tumours (*Klopp et al., 2007, Wang et al 2009*). However, the exact cell localisation and the reliable quantification of cell numbers in different organs cannot be achieved with BLI due to its poor spatial resolution and light scattering. Similar problems

have been demonstrated in tracking MSCs labelled with the fluorescent dye SP-Dil to tumours (*Studený et al., 2002*)

The nuclear imaging approach using ^{111}In -oxine has been utilized to track MSCs after IV injection in a canine model of myocardial infarct which showed an initial high cell uptake in lung followed by redistribution to the liver and spleen (*Kraitichman et al., 2005*). Moreover, the same distribution pattern has been reported in patients with advanced liver cirrhosis which showed a reduction in the percentage radioactivity within the lung followed by an increase in liver and spleen at 10 days after IV infusing of ^{111}In -oxine labelled MSCs (*Gholamrezanezhad et al., 2011*). Administration of the vasodilator, sodium nitroprusside, before IV infusion of ^{111}In -oxine labelled cells has been shown to be effective in reducing pulmonary entrapment, which leads to a larger redistribution in liver and other organs (*Gao et al., 2001*). The similarity of cell distribution pattern in both animals and humans regardless of the disease, suggested that cells trapping within the lung capillaries is the major hurdle in stem cell delivery using the IV route. In addition, these results highlight the high sensitivity and quantitative imaging of nuclear imaging which is useful for determining whole body cell distribution.

Although cell accumulation in the lungs after IV injection is not desirable in delivering stem cells to distal organs, it can be exploited to treat lung tumours with MSC-based anticancer therapy. MSCs have been shown to localize in lung metastases after IV injection and are able to initiate tumour cell apoptosis by using TRAIL (*Loebinger et al., 2009*). IV administration was also reported to provide a higher MSC-TRAIL engraftment in pleural mesothelioma when compared to intrapleural delivery using NIR dyes (*Sage et al., 2014*).

Intra-arterial (IA) injection

Many comparative studies between IV and IA injection of MSCs have demonstrated that IA injection can provide better engraftment of cells in multiple organs, especially in kidney and brain, due to the physiological flow of the arteries which bypasses the lungs. This has been confirmed by BLI, where Tögel *et al.* reported that intra-arterial cell infusion via carotid artery offered better cell uptake in kidneys by reducing the cell accumulation in the lungs (*Tögel et al., 2008*). Due to the blood brain barrier, cells delivery to brain has proven to be difficult. In a rat model of ischemic stroke, an increased level of cell engraftment in the brain was obtained by injection of SPION labelled MSC through the carotid artery (*Walczak et al., 2008, Cui et al., 2015*). However, the risk of vascular occlusion was detected by MRI which raises safety concerns in the use of IA injection and highlighting the importance of imaging in monitoring the safety of cell therapies.

In small animal studies, carotid artery cell infusion is commonly performed to study the distribution of cells after IA injection. However, this method is invasive and can cause haemorrhage and increase mortality. Therefore, many preclinical studies have increasingly conducted ultrasound-guided intracardiac (IC) injections via the left ventricular cavity as an alternative to IA injection to develop brain metastases (*Connell et al., 2013*), to improve stem cells delivery to intestine (*Dave et al., 2017*) and delivery to brain tumours (*Cheng et al., 2016*).

Ultrasound is one of the most widely used non-invasive imaging modalities in the clinic. The concept of ultrasound is based on the interaction of high frequency sound waves which are generated from the piezoelectric crystals in the ultrasound transducer and its interaction with different types of tissue within the body. During this interaction, attenuation, reflection, scattering, absorption and refraction of the ultrasound waves occur depending on the density of the tissue. Sound waves are returned to the transducer as different levels of reflected echoes which initiate electrical pluses in the transducer crystals to form ultrasound images. Due to the excellent temporal resolution of ultrasound, it is suitable for image-guided injection to various organs, and especially blood vessels. Ultrasound-guided vascular access have been routinely performed in the clinic to administer fluids and drugs (*Weiner et al., 2013*). Therefore, further development of ultrasound-guided injection in pre-clinical studies could be easily translatable to the clinic.

Local injection routes

In order to improve cell uptake in target organs, many studies have explored different types of direct injection routes such as renal parenchymal injection (*Alfarano et al., 2012*), direct intracranial injection (*Kondo et al., 2009*), intratumoural injection (*Otsu et al., 2009*) or injection into the local blood supply, for example, renal artery injection (*Bos et al., 2004; Sun et al., 2008*) and portal vein injection (*Bos et al., 2004*). There are several studies which have shown the importance of *in vivo* imaging in assessing the accuracy and safety of these injection routes. The dual labelling approach using ^{111}In -oxine and SPION has been successfully used to track stem cell migration to glioma after intranasal delivery (*Balyasnikova et al., 2014*). In a pig model of myocardial infarct, the increase retention of SPION labelled cells in the infarct area has been demonstrated after successful direct intramyocardial injection (*Amado et al., 2005*). Finally, one clinical study assessed the accuracy of dendritic cell delivery to regional lymph nodes in patients with melanoma by using SPION-based MR cell tracking techniques (*de Vries et al., 2005*).

1.8 Assessment of therapeutic response

Another advantage of using *in vivo* imaging in cell therapies is that it can be utilized to assess the functional improvement of the target organ after transplantation. More importantly, the level of responsiveness to treatment could be evaluated and correlated to the localization and viability of the transplanted cells within the target organ by using the same imaging modality. For example, in studies of cardiac regeneration after myocardial infarct, the exact localisation of SPION labelled stem cells in myocardium has been correlated to the MRI assessment of cardiac function and infarct size to predict therapeutic efficacy (Amado *et al.*, 2005). In addition, due to its superb soft tissue contrast, MRI can provide the status of diseased organs, for example in ischemic stroke, not only the size of the lesion but also information about the surrounding brain tissues such as oedema, inflammation and haemorrhage can be detected by using MRI (Burgess *et al.*, 2011). Moreover, in stem cell-based anti-cancer therapies, both tumour growth and tumour perfusion can be studied with MRI (Principi *et al.*, 2003). However, the presence of MR labelling agents that affect the tissue signal of target organs, such as SPION will interfere with functional assessments.

Although the spatial resolution of SPECT/PET imaging is not as high as MRI, their unique property is the ability to monitor the metabolic status of diseased organs such as glucose metabolism (Reivich *et al.*, 1979), apoptosis (Elvas *et al.*, 2015) and tumour hypoxia (Xu *et al.*, 2017). By exploiting the strength of PA imaging in visualising the endogenous chromophore haemoglobin, blood vessels involved in tumour angiogenesis can be imaged (Siphanto *et al.*, 2005) and therapeutic changes can be assessed in relation to cell localisation and viability. Whereas, in MSC-based anticancer therapies for lung tumour, CT imaging could be used to monitor the size of the tumour and the localization of stem cells by using gold nanoparticles.

Moreover, the application of *in vivo* imaging can be extended to evaluate the enhancement of immune interaction in improving target organ engraftment. This may be done by treating stem cells with various cytokines and chemokines (Xinaris *et al.*, 2013; Shi *et al.*, 2007), overexpressing growth factors, or surface receptor modification prior to transplantation to improve the homing of cells to sites of injury, inflammation and tumour (Haider *et al.*, 2008; Sarkar *et al.*, 2011; Kalimuthu *et al.*, 2017).

1.9 Which imaging techniques should we use?

Table 1. Summary of strengths and drawbacks of currently available *in vivo* imaging technologies for cell tracking (Adapted from *Zheng et al., 2017*).

Imaging techniques	Spatial resolution	Penetration depth	Sensitivity	Clinical use	Strengths	Drawbacks
FLI (e.g. NIR dye, QD)	>2 mm	< 1 cm	nM- μ M	No	Simple, fast & affordable	Limited tissue penetration, poor resolution
BLI (luciferase reporter gene)	>2 mm	<1 cm	nM	No	High sensitivity, detect cell viability	Limited tissue penetration, poor resolution
MRI (e.g. SPION)	>25 μ m	No limit	mM- μ M	Yes	High resolution, excellent tissue contrast	Low sensitivity, false positive signal
MRI reporter gene					Long term imaging	Potential toxicity
Nuclear imaging (e.g. ^{18}F , ^{111}In)	>1 mm	No limit	pM	Yes	High sensitivity, quantitative imaging	Radiation risk, tracer dilution, low resolution
Nuclear reporter gene				Yes	Detect cell viability, quantitative imaging	High background, low resolution

Although the current imaging modalities provide valuable information required for monitoring stem cell therapies, no individual imaging technique is ideal. Depending on the research question and the target organ that are being investigated, the suitable labelling method and imaging strategy should be selected. In addition, the spatial resolution, the sensitivity and the possibility to do quantitative imaging should also be taken into accounts (Table 1). Moreover, the cost and availability of imaging scanners also plays a significant role in choosing the appropriate the imaging methods. For example, MRI machines are more expensive and less available than PET/SPECT scanners in most hospitals. Although the standard PET/SPECT radiotracers are commonly used in research facilities and hospitals, there are a number of issues which need to be considered. For example, the enhanced spatial resolution and sensitivity of PET is a desirable feature for cell tracking but there are fewer PET scanners than SPECT scanners due to the need for an on-site cyclotron that is required for short half-life PET tracers. Nonetheless, even though SPECT radiotracers are more available to many research centres, there is less flexibility when designing imaging probes due to their rigid chemical structures (Vallabhajosula *et al.*, 2009).

1.10 Limitations of *in vivo* imaging

Although *in vivo* imaging plays a critical role in monitoring stem cell therapies, there are some questions that cannot be addressed using current imaging technologies. For example, the detailed signalling pathways behind stem cell migration, the fate of cells that subsequently die after transplantation and their clearance mechanisms from the body cannot be investigated by using *in vivo* imaging. In addition, the cost and potential toxicity of exogenous labelling agents, the concerns over the non-specific information due to leakage of the imaging probes and the potential complications of genetic manipulation of stem cells are the main issues preventing the widespread use of *in vivo* stem cell tracking technologies in the clinic.

1.11 Summary and research aims

In summary, advances in molecular biology and imaging technology have allowed researchers to monitor the fate of the stem cells in target organs after transplantation with correlation to functional assessment for therapeutic efficacy evaluation. Moreover, non-invasive *in vivo* imaging methods have not only assisted in selecting the optimal injection routes but have also assessed the safety of these delivery routes. However, each imaging modality and labelling strategy has advantages and drawbacks. It is clear that there is no single imaging modality/labelling approach which can provide all the key information required to evaluate the therapeutic efficacy of stem cell therapy. Therefore, the development of

multi-modal imaging approaches is required to provide a better solution to address the complexity of issues posed in the area of stem cell therapies.

In this thesis, a multi-modal imaging strategy that combines reporter gene imaging with different direct labelling methods, has been applied to quantify cell localisation alongside information on cell survival. The aims of this project were; 1) to synthesize a novel nuclear/MRI dual imaging probe using the SPECT radiotracer ^{111}In and SPION (SPECT/MRI); 2) to label the luciferase expressing MSCs with the newly synthesized dual SPECT/MRI imaging probe thereby producing tri-modal imaging (BLI, SPECT and MRI) capability; 3) to compare the whole body distribution of labelled MSCs following IV and IC injection using tri-modal imaging; 4) to compare MSCs delivery to orthotopic distal breast tumours following IV and IC injections using tri-modal imaging; 5) to evaluate gold nanorod labelled MSC delivery to kidney following a novel ultrasound-guided renal artery injection using BLI and PA imaging and 6) to explore the potential applications of gold nanoparticles as stem cell tracking agents using CT and BLI.

Chapter 2

General methods

2.1 Materials

All chemical materials were from Sigma-Aldrich (St Louis, USA), unless otherwise stated.

2.2 Cell culture

All experiments were performed using human adipose derived mesenchymal stem cells (ADSCs). Isolation and characterisation of ADSCs were conducted by Dr Michelle Griffin, UCL Plastic and Reconstructive Surgery Department.

2.2.1 Isolation and characterisation of ADSCs

ADSCs were isolated according to the procedure described in *Naderi et al., 2014*. After removal of fibrous tissue and visible blood vessels, fat tissue samples were cut into small pieces (3 mm³) and digested in Dulbecco's modified Eagle's medium nutrient mixture F12 Ham (DMEM-F12, Invitrogen, Paisley, UK) containing 300 U/ml crude collagenase II (Invitrogen, Paisley, UK) for 30 minutes in a humidified incubator at 37°C with 95% air and 5% CO₂. The dispersed material was filtered through 70 µm cell strainers (BD Biosciences, Oxford, UK). The ADSC-rich cell pellets were formed after centrifugation at 290 g for 5 minutes. The numbers of viable cells were determined by Trypan blue exclusion. Immunophenotypic characterisation of ADSC was performed using flow cytometry. ADSCs were stained with antibodies for different cluster of differentiation (CD) antigens such as CD45, CD34, CD19, CD14, CD73, CD90 and CD105 as previously described in *Naderi et al., 2014*.

2.2.2 Transduction of ADSCs

Transduction of ADSCs to express luciferase enzyme was conducted with the help of Dr Stephen Patrick, CABI, UCL. ADSCs (cell passage 2-4) were transduced with a lentiviral vector using plasmid pSEW (*Demaison C et al. 2004*) to express green fluorescent protein (GFP) and firefly luciferase enzyme (*Law et al. 2006*) under the control of the Friend murine leukaemia virus FB29 promoter. The successful transduction was confirmed by GFP expression using fluorescence microscope (EVOS FL Auto cell imaging system, ThermoFisher Scientific, Massachusetts, USA) and the transduction efficiency was $42.56 \pm 7.43\%$. The transduced ADSCs were cultured for two weeks prior to further analysis. To evaluate the effective intensity of luciferase activity, an *in vitro* luciferase assay was performed using BLI which showed 15900 ± 2770 photons/s/cell. The effect of luciferase expression on cell viability and differentiation capability were assessed and no adverse effect was observed (the data from differentiation assay performed by Dr Michelle Griffin).

The transduced ADSCs (cell passage 4-7) were grown in T175 flasks (Fisher Scientific, Loughborough, UK) in DMEM-F12, supplemented with 10% fetal calf serum (FCS,

Invitrogen, Paisley, UK) in a humidified incubator at 37°C with 95% air and 5% CO₂. Cells were grown to 80% confluence before being trypsinised, centrifuged for pelleting at 300 g, counted and then plated for *in vitro* studies or re-suspended in PBS for *in vivo* cell injection.

2.2.3 Differentiation assay

To determine the effect of labelling on the differentiation potential of ADSCs, a differentiation assay was performed as previously described (New *et al.*, 2015).

Adipogenic differentiation

Adipogenic differentiation was induced with DMEM-F12 medium containing 10% FCS, 1% penicillin/streptomycin, 10 ng/ml insulin, 1 µM dexamethasone, 500 µM 3-isobutyl-1-methylxanthine and 1 mM rosiglitazone. After 3 weeks, cells were fixed in 10% formalin for 30 minutes, washed with deionised water and then washed again with 60% isopropanol for 5 minutes prior to staining with Oil Red O working solution (Appendix 1) for 10 minutes. After staining, cells were washed several times with tap water.

Chondrogenic differentiation

Chondrogenic differentiation was induced with DMEM-F12 medium containing 10% FCS, 1% penicillin/streptomycin, 0.1 µM dexamethasone, 50 µg/ml ascorbate, 10 ng/ml transforming growth factor (TGF) β1 (Life technologies, Paisley, UK) and insulin, transferrin, selenium. After 3 weeks, cells were fixed in 4% paraformaldehyde (PFA) for 30 minutes and then washed with deionised water. Then rinsed with 0.1 M HCl for 5 minutes and stained with Alcian Blue staining (1% in 0.1 M HCl) for 30 minutes. After staining the cells were washed with tap water 3 times.

Osteogenic differentiation

Osteogenic differentiation was induced with DMEM-F12 medium containing 10% FCS, 1% penicillin/streptomycin, 0.1 µM dexamethasone, 10 mM β-glycerophosphate and 100 µg/ml ascorbate. After 3 weeks, cells were fixed in ice-cold 70% ethanol for 1 hour and washed with deionised water. Then the cells were stained with Alizarin Red staining (1% in deionised water, pH 4.1 - 4.3, Appendix 1). After staining, cells were washed with tap water 3 times.

2.3 Transmission Electron Microscopy (TEM)

TEM protocols were kindly provided by Dr Mark Turmaine, UCL Biosciences EM facility.

ADSCs were seeded at 0.22×10^5 per well on coverslips (VWR) in 24-well plates (Corning) and then left to attach overnight. Next day the cells were fixed in 2% PFA and 1.5% glutaraldehyde in 0.1 M sodium cacodylate buffer (pH 7.3) for 24 hours at 3°C then washed 2 times with the same buffer for 30 minutes. The cells were then post fixed in 1% osmium tetroxide/1.5% potassium ferrocyanine in 0.1 M cacodylate buffer for 1 hour at 3°C. Then the cells were dehydrated in a graded ethanol-water series and infiltrated with Agar 100 epoxy resin. After dehydration, the cells were placed onto a resin filled Beem capsule with the coverslip side down and hardened at 60°C for 48 hours and then the coverslips were removed by hydrochloric acid (HCl). A representative area was selected and ultra-thin sections were cut at 70-80 nm using a diamond knife on a Reichert ultra-cut S microtome. Sections were collected on 300 mesh copper and stained with lead citrate. Then viewed with a Joel 1010 transmission electron microscope and the images were recorded using a Gatan Orius CCD camera.

2.4 *In vivo* studies

All animal studies were approved by the University College London Biological Services Ethical Review Committee and licensed under the UK Home Office regulations and the Guidance for the Operation of Animals (Scientific Procedures) Act 1986 (Home Office, London, United Kingdom) All mice were 6-8 week old female non-obese diabetic/severe combined immunodeficiency/gamma (NSG) mice (Charles River Laboratories, UK), unless otherwise stated. All *in vivo* imaging experiments were performed under isoflurane anaesthesia (1.5% – 2.5% isoflurane in oxygen 1.5 - 2 L/min). The signs of stress and the general wellbeing of the animals were observed throughout the study by monitoring the body weight.

2.4.1 Ultrasound-guided intracardiac injection

Under anaesthesia, mice were positioned in supine position on the ultrasound platform (VEVO 2100; Visualsonics, Canada) and the limbs were secured with the tape (Figure 2.1a). The hair from the chest area was removed by hair removal cream (Veet). The ultrasound platform was rotated 45° clockwise to have the apex of the heart facing towards the injection mount. Microscan™ transducer MS-550D was placed onto the chest and the long axis view of the heart was acquired before and after injection using B mode for visualisation and M mode for ejection fraction (EF) analysis. The cell suspension (in 100 µl of PBS) was injected slowly into the left ventricular cavity of the heart using a 1 ml syringe with a 29 gauge needle (Figure 2.1b). The successful injection was visualised by the presence of hyperechogenic contrast in the left ventricular cavity (Figure 2.1c). The needle was slowly withdrawn from the body and the long axis view of the heart was acquired again. The animals were recovered from anaesthesia and the signs of stress or trauma were observed. To assess the effect of injection on cardiac function, EF of pre-injection and post-injection were analysed using cardiac package Vevo lab software version 3.1.1 (Visualsonic, Canada).

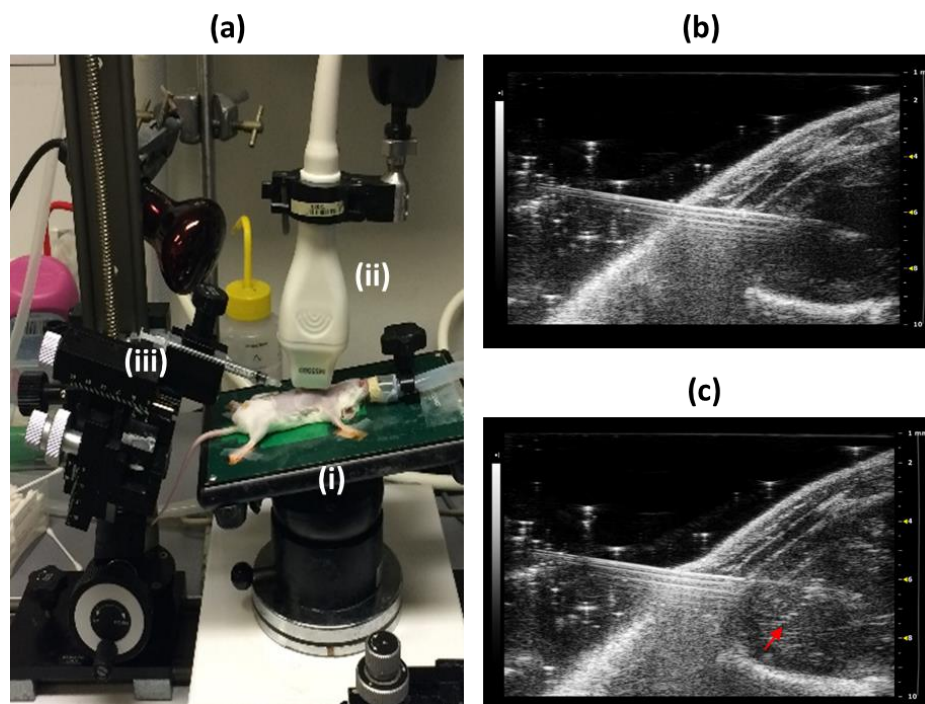


Figure 2.1 Ultrasound-guided intracardiac injection through left ventricular cavity. (a) The animal was positioned in supine position on the platform (i) with the ultrasound transducer (ii) on the chest and the syringe in injection mount (iii) facing towards the apex of the heart. (b) The needle was pierced through the skin, the chest wall and left ventricular wall. (c) The successful injection was visualised by the presence of hyperechogenic contrast (indicated by arrow).

2.4.2 BLI

Mice were anaesthetised and *in vivo* BLI was performed using IVIS Lumina (PerkinElmer, USA). Mice were injected intraperitoneally with 75 mg/kg D-luciferin (Promega) in 200 μ l of PBS. Sequential BLI images were acquired 5 minutes after luciferin injection using auto exposure time with 0.5 minutes delay between two consecutive acquisitions. A rectangular region of interest (ROI) was placed over the whole body on the first image and subsequently pasted over every new image acquired until all ROIs reach their maximum intensity. The total signal in the ROI was quantified as total flux (photons/s) by using Living Image software version 4.5 (PerkinElmer). Representative images were presented using radiance (the number of photons per second that leave a square centimetre of tissue and radiate into a solid angle of one steradian (sr) = p/sec/cm²/sr) as colour scale by utilizing the same software.

2.4.3 SPECT/CT

Mice were anaesthetised and whole body SPECT/CT scans were acquired using a NanoSPECT/CT scanner (Mediso, Hungary). CT images were acquired using a 45 kilo volt peak (kVp) X-ray source, 500 ms exposure time in 180 projections, a pitch of 1.5 with an acquisition time of 7 minutes. SPECT images were obtained with a 4-head scanner with nine 1.4 mm pinhole apertures in helical scan mode using a time per view of 60 - 90 second resulting in a scan time of 36 – 60 minutes and respiration was monitored throughout the scan and body temperature maintained with a warm air blower. CT images were reconstructed in voxel size 124 x 124 x 124 μ m using Bioscan InVivoScope (Bioscan, USA) software, whereas SPECT images were reconstructed in a 256 x 256 matrix using HiSPECT (ScivisGmbH, Bioscan). Images were fused and analysed using InVivoScope (Version1.44, Bioscan). 3D region of interests (ROI) were created for organs of interest using VivoQuant (inviCRO version 2.5 patch1) software. After correcting for ¹¹¹In decay, the 3D ROIs were calculated as the percentage of injected dose per mm³ (%ID/mm³). Representative maximum intensity projection (MIP) images were presented using %ID/mm³ as colour scale after decay correction and Gaussian filtering of 0.8 by utilizing the same software.

2.4.4 MRI

Mice were anaesthetised and positioned in a custom cradle with temperature and respiration monitoring. MRI studies were performed using a 9.4T Varian scanner (Agilent, USA) for liver and brain imaging and a 1T ICON scanner (Bruker, Germany) for kidney imaging. For liver imaging, a 35 mm volume radiofrequency coil (Rapid, Germany) and respiration-gated sequences were used. T₂^{*}-weighted liver images were acquired using a fast spin echo multi slice sequence with the following parameters: repetition time (TR) = 1000 ms; echo time

(TE) = 20 ms; spatial resolution = 115 $\mu\text{m}/\text{pixel}$; slice thickness = 1 mm. For brain imaging, a 72 mm volume radiofrequency coil was used with a surface receive coil positioned over the skull. T_2^* -weighted brain images were acquired with a gradient echo sequence using TR = 500 ms; TE = 4.1 ms; in plane resolution = 130 μm^2 ; slice thickness = 0.6 mm. T_2^* -weighted kidney images were acquired using TR = 147.5 ms; TE = 5 ms; spatial resolution = 216 $\mu\text{m}/\text{pixel}$; slice thickness = 1 mm. Acquisition time = ~15 minutes for each scan. Images were analysed using ImageJ software.

2.5 Ex vivo BLI and biodistribution study

Under anaesthesia, mice were injected intraperitoneally with 75 mg/kg D-luciferin. At 10 minutes after injection, mice were sacrificed and the organs of interest were excised quickly and *ex vivo* BLI was performed using 5 minutes exposure time and binning 8. Directly after *ex vivo* BLI, each sample was weighed and counted with a gamma counter (Wizard² 3", PerkinElmer, Massachusetts, USA) and the amount of radioactivity was decay corrected and calculated as the percentage of injected dose per gram (%ID/g).

2.6 Histology and immunohistochemistry (IHC)

Histology studies were conducted by Dr Angela Richard-Londt, IQPath, UCL.

At the end of imaging sessions, selected mice were sacrificed and tissue samples were excised, fixed in 10% neutral buffered formalin and embedded in paraffin. Then 5 μm tissue sections were prepared for different histological staining. To assess morphological changes, haematoxylin and eosin (H & E) staining was performed. Human specific vimentin (CONFIRM™ anti-Vimentin (V9) primary mouse monoclonal antibody, Roche) and Iba1 (anti-Iba1, rabbit polyclonal antibody, Wako) staining were performed to detect the presence of ADSCs and macrophages in tissue section using Ventana Discovery XT instrument and the Ventana DAB Map detection Kit (for lung sections) or Ventana Red detection kit (for brain section). For pre-treatment, Ventana CC1, equivalent to EDTA buffer, was used. The slides were counterstained with haematoxylin. The adjacent 5 μm sections from IHC stained sections were stained with Prussian blue staining to demonstrate the presence of SPIONs. In brief, deparaffinised and hydrated sections were immersed in the freshly prepared Perl's solution (equal part of 2% hydrochloric acid and 2% potassium ferrocyanide) for 10 minutes and washed 3 times with distilled water. Next the slides were counterstained with nuclear fast red for 1 minute and washed 2 times with distilled water. Then the slides were mounted with resinous mounting medium and scanned with Nanozoomer slide scanner (Hamamatsu

Photonics, Japan). The images were viewed with NanoZoomer Digital Pathology software (NDP Version 2.7.25).

Chapter 3

Synthesis and characterisation of a SPECT/MRI dual imaging probe

3.1 Abstract

Due to the increased demand of new *in vivo* imaging technologies to provide better efficiency and accuracy, novel multi-modal imaging designs have been developed to overcome the limitation of a single imaging technique. Among different combinations of multi-modal imaging strategy, nanoparticles-based nuclear/MRI combination has great potential for applying in stem cell applications.

The aim of the work presented in this chapter was to conjugate SPECT radiotracer, ^{111}In to superparamagnetic iron oxide nanoparticles (SPIONs) via a 1,4,7,10-tetraazacyclododecane-1,4,7,10-tetraacetic acid (DOTA) for dual imaging with both SPECT and MRI.

DOTA was functionalised with an amine group which was used to form a peptide bond with carboxyl groups on citrate coated SPION (FluidMAG-CT). ^{111}In was chelated using HEPES buffer (pH 5.5) with magnetic purification to form ^{111}In -DOTA-SPION dual imaging particles. A series of *in vitro* stability studies were performed to compare the difference in stability of ^{111}In -DOTA-SPION conjugates and electrostatic binding of ^{111}In -SPION. *In vivo* stability of ^{111}In -DOTA-SPION conjugates was assessed by injecting intravenously into the mice and imaged with SPECT/CT serially for 7 days and then the results were compared with ^{111}In -SPION and $^{111}\text{InCl}_3$ only injected groups.

In vitro chelation specificity tests showed the radiolabelling yield of ^{111}In -DOTA-SPION was $92 \pm 7.23\%$ and 1.5 fold higher than ^{111}In -SPION. *In vitro* stability test showed the percent radioactivity of ^{111}In -DOTA-SPION was 2.5-fold higher than ^{111}In -SPION after the first PBS wash and remained stable after subsequent wash steps suggesting the strong DOTA- ^{111}In chelation compared to weak electrostatic binding of ^{111}In -SPION. *In vivo* stability assessment showed the liver uptake of ^{111}In -DOTA-SPION group was 2-fold higher than ^{111}In -SPION group with the lowest uptake of radioactivity in kidney indicating that the amount of free ^{111}In leakage is minimal in ^{111}In -DOTA-SPION group and the synthesised dual imaging particles are stable *in vivo*.

The findings presented in this chapter demonstrate that the successful development of a stable SPECT/MRI dual imaging probe which can be used for *in vivo* applications.

3.2 Introduction

Over the past few years, the concepts of combining imaging modalities has increased in demand to enhance the performance of biomedical imaging by complementing the disadvantage of a single imaging technique with the advantage of another. The first successful hybrid imaging system, PET/CT, is a classic example of the relatively poor resolution of highly sensitive PET images which is strengthened by overlaying onto high resolution CT images. Due to recent developments in biomedical imaging, novel multi-modal imaging probes have been developed to provide comprehensive information on biological processes in *in vivo*.

3.2.1 Design of multi-modal imaging probes

The advantage of using a multi-modal imaging probe is the ability to image the same molecule with the same pharmacokinetics by different techniques, instead of using multiple imaging agents for different modalities. Different combinations of multi-modal imaging probes have been developed including fluorescence/MRI (Lee *et al.*, 2007), nuclear/MRI (Xue *et al.*, 2015) and nuclear/fluorescence combinations (Li *et al.*, 2006). Although fluorescence and nuclear imaging are highly sensitive molecular imaging techniques, they cannot provide a good spatial resolution image which is the strength of MRI. Therefore, either fluorescence/MRI or nuclear/MRI combination is synergistic. However, due to limited tissue penetration depth of fluorescence imaging, the fluorescence/MR imaging probes are only applicable in small animal studies at superficial depths. Since both MRI and PET/SPECT imaging are widely used in clinic, nuclear/MRI combination has a huge potential for translating dual imaging probe as clinical applications.

One of the most studied designs in constructing nuclear/MRI combination is an iron oxide nanoparticle-based approach. Iron oxide particles are known to have low toxicity and have been used in biomedical applications such as hyperthermia (Kalber *et al.*, 2016), selective drug delivery (Aires *et al.*, 2016) and cell tracking using MRI (Stuckey *et al.*, 2006). In addition, designing multi-modal imaging with iron oxide nanoparticles is relatively straightforward due to their unique physical and chemical properties. More importantly, having a simple and rapid synthesis is one of the necessary criteria for translating small animal research to the clinic. In general, the nuclear/MRI imaging probes can be constructed by modifying the surface coating of iron oxide particles with functional components such as amine or carboxyl groups which serve as a linker for attaching targeted molecules or combining imaging modalities.

In order to add radioactive metal components to iron oxide particles, the complex formation with a chelator is required. Chelators such as DOTA and DTPA are commonly used to

chelate radiometals due to the availability and extensive knowledge on chelation chemistry for gadolinium (Gd) chelation in MRI. However, DTPA complexes have been reported to be less stable than DOTA and can release radiometals under physiological conditions (Woods *et al.*, 2004). Non-chelated radiometals inside the body display substantially different pharmacokinetics than chelated complexes; this leads to confounding results in nuclear imaging especially with long half-life radioisotopes. Therefore, DOTA is a better chelator for long term nuclear imaging and targeted molecular imaging. DOTA complexes are characterized as kinetically inert to dissociation due to its robust ring structure and can form thermodynamically stable complexes with trivalent metal cations like $^{111}\text{In}^{3+}$ (Figure 3.1, León-Rodríguez *et al.*, 2008). In addition, DOTA can be easily functionalised with a bifunctional linker without altering its chelation capabilities, for example, with amine derivatives which form covalent bonding with carboxyl groups on the surface of iron oxide particles.

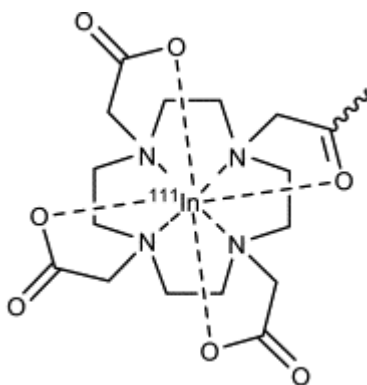


Figure 3.1 Schematic representation of the structure of ^{111}In -DOTA complex.

3.2.2 Types of radioisotopes and applications

Adding a nuclear component to a MRI contrast agent allows for the accurate quantification of nanoprobe distribution within organs. Therefore, nuclear/MRI dual imaging probes have been developed for several preclinical applications. Regarding the choice of radioisotopes, it depends on their half-lives and the application of a specific imaging agent. Due to the recent developments in PET/MRI, PET radioisotopes have become attractive candidates for dual imaging probes. For example, the PET radioisotope ^{64}Cu with a half-life of 12.7 hours has been developed as a PET/MRI imaging probe with a targeted amino acid sequence to detect glioblastoma (Lee *et al.*, 2008). However, PET radioisotopes are more expensive than SPECT and cyclotron facilities are required for isotopes generation. Although the SPECT radioisotope $^{99\text{m}}\text{Tc}$ is the most commonly used and widely available radioisotope, it is not suitable for applications like cell tracking due to its short half-life of 6 hours. Iodine-125 (^{125}I) with a half-life of 59 days has been developed as a SPECT/MRI/fluorescent imaging agent

for stem cell tracking in rats (*Tang et al., 2011*). However, ^{125}I is less efficient for whole body clinical imaging due to the low emitted gamma ray energy (35 keV). SPECT/MRI probes using ^{111}In have been reported to be able detect mesothelioma in mice up to 72 hours (*Misri et al., 2012*). Since ^{111}In has a half-life of 67.9 hours with two high energy peaks (171 and 247 keV), it is suitable for most biological applications especially for cell tracking. In addition, the ^{111}In -oxine labelling method is routinely used in clinic to label white blood cells to detect infection (*Thakur et al., 1977*). Another key consideration is that combining multiple modalities should not reduce the effectiveness of each individual application. For example, to be able to detect the uptake of a PET/MRI probe on both PET and MRI within a tumour, a higher dose of the PET component would be given when compared to that of stand-alone PET imaging (*Lee et al., 2009*). This is because PET is more sensitive than MRI. Therefore, the difference in sensitivities between imaging techniques should be considered and optimised when designing the imaging probe and its application.

In summary, recent developments in multi-modal imaging for preclinical applications demonstrate the benefit of combining imaging modalities. However, further development is still required to address clinical needs in monitoring stem cell therapy and to truly capture the advantages of combining imaging modalities.

3.2.3 Experimental approach

Synthesis of a dual imaging probe was performed in collaboration with Professor Alethea Tabor and Dr Robin Bofinger from UCL Chemistry. The commercially available iron oxide nanoparticle, FluidMAG-CT, and the SPECT radioisotope ^{111}In were selected to design a dual SPECT/MRI imaging probe for stem cell tracking. FluidMAG-CT particles have been shown to be biocompatible and have already been used to label stem cells for MRI (Kalber *et al.*, 2016). In addition, the particles have a citric acid coating functionalised with carboxyl group (Figure 3.2) allowing conjugation to the chelator for radiolabelling. The DOTA chelator was selected for ^{111}In chelation because DOTA complexes are known to be more stable than DTPA. DOTA was functionalised to produce a DOTA-amine derivative for conjugation via a peptide bond with carboxyl groups on the SPIONs surface (Figure 3.3). Subsequently, the synthesised particles were characterised and a series of experiments were performed to test the reproducibility and stability of the bifunctional linker which links the two imaging components. Since FluidMAG-CT iron oxide nanoparticles have been widely used for MRI imaging and the SPECT component offers more accurate quantification of dual imaging probes, the relaxivity of DOTA-SPION conjugates is not covered in this thesis.

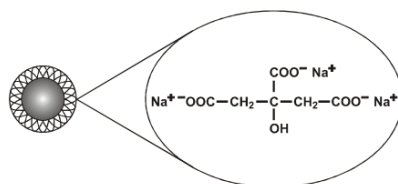


Figure 3.2 Schematic representation of the surface of FluidMAG-CT functionalised with carboxyl group.

3.2.4 Research objectives:

1. To conjugate a DOTA chelator to the surface of SPIONs using a stable bifunctional linker without affecting radiometal chelation.
2. Investigate the optimal DOTA-amine concentration and the effect of chemical reaction on the structure of DOTA-SPION by using DLS and TEM.
3. Optimise the methods for radiolabelling DOTA-SPION with ^{111}In .
4. Test the stability of ^{111}In -DOTA-SPION chelation *in vitro* and *in vivo*.

3.3 Methods

3.3.1 Synthesis and characterisation of DOTA-SPIONs

DOTA-amine synthesis was carried out with assistance from Dr Robin Bofinger (UCL Department of Chemistry). Transmission Electron microscopy (TEM) characterisation was conducted by Dr Mark Turmaine, UCL Biosciences EM facility.

A 1,4,7,10-tetraazacyclododecane-1,4,7,10-tetraacetic acid (DOTA) chelator derivative, bearing a polyethylene glycol (PEG) linker with a free amine (DOTA-amine), was synthesised as previously described (*Mitchell et al., 2013*). DOTA-amine was subsequently conjugated to the surface of a superparamagnetic iron oxide nanoparticle (SPION) via a peptide bond to a carboxyl group on the SPIONs surface (100 nm-FluidMAG-CT– Chemicell, Berlin, Germany). This was done using an EDC/sulfo-NHS (1-Ethyl-3-[3-dimethylaminopropyl]carbodiimide-hydrochloride/(N-hydroxysulfosuccinimide) coupling method (*Abdollah et al., 2014*) to produce DOTA-SPION (Figure 3.3). In brief, SPIONs (5 mg Fe, 200 μ l) were incubated with 200 μ l of EDC/sulfo-NHS activation buffer containing 1.21 mg EDC and 8.8 μ l of 230 mM sulfo-NHS prepared in 0.1 M 2-(N-morpholino)ethanesulfonic acid (MES) buffer pH 6. The reaction was allowed to proceed for 30 minutes at room temperature on a shaker and was terminated by application to a PD-10 column equilibrated with phosphate buffered saline (PBS, pH 7.4). Next, the PBS buffer was replaced by 1 ml of a DOTA-amine solution in PBS pH 8 and incubated for 3 hours at room temperature on a shaker. The nanoparticles were magnetically separated by using magnetic separator (MACSiMAG™ Separator – Miltenyi Biotec, Surrey, UK) and washed 3 times with PBS in order to remove unreacted organic molecules and stored in PBS pH 7.4.

The hydrodynamic particle diameter (nm) and the zeta potential (surface charge in mV) of SPIONs only and DOTA-SPIONs with different DOTA-amine concentrations (1 mM, 5 mM and 10 mM) were measured by dynamic light scattering (DLS, Zetasizer Nano-ZS, Malvern Instruments, UK). Both measurements were performed in PBS at 25°C. As the increasing DOTA-amine concentration appeared to have no influence on zeta potential of the formulation but did alter size (see results), all further experiments were performed using 1 mM DOTA-amine.

The iron oxide cores of DOTA-SPIONs (1 mM) were examined by using TEM. In brief, 2 μ l of either SPIONs or DOTA-SPIONs (in PBS) was placed onto the carbon surface of a 400 mesh carbon/formvar coated copper grid and was allowed to air dry for several minutes before observation. The grids were then imaged using a Jeol 1010 TEM and recorded using a Gatan Orius camera.

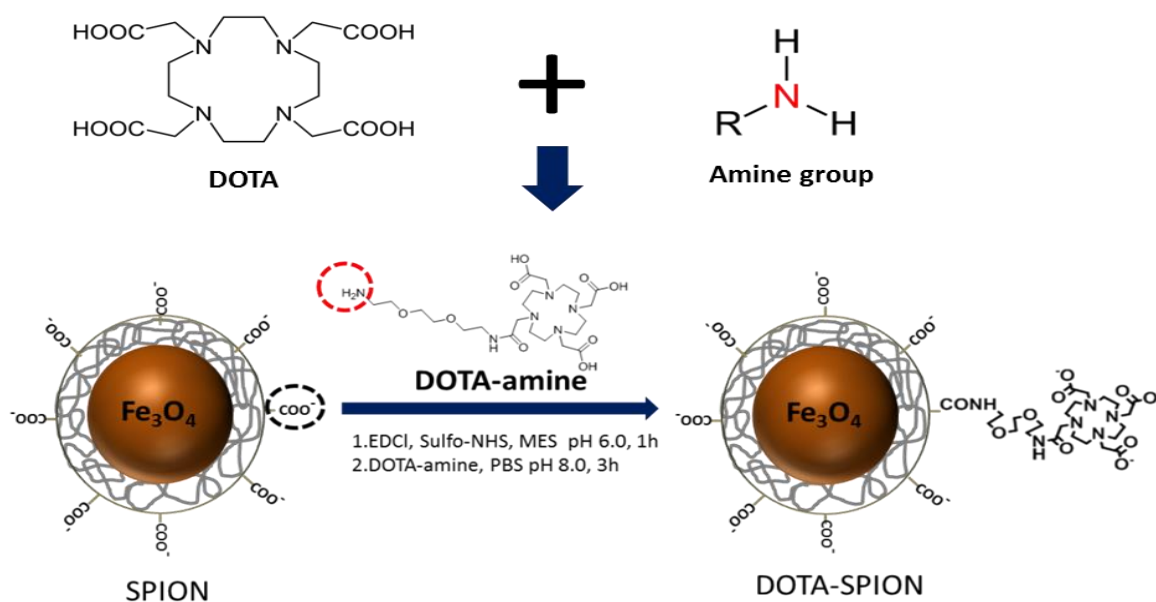


Figure 3.3 Schematic representation of the synthesis of DOTA-SPION showing a peptide bond formation between the carboxyl group (black circle) and amine group (red circle).

3.3.2 Radiolabelling DOTA-SPION with Indium-111 Chloride ($^{111}\text{InCl}_3$)

Since ammonium acetate buffer and 4-(2-hydroxyethyl)-1-piperazineethanesulfonic acid (HEPES) buffer are commonly used for radiometals chelation (*Brom et al., 2012*), 0.1 M ammonium acetate buffer (pH 6), 20 mM HEPES buffer pH 5.5 and pH 7 were tested to determine the optimal buffer for radiolabelling DOTA-SPION with $^{111}\text{InCl}_3$ (^{111}In -DOTA-SPION). 0.1 mg of DOTA-SPIONs was incubated with ~2 megabecquerel (MBq) of $^{111}\text{InCl}_3$ (250 μl , Mallinckrodt, Petten, Netherlands) using 250 μl of three buffers mentioned above. The mixture was shaken for 4 hours at 70 °C and the particles were magnetically separated and washed 3 times with PBS to remove non-specific binding. Radioactivity (MBq) was measured after each wash using an isotope calibrator (Curimenter 4, PTW, Freiburg, Germany). The results were presented as the percentage of radioactivity retained on the particles relative to 0 hour. 20 mM HEPES buffer pH 5.5 was found to be the optimal buffer for radiolabelling (see results) and was used for all further experiments.

To optimise the incubation time for DOTA-SPION radiolabelling, 0.1 mg of DOTA-SPIONs were incubated with ~2 MBq of $^{111}\text{InCl}_3$ in 20 mM HEPES buffer pH 5.5 as described above. The mixture was shaken for 4 hours at 70 °C and radiolabelling yield of the particles were determined at 1, 2, 4 and 6 hours after incubation using thin layer chromatography (TLC - Silica gel on TLC Al foils, Figure 3.4). A pencil line was drawn at 1 cm from the lower end of a TLC strip and 2 μl aliquot of radioactive particles were applied onto it. As a negative

control, an equal volume of free $^{111}\text{InCl}_3$ (without particles) was applied on another strip. When the spot of radioactivity was dry, the tip of the lower end of each TLC strip was submerged in 50 mM diethylenetriaminepentaacetic acid (DTPA) solution (pH 7) to produce the mobile phase. When the solvent almost reached the top of the TLC strip, it was cut at just above the pencil line to get the base (at the point of application) and the top (migrated) part. Then the amount of radioactivity of each part was measured using a gamma counter (Wizard² 3", PerkinElmer, Massachusetts, USA). The percentage of radiolabelling yield was calculated using the below equation.

$$\text{radiolabelling yield} = \frac{\text{radioactivity at the point of application (base)}}{\text{total radioactivity (base + top)}}$$

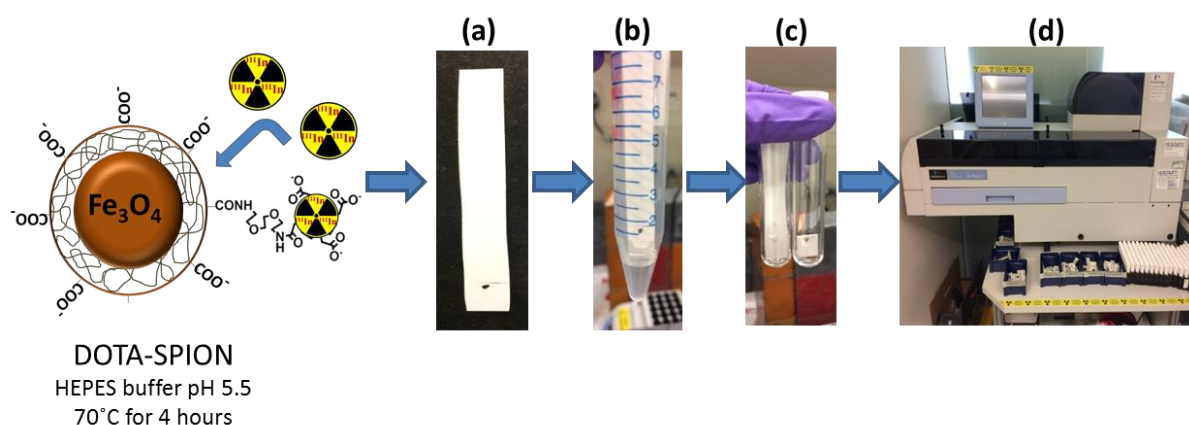


Figure 3.4 Procedure for measuring DOTA-SPION radiolabelling yield with TLC. (a) Radioactive particles were placed at the base of TLC strip. (b) TLC strip was submerged in DTPA solution. (c) The base and top part of TLC strip were cut and put into gamma counter measuring tubes. (d) Radioactivity was measured with gamma counter.

3.3.3 *In vitro* assessment of ^{111}In -DOTA-SPION chelation

Since ^{111}In is a positively charged ion (In^{3+}), it can statically bind to negatively charged carboxyl groups. To assess the chelation specificity of DOTA to ^{111}In , 0.1 mg of DOTA-SPIONs or SPIONs without DOTA were radiolabelled with ~ 2 MBq of $^{111}\text{InCl}_3$ as described above. After incubation on a shaker for 4 hours at 70°C, radiolabelling yield of the particles were determined using TLC and the percentage of radiolabelling yield was calculated as described above.

To assess chelation stability of DOTA to ^{111}In under physiological condition, 0.1 mg of SPIONs and DOTA-SPIONs were used for radiolabelling with ~ 2 MBq of $^{111}\text{InCl}_3$ as described above. After 4 hours incubation at 70°C, radiolabelled particles were incubated in DMEM-F12, supplemented with 10% FCS in an humidified incubator at 37°C with 95% air

and 5% CO₂ for 18 hours. The particles were then magnetically separated and washed 3 times with PBS. The radioactivity of the particles was measured after separation and after each wash. The results were presented as the percentage of radioactivity retained on the particles after correcting for ¹¹¹In radioactive decay. Three washes with PBS were found to be optimal to prevent non-specific binding and were used in all further experiments.

3.3.4 *In vivo* studies

All the animal procedures were performed as described in Chapter 2.4.

3.3.5 *In vivo* assessment of ¹¹¹In-DOTA-SPION chelation

To assess *in vivo* chelation stability of DOTA to ¹¹¹In, the mice were injected intravenously via a tail vein (150 µl PBS) with either (a) ~2.5 MBq of ¹¹¹InCl₃ (n = 3), (b) ~2 MBq ¹¹¹In-DOTA-SPION particles containing ~142.8 µg of Fe (n = 3) or (c) ~2 MBq ¹¹¹In-SPION particles containing ~142.8 µg of Fe (n = 3).

3.3.6 SPECT/CT

At 1 hour, 1, 3 and 7 days after injection, mice were anaesthetised and whole body SPECT/CT scans were performed as described in chapter 2.4.3. 3D ROIs were created for liver and kidney for each time point using VivoQuant software. After correcting for ¹¹¹In decay, the 3D ROIs were calculated as the percentage of injected dose/organ (%ID/mm³).

3.3.7 Statistical analysis

All *in vitro* experiments were repeated at least 3 times with 3 triplicates.

Statistical analysis was performed with GraphPad Prism version 6.01. Data were presented as mean ± standard deviation (SD). One way ANOVA test was conducted for buffer optimization and *in vivo* validation study while unpaired two-tailed t test was conducted in the rest of the experiments.

3.4 Results

3.4.1 Characterisation of DOTA-SPIONs

The hydrodynamic particle diameter (nm) and the zeta potential (surface charge in mV) of SPIONs only and DOTA-SPIONs with a range of DOTA-amine concentrations: 1 mM, 5 mM and 10 mM was measured in PBS at 25°C using DLS (Table 3.1). The conjugation of DOTA-amine to SPION increased the hydrodynamic diameter of the particle up to 2-fold larger than the original size. In terms of surface charge, all concentrations of DOTA-amine produced DOTA-SPIONs with a similar decrease in surface charge compared to SPION alone and no concentration dependent changes were seen. This is likely due to the interaction of negatively charged DOTA-SPIONs with ionic salts in PBS which leads to the particles aggregation. Therefore, the lowest DOTA-amine concentration (1 mM) was used for all further studies.

Table 3.1. Hydrodynamic diameter and zeta potential of SPION with no DOTA and DOTA-SPION with 1 mM, 5 mM and 10 mM DOTA-amine concentration in PBS at 25°C. Data are shown as means \pm SD (n = 3).

Sample	Hydrodynamic diameters (Particle size in nm)	Zeta potential (surface charge in mV)
SPION	71 \pm 0.71	-17 \pm 0.49
DOTA-SPION (1 mM)	103 \pm 1.55	-30 \pm 0.85
DOTA-SPION (5 mM)	106 \pm 1.08	-31 \pm 0.38
DOTA-SPION (10 mM)	143 \pm 4.27	-32 \pm 2.01

DOTA-SPIONs (1 mM) were examined by TEM and compared to SPIONs only. TEM images showed the aggregation of both SPION and DOTA-SPION but no obvious morphological changes were seen. The mean core size of SPION is 6.25 \pm 3.51 nm and DOTA-SPION is 7.35 \pm 2.53 nm in diameter (Figure 3.5).

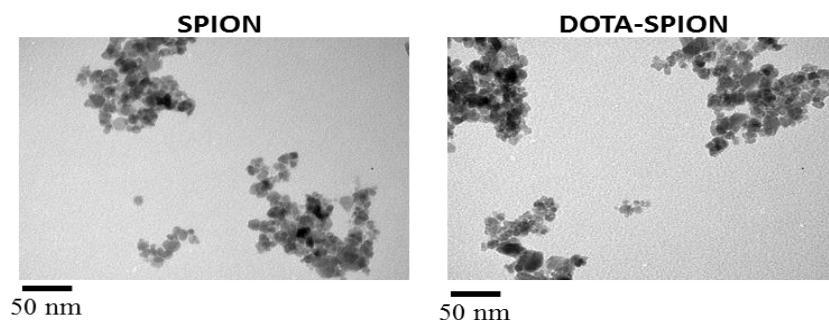


Figure 3.5 TEM micrograph of SPION and DOTA-SPION showing a similar morphological appearance. Scale bar is 50 nm.

3.4.2 Optimisation of DOTA-SPION radiolabeling

The commonly used buffers for radiometal chelation, HEPES buffer pH 5.5 (H-5.5), HEPES buffer pH 7 (H-7) and ammonium acetate buffer pH 6 (A-6), were tested to determine the optimal buffer for DOTA-¹¹¹In chelation. DOTA-SPIONs were incubated with ¹¹¹InCl₃ in all three buffers for 4 hours at 70°C and the percentage of radioactivity retained on the particles was calculated after each PBS wash step (Figure 3.6). After the first and second wash, the radioactivity of particles was reduced but no significance difference was observed among the three buffers. However, after the third wash, the radioactivity of particles incubating in H-7 and A-6 buffer was significantly lower than in H-5.5 buffer ($P = 0.0193$ & $P = 0.0092$, respectively). This apparent improvement in radiolabelling stability suggests that HEPES buffer at pH 5.5 is the optimal buffer for DOTA-¹¹¹In chelation and was used for all further studies.

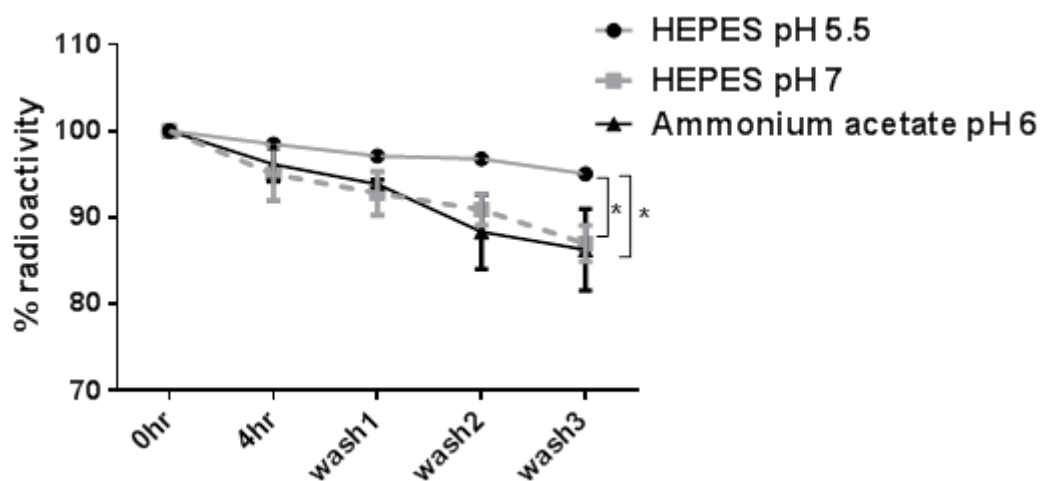


Figure 3.6 Buffer optimisation study showing the percentage of radioactivity on DOTA-SPION after 4 hours incubation with HEPES buffer pH 5.5, pH 7 or ammonium acetate buffer pH 6. * $P = 0.0193$ H-5.5 vs H-7 & * $P = 0.0092$ H-5.5 vs A-6. (All data are shown as mean \pm SD, $n = 3$)

To optimise the incubation time for DOTA-SPION radiolabelling, the particles were radiolabelled as described above and radiolabelling yield (%) of the particles were determined at 1, 2, 4 and 6 hours after incubation using TLC (Figure 3.7). At 1 hour after incubation, $54.75 \pm 4.66\%$ radiolabelling yield was achieved and it increased over time. At 4 hours after incubation, $90 \pm 2.89\%$ radiolabelling yield was achieved. No significance increase was seen at 6 hours after incubation ($P > 0.9999$). Therefore, 4 hours incubation time is optimal for DOTA-SPION radiolabelling and was used for all further studies.

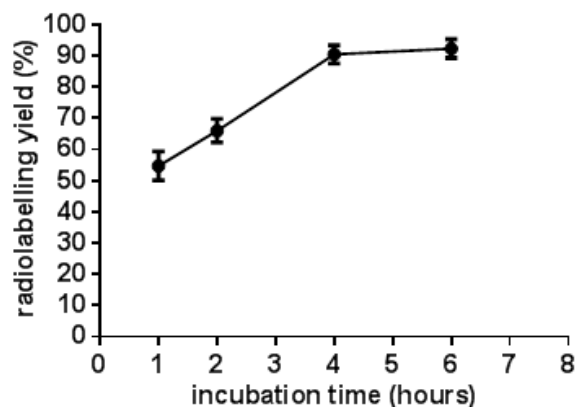


Figure 3.7 Labelling kinetic of DOTA-SPIONs after incubation with ^{111}In for 6 hours at 70°C . (Data are shown as mean \pm SD, $n = 3$)

3.4.3 *In vitro* validation of ^{111}In -DOTA-SPION chelation

In order to differentiate between static binding of In^{3+} to negative carboxyl groups and DOTA chelation (Figure 3.8a), a chelation specificity study was performed where ^{111}In bound to DOTA-SPION (^{111}In -DOTA-SPION chelation) was compared to ^{111}In bound to SPION only (^{111}In -SPION electrostatic interaction without DOTA). Radiolabelling yield of the particles was measured using TLC (Figure 3.8b). After 4 hours incubation with ^{111}In at 70°C , the amount of radioactivity bound to ^{111}In -DOTA-SPION was $92 \pm 7.23\%$ and significantly higher than ^{111}In -SPION ($P = 0.0035$).

The chelation stability of DOTA to ^{111}In under physiological condition was assessed by incubating ^{111}In -DOTA-SPION and ^{111}In -SPION in cell culture medium for 18 hours at 37°C and the percentage of radioactivity retained on the particles was calculated after each PBS wash step (Figure 3.8c). At 18 h after incubation, no significance difference in radioactivity was seen between two groups. However, after the first PBS wash, the radioactivity of ^{111}In -SPION was significantly lower than ^{111}In -DOTA-SPION ($P = 0.0131$) and further reduction was seen with subsequent wash steps. After the third wash, the radioactivity of ^{111}In -SPION was significantly lower than the 18 h time point ($P = 0.001$). However, no significant

reduction in radioactivity was observed for ^{111}In -DOTA-SPION ($P = 0.4138$). Three washes with PBS was therefore used to prevent non-specific binding in all further experiments.

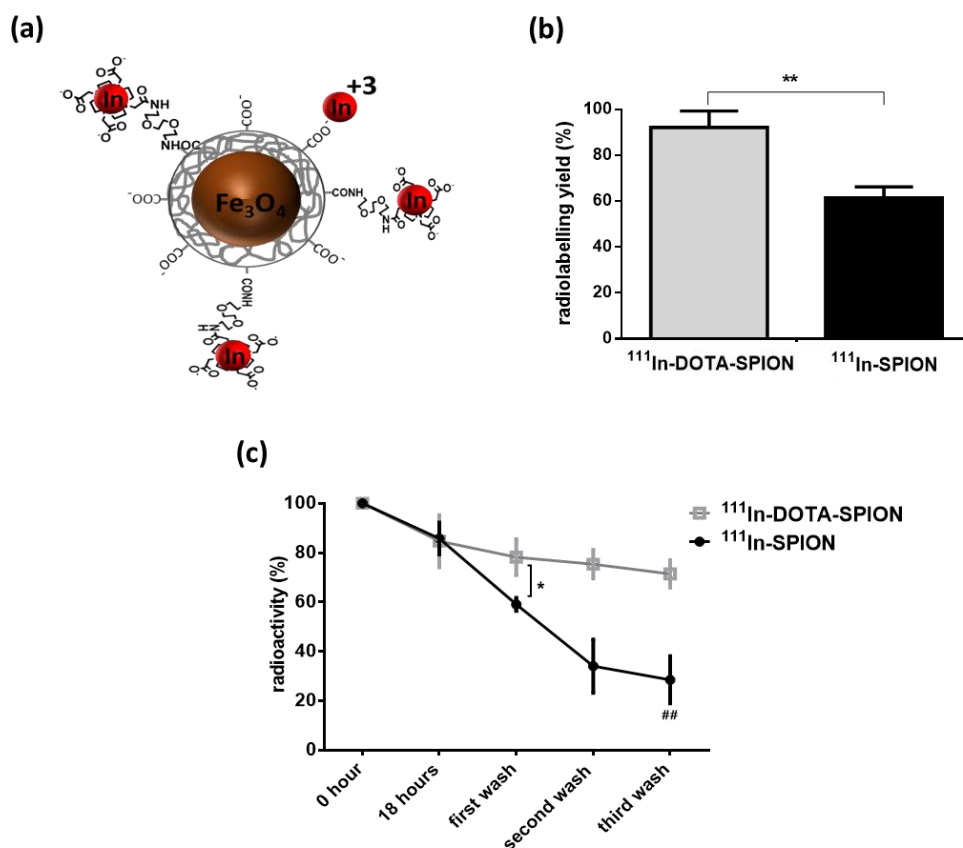


Figure 3.8 *In vitro* validation of ^{111}In -DOTA-SPION chelation (a) Schematic representation of static binding of In^{3+} to negative carboxyl groups or to DOTA chelator (b) The radiolabelling yield from TLC data after 4 hours incubation with ^{111}In at 70 °C. ** $P = 0.0035$ ^{111}In -DOTA-SPION vs ^{111}In -SPION (c) The percentage of radioactivity on DOTA-SPION and SPION from the chelation stability study after 18 hours incubation in culture media at 37°C. * $P = 0.0131$ ^{111}In -DOTA-SPION vs ^{111}In -SPION after first wash, ## $P = 0.001$ 18 h vs third wash in ^{111}In -SPION. (All data are shown as mean \pm SD, $n = 3$)

3.4.4 *In vivo* validation of ^{111}In -DOTA-SPION chelation

To study chelation stability of ^{111}In -DOTA-SPION conjugates in *in vivo*, NSG mice were injected intravenously with either ^{111}In -DOTA-SPION, ^{111}In -SPION particles or free $^{111}\text{InCl}_3$ and serially imaged with SPECT over 7 days (Figure 3.9). Since the liver is the known excretion pathway for nanoparticles (Mejias *et al.*, 2010) and the kidney is normal clearance route for free $^{111}\text{InCl}_3$ (Krenning *et al.*, 1992), the amount of radioactivity in these organs was calculated as %ID/ mm^3 (Appendix 2).

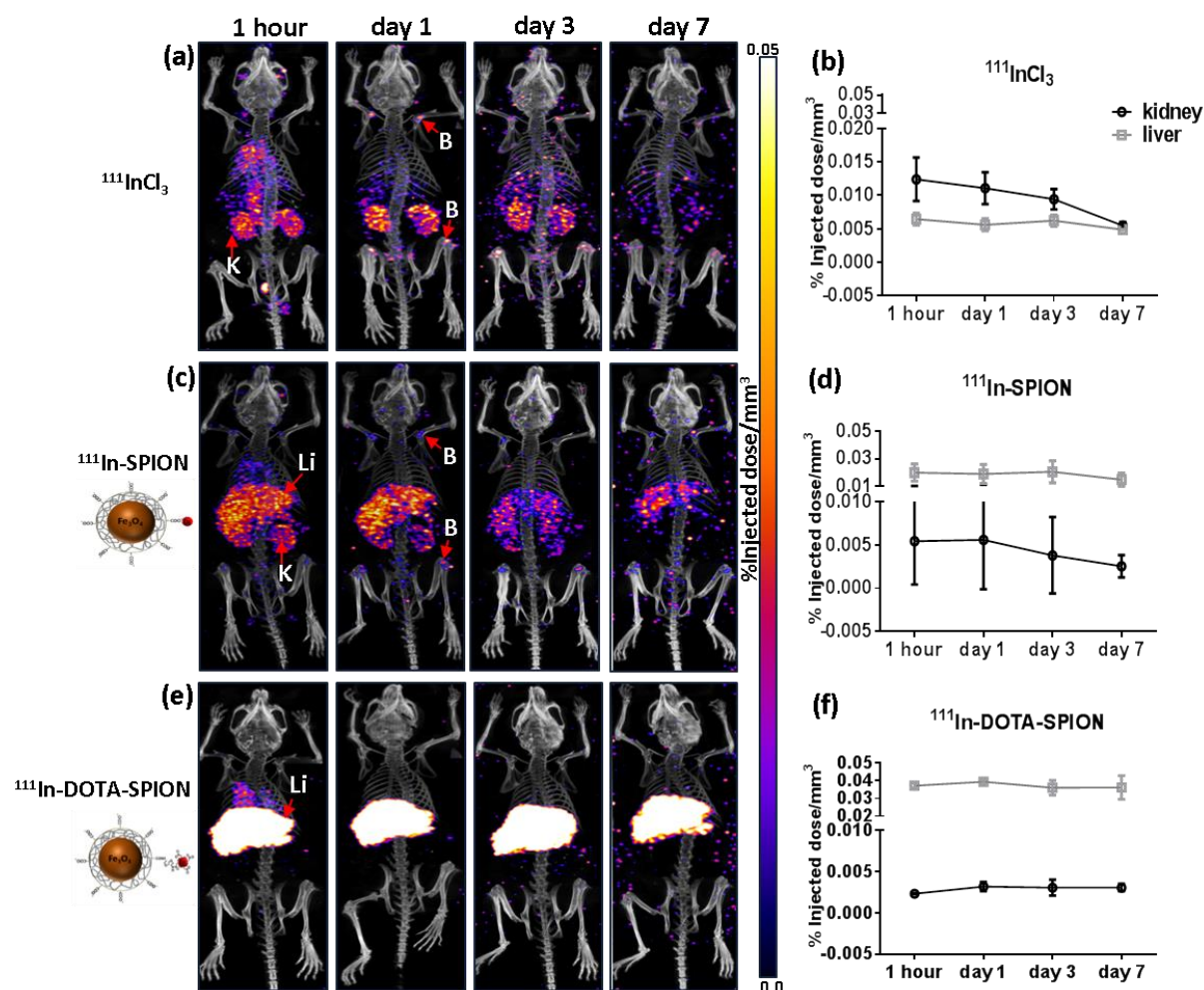


Figure 3.9 *In vivo* validation of ^{111}In -DOTA-SPION chelation. (a, c, e) SPECT/CT images at 1 hour, days 1, 3 and 7 after IV injection of ^{111}In -DOTA-SPION, ^{111}In -SPION and free $^{111}\text{InCl}_3$ (Labels: Li = Liver, K = Kidney, B = Bone). (b, d, f) 3D ROI quantification of SPECT signal in liver and kidney as calculated as %ID/ mm^3 . (All data are shown as mean \pm SD, n=3).

As expected, both nanoparticle groups showed high radioactivity distribution in the liver and $^{111}\text{InCl}_3$ showed high radioactivity distribution in kidney throughout the study (Figure 3.9). However, at 1 hour after injection, the percentage of radioactivity in liver was significantly higher in the $^{111}\text{In-DOTA-SPION}$ group compared to $^{111}\text{In-SPION}$ ($P = 0.0031$) and free $^{111}\text{InCl}_3$ ($P = 0.0001$) group (Figure 3.10). Conversely, the percentage of radioactivity in the kidney at 1 hour after injection was the lowest in the $^{111}\text{In-DOTA-SPION}$ group and was significantly lower than $^{111}\text{InCl}_3$ group ($P = 0.0273$). No significant difference was observed between $^{111}\text{InCl}_3$ and $^{111}\text{In-SPION}$ groups ($P = 0.1373$, Figure 3.10). At days 1, 3 and 7 after injection, both the $^{111}\text{InCl}_3$ and $^{111}\text{In-SPION}$ group showed increasing presence of radioactivity in shoulder joint, knee joint and spine but this distribution was not seen in $^{111}\text{In-DOTA-SPION}$ group (Figure 3.9 a, c, e).

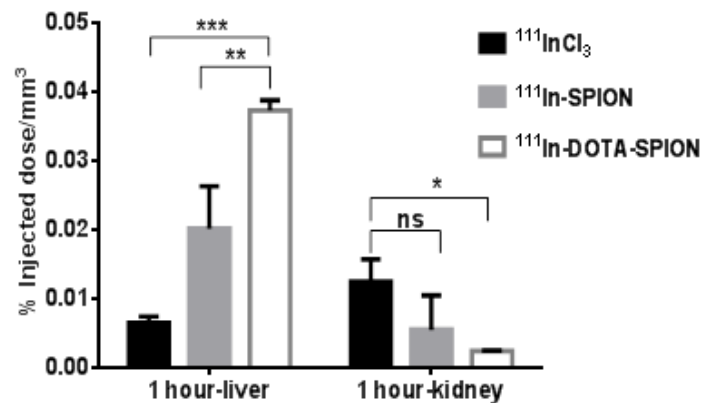


Figure 3.10 3D ROI quantification of SPECT signal in liver and kidney at 1 hour after IV injection as calculated as $\%ID/mm^3$. In liver, ** $P = 0.0031$ $^{111}\text{In-DOTA-SPION}$ vs $^{111}\text{In-SPION}$ & *** $P = 0.0001$ $^{111}\text{In-DOTA-SPION}$ vs $^{111}\text{InCl}_3$. In kidney, * $P = 0.0273$ $^{111}\text{In-DOTA-SPION}$ vs $^{111}\text{InCl}_3$. (All data are shown as mean \pm SD, $n=3$).

3.5 Discussion

The work presented in this chapter aimed to conjugate a DOTA chelator to the surface of SPIONs to develop a dual SPECT/MRI imaging probe and to test the reproducibility and stability of ^{111}In -DOTA-SPION conjugates.

A series of experiments were performed to characterise DOTA-SPION conjugates, optimise the radiolabelling process and validate the stability of ^{111}In -DOTA-SPION chelation. DLS results showed the hydrodynamic diameter of the particle increased after conjugation suggesting the presence of DOTA molecules on the surface. However, these measurements might be overestimated because negatively charged DOTA-SPION conjugates can attract water molecules and form a complex which leads to a larger hydrodynamic diameter. A reduction in surface charge of the DOTA-SPION compared to SPION alone is also indicative of DOTA conjugation to the SPION, as DOTA contains three additional carboxyl groups (originally four but one is functionalized to the PEG amine). More importantly, no concentration dependent decrease in surface charge indicates that high DOTA-amine concentration may cause destabilization and aggregation in physiological medium due to interaction with ionic salts in PBS. Therefore, the 1 mM concentration was used for all further studies. In addition, the aggregations of SPION and DOTA-SPION were detected in TEM images. These results are in agreement with findings from *Safi et al., 2010*; *Andreas et al., 2012* which reported the destabilization and aggregation of citrate-coated SPIONs in physiological medium. However, TEM images showed no morphological changes of SPION after conjugation with DOTA-amine which suggests that the chemical reaction was gentle and maintained the structure of SPIONs. Different batches of DOTA-SPION conjugates showed similar results which indicates good reproducibility of the synthesis process.

To ensure maximal DOTA- ^{111}In chelation, the incubation time and the buffer for radiolabeling were optimised, with 4 hours incubation time found to be optimal. Two common buffers for radiometal chelation were tested and HEPES buffer at pH 5.5 was found to be the optimal buffer, performing better than pH 7 which is consistent with published literature (*Brom et al., 2012*). This is likely due to slightly acidic buffer favoring the complex formation of acidic cations such as ^{111}In which can cause precipitation at neutral pH (*Anderson et al., 1999*, *Breeman et al., 2003*).

DOTA- ^{111}In chelation specificity was tested to differentiate from electrostatic binding of ^{111}In to the negative carboxyl groups on SPIONs. The results showed the radiolabeling yield of ^{111}In -DOTA-SPION was 1.5-fold higher than ^{111}In -SPION indicating that ^{111}In is indeed chelated to DOTA. This finding was further supported by the DOTA- ^{111}In chelation stability which showed that the radioactivity of ^{111}In -DOTA-SPION was 2.5-fold higher than ^{111}In -

SPION after the first PBS wash and that no significant reduction was seen for ^{111}In -DOTA-SPION throughout the study. These results suggest that DOTA- ^{111}In chelation is robust and the ^{111}In -DOTA-SPION conjugates are stable in physiological conditions. This is likely due to thermodynamic stability of DOTA complexes and resistance to dissociation by chelating ^{111}In inside its rigid ring structure (León-Rodríguez *et al.*, 2008).

The chelation stability of ^{111}In -DOTA-SPION *in vivo* was further tested to validate the *in vitro* results and confirm that the particles were stable from *in vivo* enzymatic reactions. Both ^{111}In -DOTA-SPION and ^{111}In -SPION groups showed high radioactivity distribution in the liver. This is because SPIONs are known to be preferentially taken up by *in situ* macrophages within the liver (Abdollah *et al.*, 2018) as part of clearance via the reticuloendothelial system (RES). However, the radioactivity in the liver was 2-fold higher in the ^{111}In -DOTA-SPION group compared to the ^{111}In -SPION group, which is consistent with the *in vitro* chelation specificity study. ^{111}In -DOTA-SPION showed the lowest radioactive uptake in kidney, indicating that ^{111}In -DOTA-SPION chelation is stable unlike the static ^{111}In -SPION binding, which showed signs of free ^{111}In leakage and clearance from the body via the kidney. In addition, the radioactive uptake in bone was observed in the $^{111}\text{InCl}_3$ and ^{111}In -SPION groups indicating the deposition of free ^{111}In in bone marrow by binding to the plasma protein transferrin due to its similarities with iron (Harris *et al.*, 1994). This distribution was not seen in the ^{111}In -DOTA-SPION group. These results suggest that ^{111}In is stably chelated to DOTA *in vivo* and is consistent with *in vitro* assessments.

3.6 Conclusion

The data presented in this chapter demonstrates the robust testing of the reproducibility and stability of the DOTA chelator and bifunctional linker which combines the SPECT and MRI components. These results highly suggest that the first important step in developing the dual imaging probe was completed successfully.

Chapter 4

Multi-modal imaging of stem cell distribution after systemic injections

4.1 Abstract

Stem cell therapies have been extensively studied in clinical trials to provide regenerative therapies for various diseases or adjuvant therapies for cancers. However, imaging cells distribution throughout the body is challenging and no single imaging modality can provide a complete view on stem cell behaviour after transplantation.

The main aims of this chapter were 1) to investigate the applicability of SPECT/MRI (^{111}In -DOTA-SPIONs) dual imaging nanoparticles as stem cell tracking agents and 2) to compare the differences in whole body cell distribution patterns after intravenous (IV) and intracardiac (IC) injection using multi-modal imaging.

Luciferase expressing human adipocyte derived mesenchymal stem cells (ADSC) were labelled with ^{111}In -DOTA-SPIONs dual imaging agents and the effect of labelling agents on cell function and cell viability was evaluated. To study *in vivo* cell distribution pattern, ^{111}In -DOTA-SPIONs labelled ADSCs were injected either IV or IC into NSG mice and imaged with BLI, SPECT/CT and MRI serially over 7 days.

In vitro results showed ^{111}In -DOTA-SPIONs had no effect on migratory and differentiation capabilities of ADSCs. Although the cell proliferation and viability were reduced due to ^{111}In -DOTA-SPIONs labelling, the conventional radiolabeling method ^{111}In -oxine showed more adverse effect on the cells. *In vivo* SPECT images at day 0 after IV injection showed the majority of ADSCs were accumulated in lungs while the cells uptake after IC injection showed the 9-fold reduction of lung signal, 5-fold and 1.6-fold increase uptake in brain and kidney respectively. These results were further supported by BLI and MRI images. Histological analysis at day 7 after injection showed co-localisation of SPION and ADSCs in lungs which suggest that the labelling agents retained in the grafted ADSCs throughout the experiments.

These findings demonstrate that the IC injection is more efficient than IV in delivering stem cells to multiple organs and the benefits of multi-modal imaging in obtaining the comprehensive information on the fate of stem cell after transplantation.

4.2 Introduction

4.2.1 The role of multi-modal imaging in cell tracking

Recently, nanoparticle-based multi-modal imaging probes have become an attractive candidate in stem cell tracking. This is because cells labelled with these agents can be simultaneously or successively tracked across scale (whole body to sub-cellular levels) using multiple *in vivo* imaging platforms (PET/SPECT, MRI and PAI) to *ex vivo* validation methods such as transmission electron microscopy. Among the different combinations of multi-modal imaging probes, the nuclear/MRI combination can offer the most comprehensive information on cell localisation. For example, by using iron oxide-based nuclear/MRI probes, the number of cells in a target organ can be quantified from nuclear imaging and the precise cell localisation in relation to anatomical area can be visualised from high resolution MR imaging. However, knowledge on cell localisation alone is not adequate for *in vivo* stem cell tracking. The information on cell viability at the engraftment site is also very important in optimising stem cell therapy. Therefore, multi-modal direct cell labelling probes must be combined with reporter gene imaging to acquire the complete picture of the fate of transplanted cells within the body. Although BLI imaging can only be applied in small animal models, it has the highest sensitivity for cell detection when compared to nuclear reporter gene imaging due to lack of background signal. Hence, combining BLI (reporter imaging) with nanoparticle based nuclear/MRI imaging probes will greatly benefit preclinical research on stem cell tracking and stem cell therapy applications.

4.2.2 Challenges

Many studies have reported the effectiveness of nuclear/MRI imaging probes in preclinical *in vivo* imaging applications including tumour imaging (*Lee et al., 2008*), lymph node imaging (*Madru et al., 2014*) and atherosclerosis (*Cheng et al., 2015*). However, until now, only one study has shown the benefits of using SPECT/MRI/fluorescent probes in stem cells tracking (*Tang et al., 2015*). This is mainly because cell tracking, unlike other applications, requires the effect of the labelling agent on cell cytotoxicity and functionality to be tested extensively before it can be used in *in vivo* applications. Another major limitation of direct labelling is that imaging only identifies the imaging agent whether within the cell or not (leakage and clearance after death/subsequent uptake by phagocytic cells), creating a false-positive distribution. This problem could be resolved by combining with cell-specific imaging agents such as reporter gene imaging. However, discrepancies can arise between imaging modalities due to the differences in sensitivity. Therefore, not only the validation studies on the specificity of the imaging agents but also the sensitivity between imaging techniques must also be considered during the interpretation of results. Another issue with multi-modal

imaging is the co-registration of images obtained from the different techniques. This problem could be overcome by using new hybrid scanners such as PET/MRI and effective computer algorithms. In addition, due to multiple and longer imaging sessions, the effect of increased anaesthesia dose on animals needs to be carefully monitored. All these problems together with the possible solutions must be considered when planning the experimental model. Nonetheless, many studies have demonstrated the urgent need to develop a well validated multi-modal imaging probe for stem cell tracking.

4.2.3 Experimental approach

In this study, human adipose derived mesenchymal stem cells (ADSCs) were selected to label with SPECT/MRI (^{111}In -DOTA-SPION) imaging probes due to a number of reasons: 1) murine MSCs have previously been shown to transform into a malignant sarcoma due to chromosomal instability (*Miura et al., 2006*); 2) human ADSCs are readily accessible as a primary source from UCL Royal Free Hospital; 3) they can be readily isolated and expanded from adipose tissue which is commonly available from various plastic surgeries such as liposuction with no ethical concerns (*Naderi et al., 2014*); 4) the extensive characterisation of these cells has been done and published in many journals (*Naderi et al., 2014, 2017; Griffin et al., 2014*); and 5) they have already been used in clinical trials to treat radiotherapy tissue damage (*Rigotti et al., 2007*) and patients with scleroderma (*Griffin et al., 2017, Varghese et al., 2017*). Therefore, the methods of isolation and characterisation of ADSCs is not covered in this thesis. ADSCs were transduced with lentivirus to express luciferase for BLI imaging. These luciferase expressing ADSCs were labelled with SPECT/MRI dual imaging probes (Chapter 3) to enable tri-modal imaging capabilities (Figure 4.1).

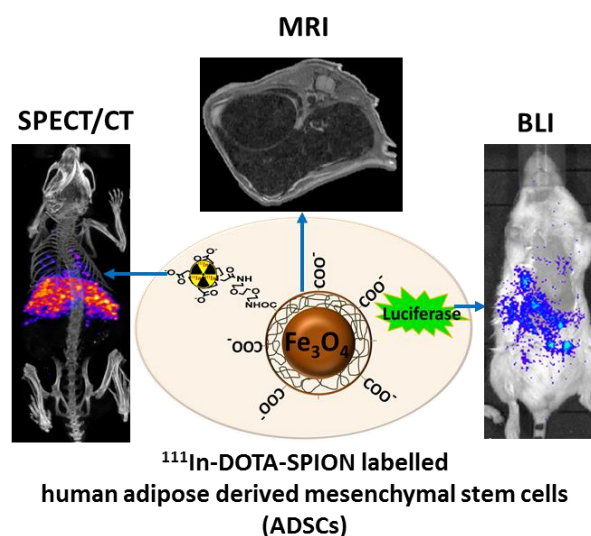


Figure 4.1 Schematic representation of a tri-modal (BLI, SPECT/CT & MRI) imaging agent for stem cell tracking.

4.2.4 Research Objectives

1. Evaluate intracellular uptake and retention of ^{111}In -DOTA-SPIONs in ADSCs.
2. Evaluate the effect of ^{111}In -DOTA-SPIONs labelling on cell function and cell viability.
3. Assess the whole body distribution of ^{111}In -DOTA-SPION labelled luciferase expressing ADSCs following intravenous injection (IV) or intracardiac injection (IC) through left ventricular cavity.
4. Validate the specificity of *in vivo* imaging results.
5. Assess any adverse effects derived from labelling agents, cell transplantation or experimental procedures on control animals.

4.3 Method

4.3.1 Cell culture

All experiments were performed using luciferase expressing human adipose derived mesenchymal stem cells (ADSCs). A series of detailed protocols were previously described in Chapter 2.2.

4.3.2 Intracellular iron uptake

Ferrozine assay

To measure intracellular iron uptake by ADSCs, the ferrozine assay was performed as previously described (*Riemer et al., 2004*). ADSCs were plated in 24-well plates at a concentration of 0.22×10^5 per well in triplicates and left to attach overnight. The next day, the cells were incubated with ^{111}In -DOTA-SPION at concentration of either 0.1 mg/ml Fe (~7 MBq of ^{111}In), 0.2 mg/ml Fe (~14 MBq of ^{111}In) or 0.4 mg/ml Fe (~28 MBq of ^{111}In) for 16 hours. After washing 3 times with PBS, the labelled ADSCs were trypsinised and pelleted. The cell pellets were frozen and stored at $-20\text{ }^\circ\text{C}$. Frozen cells were lysed by adding 50 μl of 1.2 M HCl and incubated for 2 hours at $60\text{ }^\circ\text{C}$. The samples were cooled and centrifuged to collect all condensate. Then 50 μl of deionized water (solvent of SPIONs) was added. To create a standard curve of iron samples with known concentrations, serial dilution of SPIONs at 0, 0.3, 0.625, 1.25, 2.5, 5, 10 and 20 $\mu\text{g/ml}$ Fe were prepared from the stock solution and 50 μl of 1.2 M HCl was added to each tube. Next, to each tube of cell lysates and SPIONs, 50 μl of iron detection reagent was added and incubated for a further 30 minutes at room temperature. 100 μl of the mixture was then transferred to a 96-well plate and the absorbance was measured at 550 nm and the background at 780 nm using a Varioskan LUX multimode microplate reader (ThermoFisher Scientific, Waltham, MA USA).

To calculate the amount of iron in the sample in μg , the background absorbance was subtracted from all samples and a calibration curve for standard was created and linear regression was performed using GraphPad Prism 6. From the equation $y = mx + c$, where m = slope and c = Y-intercept, the value of slope was calculated. The absorbance value of the samples was divided by the slope to calculate the amount of iron in μg . Next, the amount of iron in pg per cell (pgFe/cell) was calculated as follows:

$$\text{pgFe / cell} = \frac{\text{Concentration (mgFe / ml)}}{\text{number of cells / ml}} \times 10^6$$

Perl's Prussian blue staining

To visualise intracellular iron uptake by ADSCs, Prussian blue staining was performed as previously described (*Jasmin et al., 2012*). ADSCs were seeded and incubated with ^{111}In -DOTA-SPION (0.2 mg/ml Fe, ~ 14 MBq of ^{111}In) as described above. Next, the well plates were washed 3 times with PBS and the cells were fixed in 4% paraformaldehyde (PFA) for 30 minutes at room temperature. The cells were then washed 2 times with PBS followed by staining with Perl's solution (Appendix 1) for 20 minutes and counterstained with 1% Nuclear Fast Red and then imaged with EVOS FL Auto cell imaging system (ThermoFisher Scientific, Massachusetts, USA).

Transmission Electron Microscopy (TEM)

Control ADSCs and ^{111}In -DOTA-SPION labelled ADSCs (~ 0.2 MBq of ^{111}In , 18 μg of Fe) were seeded at 0.22×10^5 per well on coverslips (VWR) in 24-well plates (Corning) and then left to attach overnight. Next day, TEM was performed as previously described in Chapter 2.3.

Retention of ^{111}In -DOTA-SPIONs after intracellular uptake

To study the leakage of radioactivity from ^{111}In -DOTA-SPION after intracellular uptake, the radiolabelled cells were plated in 24-well plates at a concentration of 0.22×10^5 per well (~ 0.2 MBq of ^{111}In , 18 μg of Fe per well) in triplicates. The media was removed and measured with a gamma counter (Wizard 2480, Perkin Elmer) at days 1, 2, 3 and 7 after plating. The percentage of radioactivity retained was calculated by subtracting the amount of radioactivity in the media from the initial activity measure in the labelled cells at day 0 after decay correction and multiplied by 100.

To investigate ^{111}In -DOTA-SPION release from dead cells, ADSCs were seeded in 48-well plates at a concentration of 0.1×10^5 per well in triplicates and left to attach overnight. The next day, the cells were incubated with ^{111}In -DOTA-SPION (~ 0.1 MBq of ^{111}In , 9 μg of Fe per well) for 16 hours. Next, the well plates were washed 3 times and treated with 3.5 mM H_2O_2 for one hour followed by 2 washes of PBS done carefully to not disturb adhered cells. Then the well plates were replaced with normal cell culture media and monitored for cell death with a time lapse microscope (Nikon BioStation CT, Nikon Instruments Europe BV, Amsterdam, Netherlands).

4.3.3 The effect of ^{111}In -DOTA-SPION labelling on cell function

Migration assay

To assess the migration capability of ADSCs after dual labelling, ^{111}In -DOTA-SPION labelled ADSCs (~ 0.1 MBq of ^{111}In , $9 \mu\text{g}$ of Fe per well) were seeded at a concentration of 0.1×10^5 per well in 4-well silicone inserts with 4 defined $500 \mu\text{m}$ cell-free gaps (IBIDI, Martinsried, Germany, Figure 4.2). The inserts were removed the next day and cell migration was monitored. After 30 hours, the cells were stained with Hoechst 33342 (ThermoFisher Scientific, Massachusetts, USA) and the number of cells between the gaps was analysed using Image J software and compared with the results from control ADSCs.

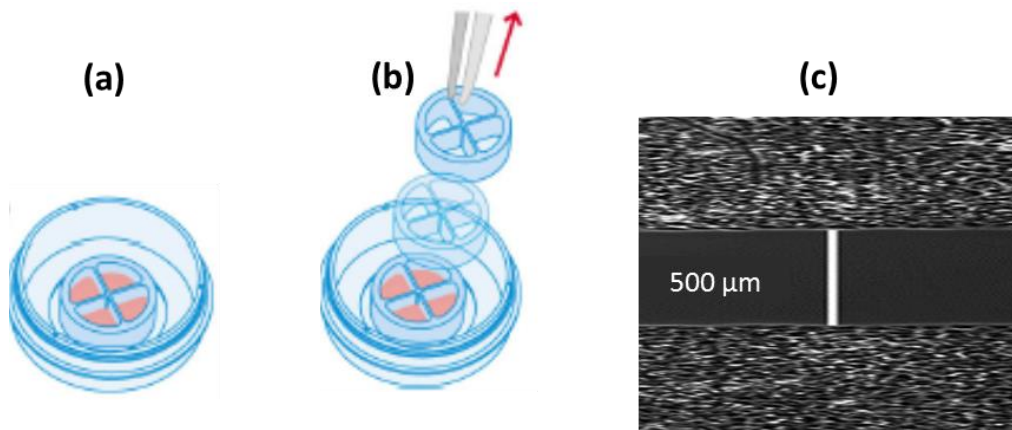


Figure 4.2 Assessment of migration capability using IBIDI culture inserts (adapted from IBIDI's supporting material: instructions for culture inserts). (a) Cells were seeded in 4-well silicone inserts. (b) The insert was removed the next day. (c) Cell migration between a defined gaps of $500 \mu\text{m}$ was monitored.

Differentiation assay

To determine the effect of labelling on the differentiation potential of ADSCs, a differentiation assay was performed as previously described (New *et al.*, 2015). ADSCs were labelled with ^{111}In -DOTA-SPION (~ 0.2 MBq of ^{111}In and $18 \mu\text{g}$ of Fe) and plated in 24-well plates (Corning) at a concentration of 0.22×10^5 per well in triplicates. When both labelled and control cells reached 90-100% confluency, the regular media was removed and differentiation media (adipogenic, chondrogenic or osteogenic) was added to appropriate wells and was changed every three days. Undifferentiated wells received regular media. After 3 weeks staining was conducted for each differentiation, the cells were imaged using the EVOS FL Auto cell imaging system.

4.3.4 The effect of radiolabelling on cell proliferation and cell death

Since direct labelling with ^{111}In -oxine has been shown to be cytotoxic to cells (Gholamrezanezhad *et al.*, 2009), the effect of radiolabelling on cell proliferation and cell death was compared between ^{111}In -oxine and ^{111}In -DOTA-SPION labelling.

ADSC labelling with ^{111}In -oxine

50.16 MBq of $^{111}\text{InCl}_3$ in 1 M HCl was diluted to 500 μl with HPLC grade water, and neutralised using 1 μl aliquots of 1 M NaOH. Next, 5 μl of a 10 mg/ml solution of 8-hydroxyquinoline in chloroform was added and vortexed in a round-bottomed Pyrex tube for 5 minutes. 500 μl of chloroform was added followed by a brief centrifugation at 300 g and vortexing for 25 minutes. The chloroform phase containing the ^{111}In -oxine complex was extracted from below the water phase containing free ^{111}In , and evaporated at 80°C in a conical bottom HPLC vial, before resuspension in 20 μl of dimethyl sulfoxide (DMSO).

ADSCs were trypsinised, counted, re-suspended in PBS and divided into two samples (3×10^5 cells). The first sample was incubated with 22.4 MBq of ^{111}In -oxine at 37°C for 30 minutes. The second sample received 20 μl of DMSO vehicle without ^{111}In -oxine as control. Subsequently, the cells were pelleted and washed 3 times with PBS and the radioactivity of the cell pellets was measured using an isotope calibrator (Curiementor 4, PTW). Both samples were then plated for *in vitro* luciferase assay. The labelling yield was ~10 MBq/million cells.

***In vitro* luciferase assay**

For luciferase-based cell proliferation assay, ADSCs (0.5×10^5 cells per well) were labelled with ^{111}In -oxine (~0.5 MBq), ^{111}In -DOTA-SPION (~0.5 MBq of ^{111}In , ~45 μg of Fe) and three non-radiolabelled samples: control cells, cells incubated with 20 μl of DMSO (control vehicle for ^{111}In -oxine) and DOTA-SPION labelled cells (~45 μg of Fe) were plated in 24-well plates (Corning) in triplicates. *In vitro* luciferase assay was performed using AMI-X (Spectral Instruments Imaging, USA) at days 1, 3, 5, 6, 7, 8 and 10. Images were acquired immediately after adding D-luciferin (60 $\mu\text{g}/\text{ml}$, Beetle Luciferin Potassium Salt, Promega, Madison, WI) using medium or low binning and exposure time of 120 s. A region of interest (ROI) was placed over each well and the total signal in the ROI (photons/sec) was quantified using AMIView software (version 1.7.07).

***In vitro* cell death assay**

For cell death assay, ADSCs (5×10^3 cells per well) were labelled with ^{111}In -oxine (~0.05 MBq), ^{111}In -DOTA-SPION (~0.05 MBq of ^{111}In , ~4.5 μg of Fe) and three non-radiolabelled samples: control cells, cells incubated with 10 μl of DMSO (control vehicle for ^{111}In -oxine)

and DOTA-SPION labelled cells (~4.5 µg of Fe) and were plated in 96-well plates (Corning) in triplicates. Cell death assay was performed using Propidium Iodide (Biotium, Fremont, USA) and Hoechst 33342 (NucBlue™ live cell stain, ThermoFisher Scientific, Massachusetts, USA) at days 1, 2, 3, 7 and 10 after plating. To stain the dead cells, the cells were incubated with 5 µM Propidium Iodide (150 µl/well) for 10 minutes followed by live cell staining using Hoechst 33342 (20 µl/well) which was incubated for 20 minutes. The cells were imaged using EVOS FL cell imaging system (ThermoFisher Scientific, Massachusetts, USA) and images were analysed using Image J software (version 1.46r) (ImageJ, U.S. National Institutes of Health, Bethesda, Maryland, USA). The results were calculated as below and presented as the percentage cell death.

$$\%cell\ death = \left(\frac{\text{the number of dead cells}}{\text{total number of cells (live + dead)}} \right) \times 100$$

4.3.5 *In vivo* studies

All the animal procedures were performed as described in Chapter 2.4.

4.3.6 *In vivo* cell and particle injections

***In vivo* evaluation of particle release from dead cells**

For preliminary evaluation study of particle release after cell death, mice (n = 1 for each group) were injected intravenously via a tail vein (100-150 µl PBS) with either (a) 8 MBq of ¹¹¹InCl₃, (b) 3 MBq ¹¹¹In-DOTA-SPION particles only (containing 225 µg of Fe), (c) 0.5 x 10⁵ ADSCs labelled with 0.3 MBq ¹¹¹In-DOTA-SPION (containing 70 µg of Fe) or (d) the same concentration of labelled cell lysates as (c) after 3 cycles of freeze thawing (dry ice and 37°C).

ADSCs labelling with ¹¹¹In-DOTA-SPIONs for *in vivo* experiment

For ADSCs labelling, 5 mg of DOTA-SPIONs were used for radiolabelling with 70 MBq of ¹¹¹InCl₃ as described previously and the radiolabelled particles were washed 3 times with PBS to remove free ¹¹¹InCl₃. 60.37 MBq of ¹¹¹In-DOTA-SPIONs (0.33 mg/ml of Fe in 15 ml of media) was incubated with ADSCs (7.5 x 10⁵ cells) at 37°C for 16 hours ((Figure 4.3). Labelled ADSCs were washed 3 times with PBS to remove excess particles and trypsinised, pelleted and washed again 3 times with PBS. The radioactivity of the final cell pellets was measured using an isotope calibrator. The labelling yield was ~10 MBq/million cells.

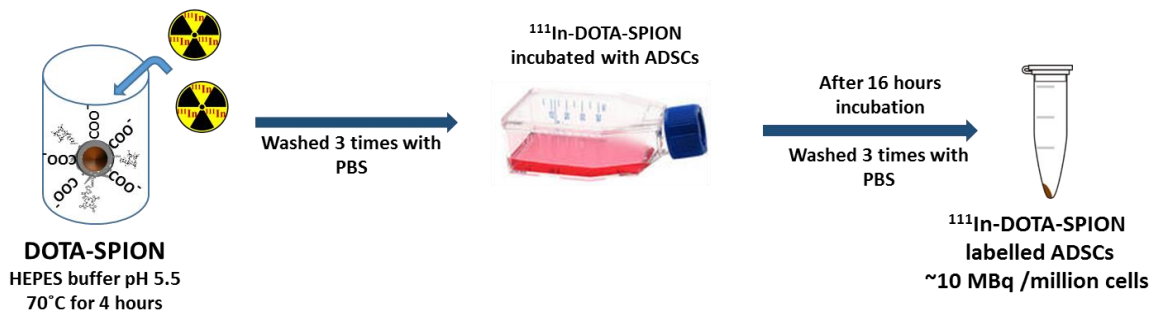


Figure 4.3 Schematic representations of ADSCs labelling with ¹¹¹In-DOTA-SPIONs.

In vivo biodistribution studies in healthy animals

For *in vivo* biodistribution studies of non-radiolabelled ADSCs, mice were injected with 1×10^5 cells in 100 μ l of PBS either intravenously ($n = 4$) via a tail vein or intracardially ($n = 3$) through the left ventricular cavity of the heart with ultrasound guidance as previously described in Chapter 2.4.1 and imaged with BLI for 7 days (Figure 4.4a).

For *in vivo* biodistribution studies of ¹¹¹In-DOTA-SPION labelled ADSCs, mice were injected with 1×10^5 dual labelled cells either intravenously (~ 1.34 MBq of ¹¹¹In, ~ 140 μ g of Fe, $n = 5$) or intracardially (~ 0.83 MBq of ¹¹¹In, ~ 100 μ g of Fe, $n = 5$). The animals were imaged with BLI, SPECT/CT and MRI serially over 7 days (Figure 4.4b).

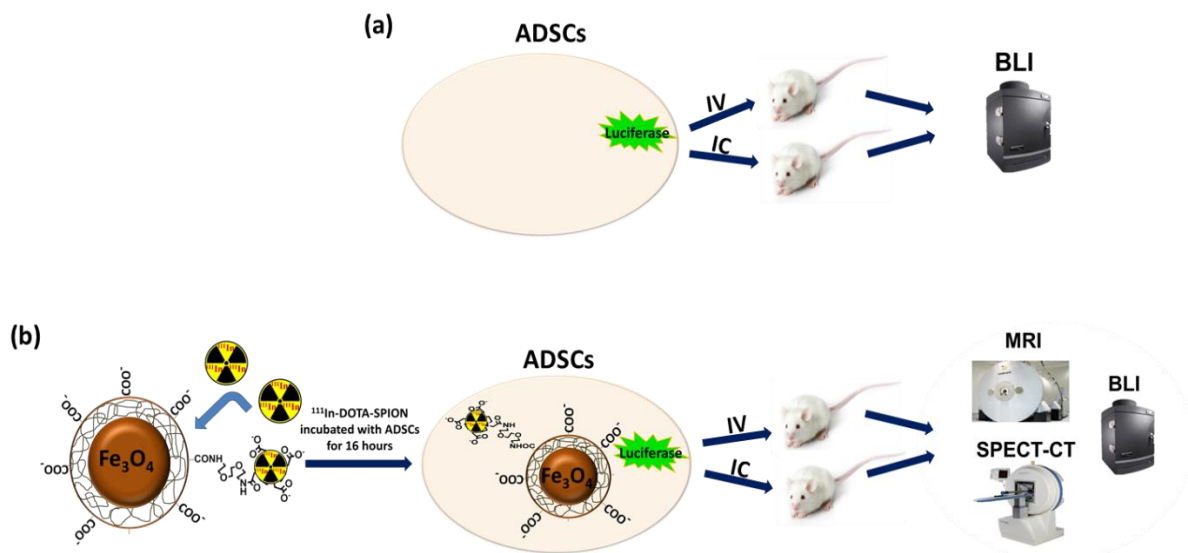


Figure 4.4 Schematic outlines of the whole body ADSCs distribution studies using multimodal imaging.

***In vivo* cell viability assessment of radiolabelled ADSCs**

For *in vivo* cell viability studies of radiolabelled ADSCs, 3 mice were injected intravenously with 1×10^5 cells labelled with ^{111}In -oxine (~ 1.45 MBq of ^{111}In) and imaged with BLI for 7 days. These results were compared with the results from after intravenous injection with ^{111}In -DOTA-SPION labelled and non-radiolabelled ADSCs as mentioned above.

4.3.7 *In vivo* imaging

BLI

Mice were anaesthetised and *in vivo* BLI was performed at 1 hour, days 1, 3 and 7 after injection.

SPECT/CT

Directly after BLI imaging, mice were anaesthetised and whole body SPECT/CT scans were acquired at 3-5 hour after injection (termed day 0), and then at days 1, 3 and 7. 3D ROIs were created for brain, lungs, liver and kidney for each time point and calculated as the percentage of injected dose/ mm^3 (%ID/ mm^3) after correcting for ^{111}In decay.

MRI

MRI studies were performed at days 1 and 3 after injection to acquire T_2^* -weighted liver and brain images.

4.3.8 *Ex vivo* BLI and biodistribution study

All *ex vivo* BLI and biodistribution studies were performed at 1 hour, days 1, 3 and 7 after IV or IC injection of ^{111}In -DOTA-SPION labelled ADSCs (0.5×10^5 cells containing ~ 0.5 MBq of ^{111}In , ~ 52 μg of Fe, $n = 3$ for each time point in both groups) following the procedures previously described in Chapter 2.5.

4.3.9 Histology and immunohistochemistry (IHC)

At the end of imaging sessions, selected mice were sacrificed and lungs, liver, spleen, brain and kidney tissue samples were prepared and stained with H & E as previously described in Chapter 2.6. Human specific vimentin and Iba1 staining were performed to detect the presence of ADSCs and macrophages in tissue sections using the Ventana DAB Map detection Kit (for lung sections) or Ventana Red detection kit (for brain sections). The adjacent 5 μm sections from IHC stained sections were stained with Prussian blue staining to demonstrate the presence of SPIONs.

4.3.10 Statistical analysis

All *in vitro* experiments were repeated at least 3 times with 3 triplicates.

Statistical analysis was performed with GraphPad Prism version 6.01. Data were presented as mean \pm standard deviation (SD). Two way ANOVA test was conducted for cell proliferation and cell death assay and unpaired two-tailed t test was conducted in the rest of the experiments.

4.4 Results

4.4.1 Intracellular uptake and retention of ^{111}In -DOTA-SPION in ADSCs

ADSCs were incubated with different concentrations of ^{111}In -DOTA-SPION for 16 hours and intracellular iron uptake was measured using the Ferrozine iron assay which showed the increase uptake in a dose dependent manner (Figure 4.6a). The uptake of ^{111}In -DOTA-SPION by ADSCs was visualised using Prussian blue staining which showed blue aggregates inside the cytoplasm compared to control (Figure 4.6b). The internalisation of ^{111}In -DOTA-SPION by ADSCs was further confirmed by transmission electron microscopy (TEM) which showed the entrapment of SPIONs aggregates inside lysosomes (Figure 4.6c).

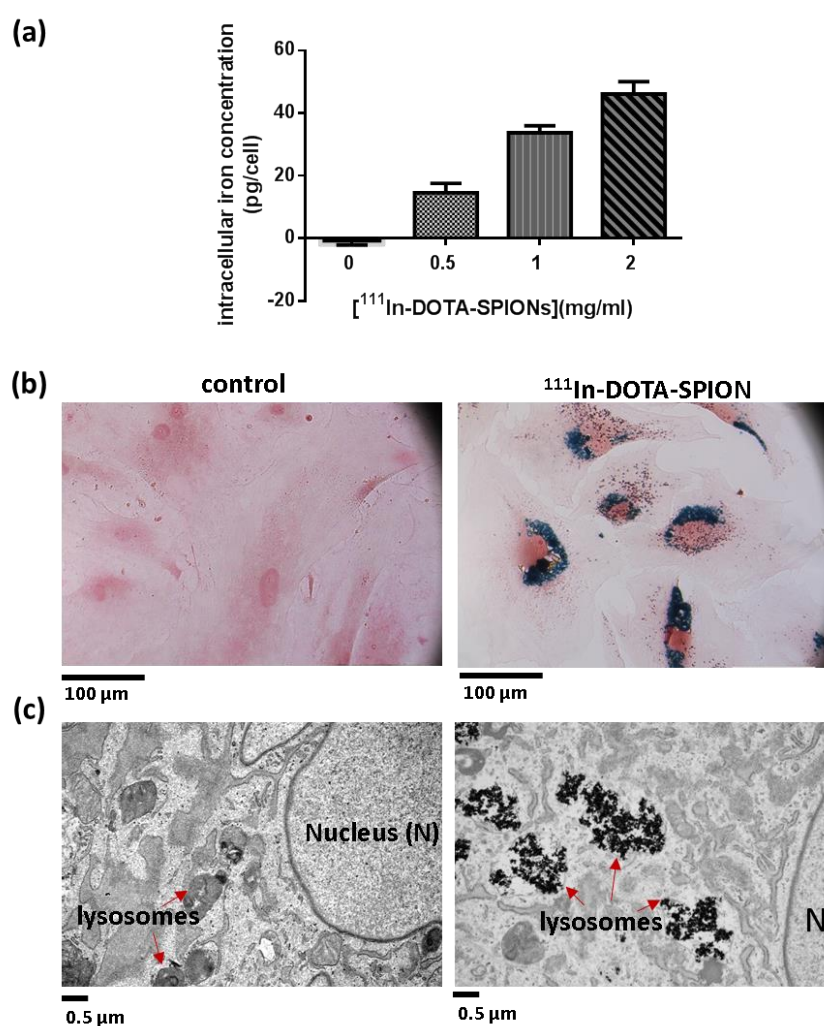


Figure 4.6 Intracellular uptake of ^{111}In -DOTA-SPIONs in ADSCs. (a) ADSCs were incubated for 16 hours with ^{111}In -DOTA-SPIONs at the concentration indicated and intracellular iron uptake was measured using Ferrozine assay (data are shown as mean \pm SD, $n = 3$). (b) Prussian blue staining of ADSCs treated with ^{111}In -DOTA-SPION showing blue aggregates compared to untreated control (scale bar = 100 μm). (c) TEM images showing SPION aggregates in lysosomes compared to untreated control (scale bar = 0.5 μm).

To study the retention of ^{111}In -DOTA-SPION in ADSCs, the radiolabelled cells were cultured in 24-well plates and the media was removed and measured with a gamma counter at days 1, 2, 3 and 7 after plating. The results (Figure 4.7) showed that 78.94 ± 2.392 % of radioactivity was retained within ADSCs throughout the study.

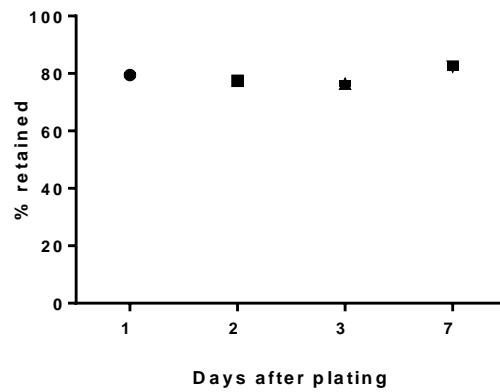


Figure 4.7 The retention of ^{111}In -DOTA-SPION in ADSCs showing the percentage of radioactivity retained in ADSCs up to 7 days after labelling with ^{111}In -DOTA-SPION. (Data are shown as mean \pm SD, n = 3).

4.4.2 The effect of ^{111}In -DOTA-SPION labelling on cell function

The effect of ^{111}In -DOTA-SPION labelling on ADSC migration was evaluated using IBIDI culture inserts and the results showed that there was no significant difference between the control and ^{111}In -DOTA-SPION labelled cells ($P = 0.9679$, Figure 4.8).

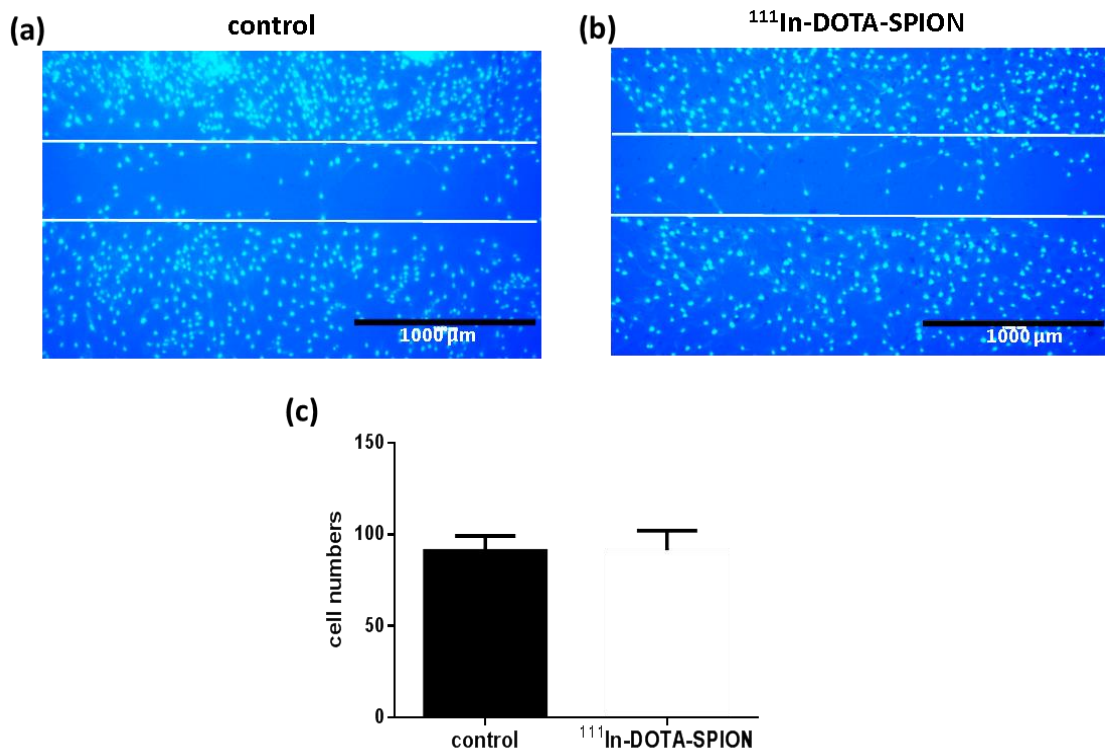


Figure 4.8 The effect of ^{111}In -DOTA-SPION labelling on ADSC migration. (a) The control cells and (b) ^{111}In -DOTA-SPION labelled ADSCs were stained with Hoechst 33342 for image analysis (scale bar = 1000 μm). (c) The number of cells between the gaps (indicated by white lines) showed no significant difference between the control group and ^{111}In -DOTA-SPION labelled group.

The differentiation assay was performed to assess tri-lineage differentiation potential (adipogenic, chondrogenic and osteogenic) of ^{111}In -DOTA-SPION labelled cells (Figure 4.9). Although ^{111}In -DOTA-SPION labelled cells showed a slower rate of chondrogenic differentiation, both the control cells and ^{111}In -DOTA-SPION labelled cells could differentiate towards tri-lineages as detected by staining with oil red O (adipogenic), alcian blue (chondrogenic) and alizarin red (osteogenic).

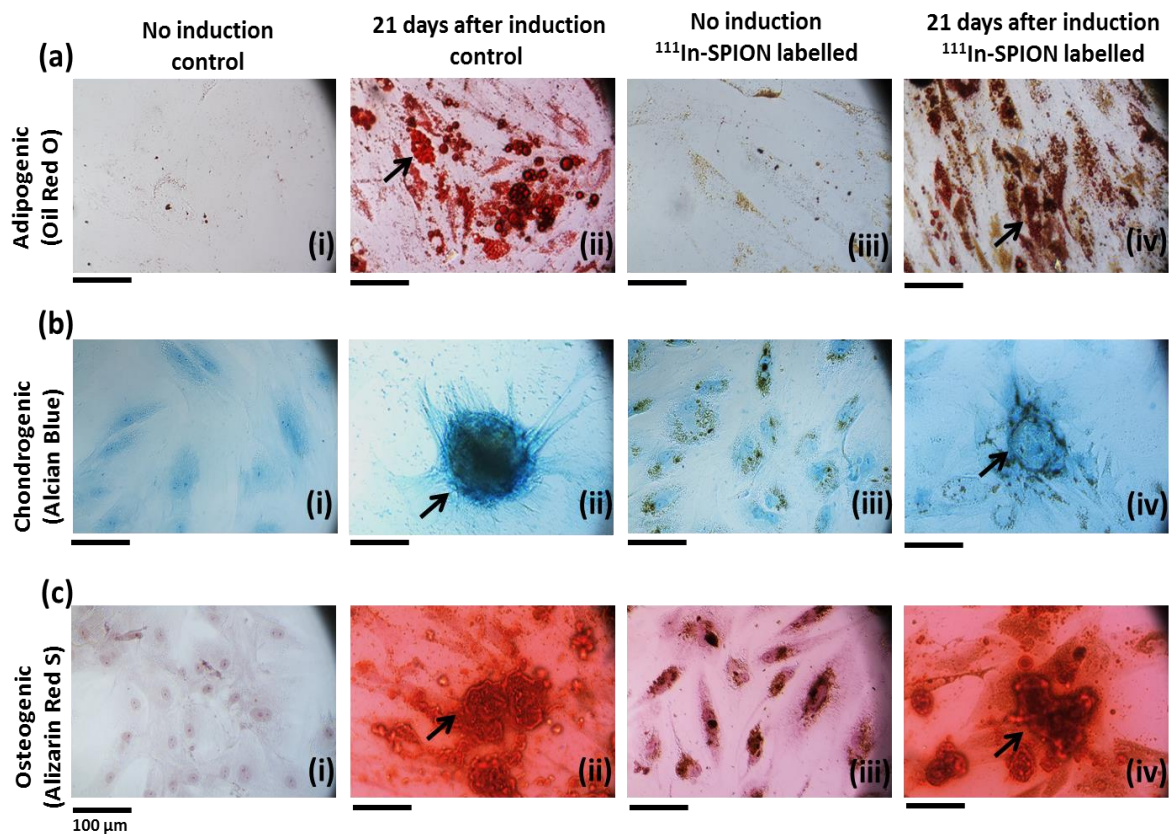


Figure 4.9 Tri-lineage differentiation of control ADSCs and ^{111}In -DOTA-SPION labelled ADSCs. (a) Oil red o staining for adipogenic differentiation which displays the red coloured oil droplets (indicated by arrows in (ii & iv)). (b) Alcian blue staining for chondrogenic differentiation which displays the blue coloured proteoglycans (indicated by arrows in (ii & iv)). (c) Alizarin red s staining for osteogenic differentiation which displays the red coloured calcium deposits (indicated by arrows in (ii & iv)). Scale bar = 100 μm .

4.4.3 The effect of radiolabelling on cell proliferation and cell death

In order to test the toxic effect of radiolabelling on ADSCs, the degree of cell proliferation and cell death were assessed by using a luciferase assay and propidium iodide based cell death assay. Luciferase expressing ADSCs were labelled with ^{111}In -oxine, ^{111}In -DOTA-SPION and three non-radiolabelled samples: control cells, cells incubated with 10 μl of DMSO (control vehicle for ^{111}In -oxine) and DOTA-SPION labelled cells (to exclude the cytotoxic effect of iron) were cultured and imaged with BLI serially over 10 days. Bioluminescence signal from three non-radiolabelled samples increased similarly prior to plateau (Figure 4.10a). Although, both the ^{111}In -oxine and ^{111}In -DOTA-SPION labelled cells showed a significant signal decrease at day 3 ($P < 0.0001$), the ^{111}In -DOTA-SPION cells showed recovery to control levels at day 5 until day 7 where the signal started to decrease. However, the bioluminescence from ^{111}In -oxine labelled cells continued to decrease from day 3 and was significantly lower than ^{111}In -DOTA-SPION labelled cells from day 5 onwards ($P < 0.0001$).

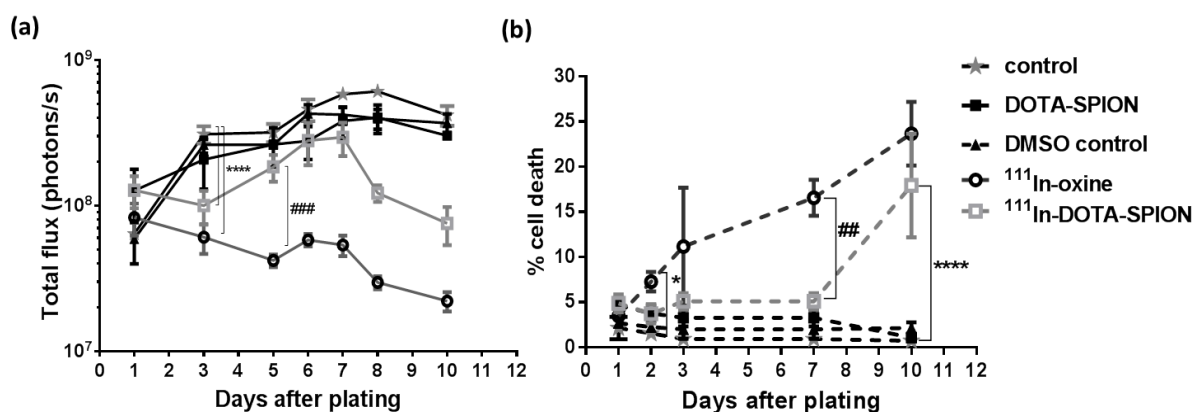


Figure 4.10 The effect of ^{111}In -DOTA-SPION labelling on cell proliferation and cell viability. (a) Luciferase-based cell proliferation assay at different time points showing BLI signals (photons/s in log scale) of three non-radiolabelled samples: control cells, cells incubated with DMSO (control vehicle for ^{111}In -oxine) and DOTA-SPION labelled cells and two radiolabelled samples: cells labelled with ^{111}In -oxine and ^{111}In -DOTA-SPIONs (**** $P < 0.0001$ radiolabelled cells vs control at 3 days and ### $P = 0.0002$ ^{111}In -oxine vs ^{111}In -DOTA-SPIONs at 5 days). (b) Cell death assay at different time points showing the percentage cell death of five different samples as described in (a) (* $P = 0.021$ ^{111}In -oxine vs control at 2 days, **** $P < 0.0001$ ^{111}In -DOTA-SPIONs vs control at 10 days, ## $P = 0.0011$ ^{111}In -oxine vs ^{111}In -DOTA-SPIONs at 7 days). Data are shown as mean \pm SD, $n = 3$.

As the luciferase assay cannot identify the degree of cell death, the percentage cell death was obtained by staining cells with propidium iodide (Figure 4.10b). ^{111}In -oxine and ^{111}In -DOTA-SPION labelled cells showed a significant increase in cell death at day 2 ($P = 0.021$)

compared to control cells. The percentage cell death of ^{111}In -oxine labelled cells continued to increase from day 2 onwards, resulting in a significant increase from ^{111}In -DOTA-SPION at day 7 ($P = 0.0011$). However, the percentage cell death in the ^{111}In -DOTA-SPION group increased after day 7 ($P < 0.0001$) with no significant difference observed between the two radiolabelling group at day 10.

4.4.4 *In vivo* cell viability study of radiolabelled ADSCs using BLI

The effect of radiolabelling on *in vivo* cell viability was assessed by comparing BLI results from control ADSCs, ^{111}In -oxine labelled and ^{111}In -DOTA-SPIONs labelled ADSCs after IV injection. All three groups showed the majority of BLI signal within the lungs at 1 hour after injection and no obvious difference in cell distribution pattern was seen throughout the study (Figure 4.11a). All groups showed a decrease in signal intensity (photons/s) over the whole body at a similar rate over the 7 day time course (Figure 4.11b).

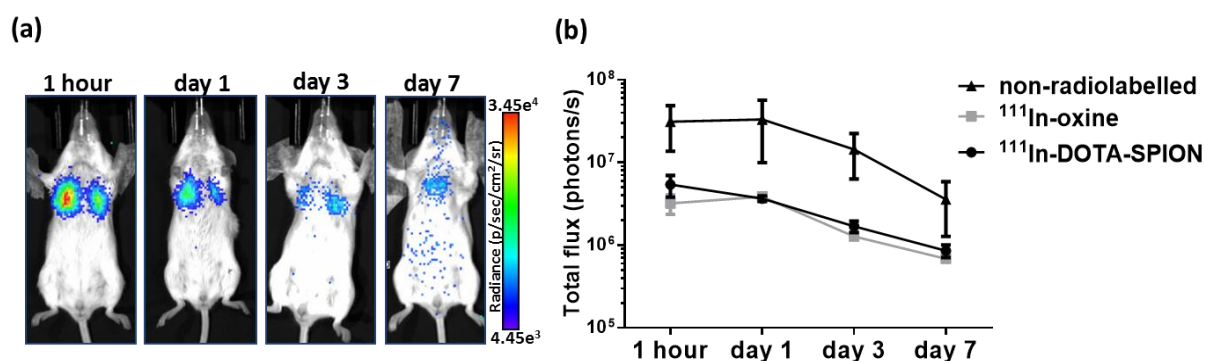


Figure 4.11 *In vivo* cell viability assessments of radiolabelled ADSCs. (a) BLI images of ^{111}In -oxine labelled ADSC at 1 hour, days 1, 3 and 7 after IV showing the signal in the chest decreased over time. (b) BLI signal in the whole body decreased over time (photon/s in log scale). All data are shown as mean \pm SD, $n = 3$.

4.4.5 *In vitro* and *in vivo* assessment of particles release from dead cells

To visualise the radiolabelled particle release from dead cells, H₂O₂ treated ¹¹¹In-DOTA-SPION labelled ADSCs were monitored using a time-lapse microscope for 24 hours. At 10 hours after treatment, the cells detached and formed aggregates but ¹¹¹In-DOTA-SPIONs remained internalised (Figure 4.12) and no obvious particles release was observed.

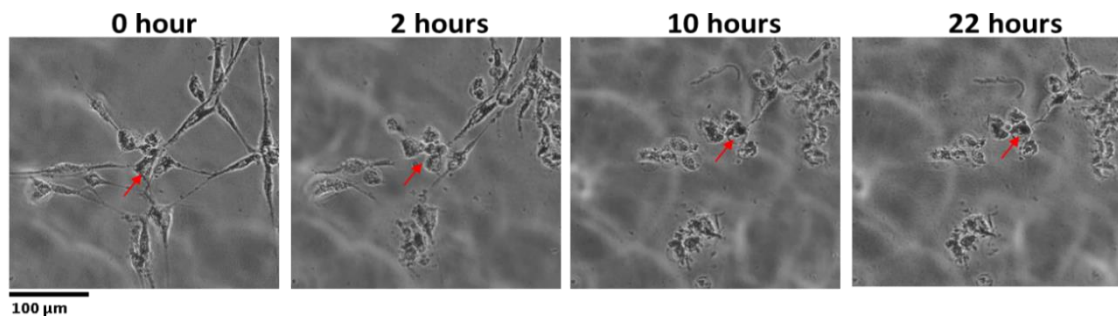


Figure 4.12 *In vitro* assessment of particles release from dead cells. The time-lapse microscopic images of H₂O₂ treated ¹¹¹In-DOTA-SPION labelled ADSCs showing the particles inside cell aggregates (indicated by arrows). Scale bar = 100 μm.

To assess the extent of this process *in vivo*, an initial optimisation study was performed by injecting mice intravenously with (a) free $^{111}\text{InCl}_3$, (b) ^{111}In -DOTA-SPION with no cells, (c) ^{111}In -DOTA-SPION labelled cells and (d) ^{111}In -DOTA-SPION labelled cell lysate (Figure 4.13). At 1 hour after IV injection, the animals were imaged with SPECT/CT. The mouse injected with free $^{111}\text{InCl}_3$ showed high radioactivity uptake in the kidney and bladder at 1 hour indicating typical clearance pathway (Figure 4.13a). The mouse injected with ^{111}In -DOTA-SPION only showed high uptake in the liver and spleen (Figure 4.13b). The mouse injected with live cells labelled with ^{111}In -DOTA-SPION showed the uptake was uniformly distributed throughout the lungs and liver (Figure 4.13c). However, the dead cell lysates were presented as multiple hot spots in the lungs with very little uptake in liver and no uptake in kidney (Figure 4.13d).

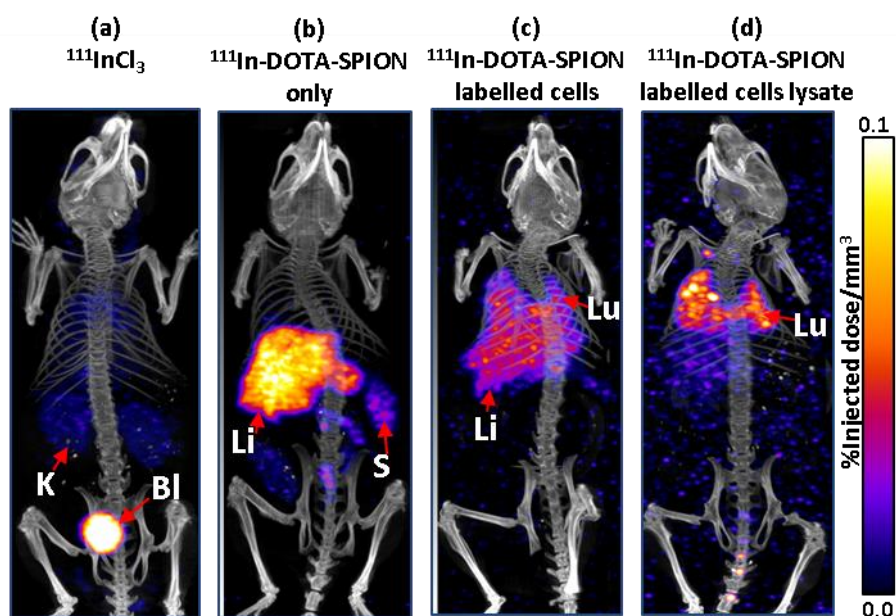


Figure 4.13 SPECT/CT images showing biodistribution of (a) $^{111}\text{InCl}_3$ only, (b) ^{111}In -DOTA-SPIONs only, (c) ^{111}In -DOTA-SPIONs labelled cells and (d) labelled cell lysates at 1 hour after intravenous injection (Labels: Lu = lungs, Li = liver, S = spleen, K = kidney and Bl = bladder, n = 1 per group). Representative images were presented using %ID/mm³ as colour scale after correction for ^{111}In decay.

4.4.6 Assessment of ^{111}In -DOTA-SPION labelled ADSCs distribution following IV or IC injection

To study *in vivo* biodistribution of ^{111}In -DOTA-SPION labelled ADSCs, NSG mice were injected with 1×10^5 cells IV or IC and imaged with BLI, SPECT/CT and MRI serially over 7 days (as defined by *in vitro* cell viability experiments). *Ex vivo* BLI and radioactivity uptake in *ex vivo* organs obtained via gamma counting (%ID/g) were performed in separate cohorts of mice to validate *in vivo* imaging results. BLI results from radiolabelled cells were compared with non-radiolabelled ADSCs following IV or IC to assess the effect of labelling agents on cell distribution.

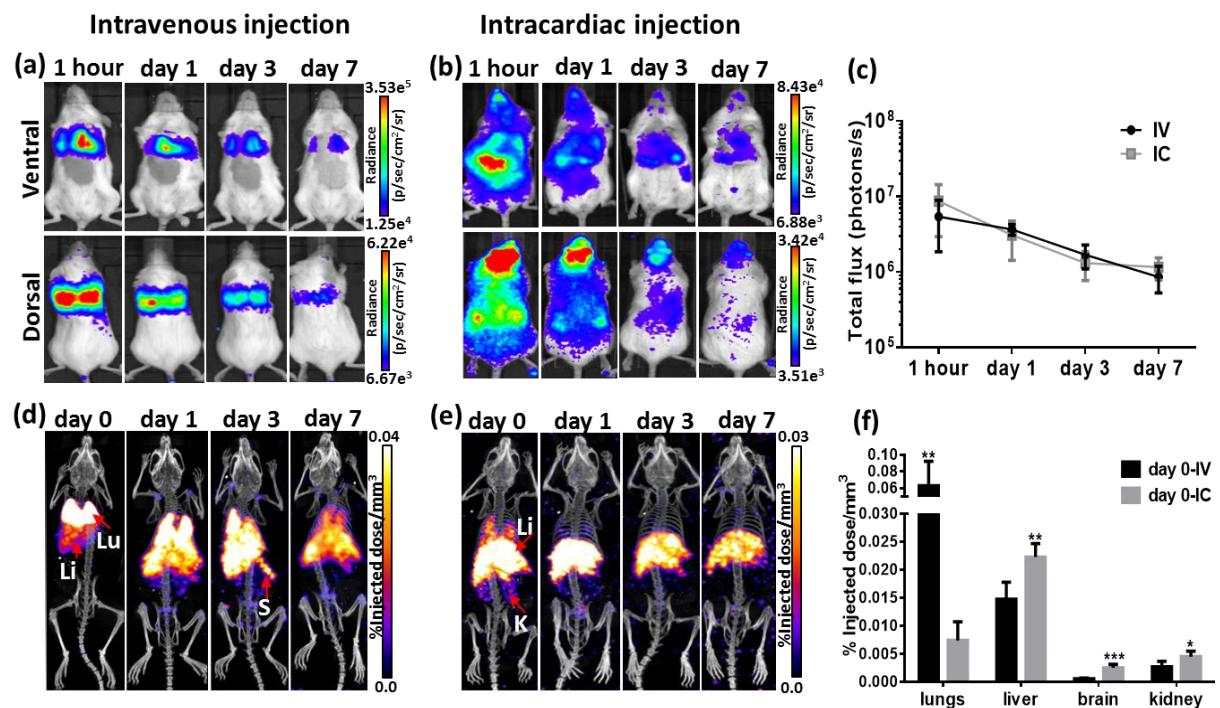


Figure 4.14 Whole body distribution of ^{111}In -DOTA-SPION labelled ADSCs following IV or IC injection at different time points. (a, b) BLI signal was mainly seen in the chest after IV injection, whereas IC presented a wider BLI distribution. (c) BLI signal from the whole body decreased similarly over time (photons/s in log scale). (d & e) Decay corrected SPECT-CT images of dual labelled ADSCs uptake in organs after IV and IC injection (Labels: Lu = lungs, Li = liver, S = spleen and K = kidney). (f) 3D ROI quantification of SPECT signal in lungs, liver, brain and kidney at day 0 after IV or IC injection calculated as %ID/mm³ after decay correction (IV vs IC ** $P = 0.0027$ in lung, ** $P = 0.0025$ in liver, *** $P = 0.0001$ in brain & * $P = 0.0217$ in kidney). Data are shown as mean \pm SD, $n = 5$.

At 1 hour after IV injection, BLI images showed the majority of signal within the lungs (Figure 4.14a, supported by *ex vivo* BLI, Figure 4.15a) with no *in vivo* BLI signal within liver and spleen (although some signal was detected in these 3 organs using *ex vivo* BLI, Figure 4.15a). In comparison, at 1 hour after IC injection, BLI signals could be detected in brain, liver, spleen and kidney but appeared to be lower in the lung (Figure 4.14b, supported by *ex vivo*

BLI, Figure 4.15b). Immediately after BLI, SPECT/CT images were acquired at 3-5 hours after injection (termed day 0, Figure 4.14d & e) which showed the cell uptake in lungs after IV injection was significantly higher than IC injection ($P = 0.0027$, Figure 4.14f) whereas the cells uptake in liver, brain and kidney after IC injection was significantly higher than IV injected group ($P = 0.0025$, $P = 0.0001$ and $P = 0.0217$ respectively) consistent with data shown by BLI.

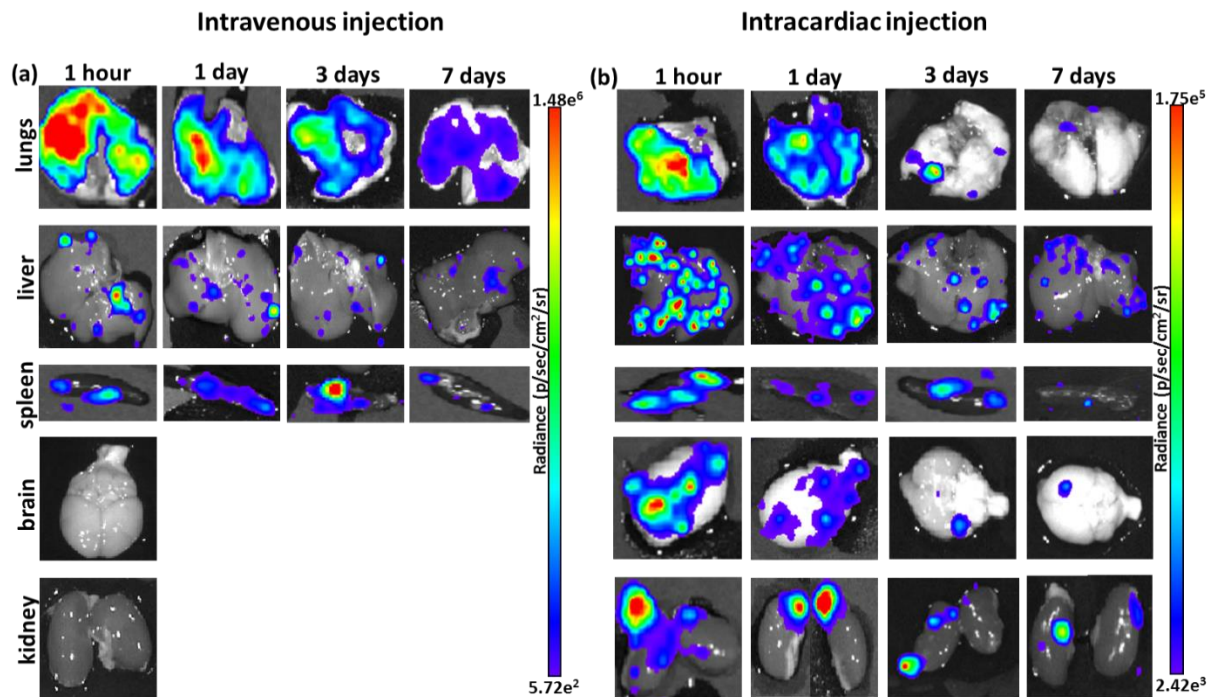


Figure 4.15 *Ex vivo* BLI images of lungs, liver, spleen, brain and kidney at 1 hour, days 1, 3 and 7 after (a) IV and (b) IC injection.

The BLI signal from IV and IC injection persisted for 7 days with similar signal intensity but decreasing over time (Figure 4.14c). SPECT/CT images at days 1, 3 and 7 after IV injection showed that cell uptake in lung reduced over time while the cell uptake in liver increased suggesting cell migration (Figure 4.16a). In comparison, the cell uptake in liver after IC injection remained stable throughout the study while the cell uptake in lungs, brain and kidney reduced (Figure 4.16b). The uptake from *ex vivo* organs showed patterns of distribution consistent with *in vivo* data (Figure 4.16c & d, full organ data in Appendix 3). Due to poor soft tissue contrast of SPECT/CT images, the more accurate quantification of cell uptake in spleen was obtained from *ex vivo* organs which showed the uptake was highest at day 3 after IV injection (Figure 4.15c), consistent with observation from *in vivo* SPECT images (Figure 4.14d). Observation across the body showed very low SPECT signal in common ^{111}In deposition area: shoulder, knee joint, spine and bladder throughout the study (Figure 4.14d & e) suggesting that free ^{111}In leakage from the cells is minimal after both injections.

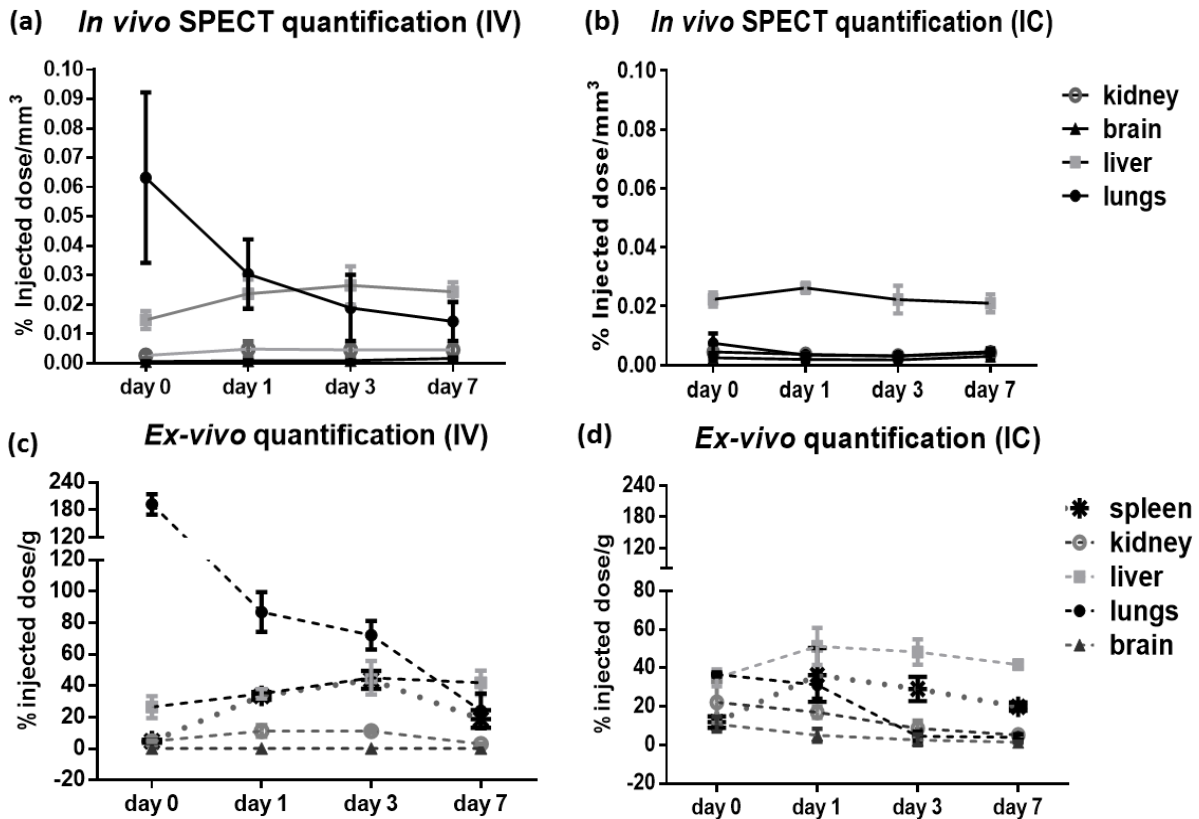


Figure 4.16 *In vivo* and *ex vivo* quantification of ^{111}In -DOTA-SPION labelled cells uptake in lungs, liver, spleen, brain and kidney following IV or IC injection at different time points. (a & b) 3D ROI quantification of *in vivo* SPECT signal in organs after IV & IC injection calculated as %ID/ mm^3 after decay correction (c & d) *Ex vivo* quantification of radioactivity distribution in organs after IV and IC injection calculated as %ID/g after decay correction. Data are shown as mean \pm SD, $n = 5$ (*in vivo*) and $n = 3$ (*ex vivo*).

Interestingly, BLI results from animals injected with non-radiolabelled ADSCs also showed the same cell distribution and signal intensity pattern following IV or IC injection (Figure 4.17).

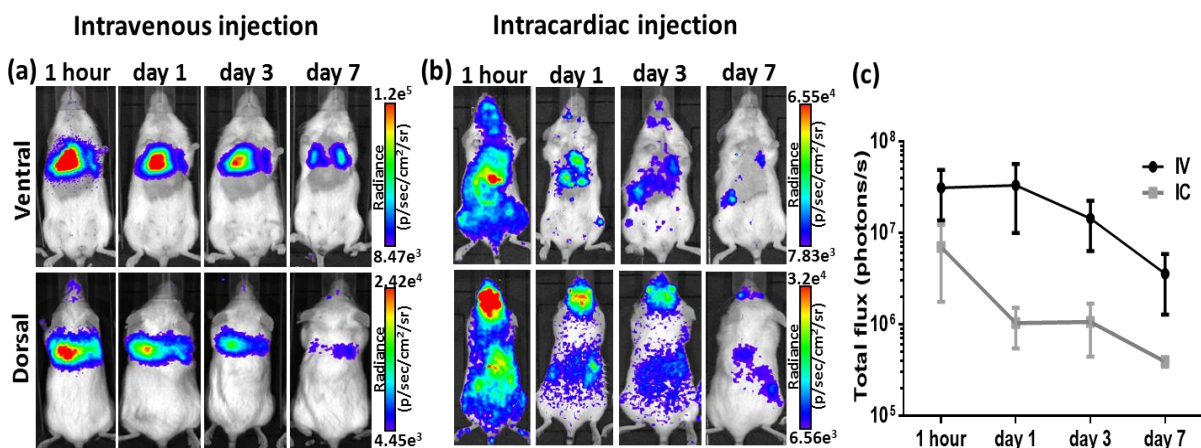


Figure 4.17 BLI images of non-radiolabelled ADSC at 1 hour, days 1, 3 and 7 following IV or IC injection. (a, c) BLI signal in the chest and the whole body decreased over time. (b, c) BLI signal in the whole body decreased over time (photons/s in log scale). Data are shown as mean \pm SD, $n = 4$ (IV) & $n = 3$ (IC).

Consistent with BLI and SPECT findings, T_2^* -weighted MR images of liver at day 1 after IV injection showed a global reduction in signal intensity compared to control suggesting the presence of SPIONs labelled cells throughout the liver. SPECT signal in liver co-registered well with MR signal loss which confirmed the presence of dual labelled cells (Figure 4.18a). T_2^* -weighted MR images of the brain at day 1 after IC injection showed regions of hypointense signal throughout the brain compared to control (Figure 4.18b). SPECT signals could be co-registered to some MR hypointense regions within the brain but not all. No hypointense regions within the brain were observed in IV injected mice (data not shown). T_2^* -weighted MR images of kidney at day 1 after IC injection showed areas of focal hypointensity mainly within the renal cortex compared to control and IV injected animal which showed no signs of SPIONs distribution (Figure 4.18c).

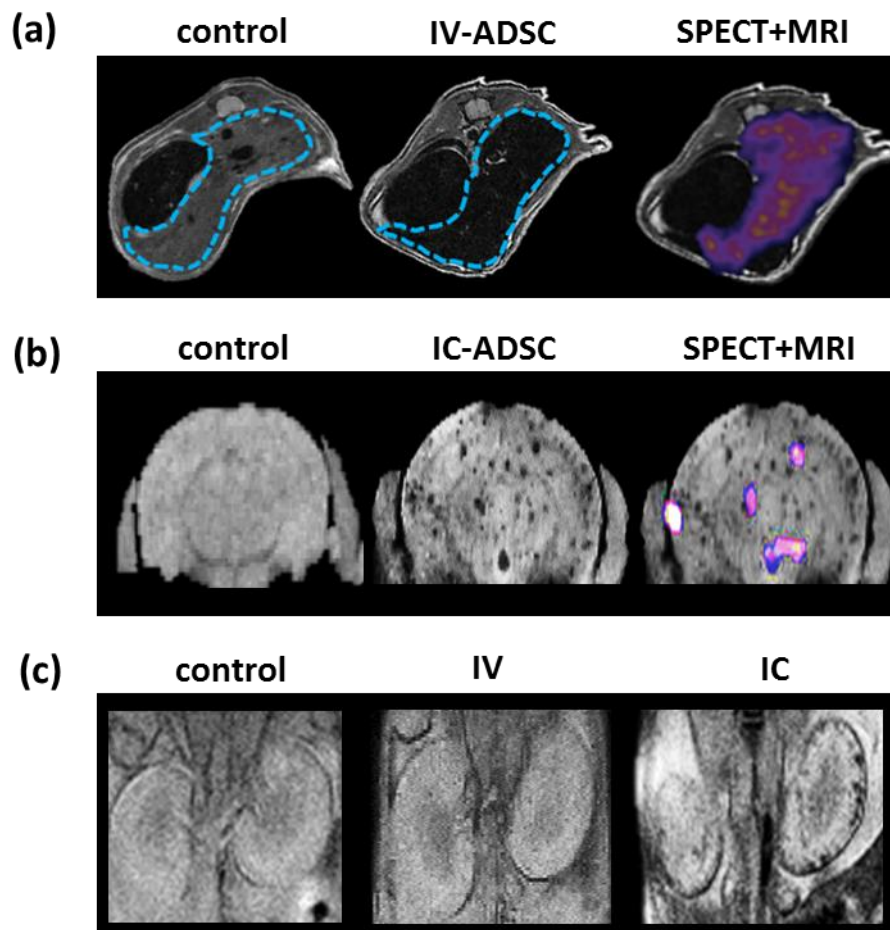


Figure 4.18 MRI images of ^{111}In -DOTA-SPION labelled ADSCs at 1 day following IV or IC injection. (a & b) T_2^* -weighted MR images of the liver (blue dotted line) and the brain in control and dual labelled cells injected animals with SPECT data co-registered. (c) T_2^* -weighted MR images of the kidney in a control mouse and mice injected with dual labelled cells intravenously and intracardially.

4.4.7 Histological analysis

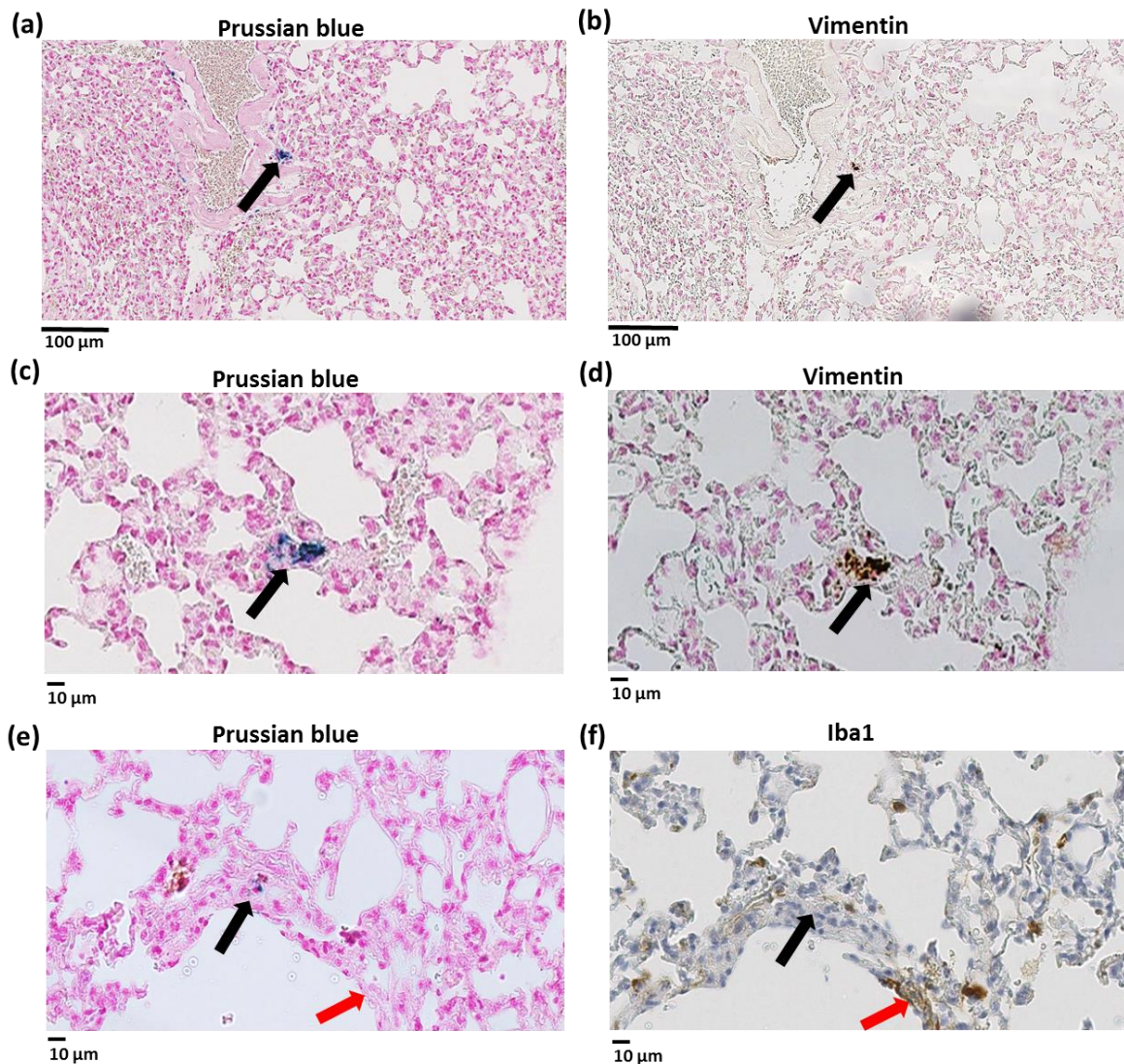


Figure 4.19 Histological analysis of ^{111}In -DOTA-SPION labelled cells uptake in lungs at 7 days after IV injection. (a, c) Positive Prussian blue (SPION) and (b, d) vimentin staining (ADSC) of adjacent lung tissue sections confirmed the presence of dual labelled cells within lungs parenchyma (indicated by arrows). (e) The dual labelled cells did not express Iba1 (indicated by black arrows). (f) The macrophages did not contain iron (indicated by red arrows). Scale bar = 100 µm & 10 µm.

No histopathologic lesions which would indicate malignant tumour or sarcoma formation were detected in any organ (lungs, liver, spleen, brain and kidney - harvested at day 7 after cell infusion). In direct cell labelling, results can potentially be confounded by the release of the labelling agents from dead cells, leading to poor specificity. In order to validate this, adjacent lung tissue sections were stained with Prussian blue (SPIONs) and human specific vimentin (ADSC). Histological images showed areas that were positive for both Prussian blue staining (Figure 4.19a & c) and vimentin (Figure 4.19b & d), confirming the retention of the dual labelling agent within ADSCs. These lung sections also showed the engraftment of

labelled ADSCs into lung parenchyma. In addition, the adjacent lung tissue sections were stained with Prussian blue and a macrophage marker, Iba1 to detect the possibility of the engulfment of dead labelled cells by macrophages. The results showed the dual labelled cells did not express Iba1 and the macrophages did not contain iron (Figure 4.19e & f).

To evaluate the extent of ADSCs distribution in brain after IC injection, adjacent brain tissue sections obtained 3 days after IC injection were stained as described above. Histological images showed the presence of vimentin and Prussian blue staining within the cerebral capillary bed (Figure 4.20).

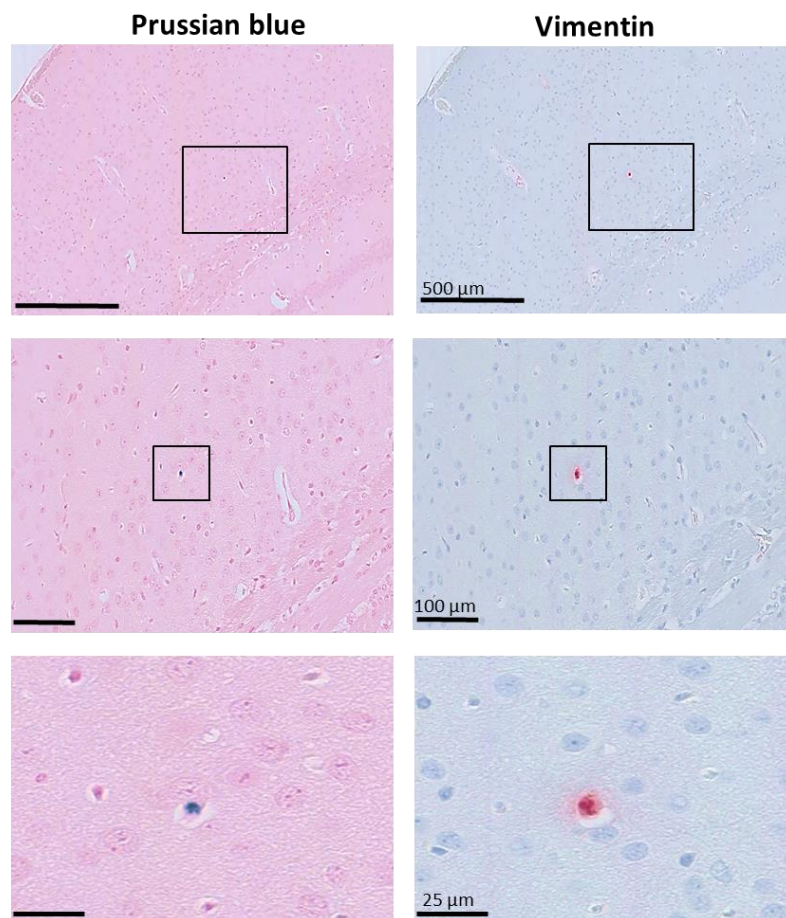


Figure 4.20 Histological analysis of ^{111}In -DOTA-SPION labelled cells uptake in brain at day 3 after IC injection. Positive Prussian blue (SPION) and vimentin (ADSC) staining of adjacent brain tissue sections confirmed the presence of dual labelled cells within the cerebral capillary bed. Scale bar = 500 µm, 100 µm & 25 µm.

Although, no positive staining was observed within the brain parenchyma, evidence of small blood vessels occlusion due to the retention of cells was seen in some parts of the brain with associated formation of micro cerebral infarcts (Figure 4.21).

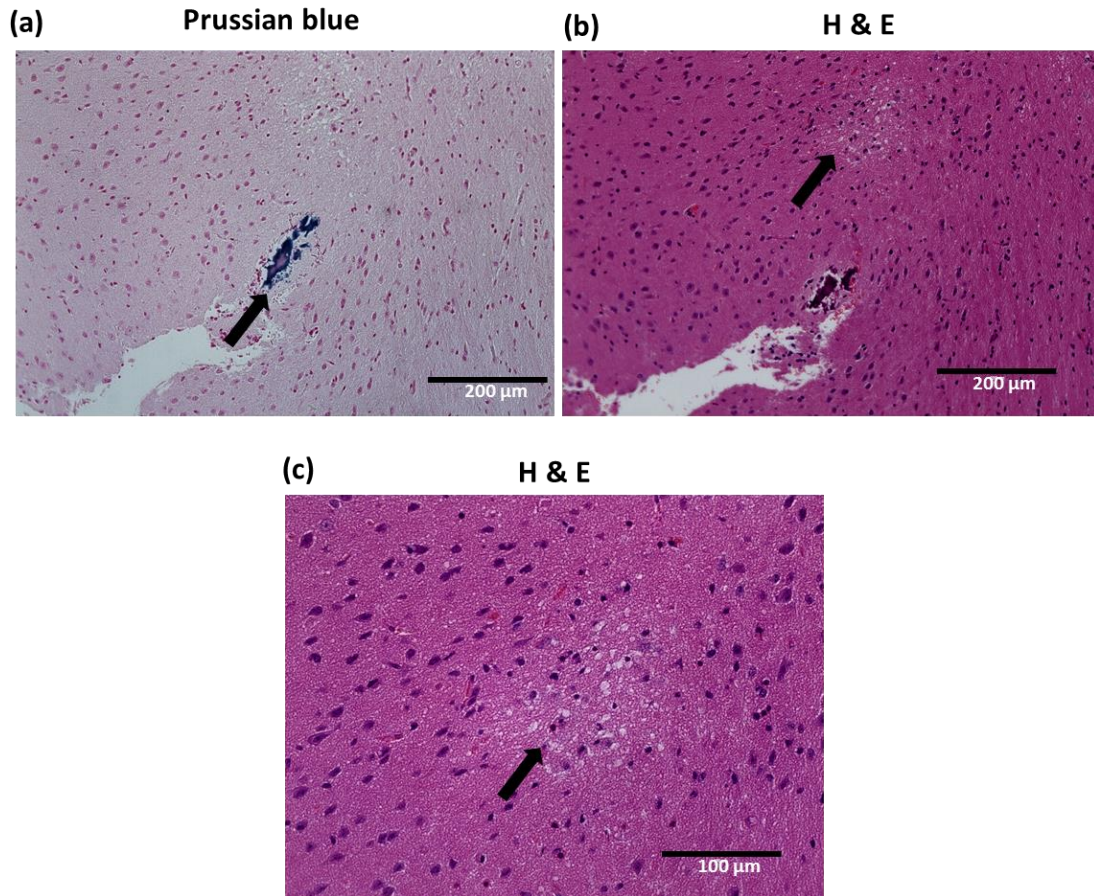


Figure 4.21 Histological analysis of brain sections at day 3 after IC injection. (a) The obstruction of cerebral blood vessels due to iron labelled cells was detected by positive Prussian blue (SPION) staining (indicated by arrow). (b) H & E staining of adjacent brain section showing a small area of cerebral infarct (c) in higher magnification (indicated by arrow, scale bar = 200 μm & 100 μm).

4.4.8 General assessment of the animals after multi-modal imaging

To evaluate the effect of multiple imaging sessions with anaesthesia, the body weight of the animals were monitored and no significant weight loss was seen throughout the study. No animal showed any adverse effects and no animal was sacrificed prior to the study end time points. Cardiac function was assessed by measuring ejection fraction of the heart before and after IC injection and no significance difference was shown ($P = 0.5802$, Figure 4.22).

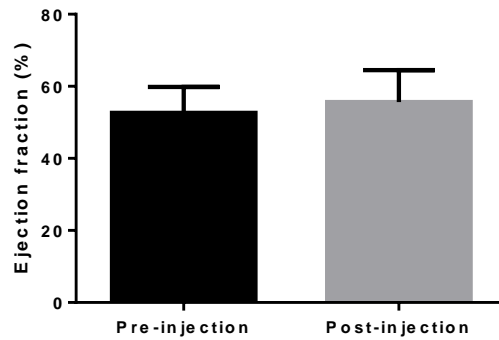


Figure 4.22 Ejection fraction analysis before and after IC injection showing the cardiac function was not impaired.

4.5 Discussion

The aims of this chapter were to assess the stability of ^{111}In -DOTA-SPIONs particles inside cells, to investigate the effect of these particles on cell phenotype/viability and to acquire comprehensive information of ^{111}In -DOTA-SPIONs labelled ADSCs distribution following two different systemic injection routes.

The cellular internalisation of ^{111}In -DOTA-SPIONs was studied and the results showed a dose dependent uptake of ^{111}In -DOTA-SPIONs by ADSCs. Intracellular uptake was further confirmed by Prussian blue staining and TEM which showed the entrapment of particles inside lysosomes suggesting the uptake appeared to be mediated by endocytosis mechanisms. These results are consistent with published literature on the uptake of SPIONs by human MSCs (*Matuszewski et al., 2005; Andreas et al., 2012*). The ^{111}In -DOTA-SPION stability study after intracellular uptake showed ~80% of radioactivity was retained within ADSCs up to 7 days indicating that both the ^{111}In -DOTA chelation and the DOTA-SPION conjugation are stable and not rapidly metabolised after intracellular uptake.

The effect of ^{111}In -DOTA-SPION labelling on ADSC function was assessed using migration and tri-lineages differentiation assays. The migration assay showed the migratory property of ADSCs was not altered by ^{111}In -DOTA-SPION labelling. Although ^{111}In -DOTA-SPION labelled cells could differentiate towards tri-lineages, a slower rate of chondrogenic differentiation from control was identified. These results are consistent with a previous study (*Andreas et al., 2012*) which showed the dose dependent inhibition of chondrogenic differentiation by citrate coated SPIONs. These results suggest that ^{111}In -DOTA-SPION particles have minimal interference on the function of ADSCs.

The major disadvantage of cell tracking with nuclear imaging is cytotoxicity caused by radiolabelling. The cytotoxic effect of ^{111}In -oxine in direct stem cell labelling has been demonstrated in many studies (*Correa et al., 2007; Gholamrezaezhad et al., 2009; Gildehaus et al., 2011*). In this study, the luciferase-based cell proliferation assay showed a significant signal difference between ^{111}In -DOTA-SPION and ^{111}In -oxine labelled cells at day 5 after plating which suggest that ^{111}In -DOTA-SPION has a less adverse effect on cell proliferation than ^{111}In -oxine. Similar findings were seen in the propidium iodide cell death assay which showed the percentage cell death of ^{111}In -oxine labelled cells were 3.2-fold higher than ^{111}In -DOTA-SPION labelled cells at day 7 after plating. This indicates that chelation of ^{111}In to DOTA is less toxic to the ADSCs compared to ^{111}In -oxine. This is most likely because DOTA chelates ^{111}In inside its rigid ring structure (as previously described in Chapter 3.2.1) which effectively stops dissociation of the tracer thereby limiting ^{111}In binding to cellular components and reducing cell death. However, in ^{111}In -oxine chelation, ^{111}In

dissociates from the chelator after crossing the cell membrane, due to its positive nature ($^{111}\text{In}^{3+}$) the radioactive tracer can bind to negative cell components such as DNA which leads to cell irradiation (Fjalling *et al.*, 1996). In addition, no significant differences in cell proliferation rate and percentage cell death was observed between DOTA-SPION only labelled cells and the control which indicates that no profound toxicity was associated with DOTA-SPION labelling and it had no effect on ADSC proliferation over the time frame studied.

The effect of radiolabelling on *in vivo* cell viability was further assessed by using BLI. Although *in vitro* results suggested that ^{111}In -DOTA-SPION labelling was less cytotoxic than ^{111}In -oxine, *in vivo* results showed no significant difference in cell distribution pattern or cell viability from control cells for both ^{111}In -oxine and ^{111}In -DOTA-SPION labelled cells. It also indicated that ADSCs were viable for a short period of time *in vivo* with or without radiolabelling. Therefore, the cytotoxic effect of ^{111}In -oxine could not be detectable *in vivo* since *in vitro* data indicate that the toxic effect is more prominent at later time points.

In vitro and *in vivo* experiments were performed to assess the release of nanoparticles from dead cells. The time-lapse microscopic images showed no obvious particle release after cell death. The *in vivo* optimisation study showed high radioactivity uptake in the kidney and bladder after injection with free $^{111}\text{InCl}_3$ which was expected as $^{111}\text{InCl}_3$ is rapidly cleared by renal excretion (Krenning *et al.*, 1992). Whereas, the ^{111}In -DOTA-SPION particle injected animal showed high uptake in the liver and spleen which was also expected as these organs are part of the reticuloendothelial system and the known clearance pathway for nanoparticles (Mejias *et al.*, 2010). In the live ^{111}In -DOTA-SPION labelled cell injected animal, the uniform cell distribution was seen in lungs and liver while the mouse injected with the dead cell lysates showed multiple focal lung uptakes possibly due to cell aggregation. As the distribution of the live labelled cells had a different distribution from that of $^{111}\text{InCl}_3$ (renal excretion and bladder) and dead cells, this suggests that there is no obvious degradation of the nanoparticle (free ^{111}In) upon internalisation and that the nanoparticles remain inside the cell after death which in agreement with *in vitro* data. Although this study cannot conclusively state that there is no free particles release after cell death, the results suggest that there is no profound particle leakage from the dead cells which would confound the imaging data. The uptake in the lung and liver from the live cell distribution can therefore be assumed as actual cell distribution. These results highlight the main limitations of using a single direct cell labelling method for *in vivo* cell tracking.

In order to overcome the limitation of using a single imaging method, *in vivo* biodistribution of ^{111}In -DOTA-SPION labelled ADSCs was studied following IV or IC and imaged with BLI, SPECT/CT and MRI serially over 7 days. BLI and SPECT results showed the majority of the

cells were accumulated within the lungs after IV injection while a whole body cell distribution was seen after IC injection but signal seemed to be lower in the lung. MRI images of liver, brain and kidney are consistent with BLI and SPECT findings. Interestingly, some regions of MR hypointensity could not be co-registered with SPECT signals. This demonstrates the difference in sensitivity and the level of information that can be obtained on cell localisation between the two imaging techniques. A focal area of SPION labelled cells can cause a spatially large reduction of the MR signal and allow for the detection of relatively low iron concentration which suggests that SPION imaging with MRI is very useful for cell detection in localised regions of organs like the brain; other organs with less consistent T2* (e.g. lungs, stomach) would present further problems in cell detection. However, it is not possible to quantify the actual number of cells present by MRI due to the susceptibility of iron oxide, which dephases the surrounding proton signal causing an overestimation of the volume of SPION labelled cells (*Rice et al., 2007*).

Although consistent findings were demonstrated over the three imaging modalities, there were some discrepancies. After IV injection, no *in vivo* BLI signal was detected in liver and spleen while SPECT images showed high radioactivity distribution. As *ex vivo* BLI confirmed that viable cells were indeed present in these organs, this discrepancy is likely due to BLI signal attenuation by haemoglobin in liver and spleen (*Jacques et al., 2013*). Otherwise, all BLI findings correlated well with SPECT and MRI images which indicate that there was minimal background distribution from free ¹¹¹In-DOTA-SPION and that the majority of particles were internalised by ADSCs. This was further validated by histological analysis in adjacent lung tissue sections which showed that areas positive for vimentin (ADSCs) staining were also positive for Prussian blue (SPIONs), confirming the retention of the dual labelling agent within ADSCs. All these data suggest that the imaging results are an accurate representation of cell biodistribution.

The mechanism for initial cell uptake in the lungs after IV injection is likely to be mainly mechanical, as the large size of ADSCs (diameter of 20-24 µm) enable their initial entrapment within small capillary beds of the lung parenchyma (10-15 µm) (*Furlani et al., 2009; Fischer et al., 2009*). This hypothesis was supported by the lung tissue sections which showed the presence of labelled ADSCs in lung parenchyma which is the first pass of a capillary bed that intravenously injected cells are exposed to. The mechanism for secondary redistribution of cells to the liver and spleen is unclear and is possibly due to entrapment in a subsequent capillary bed, a migration process or clearance via the reticuloendothelial system. Low radioactivity uptake in kidney at later time points is likely from free ¹¹¹In clearance from the cells. This hypothesis was supported by BLI and MRI images of kidney after IV injection which showed no signs of cell uptake. These findings are in agreement with

published literature on stem cell tracking after IV injection using In-oxine labelling (*Chin et al., 2003; Kraitchman et al., 2005*). However, most studies were conducted using 1×10^6 cells, an order of magnitude higher than our study with no known information regarding cell viability. The multi-modal imaging approach used in this study has been able to provide quantification of whole body cell distribution, high resolution cell localisation and correlate this to cell viability.

An additional finding observed in this study was the difference in the ADSCs distribution pattern after IV and IC injection. The major differences are the 9-fold reduction of lung signal, 5-fold and 1.6-fold increase uptake in brain and kidney at day 0 after IC injection. This is mainly due to administration of the cells through the aorta and the carotid arteries via the left ventricle of the heart thereby bypassing the lungs and the capillary bed trapping as discussed above. It is likely that ADSCs uptake in the brain is due to the retention of cells within cerebral blood vessels rather than within the brain parenchyma. This hypothesis was supported by histological images at day 3 after injection showing the presence of vimentin and Prussian blue staining within the cerebral capillary bed. These results are consistent with published literature on tracking SPION labelled MSCs in a stroke model (*Walczak et al., 2008*). Although no obvious signs of stroke were seen in IC injected animals, histological evidences of cerebral microembolisms were found in two animals which raise safety concerns. This could be due to the large size of human ADSCs obstructing the small cerebral blood vessels of a mouse. However, these adverse events have been reported in IA infusion of allogeneic bone marrow MSC in rats and embolic events are related to cell dose and infusion velocity (*Cui et al., 2015*). All these findings suggest that cell size, cell dose and infusion velocity should be considered carefully in planning stem cell therapy using arterial route. The increased cells uptake in kidney demonstrated that IC injection is better than IV injection for cell delivery to the kidney which is consistent with a published paper on MSC tracking in acute kidney injury using BLI (*Tögel et al., 2008*). However, as most studies have only used a single imaging technique, the information on cell distribution at the target organ is not comprehensive. In this study, due to the advantages of multi-modal imaging, the precise cell localisation in target organs has been provided and correlated to cell number and cell viability.

Another interesting finding from this study is no significant difference in cell distribution pattern and BLI signal intensity curve was seen between the non-radiolabelled and ^{111}In -DOTA-SPION labelled ADSCs. This indicates that ^{111}In -DOTA-SPION labelling had no effect on *in vivo* cell distribution and the short term engraftment of ADSCs in organs following IV or IC. These results are in agreement with published studies showing rapid disappearance of MSCs after transplantation (*Tögel et al., 2008; Cui et al., 2013*). These results highlight the

advantages of combining reporter gene imaging with direct cell labelling unlike other multi-modal imaging probes. For example, one study stated that they tracked MSCs long term using a SPECT/MRI/fluorescent tri-modal probe, with the incorporation of the long half-life radioisotope ^{125}I but there was no correlating information on cell viability (*Tang et al., 2015*). However, the results from this study suggest that long term cell tracking is not necessary due to the transient viability of transplanted cells.

General assessments of the animals revealed no significant weight loss and no animal loss were seen during the study suggesting no adverse effect of cell injection or multiple anaesthesia doses on animals. Histological tissue sections showed no evidence of malignant tumour formation in ADSCs injected animals indicating that these cells do not display tumorigenic effect. No significance difference in ejection fraction before and after IC injection suggests that IC injection has no detrimental effect on cardiac function.

4.6 Conclusion

In summary, this study demonstrated the successful application of multi-modal imaging probes for stem cell tracking. The findings from this study demonstrate that combining the strengths of each modality can achieve more accurate information on cell localisation correlating with cell viability and the number of transplanted cells. All this information will be very beneficial in optimising stem cell therapy applications.

Chapter 5

**Multi-modal imaging of stem cell delivery
to tumours**

5.1 Abstract

Mesenchymal stem cells (MSCs) have been used as a selective anti-cancer agent due to their unique ability to home to tumour. However, the homing mechanism is known to be inefficient and depends on the route of stem cell administration.

The main aim of this chapter was to compare the efficiency of intravenous (IV) and intracardiac (IC) injection routes in delivering stem cells to distal tumours using multi-modal imaging. Luciferase expressing human adipose derived mesenchymal stem cells (ADSCs) were labelled with ^{111}In -DOTA-SPIONs (SPECT/MRI) dual imaging probes and injected either IV or IC into mice bearing 4T1 orthotopic breast tumours and imaged with BLI, SPECT/CT and MRI serially over 3 days .

At 1 hour after IC injection, BLI showed the presence of ADSCs in tumours while BLI signals were only detected in tumours at day 3 after IV injection. SPECT data at day 0 after IC injection showed the percentage of ADSCs in tumours was 2-fold higher than IV injection. MRI also showed the presence of SPION labelled cells in tumours after IC injection. The imaging data were further confirmed by histological analysis which showed the engrafted ADSCs in the tumour at day 3 after IC injection. Although IC injection is more efficient than IV in delivering stem cells to tumour, the risk of mortality was observed in IC injection of increased cell number due to the occlusion of blood vessels.

These findings indicate that the advantages of using multi-modal imaging approach in assessing not only the stem cell distribution in tumour but also the safety of the injection routes.

5.2 Introduction

5.2.1 Mesenchymal stem cell therapy for cancer

MSCs are an attractive delivery vehicle for anti-cancer therapies due to a number of reasons; they are readily isolated and expanded from multiple sources, can be genetically manipulated *ex vivo* to express anti-cancer agents such as tumour necrosis factor-related apoptosis induced ligand (TRAIL, Sage *et al.*, 2014; Bagó *et al.*, 2016), and they show evidence of tumour tropism for targeted delivery of an anti-cancer payload. However, no consensus exists on the therapeutic efficacy of MSC therapies and the potential pro-tumorigenic effect of MSCs on tumour growth. Therefore, further assessments are required to develop MSC-based therapies for widespread clinical applications.

5.2.2 The role of non-invasive *in vivo* imaging in MSC-based cancer therapy

The efficiency of MSC tumour homing depends on a number of factors including the route of administration. Several studies have demonstrated that many MSCs are trapped in the lungs capillaries after intravenous administration and only a small proportion migrates and is retained in the tumours (Studený *et al.*, 2002; Wang *et al.*, 2009). Hence, modification of the injection route is required to improve stem cell delivery to tumours and non-invasive imaging technologies are essential to monitor the fate of these transplanted MSCs. Optical imaging including fluorescence and bioluminescence imaging is one of the most widely used techniques to track stem cell homing to tumours. MSCs have been engineered with bicistronic reporter constructs to express luciferase and fluorescent proteins which allow tracking MSC migration to brain tumours using BLI and intravital microscopy (Sasportas *et al.*, 2009). However, this technique cannot be applied in larger animals or humans due to limited tissue penetration. In addition, intravital microscopy is an invasive procedure and *ex vivo* tissue imaging is required to validate the precise cell localisation in tumours. Since stem cell imaging is required for clinical applications, clinically translatable techniques must be developed. MRI using iron oxide nanoparticles has been used in clinical trials to assess the success of stem cell delivery to target organs (McColgan *et al.*, 201; Bull *et al.*, 2014). Due to recent developments in dual imaging probes, the tumour uptake of MSCs labelled with fluorescent magnetic nanoparticles have been tracked in a mouse model of gastric cancer using fluorescence imaging and MRI (Ruan *et al.*, 2012). One drawback of MRI-based cell tracking is the difficulty in quantifying the number of transplanted cells within the target organ which is an important factor in determining treatment outcomes. In a previously published study, nuclear reporter gene imaging using ¹⁸F-FHBG was able to track HSV1-tk expressing bone marrow derived stem cells in a mouse model of glioma (Hasenbach *et al.*, 2012). The results demonstrated the advantages of nuclear imaging enabling the quantification of the

amount of tracer uptake in gliomas. However, due to poor spatial resolution, the accurate cell localisation within tumour tissue is not achievable. A wide variety of contrast agents and imaging technologies have been beneficial in *in vivo* stem cell tracking but each imaging modality has its drawback when trying to answer all the important questions in stem cell therapy. Therefore, a multi-modal imaging approach is required to have a more effective assessment for optimizing stem cell delivery to tumours.

5.2.3 Experimental approach

In this study, a multi-modal imaging approach (BLI, SPECT/CT and MRI) was applied in the tracking of ^{111}In -DOTA-SPION labelled ADSCs homing to a primary breast tumour following two different systemic injection routes. 4T1 murine breast cancer cells were used to develop a mouse model of orthotopic primary breast tumour via mammary fat pad implantation due to the following reasons: 1) 4T1 cancer cell lines have been shown to secrete inflammatory cytokines which attract MSC homing to tumours (*Gehmert et al., 2010, Fantozzi et al., 2006*); 2) a previous study using BLI has demonstrated that the engraftment of MSCs within 4T1 subcutaneous tumours after IV injection (*Klopp et al., 2007, Wang et al., 2009*); and 3) orthotopic primary breast tumour model is a well-characterised model and is believed to be more vascularised than subcutaneous tumours aiding MSC delivery (*Zhang et al., 2018*) and mammary fat pad implantation is an easy, efficient and well-established technique (*Zhang et al., 2018*). In this study, a non-surgical method was used to implant tumour cells directly into the mammary fat pad in order to avoid infection risk in NSG mice. This method has already been validated in several pilot studies. The tumour cells were implanted into mammary glands in the lower abdomen of the mouse, 5th mammary fat pad, in order to avoid the signal spill over from the very bright lung signal in BLI and SPECT/CT images.

5.2.4 Research Objectives

1. Develop a mouse model of orthotopic primary breast tumour.
2. Determine a suitable tumour size for detection with BLI, SPECT/CT and MRI by monitoring the tumour growth.
3. Evaluate the effect of ^{111}In -DOTA-SPIONs labelling on tumour homing property of ADSCs.
4. Compare the efficiency of IV and IC administration routes to deliver ^{111}In -DOTA-SPIONs labelled ADSCs to distal tumours.
5. Validate *in vivo* imaging results using immunohistochemistry.

5.3 Methods

5.3.1 Cell culture

All experiments were performed using luciferase expressing human adipose derived mesenchymal stem cells (ADSCs) as previously described in Chapter 2.2.

For the development of the orthotopic primary breast tumour model, 4T1 murine breast cancer cells (a kind gift from Dr Elnaz Yaghini, Surgery and Interventional Science, UCL) were grown in T75 flasks (Fisher Scientific, Loughborough, UK) in Dulbecco's modified Eagles medium (DMEM) (Invitrogen, Paisley, UK), supplemented with 10% FCS in an humidified incubator at 37°C with 95% air and 5% CO₂. Cells were grown to 80% confluence before being trypsinised, centrifuged for pelleting at 300 g, counted and then re-suspended in PBS.

5.3.2 *In vivo* studies

All animal procedures were performed as described in Chapter 2.4.

5.3.3 *In vivo* cell and particle injection

Orthotopic breast tumour implantation using a non-surgical method

Animals were anaesthetised and the area around the 4th and 5th mammary gland was shaved and the right fifth nipple was lifted with sterile forceps. The 4T1 tumour cell suspension (0.5 x 10⁵ cells/50 µl) was injected directly into the right 5th mammary fat pad using a 29 g insulin syringe needle (Figure 5.1). Tumour growth was monitored using MRI and ultrasound at days 9 and 12 after tumour implantation. The average tumour size used in the studies was ~40 mm³ and tumour sizes were matched between IV and IC injected groups.

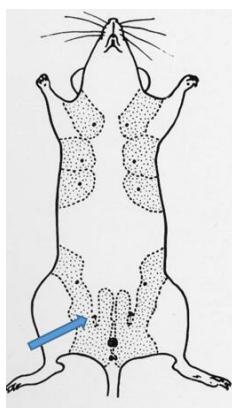


Figure 5.1 Schematic representations of mammary glands in a mouse and the mammary fat pad where 4T1 breast cancer cells were implanted (indicated by arrow).

***In vivo* biodistribution studies in tumour bearing animals**

For *in vivo* biodistribution studies of ^{111}In -DOTA-SPION labelled ADSCs, the tumour bearing mice were injected either IV ($n = 3$) or IC ($n = 3$) with 1×10^5 dual labelled ADSCs (~ 0.5 MBq of ^{111}In , $52 \mu\text{g}$ of Fe). The mice were imaged with BLI, SPECT/CT and MRI serially over 3 days (Figure 5.2a). The imaging sessions were terminated at 3 days after cell infusion as in the pilot studies some NSG mice became weak and were unable to tolerate anaesthesia at 14 days after tumour implantation.

For *in vivo* biodistribution studies of non-radiolabelled ADSCs, 1×10^5 cells were injected either IV ($n=3$) or IC ($n=3$) into tumour bearing mice and imaged with BLI serially over 3 days (Figure 5.2b).

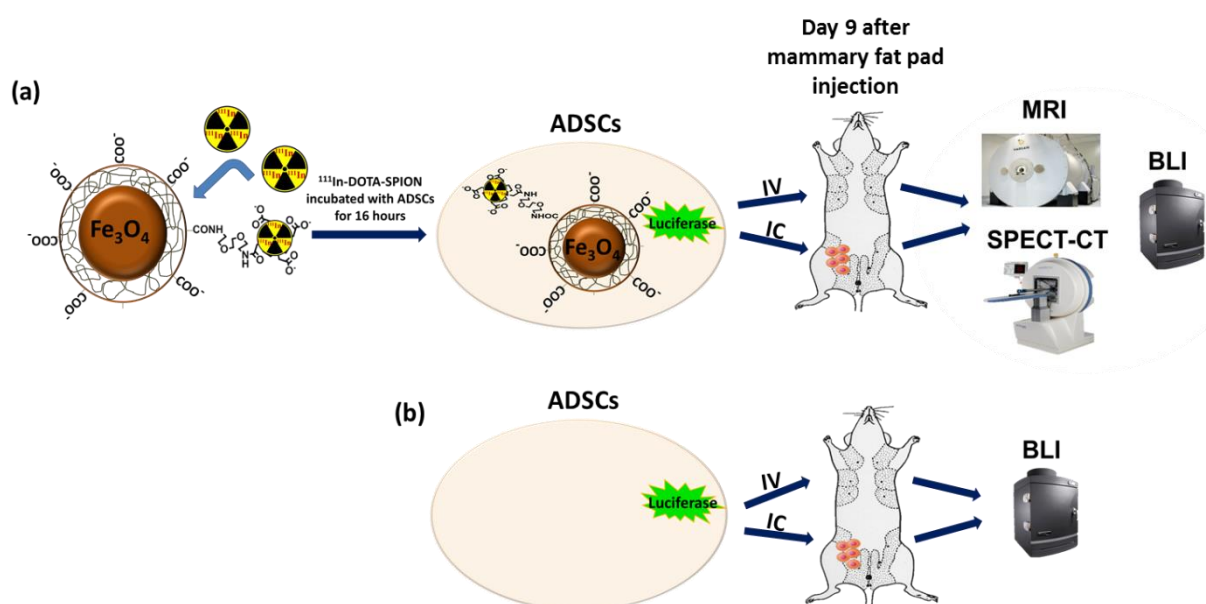


Figure 5.2 Schematic outlines of imaging ADSCs delivery to tumour using BLI, SPECT/CT and MRI.

5.3.4 *In vivo* imaging

BLI

Mice were anaesthetised and *in vivo* BLI was performed at 1 hour, days 1 and 3 after injection. To calculate the percentage of BLI signal in tumour, a circular ROI was placed over the tumour and the signal from the tumour ROI was divided by the whole body signal and presented as % signal in tumour.

SPECT/CT

Directly after BLI imaging, mice were anaesthetised and whole body SPECT/CT scans were acquired at 3-5 hour after injection (termed day 0), and then at days 1 and 3. 3D ROIs were created for brain, lungs, liver, kidney and tumour for each time point and calculated as the percentage of injected dose/mm³ (%ID/mm³) after correcting for ¹¹¹In decay.

MRI

MRI studies were performed at days 1 and 3 after IV and IC injection using a 1T ICON scanner. To detect the presence of SPION labelled cells in tumour, T₂^{*}-weighted images were acquired using the following parameters: TR = 147.5 ms; TE = 5 ms; spatial resolution = 216 μm/pixel; slice thickness = 1 mm. For monitoring tumour growth, T₂-rapid acquisition with relaxation enhancement (RARE) images of tumour were acquired at days 9 and 12 after tumour implantation using the following parameters: TR = 2483 ms; TE = 16.5 ms; rare factor = 8; spatial resolution = 287 μm/pixel; slice thickness = 1 mm. The volumetric measurement of the tumour was calculated using ImageJ software and the results were presented as the relative tumour growth from day 9 after implantation.

Ultrasound

3D ultrasound images of the tumour were acquired at days 9 and 12 after tumour implantation using a 3D stage control system (Vevo 2100, Visualsonic, Canada). Consecutive B-mode images were acquired by scanning across the tumour at intervals of 0.2 mm and which were then reconstructed into a 3D image. The arterial and venous blood supplies to the tumour were identified using colour Doppler and pulsed wave Doppler modes. The total blood supply to the tumour was visualised using 3D power Doppler mode. The heart rate, body temperature and respiration rate were monitored throughout the study. The images were analysed using the 3D analysis tool, Vevo lab software version 3.1.1.

5.3.5 Ex vivo BLI and ex vivo biodistribution study

To validate *in vivo* imaging results and to assess background free particle uptake in tumours, *ex vivo* BLI and *ex vivo* biodistribution studies using a gamma counter (%ID/g) were performed at 1 hour and 3 days after IV and IC injection of ¹¹¹In-DOTA-SPION labelled ADSCs (0.3 x 10⁵ cells containing ~0.3 MBq of ¹¹¹In, 31.2 µg of Fe) or ¹¹¹In-DOTA-SPION labelled particles only (~0.3 MBq of ¹¹¹In, 31.2 µg of Fe, n = 3 for each time point for each group) following the procedures previously described in Chapter 2.5.

5.3.6 Ex vivo MRI

At the end of the imaging sessions, mice were sacrificed (n = 1 for each group) and tissue samples were excised, fixed in 10% neutral buffered formalin and embedded in 1% agarose. *Ex vivo* MRI images of tumours were acquired using a 9.4T Varian scanner. 3D T₂^{*}-weighted images of excised tumours were acquired using TR = 10 ms; TE = 5 ms; spatial resolution = 117 µm/pixel; flip angle = 20°, acquisition time = 88 minutes. Images were analysed using ImageJ software.

5.3.7 Histology and immunohistochemistry (IHC)

At the end of imaging sessions, mice were sacrificed (n = 1 for each group) and tumour samples were prepared and sectioned as previously described in Chapter 2.6. The adjacent 5 µm tumour sections were stained with Prussian blue (SPIONs) and vimentin (ADSCs) using Ventana Red detection kit.

5.3.8 Statistical analysis

Statistical analysis was performed with GraphPad Prism version 6.01. Data were presented as mean ± standard deviation (SD). An unpaired two-tailed t test was conducted for all experiments.

5.4 Results

5.4.1 Assessment of ^{111}In -DOTA-SPION labelled ADSCs delivery to tumor following IV or IC

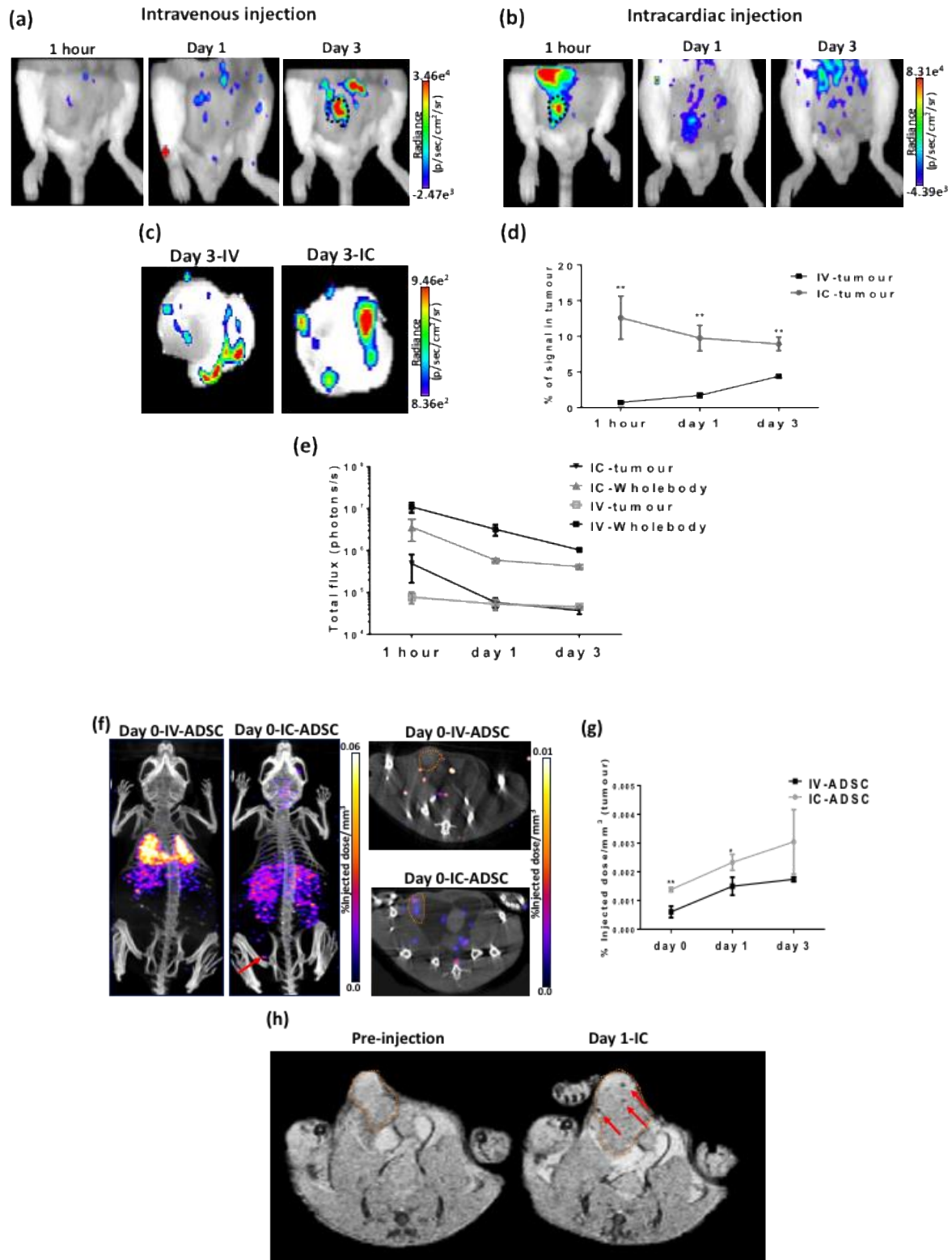


Figure 5.3. Multi-modal imaging of ^{111}In -DOTA-SPION labelled ADSCs engraftment in tumour following IV or IC injection. (a & b) BLI signal in tumour at day 3 after IV injection & 1 hour after IC injection (indicated by black dotted lines). (c) *Ex vivo* BLI images of tumour at day 3 after IV & IC injection. (d) The percentage of BLI signal in tumour relative to whole body after IV and IC injection (IV vs IC ** $P = 0.0025, 0.0016, 0.0013$ at 1 hour, days 1 & 3 respectively). (e) BLI signal from the tumour and the whole body decreased over time (photons/sec in log scale). (f) SPECT/CT images of dual labelled ADSCs at day 0 after IV and IC injection showing the tumour uptake in a mouse with IC injection (indicated by arrow and orange dotted lines). (g) 3D ROI quantification of SPECT signal in tumour at days 0, 1 & 3 after IV & IC injection calculated as $\%ID/mm^3$ after decay correction (IV vs IC ** $P = 0.0032$ at Day 0, * $P = 0.0262$ at day 1). (h) T_2^* -weighted MR images of tumour (indicated by orange dotted line) acquired at pre-injection and day 1 after IC injection of dual labelled ADSCs showing the presence of focal hypointensity within the tumour (indicated by arrows). Data are shown as mean \pm SD, $n = 3$.

To assess the efficiency of ^{111}In -DOTA-SPION labelled ADSCs delivery to distal tumours, mice bearing orthotopic 4T1 breast tumour were injected with 1×10^5 cells either IV or IC and imaged with BLI, SPECT and MRI serially over 3 days.

No BLI signal could be detected in tumour tissue until 3 days after IV injection (Figure 5.3a, supported by *ex vivo* BLI, Figure 5.3c). In comparison, BLI signal was detected within the tumour as early as 1 hour after IC injection and throughout the study (Figure 5.3b, supported by *ex vivo* BLI, Figure 5.3c). The percentage BLI signal in tumor (relative to whole body BLI signal) after IC injection was significantly higher than IV injection at all three time points ($P = 0.0025, 0.0016, 0.0013$, Figure 5.3d). The BLI signal intensity from tumours decreased similarly to that of whole body overtime after IV and IC cell infusion (Figure 5.3e). SPECT/CT images also showed cell uptake within tumour at days 0 (Figure 5.3f) and 1 after IC injection which was significantly higher than after IV injection ($P = 0.0032$ & $P = 0.0262$, Figure 5.3g). However, no significant differences were found at day 3 ($P = 0.1147$) as was shown by BLI. Both BLI and SPECT/CT images showed that the whole body cell distribution pattern for ADSCs were the same as in healthy animals (non-tumour bearing) described in chapter 4.

Consistent with BLI and SPECT findings, T_2^* -weighted MR images of tumours at 1 day after IC injection showed small areas of localized hypointensity throughout the tumour (core as well as rim) compared to the pre-injection image suggesting the presence of labelled cells within tumour tissue (Figure 5.3h). However, no hypointense region was detected by MRI in the IV injected group although both SPECT and BLI suggested that there was cell uptake within the tumours at 3 days after injection.

To validate the imaging results, histological validation was performed. Tumour tissue sections from the IC injected group showed positive vimentin staining which confirmed the presence of ADSCs within tumours (Figure 5.4). It is more likely that arterial blood flow has

caused passive entrapment of cells in the tumour vasculature by carrying the cells towards tumours rather than active cell migration process. However, Prussian blue staining was absent in adjacent tumour sections. It is likely due to the amount of iron in the cells was not sufficient enough to be able to detect with Prussian blue staining. In IV injected group, ADSCs were unable to detect in tumour tissue sections, which is probably due to the low number of cells within these tumours.

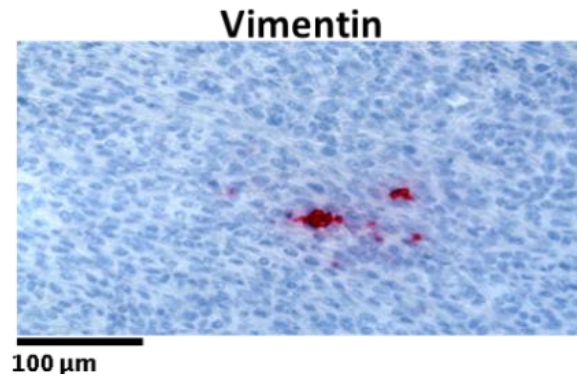


Figure 5.4 Histological analysis of ^{111}In -DOTA-SPION labelled cells uptake in tumour at 3 days after IC injection showing positive vimentin (ADSC) staining in tumour tissue section (scale bar = 100 μm).

In order to improve the level of cell detection within tumours, an increased number of ^{111}In -DOTA-SPION labelled ADSCs (2.5×10^5) were injected into tumour bearing mice via either IV or IC. During IC injection, 4 mice died although all IV injected animals survived. In order to investigate this, the dead animals were scanned with SPECT/CT which showed the multiple hot spots in heart, lungs, brain and major blood vessels including carotid arteries and common iliac arteries (Figure 5.5). Therefore, no more studies were conducted utilizing the higher cell dose.

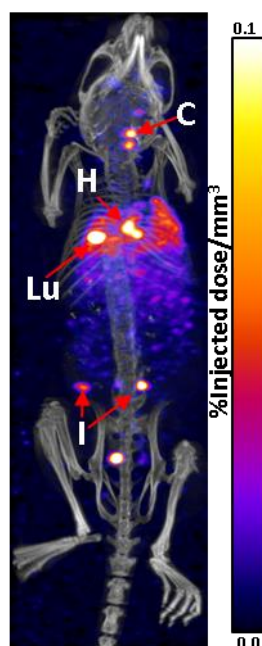


Figure 5.5 SPECT/CT images of dead tumour bearing mouse immediately after IC injection of 2.5×10^5 ^{111}In -DOTA-SPION labelled cells showing cell aggregates in heart, lungs, carotid artery and common iliac arteries (labels: H = Heart, Lu = lungs, C = carotid artery, I = common iliac arteries). Representative images were presented using %ID/ml as colour scale after correction for ^{111}In decay.

5.4.2 Assessment of non-specific background ^{111}In -DOTA-SPION particle uptake in tumour following IV or IC

To evaluate any potential non-specific background radioactivity caused by free ^{111}In -DOTA-SPION particle uptake in tumour, ^{111}In -DOTA-SPIONs labelled cells or particles only were injected either IV or IC into tumour bearing mice and *ex vivo* gamma counting (%ID/g) was performed at days 0 and 3 after injection. At day 0 after IC cell injection, the cell uptake in tumour was significantly higher than the IV cell and IC particle injection groups ($P = 0.0002$ & $P = 0.0002$, Figure 5.6a). These results are consistent with *in vivo* SPECT data and indicate that tumour uptake after IC cell injection is due to cell engraftment not free particle accumulation. No significant difference was observed between the IV cell and IV particle groups ($P = 0.7602$). At day 3 after injection, radioactivity uptake in tumour showed no significant difference among all four groups (Figure 5.6b). The radioactivity uptake in lungs, liver, spleen, brain and kidney showed no significant difference from the cell distribution pattern in healthy animals (full organ data in Appendix 4) which demonstrated that all *ex vivo* results are consistent with *in vivo* SPECT data.

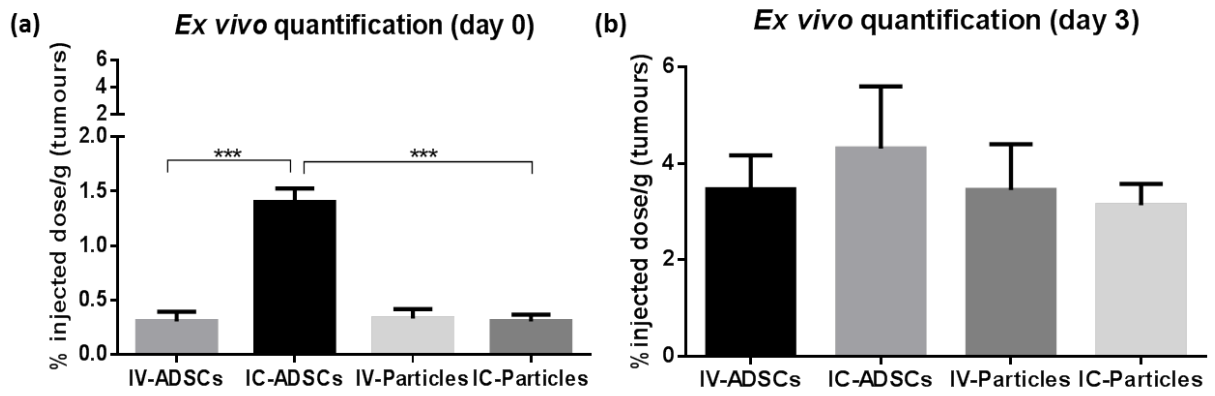


Figure 5.6 Assessment of the background particles uptake in tumour. *Ex vivo* quantification of radioactivity distribution in tumour at (a) day 0 and (b) day 3 after IV and IC injection of ^{111}In -DOTA-SPION labelled cells and particles only calculated at %ID/g after decay correction (***P* = 0.0002 IV-ADSCs vs IC-ADSCs, ***P* = 0.0002 IC-ADSCs vs IC-Particles). Data are shown as mean \pm SD, *n* = 3.

5.4.3 Ex vivo MRI

To further validate *in vivo* MRI results, selective tumours (n = 1 each group) were embedded in 1% agarose and high resolution *ex vivo* MRI was performed using the unlabeled cell (ADSCs only) injected group as a control. 3D T_2^* -weighted images showed no focal hypointense areas in the control tumour (Figure 5.7a). Although *in vivo* MRI was not able to detect cells in the IV injected group, *ex vivo* MRI images showed regions of localized hypointensity in some areas of tumour (Figure 5.7b). Areas of focal hypointensity were seen throughout the tumour that received an IC injection of ^{111}In -DOTA-SPION labelled ADSCs (Figure 5.7c), which is consistent with *in vivo* MRI findings. It is likely due to trapping of cells in tumour blood vessel due to arterial flow.

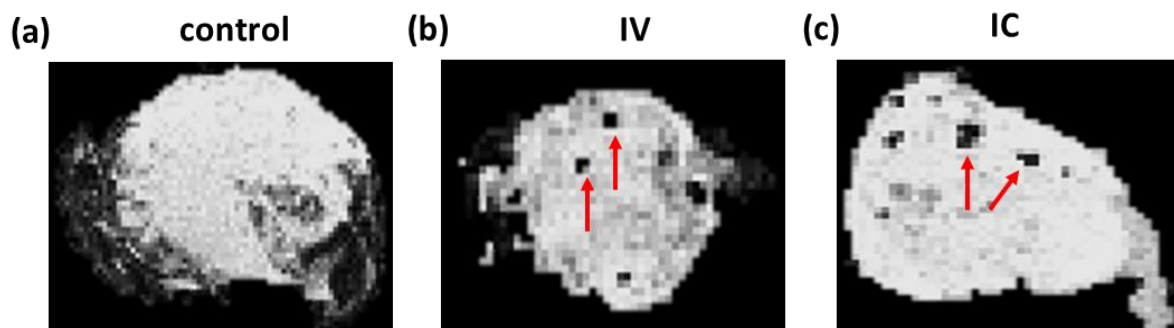


Figure 5.7 *Ex vivo* MRI assessment of the cells uptake in tumour at day 3 after IV and IC injection. T_2^* -weighted images of (a) a control tumour injected with ADSCs only (b & c) tumours injected with ^{111}In -DOTA-SPION labelled ADSCs intravenously and intracardially showing areas of focal hypointensity (indicated by arrows).

5.4.4 Assessment of non-radiolabelled ADSCs delivery to tumour following IV or IC

To assess the effect of labelling agents on cell migration to tumour, 1×10^5 non-radiolabelled ADSCs were injected into tumour bearing animals either IV or IC and imaged with BLI serially for 3 days. In comparison with BLI results from radiolabeled cells, the same cell distribution pattern to tumour tissue and throughout the whole body were observed following IV or IC injection (Figure 5.8a, b & c). The percentage BLI signal in tumour after IC injection was significantly higher than IV injection at days 0, 1 and 3 ($P = 0.008$, $P < 0.0001$ & $P = 0.0023$, Figure 5.8d). This indicates that the migratory property of ^{111}In -DOTA-SPION labelled cells is not altered *in vivo*. Histological validation in tumour tissue sections of both IV and IC injected group showed positive vimentin staining which confirmed the engraftment of ADSCs in tumour after both injection routes (Figure 5.8e & f).

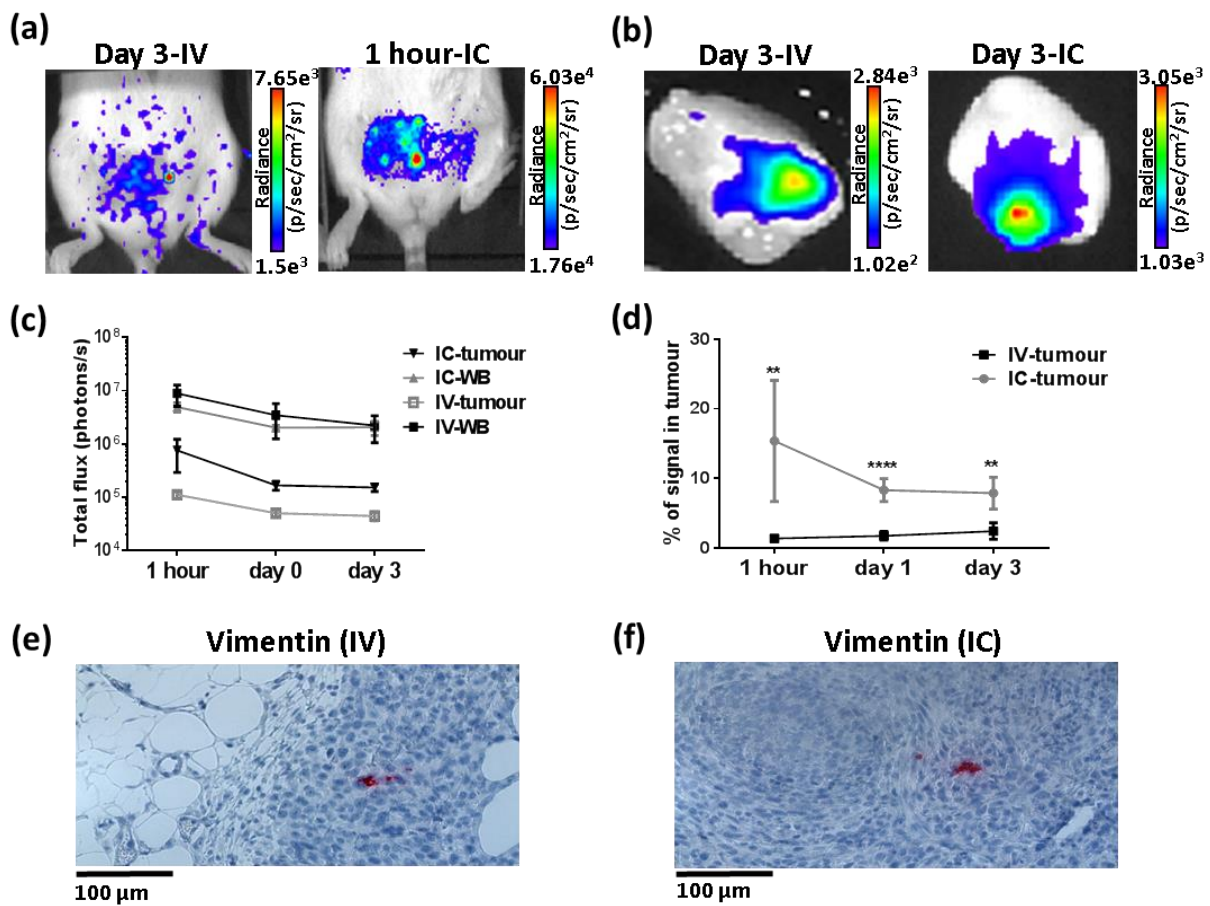


Figure 5.8 Assessment of non-radiolabelled ADSCs engraftment in tumour following IV or IC injection. (a) BLI signal in tumour at day 3 after IV injection and 1 hour after IC injection. (b) *Ex vivo* BLI images of tumour at day 3 after IV and IC injection. (c) BLI signal from the tumour and the whole body decreased over time (photons/sec in log scale). (d) The percentage of BLI signal in tumour relative to whole body after IV and IC injection (IV vs IC ** $P = 0.008$, **** $P < 0.0001$ & ** $P = 0.0023$ at 1 hour, days 1 & 3 respectively). (e & f) Histological analysis of non-radiolabelled cells uptake in tumour at 3 days after IV and IC injection showing positive vimentin (ADSC) staining in tumour tissue sections (scale bar = 100 µm).

5.4.5 Measurement of tumour growth

In order to evaluate the potential pro-tumorigenic effect of ADSCs, the rate of tumour growth was monitored using MRI and the results showed no significant difference between ADSCs injected and particles only injected groups ($P = 0.06$, Figure 5.9).

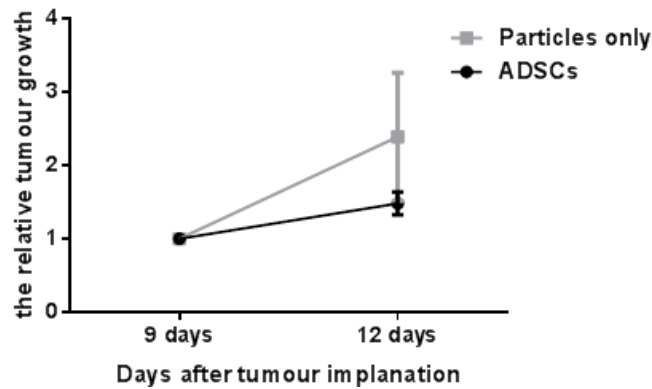


Figure 5.9 MRI measurement of the rate of tumour growth showing no significant difference between ADSC injected and particle only injected groups.

5.4.6 Assessment of blood supply to tumour

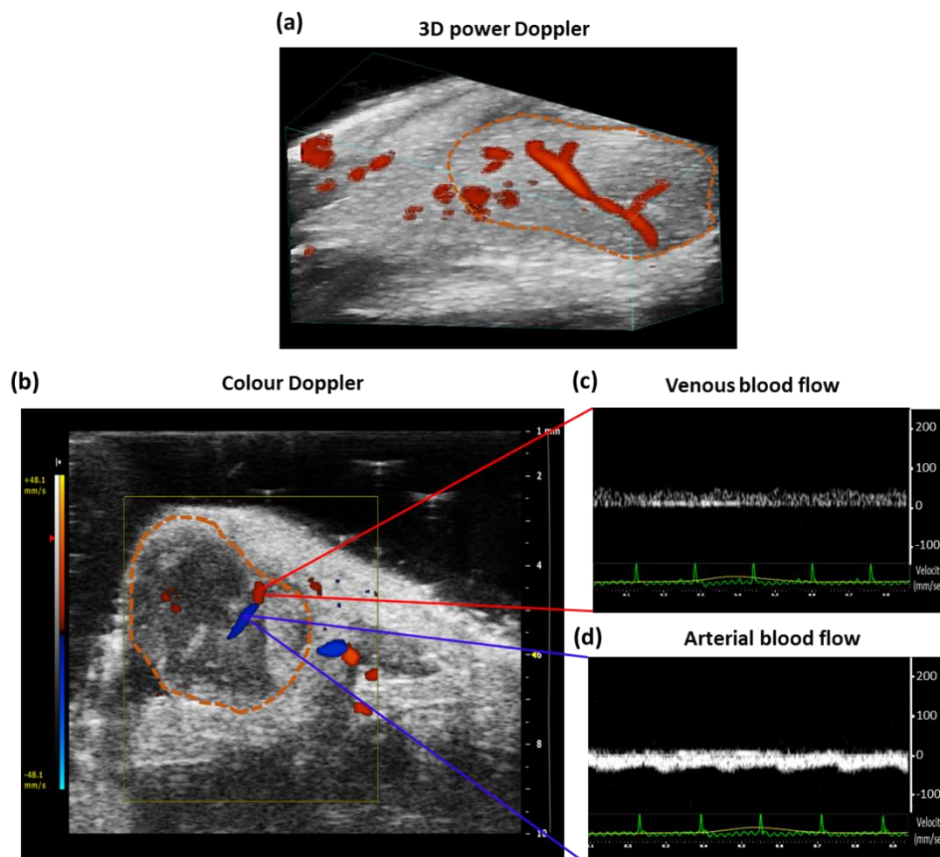


Figure 5.10 Assessment of tumour blood supply using Doppler ultrasound. (a) 3D power Doppler image of tumour showing the total blood supply. (b - d) Colour Doppler and pulsed wave Doppler image of the tumour showing the venous and arterial blood supply. (Tumour areas were indicated by orange dotted lines in ultrasound images).

Although tumour sizes were matched between groups, their blood perfusion could differ and affect cell migration. In order to evaluate this, the total blood supply to the tumour including arterial and venous origin was visualised using 3D power Doppler (Figure 5.10a) and colour Doppler ultrasound (Figure 5.10 b, c & d). However, Doppler signal was detected in 3/6 tumours in the IV group and 4/6 in IC group. It is likely because Doppler ultrasound is not sensitive enough to detect small blood vessels formation in tumour. Therefore, no association could be drawn between the amount of blood supply and the level of cell engraftment.

5.5 Discussion

The aim of this chapter was to compare the efficiency of two systemic injection routes: IV and IC to deliver ^{111}In -DOTA-SPION labelled ADSCs to a distal tumour site using BLI, SPECT/CT and MRI.

Overall this study suggested that the IC injection is more efficient than IV in delivering ADSCs to distal tumors. This is due to the physiological nature of arterial blood supply and lack of pulmonary entrapment during administration. These results support published literature on therapeutic drug delivery to liver tumours (*Mavligit et al., 1991, Vexler et al., 1995*) and brain tumours (*Tyler et al., 1986, Takeda et al., 1999*) via intra-arterial administration. The presence of ADSCs within the tumour as early as 1 hour after IC injection indicates that the process is likely due to passive retention rather than active migration. However, the indication of ADSC infiltration at 3 days after IV injection may suggest migratory capability of ADSCs from lungs to tumour. The process of MSC tumour homing is known to be stimulated by inflammatory cytokines and chemokines such as IL6 (*Shi et al., 2007*) & SDF-1 (*Lourenco et al., 2015*) released from the tumour followed by the adhesion of circulating MSCs to the vascular wall and transendothelial migration (*Lo et al., 2013*). However, these imaging data cannot conclusively answer whether this migration process is due to an active homing or a passive entrapment mechanism.

Although the three imaging techniques showed consistent findings at days 0 and 1, the discrepancies were seen at day 3 after cell infusion. This is mainly due to the difference in sensitivity among imaging techniques. Due to lack of background signal, BLI can provide a higher signal to noise ratio for cell detection compared to SPECT. However, due to light scattering, the number of cells in tumour is not possible to quantify with BLI while SPECT imaging can provide a semi-quantitative measurement. Similarly, MRI is not as sensitive as BLI in detecting small number of cells in the IV injected group although it can provide a high resolution of ADSCs localization within the tumor after IC injection. This issue could be resolved by using high resolution *ex vivo* MR imaging which improved sensitivity and remove physiological motion. However, this technique could only be applied as a validation method at the end of the study. Nonetheless, all these results highlight the advantages of combining imaging techniques to overcome their limitations.

Another interesting result from this study is that the BLI data showed no sign of ADSC proliferation in tumour and the whole body signal reduced similarly to that of healthy animals (non-tumour bearing, shown in Chapter 4) which indicates the short-term cell engraftment after transplantation. Consequently, only a low number of cells would be able to migrate from the primary lung entrapment site to distal tumour after IV injection which is why we see

discrepancies between IV and IC at day 3. This result demonstrates that the optimal time point to achieve sufficient cell engraftment within the tumour is immediately after cell infusion. Therefore, IC injection is the more efficient administration route for ADSCs delivery to distal tumours in this case. However, the results from IC injection with an increased number of ^{111}In -DOTA-SPION labelled cells showed some animals fatalities probably due to the occlusion of major arteries by cell aggregates. In contrast, all IV injected animals survived likely due to trapping of cell aggregates in the lungs which act as a sieve to filter any large clots. These are important factors to be considered in designing stem cell therapy. Another potential issue to be envisaged is the complex role of MSCs within the tumour microenvironment and their effect on tumour growth. In this study, no significant difference in tumour growth was seen between ADSCs injected and particles only injected groups which indicates ADSCs do not display either a pro-tumorigenic or anti-tumorigenic effect.

The published literature on MSCs migration to tumours (*Klopp et al., 2007, Wang et al 2009, Yao et al., 2017*) has mainly focused on the IV administration route and has been visualized using a single imaging modality. These studies have therefore not provided any correlated information on cell viability, cell localization with the quantity of cell engraftment within tumour tissue. This study has provided extensive information on MSC engraftment within tumours following venous or arterial routes by using a multi-modal imaging agent, which has demonstrated that the arterial route can deliver a 2-fold increase in MSC uptake to a distal tumour tissue at the earliest time point when cells are most viable when compared to IV administration. In addition, tri-modal imaging has also provided the quantitative assessment of whole body distribution of cells and the excellent resolution of cell localization after two systemic injections. All these information are useful in designing a targeted anti-cancer therapy using MSCs and in assessing off target effects and safety after cell infusion. Moreover, this multi-modal imaging approach will be very useful in evaluating methods used to improve MSC homing efficiency, such as priming MSCs in culture with various cytokines (*Shi et al., 2007*) and to improve targeted cell delivery to target organs by modifying IV injection routes to decrease MSC trapping in the lungs (*Gao et al., 2001, Yukawa et al., 2012*).

5.6 Conclusion

In summary, this study demonstrated the successful application of a multi-modal imaging agent for assessing stem cell delivery to tumours. The finding from this study proved that multi-modal imaging can provide comprehensive information on the uptake of transplanted cells within tumour, and the need for the optimization and safety assessment of multiple administration routes for tumour delivery. Although there are some challenges in combining imaging techniques, the advantages far outweigh the drawbacks and will help to progress stem cell therapy applications.

Chapter 6

Multi-modal imaging of stem cell delivery to kidney

6.1 Abstract

Although stem cell-based therapies can provide a promising solution for treating various kidney diseases, the major hurdle in initiating therapeutic responses is the inefficiency of injection routes in delivering stem cells to kidney. Since systemic injection routes such as IV and IC injection can deliver only a small proportion of cells to the kidney (see chapter 4) and direct delivery routes such as renal parenchymal and renal artery injection require invasive procedures, the development of a minimally invasive injection route is needed in stem cell therapy for kidney diseases.

The aim of the work in this chapter was to develop a less invasive ultrasound-guided renal artery injection to improve stem cell delivery to kidney. Luciferase expressing human adipocyte derived mesenchymal stem cells (ADSC) were labelled with gold nanorods (GNR) and injected into right renal artery using ultrasound guidance and imaged the mice with BLI and photoacoustic (PA) imaging serially over 7 days.

BLI results showed the majority of the signals were within the right kidney and remained stable for 3 days. PA images also showed the strong signals within the right kidney and GNR labelled cells were able to detect throughout the kidney including cortex and medulla. The imaging results were confirmed with histological images at day 8 after injection which showed co-localization of GNRs and grafted ADSCs throughout the right kidney. No animal loss or sign of major trauma was observed during the course of the study.

These findings indicate that a minimally invasive ultrasound-guided renal artery injection is feasible in mice and the successful injection allows a large proportion of cells retained in the kidney for 3 days. Therefore, the techniques developed here will be useful for optimising cell therapy in kidney diseases.

6.2 Introduction

6.2.1 Stem cell therapy for kidney diseases

Over the past few years, stem cell-based regenerative therapy has been vastly studied as an alternative treatment for various kidney diseases. Mesenchymal stem cells (MSCs) have been implemented in the treatment of kidney disease due to their ability of self-renewal and capability to differentiate into multiple cell lineages (*Aggarwal et al., 2013*). However, there is no clear evidence of MSC transformation into specialised renal cell types (*Murray and Woolf, 2014*). The beneficial effect of MSC therapy in repairing kidney damage is mainly due to paracrine factors secreted by MSCs (*Barnes et al., 2016*).

MSCs have the ability to release a variety of active biological factors including growth factors such as insulin-like factor 1 (IGF-1, *Imberti et al., 2007*), vascular endothelial growth factor (VEGF, *Yuan et al., 2011*) and other immune system signalling molecules, such as, transforming growth factor- β (TGF- β , *Si et al., 2015*). Through these signalling cascades, MSCs are able to recruit and promote repair process during acute kidney injury (AKI). Therefore, MSC-based therapy has been tested in several mouse models and three clinical trials to treat patients with AKI (*Peired et al., 2016*). Moreover, MSCs provides a promising solution for treating chronic renal disease due to their immunomodulatory properties (*Franguesa et al., 2012*). MSCs are believed to have the ability to migrate to the site of inflammation and transform the environment from a pro-inflammatory to anti-inflammatory state by secreting various soluble factors such as prostaglandin E2 (*Bouffi et al., 2010*) and decreasing the levels of inflammatory and pro-fibrotic cytokine such as TNF- α (*Tögel et al., 2005*).

Unlike MSCs from unrelated sources, kidney derived stem or progenitor cells have the ability to differentiate towards nephrogenic lineage and could be used for therapeutic applications (*Murray and Woolf, 2014*). In addition, due to their enhanced potency towards specific renal cell differentiation, kidney derived stem cell could be a potential solution for the side effects of MSC such as the development of unwanted differentiated cells: adipocytes and osteoblast like cells in the kidney (*Kunter et al., 2007; Abouelkheir et al., 2016*). These endogenous stem cells can be isolated from developing rodent or human kidneys and differentiated into renal cell types such as podocyte and proximal tubule-like cells (*Fuente Mora et al., 2012*). However, the results from lineage tracing studies in mouse models suggest that they are not present in adult kidneys (*Humphreys et al., 2008*). Moreover, the conflicting results have been reported on the homing and regenerative potential of adult renal progenitors cells. Although improved renal function and generation of tubular cells from these cells have been reported in a mouse model of renal tubular injury (*Agelotti et al., 2012*), another study has

shown no evidence of differentiation of these cells and functional improvement was not related to cell engraftment at injury site (*Santeramo et al., 2017*). Therefore, more studies are required to elucidate the property of renal progenitor cells.

Although many preclinical studies have demonstrated the efficacy of stem cell therapy in kidney diseases, using stem cell products as a routine clinical treatment is hindered by a number of challenges, such as selecting the optimal delivery route for effective MSC uptake within kidney parenchyma. Intravenous, intra-arterial and intraparenchymal injections have been tested in many mouse models of AKI to deliver MSCs to kidney. Although IV injection is relatively easy and non-invasive method of administration, the main problem is pulmonary entrapment of cells thereby reducing engraftment within kidney as shown in Chapters 4 and 5 (*Fischer et al., 2009*). Several studies including work shown here in Chapters 4 and 5 have shown that systemic intra-arterial delivery can provide increased cell retention in kidney (*Gooch et al., 2008; Tögel et al., 2008*). However, evidence of vascular occlusion after intra-arterial injection has been reported which raises safety concerns (*Furlani et al., 2009*). A previous study has also directly injected cells into the renal parenchyma which resulted in reduced kidney fibrosis in a rat model of renal ischemia-reperfusion (*Alfarano et al., 2012*) but this approach is difficult to implement in a clinical setting due to the risk of additional injury. Similarly, the delivery of MSCs directly into the renal artery of an injured kidney has been shown to increase cell engraftment in preclinical studies (*Bos et al., 2004, Cai et al., 2014*) but this method is invasive and is usually conducted at the end of the open abdominal surgery to induce renal ischemia. Therefore, the development of a less invasive and more efficient injection route is urgently required to improve stem cell delivery to preclinical kidney injury models.

6.2.2 Photoacoustic imaging for stem cell tracking to kidney

In addition to establishing the optimal route for stem cell delivery, tracking of transplanted cells and verifying their viability within the target organ is equally important in determining therapeutic efficacy of the cell therapy. Nuclear imaging using ^{111}In -oxine labelling has been used to track stem cells in a mouse model of renal ischemia-reperfusion injury (*Liu et al., 2012*). However, due to its low spatial resolution, it lacks detailed information on cell localisation. Iron oxide particles are one of the most widely used MRI-based cell tracking agents for locating transplanted cells in kidney (*Bos et al., 2004, Hauger et al., 2006, Sun et al., 2008*). Although MRI can provide excellent spatial resolution, iron oxide particles produce negative contrast which make it difficult to quantify the number of cells in kidney. In addition, the presence of iron oxide particles will interfere with potential functional MRI assessments utilized for kidney diseases such as blood flow measurements (*Hueper et al., 2014*). Despite

many studies having explored the applicability of various fluorescent probes, such as near infrared dye for stem cell tracking in kidney (*Hu et al., 2013; Grange et al., 2014*), the utility of optical imaging is limited owing to light scattering which reduces the spatial resolution and penetration depth.

Compared to current imaging modalities, photoacoustic (PA) imaging is a relatively new but rapidly expanding non-invasive medical imaging field. It is a combined technology of ultrasound and optical imaging. The mechanism of PA is based on the detection of light absorption in ultrasound (acoustic) wave form generated by laser excited chromophores within tissue, for example, haemoglobin. Since acoustic waves are not scattered as much as light photons, the advantages of PA are deeper tissue penetration and better spatial resolution than optical imaging. PA imaging has been used in the detection of skin melanoma (*Oh et al., 2006*) and in investigating tumour angiogenesis (*Siphanto et al., 2005*) but applications in cell tracking is still in its infancy. A previous study has demonstrated the great potential of PA as a cell tracking tool by using a tyrosinase-based genetic reporter (*Jathoul et al., 2015*). However, the production of melanin from this reporter gene is believed to be cytotoxic and not suitable for cell tracking (*Urabe et al., 1994*). Therefore, to use PA imaging in tracking cell therapies, the contrast agents need to have minimal cytotoxicity with little interference in the cell's biological functions.

Since gold is known to be non-cytotoxic and inert in biological environment, gold nanoparticles have been extensively used *in vitro* cell imaging. Gold nanoparticles are also promising PA contrast agents due to their unique optical properties which allow optical absorption in the near infrared window where background tissue absorbance is minimal. In addition, the sensitivity of PA imaging can be improved by modifying the shapes of gold nanoparticles such as gold nanorods (GNRs) because of their tunable optical wavelength which results from surface plasmon resonance (*Li et al., 2015*). Moreover, unlike iron oxide nanoparticles, GNRs do not impede any functional assessment of the target organ by MRI. For these reasons, gold nanorods (GNRs) have been successfully applied as stem cell tracking agents for PA imaging (*Comenge et al., 2016*). As many studies have showed the advantages of PA imaging in detecting kidney disease such as ischemic kidney damage (*Berndel et al., 2018*), early kidney injury (*Pan et al., 2018*), Adriamycin-induced nephropathy (*Scarfe et al., 2015*) and polycystic kidney diseases (*Ogunlade et al., 2018*), tracking GNRs labelled MSCs in kidney with PA imaging will be able to provide accurate cell localisation which corresponds to structural and functional status of the kidney.

6.2.3 Experimental approach

A dual imaging (BLI and PA) approach was applied in this study by labelling luciferase expressing ADSCs with GNRs and the cell viability and localisation of these cells within the kidney were identified after renal artery injection. Since ultrasound imaging has been widely used in the clinic and preclinical studies to perform image-guided injections, a novel less invasive ultrasound-guided renal artery injection was developed to improve stem cell delivery to the kidney without the need for open abdominal surgery. In this study, silica coated GNRs (a kind gift from Dr Joan Comenge, University of Liverpool) were used to label ADSCs. Since the application of PA imaging using the same formulations of GNRs has already been published in *Comenge et al., 2016*, the detail synthesis and characterisation of GNRs and the unique properties of silica coating in PA imaging are not covered in this thesis.

6.2.4 Research objectives

1. Determine the effect of GNR labelling on ADSC proliferation and differentiation potential.
2. Develop a less invasive ultrasound-guided renal artery injection protocol.
3. Evaluate the efficiency of renal artery injection using ^{111}In -DOTA-SPIONs particles.
4. Track GNR labelled ADSCs in kidney using BLI and PA after renal artery injection.
5. Validate *in vivo* imaging results using immunohistochemistry.

6.3 Material

6.3.1 Gold nanorods (GNRs)

All experiments were performed using silica coated GNRs which were kindly provided by Dr Joan Comenge, Institute of Integrative Biology, University of Liverpool. Detailed synthesis and characterisation of these GNRs were published in *Comenge et al., 2016*. TEM measurement of the core size of GNRs used in this chapter was 21 ± 3 nm in width and 49 ± 5 nm in length with silica shell thickness of 34 ± 2 nm (Figure 6.1a). The GNRs were suspended in ethanol and ultraviolet-visible spectroscopy (Shimadzu SpectraMax Plus 384, Molecular Devices, California, USA) measurements were performed which showed the absorption peak at 756 nm with the optical density of 0.74 (Figure 6.1b). Therefore, the optical absorption spectrum of GNR is in the near infra-red window where the absorption of haemoglobin is minimal (Figure 6.1c).

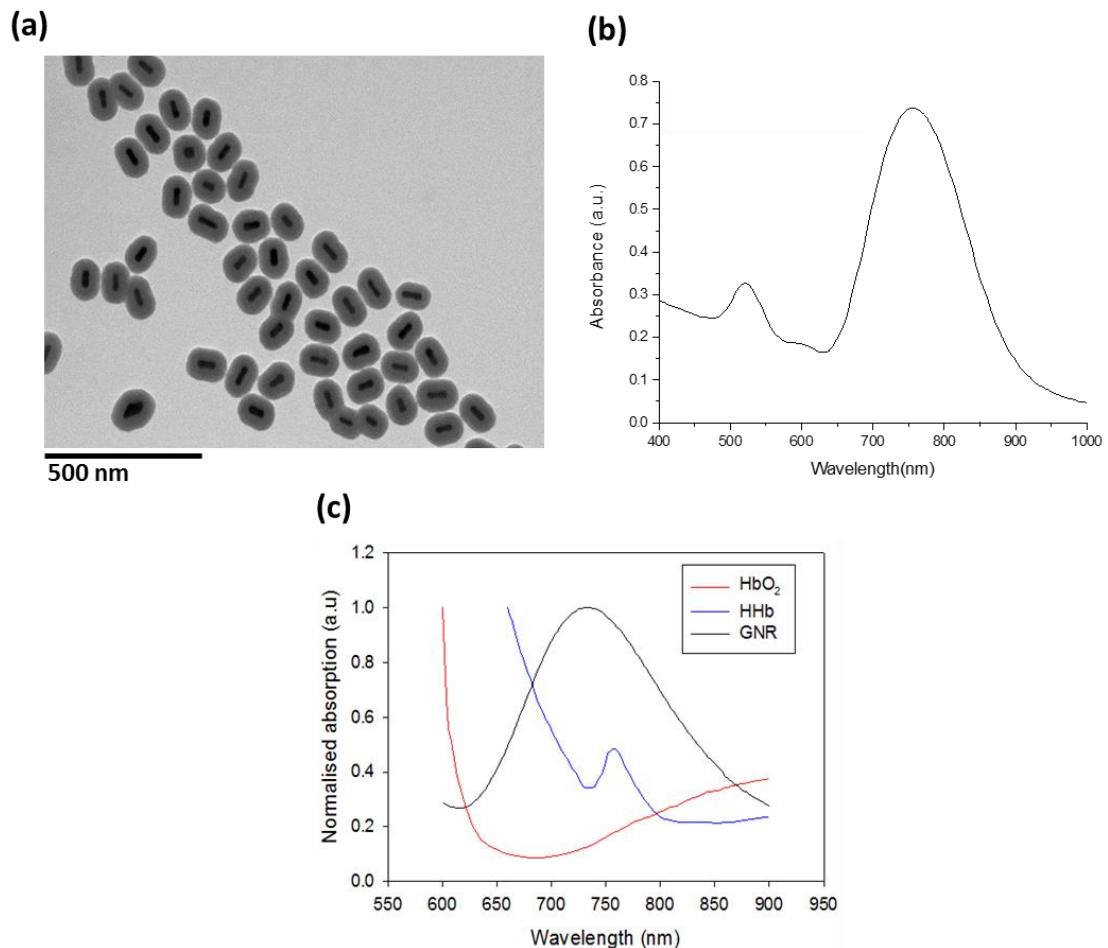


Figure 6.1 Characterisation of GNRs. (a) TEM images of GNRs coated with 34 nm silica shell (scale bar = 500 nm). (b) Ultraviolet-visible spectrum of silica coated GNRs in ethanol. (c) Optical absorption spectrum of GNRs and haemoglobin showing the absorption band of GNR is in the near infra-red window where the absorption of oxyhaemoglobin (HbO₂) and deoxyhaemoglobin (HHb) is minimal.

6.4 Methods

6.4.1 Cell culture

All experiments were performed using luciferase expressing human adipose derived mesenchymal stem cells (ADSCs) as previously described in Chapter 2.2.

6.4.2 ADSC labelling with GNRs

3×10^5 ADSCs were seeded in a T25 flask with 5 ml of DMEM-F12 supplemented with 10 % FCS and left to attach overnight. The next day, the cells were incubated with GNRs at a concentration of 0.04235 mgAu/ml (80% medium + 20% GNRs in water) for 24 hours. After washing 3 times with PBS, the labelled ADSCs were trypsinised, centrifuged for pelleting at 300 g, counted and then plated for *in vitro* studies or re-suspended in 0.6% alginate solution for *in vivo* cell injection.

6.4.3 Internalisation of GNRs by ADSCs

Silver enhancement staining

To visualise intracellular GNR uptake by ADSCs, silver enhancement staining was performed according to manufacturer's instructions (silver enhancer kit, Sigma-Aldrich, St Louis, USA). GNR labelled ADSCs were plated in 24-well plates at a concentration of 0.22×10^5 per well in triplicates and left to attach overnight. Next, the well plates were washed 3 times with PBS and the cells were fixed in 4% PFA for 30 minutes at room temperature. The cells were then washed 2 times with PBS followed by staining with silver enhancer mixture for 10 minutes at 20 °C. Then, the cells were washed 2 times with distilled water and fixed with 2.5% sodium thiosulfate solution for 3 minutes. Fixative was removed by washing 3 times with distilled water and the cells were counterstained with 1% Nuclear Fast Red and then imaged with EVOS FL Auto cell imaging system.

6.4.4 The effect of GNR labelling on cell proliferation

***In vitro* luciferase assay**

For luciferase-based cell proliferation assay, control ADSCs and GNR labelled ADSCs were plated in 96-well plates at a concentration of 5×10^3 per well in triplicates. *In vitro* luciferase assay was performed using a Varioskan LUX multimode microplate reader at days 1, 2, 3, 6 and 9 after plating. The measurements were acquired immediately after adding 300 µg/ml of D-luciferin and the results were presented as luminescence.

6.4.5 The effect of GNR labelling on differentiation potential

Differentiation assay

To determine the effect of GNR labelling on the differentiation potential of ADSCs, the differentiation assay was performed as previously described in Chapter 2.2.3.

6.4.6 *In vivo* studies

All animal procedures were performed as described in Chapter 2.4. All *in vivo* experiments were performed using 6-8 week old female CD-1 nude mice (Charles River Laboratories, UK) in order to avoid the whole body shaving required for PA imaging.

6.4.7 *In vivo* cell and particle injections

For preliminary evaluation of ultrasound-guided renal artery injection, ^{111}In -DOTA-SPION particles only (labelling steps were described in Chapter 3.3.2) at a concentration of ~ 1.5 MBq of ^{111}In and ~ 157 μg of Fe were injected into the right renal artery of mice ($n = 2$) as mentioned above. The mice were imaged serially with SPECT/CT and MRI for 8 days (Figure 6.2a).

For assessments of stem cell delivery to kidney, 2×10^5 GNR labelled ADSCs were re-suspended in 100 μl of 0.6 % alginate solution and injected into the right renal artery of mice ($n = 3$) with ultrasound guidance (VEVO 2100) under anaesthesia and imaged serially with BLI and PA for 7 days (Figure 6.2b).

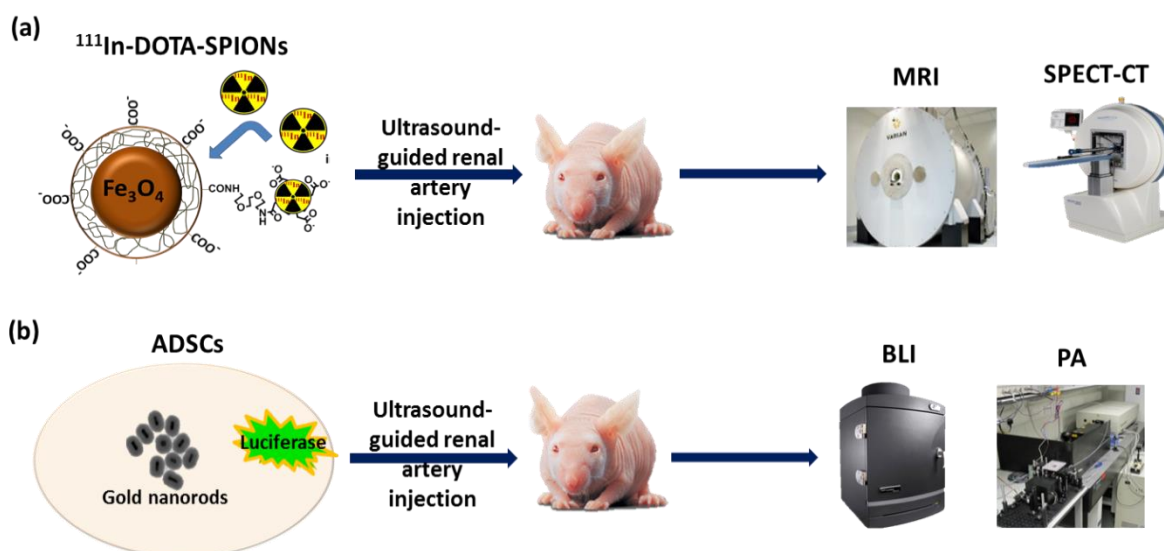


Figure 6.2 Schematic outlines of multi-modal imaging of stem cell delivery to kidney following ultrasound-guided renal artery injection.

6.4.8 *In vivo* imaging

BLI

In vivo BLI was performed at 1 hour, days 1, 3 and 7 after renal artery injection using the same procedures as previously described in Chapter 2.4.2.

PA imaging

PA imaging was conducted by Dr Olumide Ogunlade, Department of Medical Physics and Biomedical Engineering, UCL.

Directly after BLI imaging, mice were anaesthetised and PA scans were acquired at 3-5 hour after injection (termed day 0), and then at days 3 and 7 using a planar PA scanner (built in the Department of Medical Physics and Biomedical Engineering, UCL) based on a Fabry-Pérot (FP) polymer film ultrasound sensor and a tunable oscillator laser system (Quanta Ray Pro-270/premiScan; Newport Spectra Physics/GWU Lasertechnik). The PA images of right and left kidneys were acquired as previously described in *Ogunlade et al., 2018*. In brief, the animals were placed in a supine position and a small amount of ultrasound gel was applied to the lower back of the animals. Laser light pulses were excited onto tissue at 7 ns with a pulse repetition frequency of 50 Hz. Photoacoustic signals were produced and detected by the FP ultrasound sensor using a wavelength between 600-900 nm. An integrated heater and thermal chamber with temperature set to 34 °C was used during the imaging to maintain core body temperature. The images were displayed as MIPs and 3D volume-rendered images. False colouring, manual segmentation and extracting of the vasculature architecture was performed using Amira (FEI Visualization Sciences).

SPECT/CT

Mice were anaesthetised and whole body SPECT/CT scans were acquired at 1 hour, days 1, 3 and 8 after renal artery injection using the same procedures as previously described in Chapter 2.4.3. 3D ROIs were created for brain, lungs, liver, right kidney and left kidney and calculated as %ID/mm³ after correcting for ¹¹¹In decay.

MRI

MRI studies were performed at 5 hours, day 1 and 7 after renal artery injection using a 1T ICON scanner (Bruker, Germany). T₂^{*}-weighted kidney images were acquired using the same parameters as previously described in Chapter 2.4.4.

6.4.9 *Ex vivo* BLI imaging

Ex vivo BLI was performed at 1 hour and day 8 after renal artery injection using the same procedures as previously described in Chapter 2.5.

6.4.10 Histology and immunohistochemistry (IHC)

At day 8 after renal artery injection, right and left kidneys were harvested and histological validation was performed as previously described in Chapter 2.6. Vimentin (ADSCs) and silver enhancement staining (GMR) were performed on 5 µm kidney tissue sections to demonstrate the presence of GMR labelled ADSCs in the kidney. Vimentin staining was conducted as described in Chapter 2.6 using Ventana Red detection kit and silver enhancement staining was performed according to manufacturer's instructions.

6.4.11 Statistical analysis

All *in vitro* experiments were repeated at least 3 times with 3 triplicates.

Statistical analysis was performed with GraphPad Prism version 6.01. Data were presented as mean ± standard deviation (SD).

6.5 Results

6.5.1 Intracellular uptake of GNRs and their effect on cell proliferation and differentiation potential

Internalisation of GNRs by ADSCs was visualised under light microscope using silver enhancement staining which showed the presence of dark aggregates inside the cytoplasm of ADSCs compared to control (Figure 6.3a & b). The effect on cell proliferation of ADSCs after GNR labelling was studied by measuring bioluminescence emission as a surrogate measurement of cell proliferation. The signal intensity of both control and GNR labelled groups showed an increase from day 1 to day 3 after plating and then remained stable throughout the study (Figure 6.3c). The effect on tri-lineage (adipogenic, chondrogenic and osteogenic) differentiation potential of ADSCs after GNR labelling was assessed by performing the differentiation assay (Figure 6.4). The results showed both the control and GNR labelled cells could differentiate towards tri-lineages in a similar rate. All these results indicated that GNR labelling has no adverse effect on cell proliferation and differentiation potential of ADSCs.

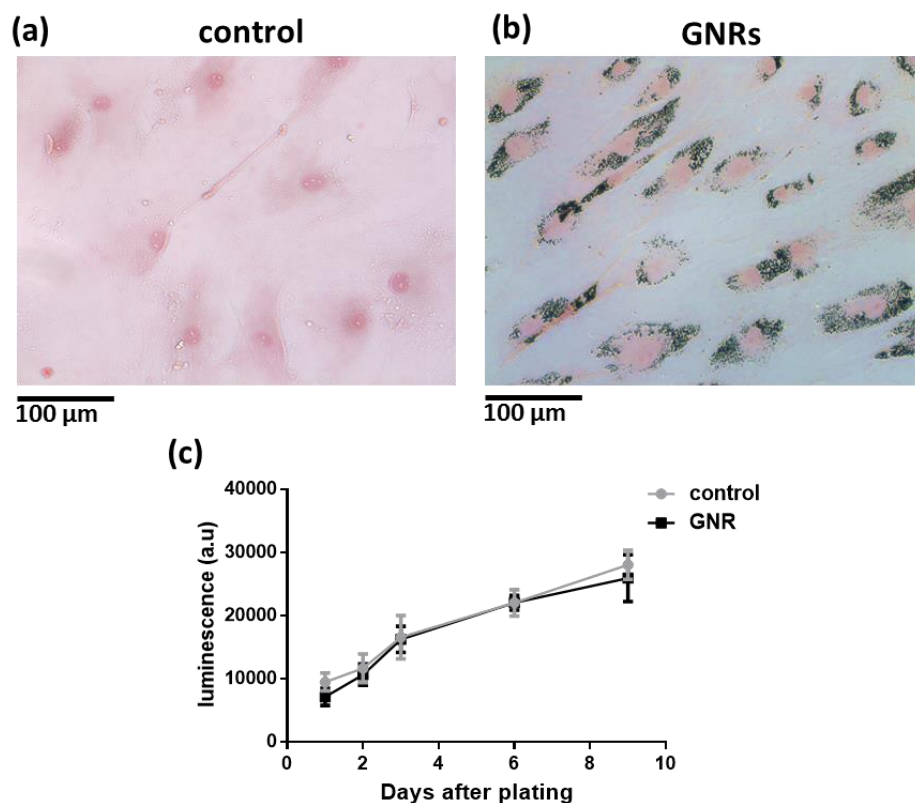


Figure 6.3 Intracellular uptakes of GNRs in ADSCs and the effect on cell proliferation. (a & b) Sliver enhancement staining of ADSCs treated with GNRs showing the dark aggregates inside the cytoplasm compared to untreated control (scale bar = 100 μm). (c) Luciferase-based cell proliferation assay at different time points showing no significant difference between luminescence signals of control and GNR labelled ADSCs (data are shown as mean ± SD, n = 3).

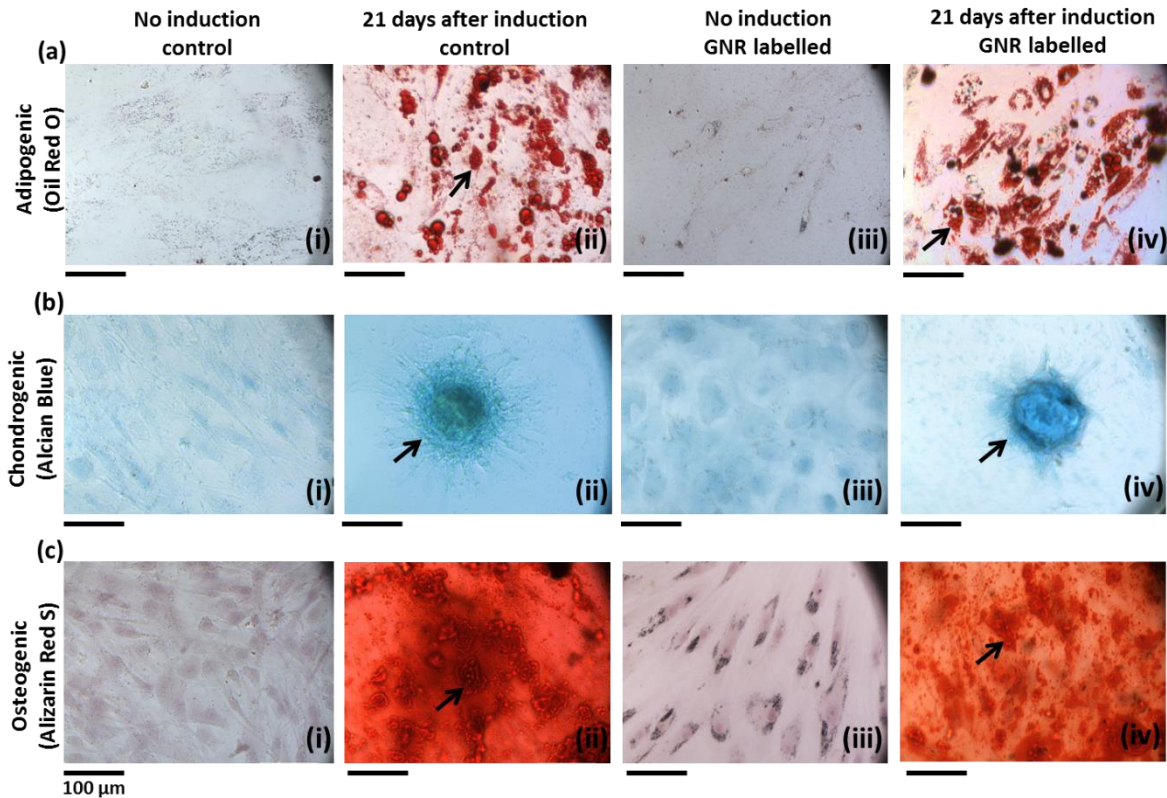


Figure 6.4 Tri-lineage differentiation of control ADSCs and GNR labelled ADSCs. (a) Oil red o staining for adipogenic differentiation which displays the red coloured oil droplets (indicated by arrows in (ii & iv)). (b) Alcian blue staining for chondrogenic differentiation which displays the blue coloured proteoglycans (indicated by arrows in (ii & iv)). (c) Alizarin red s staining for osteogenic differentiation which displays the red coloured calcium deposits (indicated by arrows in (ii & iv)). Scale bar = 100 µm.

6.5.2 Stem cell delivery to kidney via ultrasound-guided renal artery injection

Ultrasound-guided renal artery injection was performed using 6-8 week old female nude mice. Under anaesthesia, mice were positioned in left lateral position on the ultrasound platform and the limbs were secured with tape. The injection mount with syringe holder was positioned towards the paravertebral muscle of the animal (Figure 6.5a). Ultrasound gel was applied to the right lower quadrant of the abdomen and the right kidney was located by using the liver as a reference. A colour Doppler image was acquired to visualise the blood vessels of the right kidney (Figure 6.5b). In order to identify the arterial and venous flow velocity waveforms of the kidney blood vessels, the pulsed wave Doppler sample gate was placed within the vessels at the appropriate angle relative to flow direction (Figure 6.5c & d). ^{111}In -DOTA-SPION particles only or 2×10^5 GNR labelled ADSCs were suspended in 100 µl of 0.6% alginate solution and injected slowly into the renal artery using a 1 ml syringe with a 29 g needle. In order to avoid other organs damage, the needle was penetrated into the renal artery by passing through paravertebral muscle (Figure 6.5e). Successful injection was

visualised by the presence of hyperechogenic contrast from the alginate solution around the renal cortex (Figure 6.5f). The needle was slowly withdrawn from the body and the colour Doppler image was acquired to assess the blood flow to the kidney. The heart rate, body temperature and respiration rate were monitored during the injection and imaging of the kidney which took approximately 15 minutes. The animals were then recovered from anaesthesia and no significant weight loss or sign of major trauma was observed as monitored by body weight and colour of the urine throughout the study.

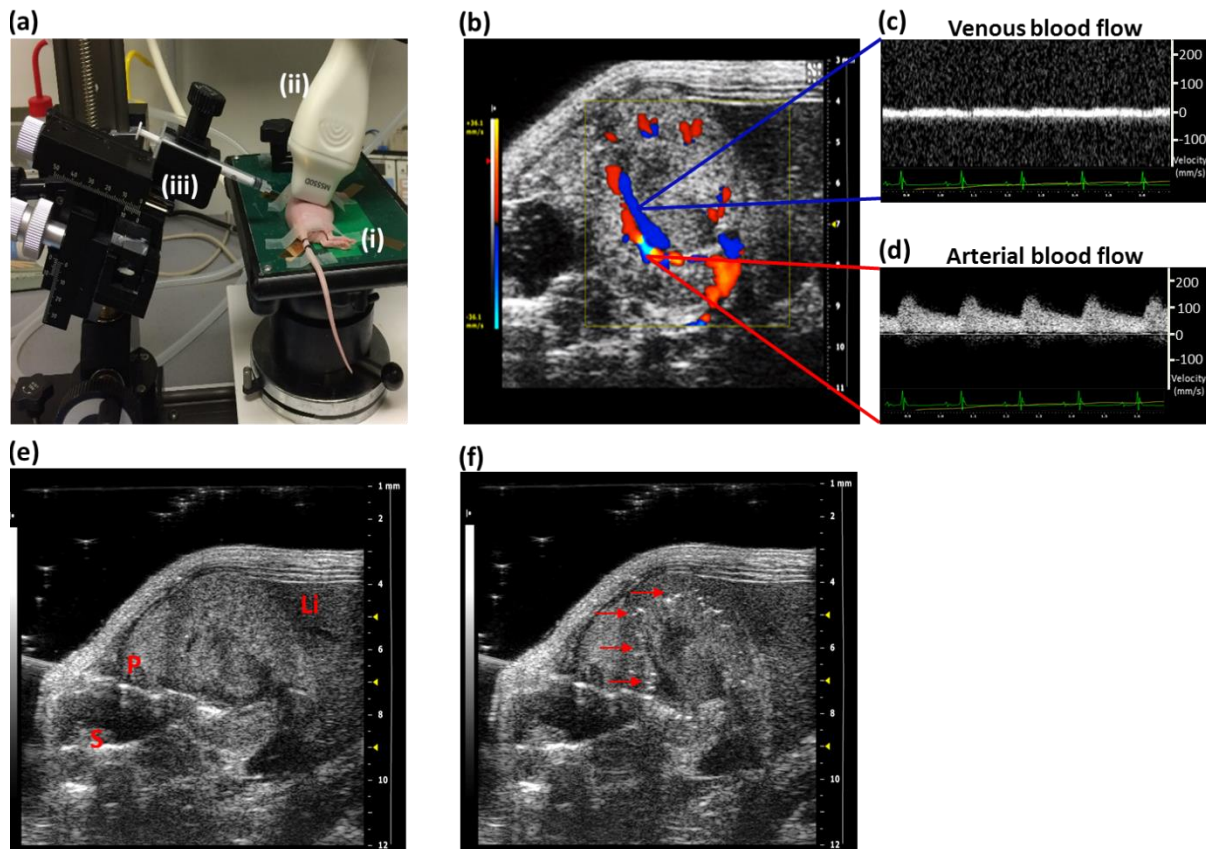


Figure 6.5 Less invasive ultrasound-guided renal artery injection. (a) The animal was positioned in left lateral position on the platform (i) with the ultrasound transducer (ii) on the right lower quadrant of the abdomen and the syringe in injection mount (iii) facing towards the paravertebral muscle of the animal. (b) Colour Doppler image of the kidney showing renal blood supply (c & d) Pulsed wave Doppler images identifying the venous and arterial flow velocity pattern. (e) The needle was pierced through the skin and the vertebral muscle of the animal to penetrate into the right renal artery (labels: P = paravertebral muscle, S = spine, Li = liver). (f) The successful injection was visualised by the presence of hyperechogenic contrast around renal cortex (indicated by arrows).

6.5.3 Quantitative assessment of ultrasound-guided renal artery injection using ^{111}In -DOTA-SPION particles

To exploit the strength of SPECT imaging in quantitative measurement, the preliminary evaluation of ultrasound-guided renal artery injection was performed by injecting ^{111}In -DOTA-SPION particles only into the right renal artery of mice as mentioned above and imaged with SPECT/CT and MRI serially for 7 days.

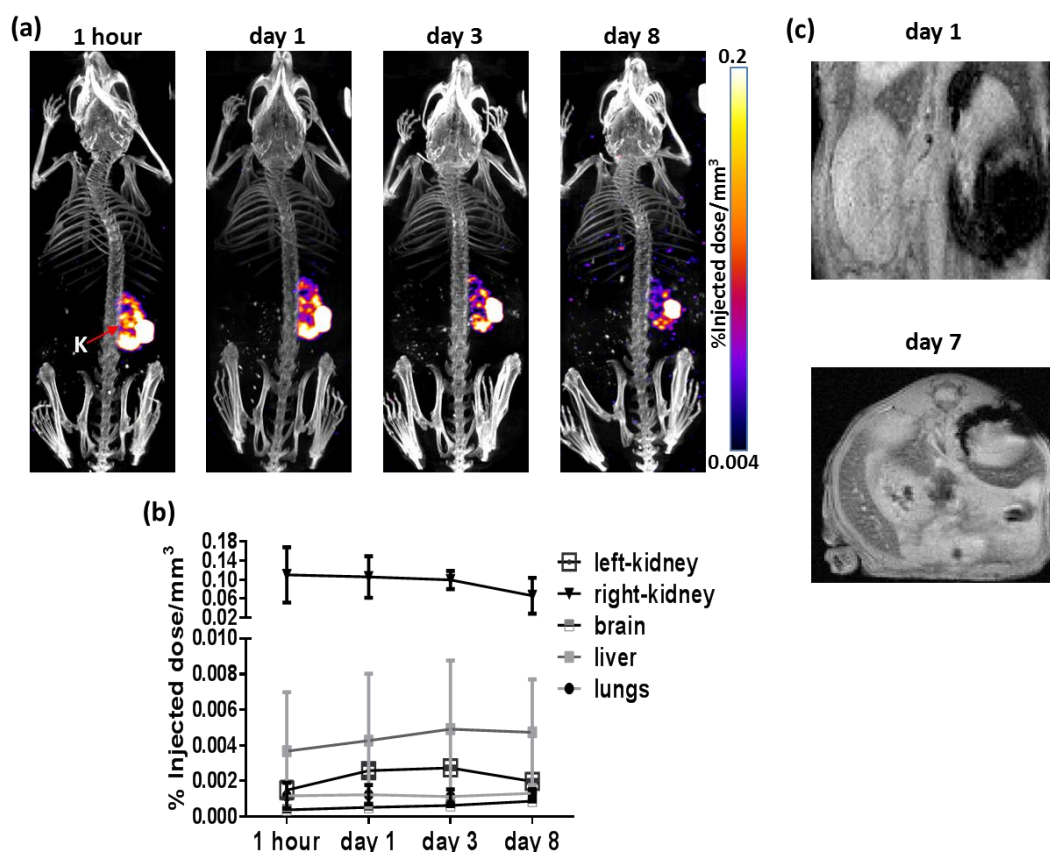


Figure 6.6 Quantitative assessment of ultrasound-guided right renal artery injection at different time points. (a) Decay corrected SPECT/CT images showing the retention of ^{111}In -DOTA-SPION particles in the right kidney for 8 days after injection (Label: K = kidney). (b) 3D ROI quantification of SPECT signal in lungs, liver, brain, right and left kidney at 1 hour, days 1, 3 and 8 after injection calculated as %ID/mm³ after decay correction (data are shown as mean \pm SD, n = 2). (c) T₂*-weighted MR images of both kidneys at day 1 and 7 after injection showing a large area of signal hypointensity in the right kidney compared to left kidney.

At 1 hour after injection, SPECT/CT images showed the majority of radioactivity was widely distributed throughout the right kidney and remained stable for 8 days (Figure 6.6a). The average amount of radioactivity (%ID/mm³ from 3D ROI) in the right kidney was 25-fold

higher than the liver, 50-fold higher than the left kidney, 100-fold higher than the lungs and 167-fold higher than the brain during the course of the study (Figure 6.6b).

In T_2^* -weighted MR image of the kidney at 5 hours after injection, a widespread reduction of MR signal intensity was seen in the right kidney compared to the left kidney (Figure 6.6c). Although the precise localization of ^{111}In -DOTA-SPIONs inside the kidney was undetectable due to susceptibility artifact, the persistence of MR signal was observed for 7 days. Nonetheless, the results from SPECT/CT and MRI demonstrate the success of the ultrasound guided-renal artery injection that can be utilized for subsequent cell injections.

6.5.4 Assessment of the cell viability and cell localisation following renal artery injection

To assess the viability and localisation of GNR labelled ADSCs in kidney, the animals were imaged with BLI and photoacoustic imaging serially for 7 days after ultrasound-guided right renal artery injection. *Ex vivo* BLI was performed at 1 hour and day 8 after injection to validate *in vivo* results.

At 1 hour after injection, BLI images showed the majority of BLI signal was coming from the right kidney (Figure 6.7a, supported by *ex vivo* BLI, Figure 6.7c) with some signal from the lungs. Immediately after BLI, PA images of both kidneys were acquired at 3-5 hours after injection (termed day 0) using a range of wavelength from 600 to 900 nm (Figure 6.7d & e). PA images appeared to show a stronger PA signal within the right kidney compared to the left kidney. Images acquired at 730 nm showed the highest PA contrast in the right kidney than the surrounding renal blood vessels (Figure 6.7d) consistent with the absorption peak of the GNRs (750 nm) which indicated the presence of GNR labelled cells within the right kidney. In addition, the labelled cells were detected throughout the right kidney including cortex and medulla in 3D volume rendered PA images (Figure 6.7e).

BLI images at days 1 and 3 after injection showed the persistence of the signal within the right kidney (Figure 6.7a). Similarly, PA images showed the signal intensity remained stable for 3 days (Figure 6.7f). At day 7 after injection, although BLI images showed very low signal within the right kidney (Figure 6.6a supported by *ex vivo* BLI at day 8, Figure 6.7c), high signal intensity was still detectable in PA images (Figure 6.7g). Observation across the rest of the body showed the BLI signal intensity from the lungs and the whole body decreased over time (Figure 6.7b) and no sign of cell migration to other organs was seen.

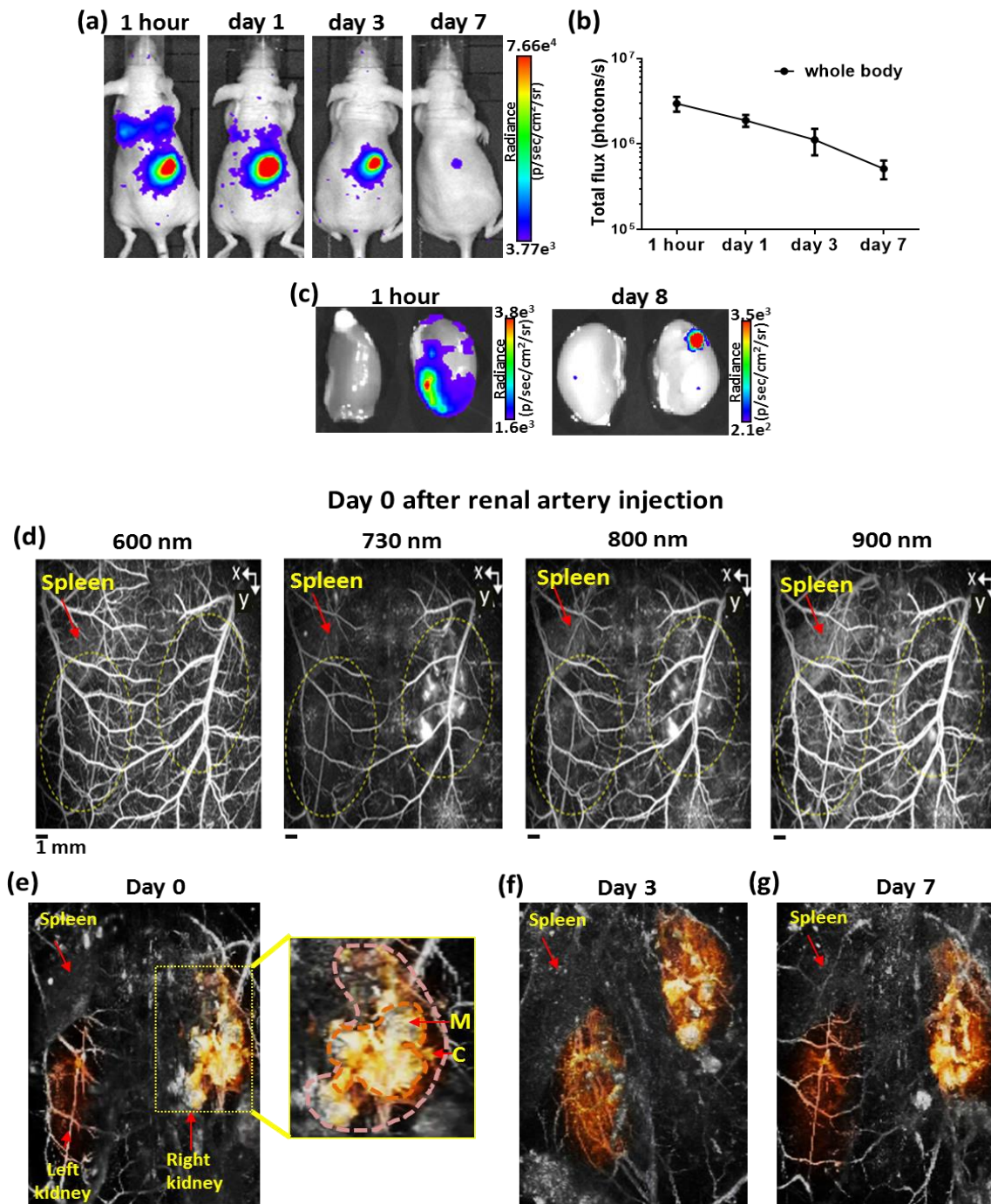


Figure 6.7 BLI and PA images of GNR labelled ADSCs in right kidney at different time points after right renal artery injection. (a) BLI images at 1 hour, days 1, 3 and 7 after injection showing the majority of signal within the right kidney and some signal from the lungs. (b) BLI signal from the whole body decreased over time (photons/s in log scale, data are shown as mean \pm SD, $n = 3$). (c) *Ex vivo* BLI images of both kidneys at 1 hour and day 8 after injection showing BLI signal from the right kidney. (d) PA images acquired at different wavelengths showing the higher PA contrast in right kidney (indicated by yellow dotted lines) than the surrounding renal blood vessels at 730 nm using the spleen as anatomical landmark (images are presented as MIP). (e-g) 3D volume-rendered PA images at days 0, 3 and 7 after injection showing the widespread PA contrast in right kidney including cortex (C) and medulla (M), compared to left kidney (the kidneys are manually segment and false coloured).

6.5.5 Histological analysis

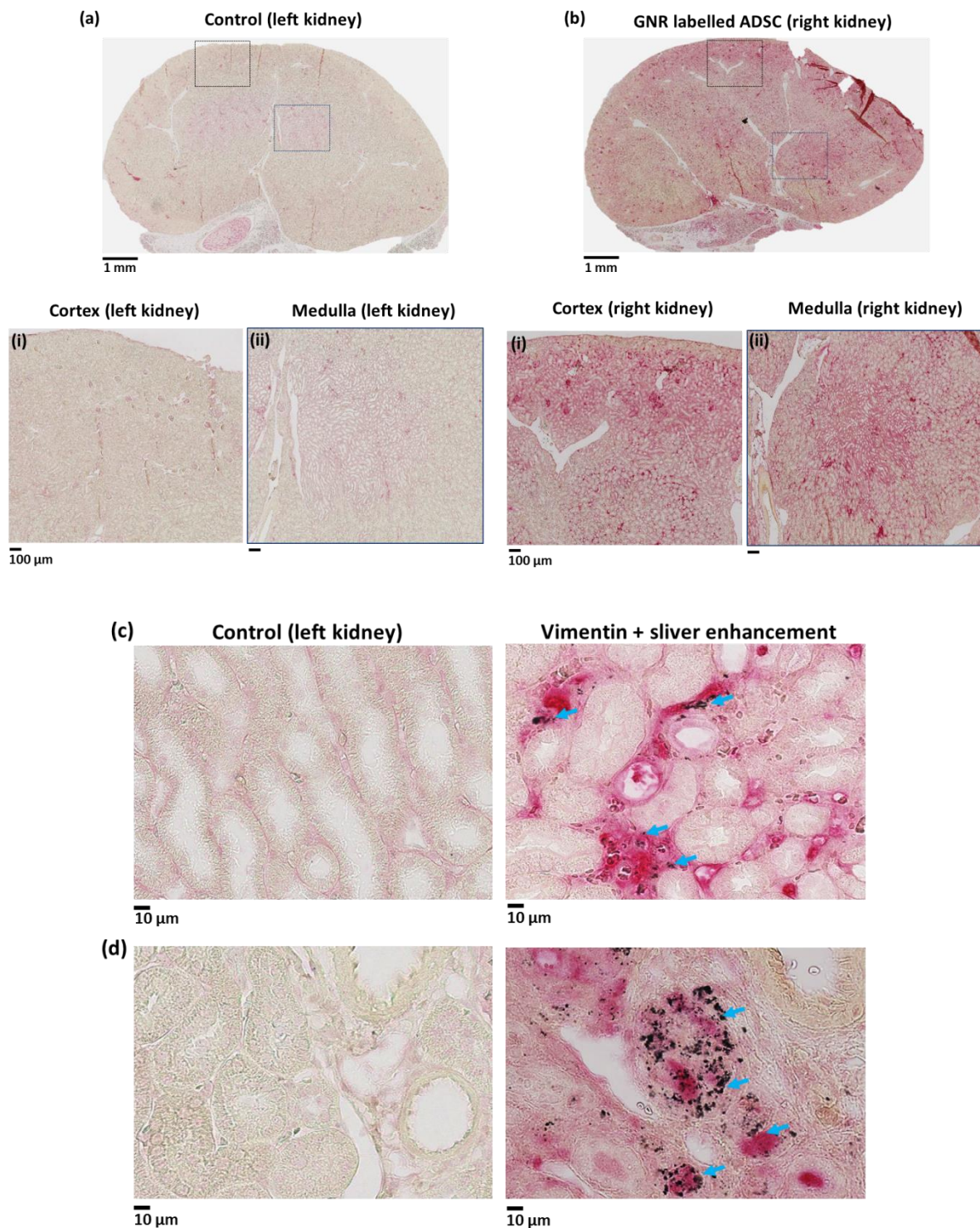


Figure 6.8 Histological analysis of GNR labelled ADSCs uptake in kidney at day 8 after right renal artery injection. (a & b) Vimentin (ADSC) staining of control (left kidney) and injected right kidney sections showing the widespread red staining in the cortex and medulla of right kidney compared to the control. Positive vimentin (ADSC) and silver enhancement staining of right kidney tissue sections showing the presence of dual labelled cells within the renal (c) capillary bed and (d) parenchyma compared to control (indicated by arrows, scale bar = 10 μm).

In order to validate the presence of GNR labelled ADSCs in the right kidney after renal artery injection, the kidney sections from day 8 after injection were stained with vimentin (ADSCs) and silver enhancement (GNRs) using the left kidney as control tissue sections (Figure 6.8a). Histological images showed widespread vimentin staining throughout the right kidney including cortex and medulla confirming the presence of ADSCs in the right kidney (Figure 6.8b). Higher magnification images showed the areas positive for vimentin staining were also positive for silver enhancement staining (Figure 6.8 c & d), confirming the retention of GNRs within ADSCs. In addition, the dual labelled cells were detected within the renal capillary bed (Figure 6.9c) and renal parenchyma (Figure 6.9d) compared to the left kidney tissue section. Observation across the whole right kidney sections showed no signs of malignant tumour formation or area of injury was observed.

6.6 Discussion

The aims of this chapter were to improve ADSCs delivery to kidney by developing a less invasive ultrasound-guided renal artery injection and to assess the viability and localisation of GNR labelled ADSCs after injection using BLI and PA.

The intracellular uptake of GNRs was first studied and the results showed GNRs were internalised inside the cytoplasm. These results were consistent with TEM findings previously published by *Comenge et al., 2016* showing the entrapment of the same formulation of GNRs in the cytoplasmic organelles. The results from *in vitro* luciferase assays and differentiation assays demonstrated that GNRs labelling had no effect on ADSC proliferation and tri-lineage differentiation potential indicating that GNRs have no cytotoxic effect on ADSCs which is also consistent with the findings from *Comenge et al., 2016*.

¹¹¹In-DOTA-SPION particles were used to evaluate and quantify the success of the ultrasound guided renal injection prior to cell injection. SPECT/CT showed the highest radioactivity distribution was in the injected right kidney and that this uptake remained stable for 7 days. Consistent with SPECT findings, a widespread MR signal reduction was seen in the right kidney but the localisation of the SPIONs relating to the anatomical structure of the kidney was unable to be visualised owing to the susceptibility effect of iron oxide obscuring the renal architecture. Although both SPECT and MRI results suggest that the ultrasound-guided renal artery injection is an efficient targeted delivery route for kidney, studies with more animal numbers are required to assess the reproducibility of the injection.

Ultrasound-guided renal artery injection of GNR labelled cells demonstrated that this method is feasible, fast and less invasive than the routine renal artery injection using open abdomen surgical techniques. The main strength of the ultrasound-guided technique is a faster recovery and healing time with fewer complications such as infections in immunocompromised mice. In addition, the high temporal resolution of ultrasound allows for the optimisation of the injection techniques. During initial studies, the spillage of cells into the abdominal cavity was observed when the cells were re-suspended in PBS (results not shown). Since the alginate solution is known to be viscous (*Lee et al., 2012*) and commonly used in ultrasound contrast agents (*Wheatley et al., 1990*), the re-suspension medium was changed to 0.6% alginate solution to prevent spillage and to improve the accuracy of the injection by taking advantage of the ultrasound contrast provided by alginate.

The distribution of GNR labelled cells in the kidney after injection was assessed by using BLI and PA imaging. At 1 hour after injection, although the majority of the signal was detected in the injected right kidney, there was some signal from the lungs in BLI images. This may be due to leakage of cells into the renal vein which is situated alongside the renal artery during

the injection. Therefore, it is likely that the cells are transported to the lungs via venous drainage from the right ventricle as the blood from the renal vein drains into the inferior vena cava and then into the right atrium. Interestingly, BLI signal from the lungs decreased from day 1 after injection and was not detectable at day 7. However, in chapter 4, the persistence of BLI signal within the lungs after IV injection was observed for 7 days. This is likely due to differences in the number of cells entrapped in the lung capillaries (small percentage rather than the majority of cells).

More importantly, both BLI and PA images at the early time points suggested that the majority of the GNR labelled cells were retained in the right kidney for 3 days and the ultrasound-guided renal artery injection was successful. In addition, the widespread cell distribution across the kidney, including the cortex and medulla was detected in PA images and further confirmed by histological analysis. These results highlight the advantages of using PA imaging which can provide the high spatial resolution of cell localisation in the kidney.

Although consistent findings were seen between BLI and PA images at early time points, discrepancies were observed at day 7 after injection. This is likely due to differences in cell labelling methods. Since BLI is a reporter gene-based cell tracking method that requires ATP, the signal generation depends on cell survival, while in PA imaging, the presence of signal only represents the existence of the direct labelling agent, GNR, not the cell itself. These results also suggest that only a small number of cells remain viable 7 days after injection and that the majority of dead cells are retained within the kidney. These findings were further validated by histological images acquired at day 8 after injection which raises safety concerns regarding MSC-based therapies for kidney diseases. In addition, the maldifferentiation of MSC into glomerular adipocytes and sclerosis after renal artery injection have been reported in a rat model of renal failure (*Kunter et al., 2007*). Therefore, more studies are required to investigate the long term fate of MSCs in recipient's organ after transplantation.

6.7 Conclusion

In summary, the results presented in this chapter demonstrated that the successful development of a less invasive ultrasound-guided renal artery injection which can improve stem cell delivery to the kidney. The findings from this study displayed the benefits of combining a reporter gene (luciferase, BLI) with a direct cell labelling method (GMR, PA) which can provide both cell viability and cell localisation in the target organ. The new techniques which have been developed in this study can be applied to track other stem cell types such as kidney derived stem or progenitor cells. In addition, the information acquired from this study will be useful for optimising cell therapies in various rodent models of kidney diseases such as acute kidney injury.

Chapter 7

Developing gold nanoparticles as a stem cell tracking agent for computed tomography

7.1 Abstract

Owing to new developments in biomedical imaging techniques, the role of non-invasive *in vivo* imaging become important in improving stem cell therapy. Imaging techniques are not only useful in determining the success or failure of cell delivery to target organ but also they can provide information on cell fate after delivery. At present, iron oxide labelled cells for MRI, or direct radiotracer labelling for nuclear imaging has been used to detect cell delivery. However, the difficulty in quantifying the negative MRI contrast, the short half-life of radiotracer and cytotoxic effect on cells are strong disadvantages. Computed tomography (CT) imaging is widely available and most frequently used in the clinic but studies into stem cell tracking are still lagging.

The work presented in this chapter aimed to investigate the use of commercially available gold nanoparticles (GNP) as an *in vivo* stem cell tracking agent for CT. Luciferase expressing human adipocyte derived mesenchymal stem cells (ADSCs) were labelled with GNPs and transplanted either subcutaneously or intratracheally delivered into the lungs and imaged with BLI and CT at different time points. In addition, the dual labelled (GNP and ⁸⁹Zr-oxine) ADSCs were injected into kidney via ultrasound-guided renal artery injection to explore their potential application as multi-modal stem cell imaging agents using BLI and PET/CT scanner.

The results showed GNP labelled cells were able to detect *in vivo* using CT and the labelled cells were viable and retained at the subcutaneous implantation site for up to 2 months which suggests that GNP labelling has no cytotoxic effect on the cells. CT lung images showed the presence of GNP labelled cells distributed throughout the lungs which demonstrate that GNPs can be used to track stem cells in lungs using CT. CT images after renal artery injection showed the dual labelled cells were at renal pelvis outside the kidney suggesting the unsuccessful renal artery injection and further supported by PET/CT co-localised images.

These findings demonstrate that GNPs are a promising cell tracking agent for CT imaging but further investigations are required to identify their practicality in different disease models.

7.2 Introduction

7.2.1 Gold nanoparticles as CT contrast agents

Among the current medical imaging modalities, CT imaging is one of the most widely used techniques in the clinic due to its high availability, efficiency and cost effectiveness. CT imaging is usually characterised as a high-resolution imaging technique which can provide 3D information of anatomical structures. It is commonly used for the routine screening of lung cancer due to significant inherent contrast between air filled lungs and surrounding soft tissue. However, the main limitation of CT is the difficulty in differentiating between soft tissues which have similar densities. To improve soft tissue and vascular contrast, exogenous CT contrast agents such as iodinated molecules have been used in clinic. Since CT contrast agents are notoriously well-known for their toxicity, present contrast agents are predominantly based on low-molecular weight iodinated formulations which display low toxicity (*Lusic et al., 2013*). However, iodinated molecules can only provide a short imaging window due to rapid clearance from the kidney.

Recent developments in nanoparticle research has changed the field of medical imaging due to the availability of next generation metal nanoparticles which exhibit many advantages over conventional contrast agents. Among them, gold nanoparticles (GNP) are the most attractive candidates for CT contrast agents. Due to the high atomic number of gold, GNPs can provide superior X-ray attenuation and better CT contrast than iodine. Moreover, GNPs can offer longitudinal imaging due to their prolonged blood circulation time. For these reasons, GNPs have been successfully applied to the characterisation of a mouse model of vascular malformation using CT (*Castillo et al., 2016*).

7.2.2 Gold nanoparticles as CT stem cell tracking agents

In contrast to other imaging modalities, CT is not an established imaging technique for cell tracking. Since gold is recognised as an inert metal with no toxic effect on cells, GNPs have been used to track MSCs in rat brain with CT for potential application in neuropsychiatric disorders (*Betzer et al., 2014*). Another study reported the successful tracking of tumour specific T-cells in a mouse model of human melanoma using GNPs (*Meir et al., 2015*). More importantly, due to their positive CT contrast, GNPs can provide more reliable signal quantification than the negative MRI contrast agent SPIONs. In addition, GNPs can be used as a targeted drug delivery system by functionalizing the surface coating with a number of molecules such as tumour targeting ligands (*Lee et al., 2014*) antibodies (*Jiang et al., 2008*) and anti-cancer drug (*Patra et al., 2008*). Therefore, further development in GNPs as a stem cell tracking agent for CT will be beneficial for optimizing MSC-based cell therapy. Moreover, acquiring CT contrast for cell localisation will be valuable for multi-modal imaging approach

as most nuclear scanner (PET/SPECT) are fused with CT component to obtain anatomical information.

7.2.3 Experimental approach

In this preliminary study, commercially available GNPs from BBI solution were used to label luciferase expressing ADSCs and their applicability as a stem cell tracking agent was assessed using multi-modal imaging (BLI, CT & PET/CT). *In vitro* and *in vivo* CT of GNP labelled cells were evaluated using the CT component of a Mediso nanoScan PET/CT scanner due to the unavailability of a standalone CT machine. Nevertheless, the efficiency of this CT component has been demonstrated using a GNP-based vascular CT contrast agent to detect vascular malformation (Figure 7.1, *Castillo et al., 2016*). The results from pilot studies showed high dose (8×10^5) of GNP labelled cells were unable to detect in lungs after intravenous injection probably due to low sensitivity of CT imaging. In order to improve the level of cell detection in lungs, intratracheal intubation was performed to deliver the labelled cells directly into the lungs. Since the characterisation of GNPs, their effect on cell viability and cell differentiation have already been published (*Klingberg et al., 2015, Mok et al., 2017*), these topics are not discussed in this thesis.



Figure 7.1 Assessment of the efficiency of CT components from PET/CT scanner. 3D rendered CT image of a mouse model of vascular malformation after GNP-based vascular contrast agent injection.

7.2.4 Research objectives

1. Determine the intracellular uptake of GNPs (BBI) by ADSCs and assess the *in vitro* CT contrast of labelled cells.
2. Investigate the application of GNP labelled ADSCs for long term *in vivo* stem cell tracking.
3. Investigate the application of GNP labelled ADSCs in lungs using BLI and CT after intratracheal intubation.
4. Track GNP labelled ADSCs in kidney using BLI, CT and PET/CT after renal artery injection.

7.3 Materials

All chemical materials were from Sigma-Aldrich (St Louis, USA), unless otherwise stated.

7.3.1 Gold nanoparticles

All experiments were performed using commercially available citrate coated spherical GNPs (BBI solution, Crumlin, UK) which have a mean diameter of 79.4 nm with $\leq 8\%$ coefficient of variation.

7.4 Methods

7.4.1 Cell culture

All experiments were performed using luciferase expressing human adipose derived mesenchymal stem cells (ADSCs) as previously described in Chapter 2.2.

7.4.2 Internalisation of GNPs by ADSCs

ADSC labelling with GNPs

ADSCs were grown in T25 flasks with 5 ml of DMEM-F12 supplemented with 10 % FCS and left to attach overnight. The next day cells were incubated with GNPs at a concentration of 0.04 mg/ml (80% medium + 20% GNRs in water) for 24 hours. After washing 3 times with PBS, labelled ADSCs were trypsinised, centrifuged for pelleting at 300 g, counted and then plated for *in vitro* studies or re-suspended in PBS for *in vivo* cell injection. Phase contrast microscopic images of control and GNP labelled ADSCs were acquired with EVOS FL Auto cell imaging system.

TEM

To study Intracellular uptake of GNPs by ADSCs, GNP labelled cells were seeded at 0.22×10^5 per well on coverslips in 24-well plates and TEM imaging was performed as described in Chapter 2.3.

7.4.3 *In vitro* CT imaging

To determine the CT contrast of GNP labelled ADSCs *in vitro*, the cells were seeded at 0.5×10^5 per well in 24-well plates and left to attach overnight. The next day, the cells were incubated with GNPs at concentration of either 0.04 mg/ml or 0.08 mg/ml or 0.2 mg/ml for 24 hours. After washing 3 times with PBS, the labelled ADSCs were trypsinised and pelleted. The cell pellets were transferred into clear Eppendorf tubes and CT images were acquired with nanoScan PET/CT scanner (Mediso, Budapest, Hungary) by using these acquisition parameters: 50 kVp, 300 ms exposure time, 720 projections, medium zoom and semicircular

scan. CT images were reconstructed in voxel size of 68 x 68 x 68 mm using Nucline software (Mediso version 2.01). The amount of CT signal was quantified as Hounsfield Units (HU) and 3D visualization were performed using VivoQuant software (InviCRO version 1.23patch3). Representative images were presented as maximum intensity projection (MIP) images.

7.4.4 ADSC labelling with Zirconium-89 (⁸⁹Zr)-oxine

20.17 MBq of ⁸⁹Zr in 1 M oxalic acid was diluted to 500 µl with HPLC grade water and neutralised using 5 µl aliquots of 1 M NaOH. Next, 5 µl of a 10 mg/ml solution of 8-hydroxyquinoline in chloroform was added and vortexed in a round-bottomed Pyrex tube for 5 minutes. 500 µl of chloroform was added followed by a brief centrifugation at 300 g and vortexing for 25 minutes. The chloroform phase containing the ⁸⁹Zr-oxine complex was extracted from below the water phase containing free ⁸⁹Zr, and evaporated at 80°C in a conical bottom HPLC vial, before resuspension in a 20 µl of dimethyl sulfoxide (DMSO).

3 x 10⁵ GNR labelled ADSCs were trypsinised, re-suspended µl and incubated with 5.9 MBq of ⁸⁹Zr-oxine (in 100 µl of PBS) at 37 °C for 30 minutes. Subsequently, the cells were pelleted and washed 3 times with PBS and the radioactivity of cell pellets was measured using an isotope calibrator.

7.4.5 *In vivo* studies

All animal procedures were performed as described in Chapter 2.4. All *in vivo* experiments were performed using 6-8 week old NSG mice (Charles River Laboratories, UK).

7.4.6 *In vivo* cells injection

To determine the applicability of GNPs as a long term *in vivo* cell tracking agent for CT, 2 x 10⁵ GNP labelled ADSCs (which contained ~0.23 mg of Au) in 50 µl of PBS was injected subcutaneously into the left flank of a mouse (n = 1) and imaged with BLI and CT serially for 2 months (Figure 7.2a).

To test the applicability of GNPs as a stem cell tracking agent in lungs, either 50 µl of PBS or 8 x 10⁵ GNP labelled ADSCs (which contained ~0.75 mg of Au) in the same volume of PBS was delivered directly to the lungs via non-invasive intratracheal intubation (n=1 for each) and imaged with BLI and CT at 1 day after intubation (Figure 7.2b).

To test the applicability of GNPs as a stem cell tracking agent in kidney, 3 x 10⁵ ADSCs were dual labelled with GNPs and ⁸⁹Zr-oxine (which contained ~0.45 mg of Au and ~0.5 MBq of ⁸⁹Zr) and injected into the right renal artery of a mouse (n =1) using ultrasound

guidance as described previously in Chapter 6.4.2. Then the animal was imaged with BLI and PET/CT at 3 hours after injection (Figure 7.2c).

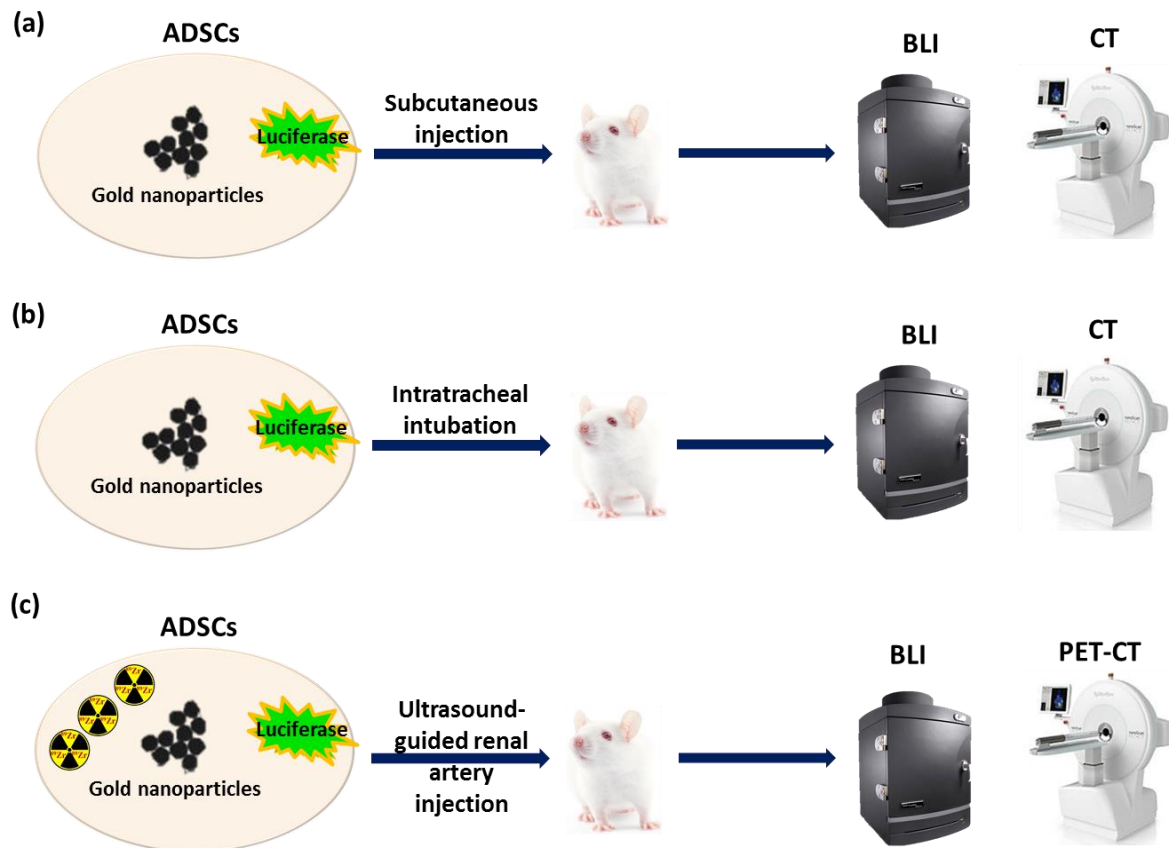


Figure 7.2 Schematic outlines of investigating the applicability of GNP as a stem cell tracking agent for CT following different delivery methods.

7.4.7 *In vivo* imaging

BLI

In vivo BLI was performed using the same procedures as previously described in Chapter 2.4.2.

PET/CT

Mice were anaesthetized and whole body static PET scans were acquired using nanoScan PET/CT (Mediso, Budapest, Hungary) followed by CT image acquisition. PET images were acquired using 1-5 coincidence mode and recorded for 20 minutes. CT images were acquired using a 50 kVp and 300 ms exposure time in 720 projections with an acquisition time of 7 minutes. Non-respiratory gated CT lung images were acquired using the same parameters with an acquisition time of 4 minutes. Respiration rate was monitored throughout the scan. PET images were reconstructed using Tera-Tomo™ 3D PET reconstruction

software (Mediso version 2.01). CT images were reconstructed in voxel size of 68 x 68 x 68 mm using Nucline software (Mediso version 2.01). Image analysis and three-dimensional (3D) visualization were performed using VivoQuant software (InviCRO version 1.23patch3). CT signal at the subcutaneous injection site was quantified and presented as the relative Hounsfield unit from the opposite side of the flank. For CT lung image analysis, a region of interest was drawn around the thoracic cage and the air within this region was segmented and quantified by batch processing and produced representative 3D models of lungs using CTAnalyser and CTVolume software (Skyscan version 1.10.11.0).

7.5 Results

7.5.1 Internalisation of GNPs in ADSCs

The uptake of GNPs by ADSCs was visualised using a phase contrast microscope which showed dark aggregates inside the cytoplasm when compared to untreated control (Figure 7.3 a & b). The internalisation of GNPs by ADSCs was further confirmed by TEM images which showed GNPs were trapped inside endosomes (Figure 7.3c).

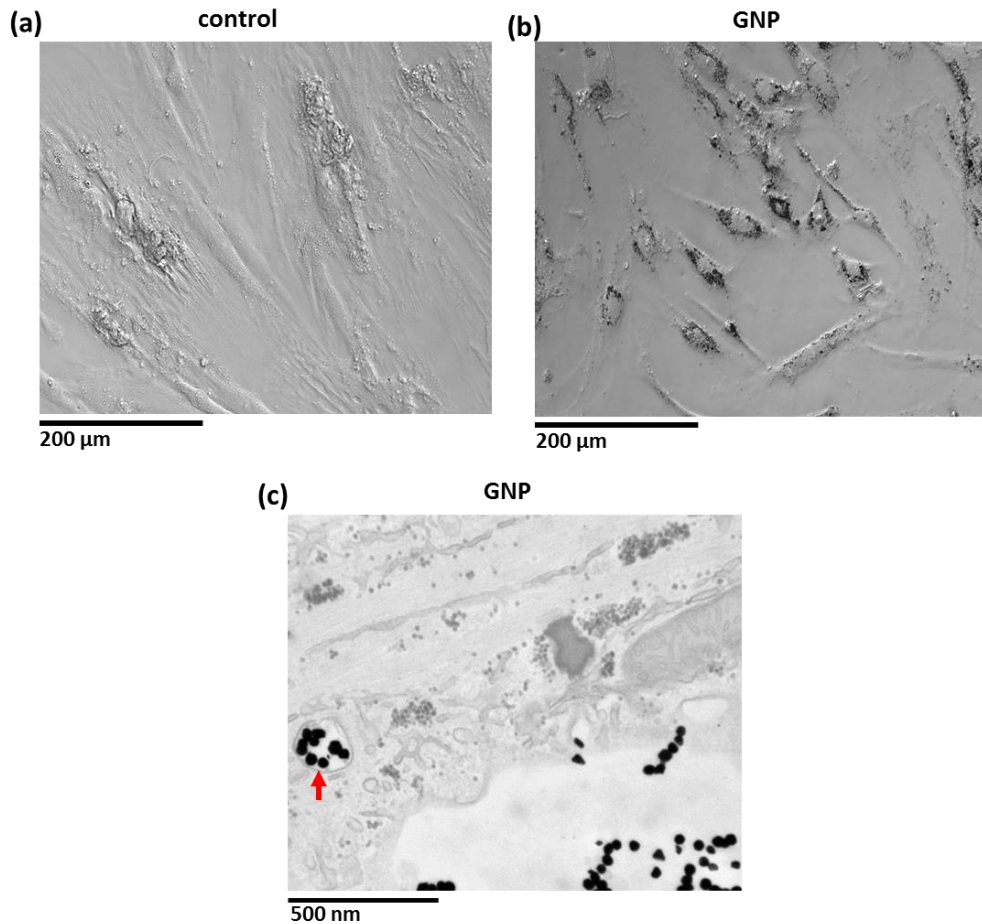


Figure 7.3 Intracellular uptakes of GNPs in ADSCs. (a & b) Phase contrast microscopic image of ADSCs treated with GNPs showing the dark aggregates inside the cytoplasm compared to untreated control (scale bar = 200 μm). (c) TEM image of GNP labelled ADSCs showing the entrapment of GNPs inside endosomes (indicated by arrow, scale bar = 500 nm).

7.5.2 *In vitro* CT contrast of GNP labelled ADSCs

In vitro CT contrast of GNP labelled ADSCs was assessed by imaging cell pellets labelled with different concentrations of GNPs. The CT signal intensity was found to increase in a dose dependent manner (Figure 7.4). CT HU measurements for 0.04 mg/ml, 0.08 mg/ml and 0.2 mg/ml of GNP labelled cell pellets were 5258, 6328 and 12413 HU respectively indicating that the lowest (0.04 mg/ml) concentration was sufficient to provide *in vitro* CT contrast. Therefore, 0.04 mg/ml concentration was used for further *in vivo* testing.

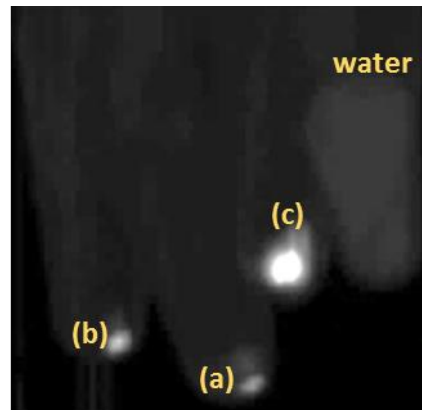


Figure 7.4 Assessing the CT contrast of GNP labelled ADSCs *in vitro*. 0.5×10^5 cell pellets incubated with (a) 0.04 mg/ml (b) 0.08 mg/ml and (c) 0.2 mg/ml of GNPs showing the positive CT contrast compared to water.

7.5.3 *In vivo* CT contrast of GNP labelled ADSCs

For preliminary investigation of GNP as an *in vivo* cell tracking agent for CT, 2×10^5 GNP labelled ADSCs were injected subcutaneously and imaged with BLI and CT serially for 2 months. BLI images at day 1 after injection showed the presence of labelled cells at the site of implantation (Figure 7.5a). Consistent with BLI images, CT images also showed regions of high signal intensity at the same location (Figure 7.5b). Although BLI signal at the injection site decreased over time (Figure 7.5c), the relative CT HU measurement was relatively stable throughout the study with the average value (\pm standard deviation) of 2.853 ± 0.1598 HU (Figure 7.5d). Nonetheless, both BLI and CT images showed that labelled cells were retained at the injection site and both modalities were able to detect ADSCs for up to 2 months after injection with no sign of cells migration.

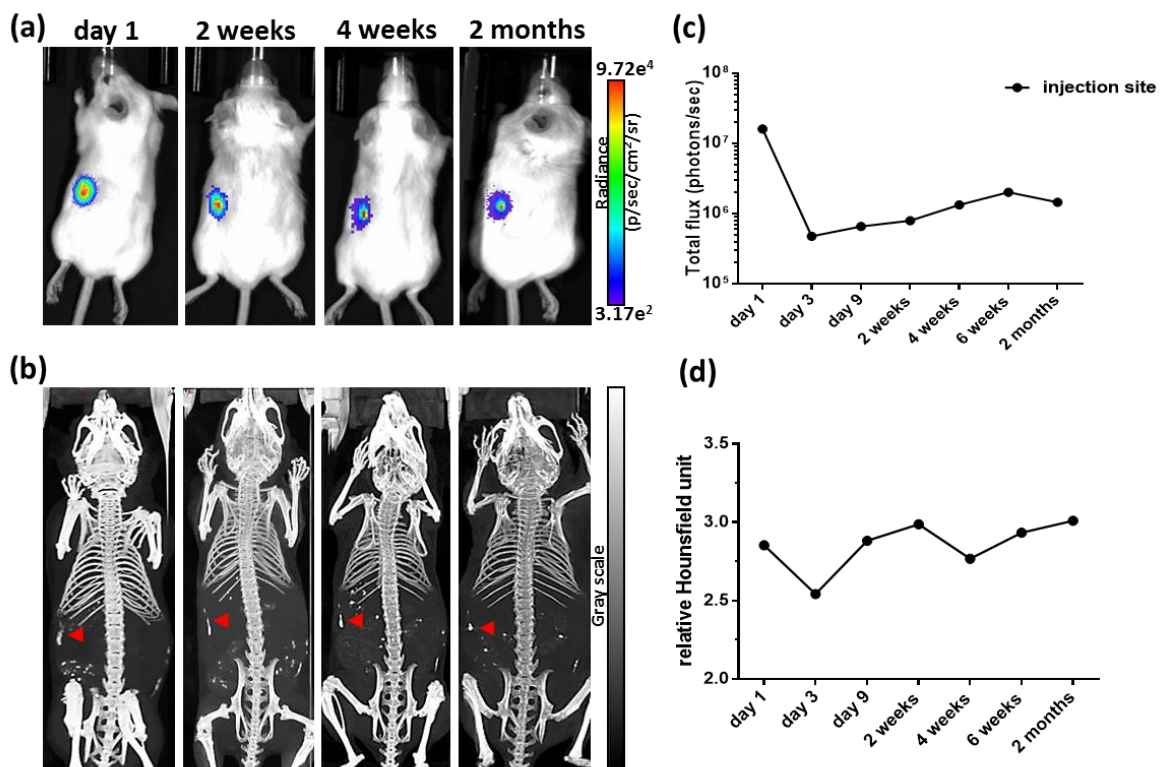


Figure 7.5 BLI and CT images of GNP labelled ADSCs which acquired serially up to 2 months after subcutaneous injection into the left side of the flank. (a) BLI images showing the presence of GNP labelled cells at the injection site. (b) CT images showing the positive contrast from GNP labelled cells at the same location (indicated by arrows). (c) BLI signal from the injection site decreased over time (photons/s in log scale). (d) Quantification of CT signal at the injection site remained stable (presented as the relative Hounsfield unit from the opposite side of the flank).

7.5.4 Tracking GNP labelled ADSCs in lungs

To study the distribution of GNP labelled ADSCs in lungs, either PBS or 8×10^5 labelled ADSCs (PBS vehicle) was delivered directly into the lungs via intratracheal intubation and imaged 1 day later by CT and BLI. CT images of GNP labelled ADSCs showed the presence of positive contrast in both right and left lobes of the lungs (Figure 7.6b) compared to the control lungs with PBS instillation (Figure 7.6a) demonstrating that CT was able to detect GNP labelled cells within the lungs. BLI of the same animal showed the presence of viable cells in the trachea and both sides of the lungs (Figure 7.6c) indicating that some cells were still retained in the trachea at 1 day after intubation. However, no region of high CT signal was detected in trachea suggesting that CT is not as sensitive as BLI in detecting small number of cells.

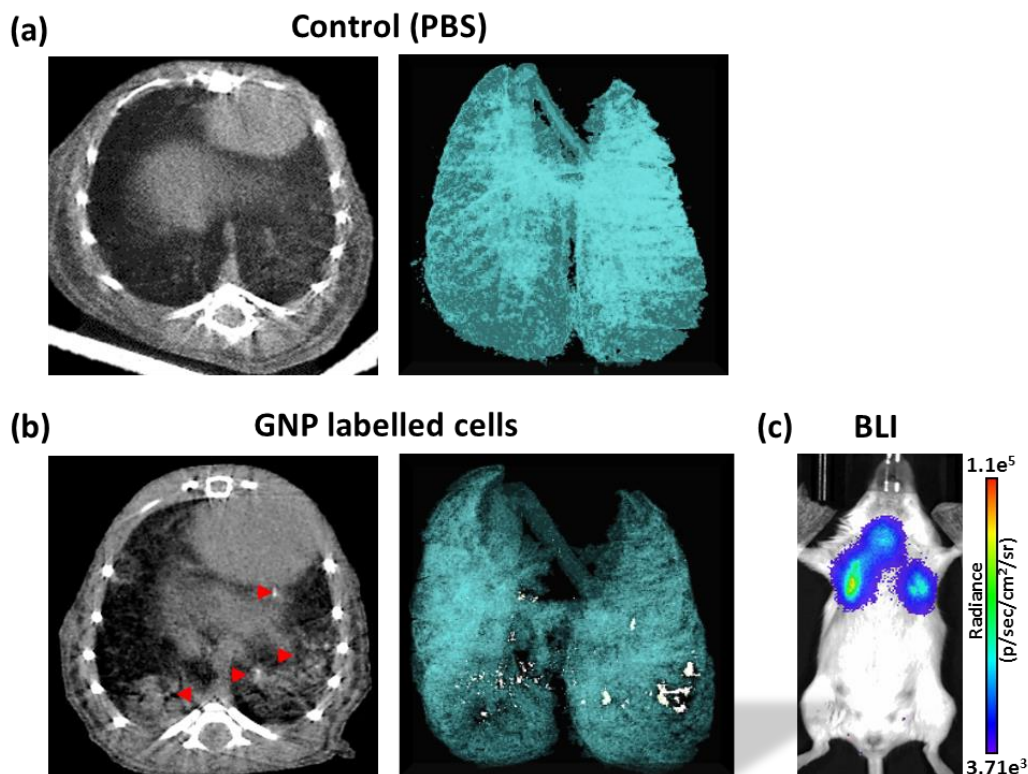


Figure 7.6 CT and BLI images of the control (PBS) and GNP labelled ADSCs in the lungs at 1 day after intratracheal intubation. Cross section and 3D model CT lung images of (a) the control showing absence of positive contrast in the lungs and (b) GNP labelled ADSCs showing the widespread positive contrast in both right and left lobes of the lungs (indicated by arrows). (c) BLI images of GNP labelled ADSCs showing the presence of cells in the trachea and both lobes of the lungs.

7.5.5 Tracking GNP labelled ADSCs in kidney

To study the distribution of GNP labelled ADSCs in kidney using multi-modal imaging, 3×10^5 ADSCs were dual labelled with GNPs and ^{89}Zr -oxine and injected into the right renal artery via ultrasound guidance. The animal was then imaged with BLI and PET/CT at 3 hours after injection. BLI showed that the majority of signal was from the right kidney (Figure 7.7a) while the CT image showed positive contrast within the right renal pelvis, just outside the kidney (Figure 7.7b). The co-registered PET/CT image also shows that the ^{89}Zr PET signal completely overlays with the positive contrast on CT (Figure 7.7c) confirming that this is in fact an unsuccessful renal artery injection.

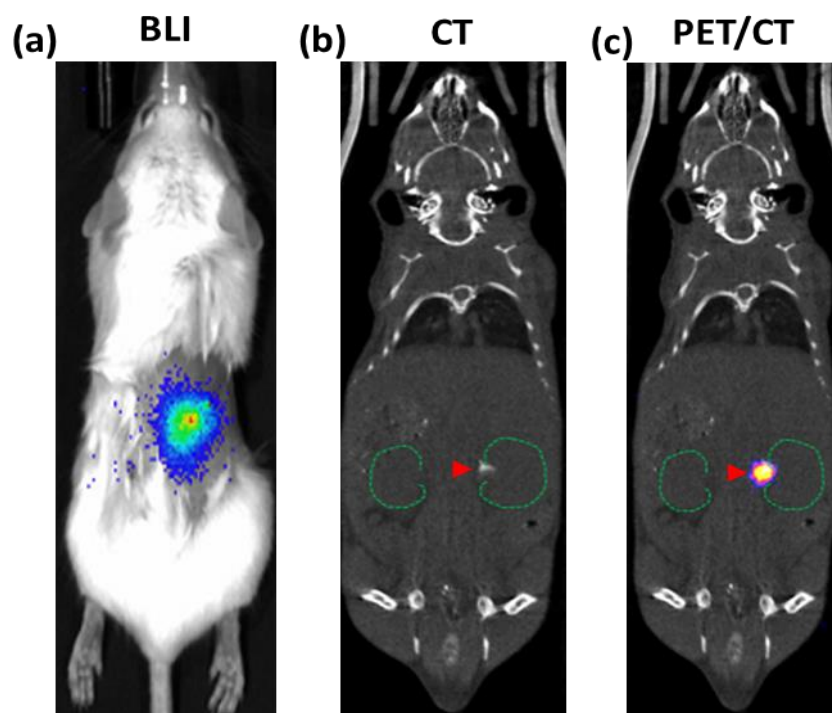


Figure 7.7 BLI and PET/CT images of GNP labelled ADSCs in kidney at 3 hours after renal artery injection. (a) BLI image showing the signal appeared to be coming from the right kidney. (b) CT image showing the positive contrast at the right renal pelvis. (c) Co-registered PET/CT image showing the radioactive signal at the same location.

7.6 Discussion

The aim of this chapter was to develop gold nanoparticles as stem cell tracking agents for CT.

Firstly, the internalisation of citric acid coated GNPs (BBI) was studied and the results showed the entrapment of particles inside cytoplasmic endosomes. These results were consistent with published literature on human MSC uptake using the same formulation of GNPs (Mok *et al.*, 2017). *In vitro* CT contrast of GNP labelled cells was assessed and the results showed dose dependent increase of CT signal intensity (HU) in GNP labelled cell pellets which indicate that quantitative measurement of positive CT contrast could be achieved by using GNPs.

In vivo CT contrast of GNP labelled cells was first studied after subcutaneous implantation and the results showed that CT was able to detect GNP labelled cells for up to 2 months after injection and that they remained viable for this time period (BLI). This suggests that GNP labelling does not have an adverse effect on ADSCs. Although the co-localisation of CT contrast with BLI signal was seen throughout the study and there were some discrepancies between the quantification of BLI and CT HU measurement. This is most likely due to the difference in labelling techniques. CT HU measurement only represents the presence of GNPs at the injection site with no cell-specific information while BLI defines the viability of the labelled cells. This discrepancy also suggests that some of the GNP labelled cells died after injection but were retained at the injection site. Nonetheless, these results indicate that GNP labelled ADSCs were identifiable *in vivo* by CT and GNPs can be potentially useful in assessing long term stem cells engraftment after direct implantation.

Since CT is the most common imaging modality for lung tumour imaging, the applicability of GNPs as a stem cell tracking agent in lungs was studied by delivering GNP labelled ADSCs into the lungs via intratracheal intubation. The results showed widespread positive CT contrast throughout the lungs indicating that GNP labelled ADSCs were readily detected in lungs using CT imaging and thus could have a potential future use in lung tumour models. However, the cell dose required to achieve sufficient CT contrast was eight times higher (8×10^5 vs 1×10^5) than the ^{111}In -DOTA-SPION labelling method as described previously in Chapter 4. Moreover, in order to acquire adequate contrast, GNP labelled cells were needed to be delivered locally into the lungs compared to the highly sensitive detection in lung after systemic IV injections of ^{111}In -DOTA-SPION labelled cells. This is mainly due to the low sensitivity of CT imaging and the requirement of millimolar contrast agent concentrations to achieve sufficient contrast compared with micromolar concentrations of SPIONs and picomolar concentrations of ^{111}In .

Since combined PET/SPECT/CT scanners are widely used in clinic and preclinical research, the multi-modal imaging approach was explored in tracking stem cells in kidney by injecting GNP and ⁸⁹Zr-oxine dual labelled ADSCs into the renal artery. Although BLI signal suggested that the labelled cells were throughout the kidney, co-localised PET/CT signal showed that cells were actually within the renal pelvis outside the kidney. These results demonstrate the advantages of GNP positive CT contrast which can provide accurate cell localization in 3D high resolution, their additive value to nuclear imaging and potential application in determining the efficiency of stem cell delivery to target organ.

7.7 Conclusion

The results presented in this chapter demonstrate that GNPs are a promising cell tracking agent for transplanted stem cells in CT imaging. This technique has specific advantages over currently used methods as a reliable quantification of positive contrast and can be repeatedly longitudinally. However, due to the low sensitivity of CT imaging, it is only suitable for detecting cells in localized regions of specific target organs, for example, in the lungs.

Chapter 8

Final discussion

Non-invasive *in vivo* imaging plays a crucial role in the monitoring of stem cell therapies in both preclinical and clinical studies. However, a single imaging modality cannot provide the comprehensive information that is required to assess the therapeutic potential and safety of stem cell therapies. In order to overcome the limitations of each imaging modality, new developments in multi-modal imaging have been made and applied in preclinical studies (Lee *et al.*, 2008, Madru *et al.*, 2014, Ruan *et al.*, 2012). Most studies have used a combination of direct cell labelling methods, for example, an ^{111}In /SPION/fluorescent probe (Tang *et al.*, 2015). However, direct labelling methods can only provide information on cell localisation not cell viability. Alternatively, studies have utilised a fusion of two imaging reporter genes, for example, a bicistronic BLI/PET reporter gene has been used to track neural progenitor cells in mouse and rat models of gliomas (Waerzeggers *et al.*, 2008). However, due to the poor spatial resolution of both BLI and PET, the detection of exact cell localisation in the tumour has been shown to be challenging.

The main aim of the work described in this thesis was to acquire comprehensive information of transplanted ADSC distribution throughout the whole body using a multi-modal imaging strategy that combined the benefits of direct labelling with reporter gene imaging. In this study, detailed information of cell localisation achieved from different direct cell labelling methods (SPECT, MRI, PA and CT) was complemented by information on cell viability provided by BLI reporter gene imaging, truly capturing the benefits of a multi-modal imaging approach. The major strength of this project was the ability to compare different administration routes to improve stem cell engraftment in tumours so that MSC-based cancer therapies can be optimised. In addition, the new injection route to improve stem cell delivery to kidney was successfully developed and the exciting prospect of gold-based nanomaterials as cell tracking agents was also explored in this thesis. Although this thesis has focused on the use of cell-based tumour therapies, this multi-modal approach can be easily translated to regenerative models and organ systems.

Chapter 3 demonstrated the importance of vigorous testing during the first step of developing a dual imaging probe. A series of experiments were conducted to ensure the reproducibility and stability of the DOTA chelator and bifunctional linker which unites the SPECT and MRI components. In addition, different optimization methods were performed to acquire consistent maximum labelling efficiency of the SPECT/MRI (^{111}In -DOTA-SPION) imaging probe. More importantly, the successful application of the ^{111}In -DOTA-SPION imaging probe as *in vivo* stem cell tracking agents was achieved in chapter 4 and 5 due to robust *in vitro* and *in vivo* stability tests performed in chapter 3.

In chapter 4, *in vitro* assessments on the stability of ^{111}In -DOTA-SPION inside ADSCs showed the dual imaging probe was retained within ADSCs for up to 7 days. No adverse effects on ADSC differentiation or migratory properties were observed after ^{111}In -DOTA-SPION internalisation during the study. Although ^{111}In -DOTA-SPION showed an inhibitory effect on cell proliferation and viability, the dual labelling method was less cytotoxic than the conventional ^{111}In -oxine labelling method. The main focus of chapter 4 was to compare the effect of two systemic injection routes: IV and IC on the whole body cell distribution pattern by using BLI and ^{111}In -DOTA-SPION imaging probes. The reduction of ADSC entrapment within the lung with associated increase of ADSCs retention in the brain and kidney was the main difference between IC and IV injection in healthy immunocompromised mice. Due to the advantages of multi-modal imaging, the exact cell localisation in brain and kidney could be visualised, the percentage population of cells injected and retained in different organs could be quantified; alongside information on cell viability. This information is useful not only in optimising stem cell delivery to target organs but also in monitoring cell behaviour in non-target organs.

The main focus of chapter 5 was to compare the efficiency of IV and IC injection routes in delivering stem cells to a distal tumour site (an orthotopic breast tumour) using multi-modal imaging. IC injection was found to be more efficient than IV in delivering ADSCs to distal tumours, with 2-fold higher cell uptake in tumours and as early as 1 hour after administration. However, extra precautions in cell preparation and cell number selection are required for IC injection due to the risk of mortality caused by vascular occlusion. Although only a small number of cells were shown to engraft in tumour tissue after IV injection, IV injection was found to be a safer delivery route for stem cell transplantation. In addition to the efficiency and safety of the administration routes, the ability to assess the precise cell localisation, the length of cell survival and the percentage population of cells injected within the tumour were provided by using this multi-modal imaging approach. Although no therapeutic treatment has been applied in this study, this multi-modal imaging strategy could be used to correlate the distribution of cells with treatment response in a therapeutic tumour experiment.

The main objective of chapter 6 was to develop a less invasive injection route to improve stem cell delivery to kidney. In this study, ultrasound-guided renal artery injection was successfully developed and evaluated with multi-modal imaging (BLI, PA, SPECT/CT & MRI) which showed the increase retention of cells in kidney after injection. Although further assessments with increased number of animals are required, the amount of radioactivity in the kidney ($\%ID/mm^3$) after renal artery injection was 24-fold higher than after IC injection performed in chapter 4 (0.095 ± 0.019 vs 0.004 ± 0.001 , average value for all the time points). Moreover, in chapter 4, by using MRI, the presence of ^{111}In -DOTA-SPION labelled

cells were detected only in the cortex of the kidney after IC injection while PA images after renal artery injection showed widespread distribution of GNR labelled cells throughout the kidney including cortex and medulla. These results suggest that the ultrasound-guided renal artery injection is more efficient than IC injection in delivering cells to kidney although additional validations are necessary to assess its applicability in mouse models of kidney diseases.

Another interesting finding from this study is the short term cell viability *in vivo* after renal artery injection which is consistent with the results from IV and IC injection in chapter 4 and 5. These results suggest that independent of injection routes and disease condition, transplanted cells stop proliferating and only a small number of transplanted cells survive in the recipients' organs. Although all *in vivo* studies have been carried out in immunocompromised animals, these imaging data cannot conclusively answer the possible involvement of murine immune system in rejection of human stem cells. Nonetheless, many published studies using syngeneic stem cells have also reported short term cell engraftment in various animal models (Tögel *et al.*, 2008, Gao *et al.*, 2001, Müller-Ehmsen *et al.*, 2006). This information is important in determining the optimal cell dose and frequency of cell transplantation to initiate therapeutic effect.

In chapter 7, the applicability of GNPs as stem cell tracking agents for CT was explored in different organs using multi-modal imaging. Although the results are encouraging, the detection of GNP labelled cells with CT imaging is less sensitive than other established cell tracking methods. In preclinical studies, a CT-based cell tracking strategy could be potentially useful in visualizing cells within the lungs where CT can provide adequate tissue contrast or combined with nuclear imaging to gain the additive co-registration value needed in widely available SPECT/PET/CT scanners. However, the possibility of translating this method to the clinic is uncertain due to the fundamental limitations in the sensitivity of CT imaging.

Although multi-modal imaging approach can provide more comprehensive information than a single modality, there are a few limitations such as long scanning time and multiple anaesthesia dose. In addition, due to the differences in sensitivities and labelling methods, inconsistency findings among different imaging modalities can cause misinterpretation of the data. Therefore, a series of validation studies such as *ex vivo* BLI, *ex vivo* MRI and gamma counting studies have been performed in this study to confirm *in vivo* imaging results. Another challenge in elucidating the imaging data is to exclude the false positive results arising from the release of the direct labelling agent from the dead cells or subsequent uptake by phagocytic cells. In this study, the results from histological validation suggest that

the direct cell labelling agents developed in this thesis are retained in cells and that the imaging results are a correct depiction of ADSC distribution. Although less cytotoxic effect of SPECT/MRI nanoparticles was shown in this thesis (Chapter 4), the nuclear imaging is not ideal to be included in every stem cell therapy. It would be more beneficial in validating and optimising new stem cell therapy. Therefore, for future studies, multi-modal imaging approach will be applied in evaluating the safety and optimising the delivery of MSC-based anti-cancer agents, for example, TRAIL. Since BLI is not applicable in large animals and humans, for future studies, nuclear reporter gene imaging will be combined with dual SPECT/MRI imaging nanoparticles to progress these imaging techniques to clinical translation.

In summary, the findings presented in this thesis highly suggest the need for multi-modal imaging in optimising stem cell therapy. Despite some challenges, the advantages of using a multi-modal imaging approach in stem cell tracking would greatly assist the future clinical applications of stem cell-based therapy.

References

1. Abdollah, M. R., et al. (2014). "Prolonging the circulatory retention of SPIONs using dextran sulfate: in vivo tracking achieved by functionalisation with near-infrared dyes." Faraday Discuss **175**: 41-58.
2. Abdollah, M. R. A., et al. (2018). "Fucoidan Prolongs the Circulation Time of Dextran-Coated Iron Oxide Nanoparticles." ACS Nano **12**(2): 1156-1169.
3. Abouelkheir, M., et al. (2016). Mesenchymal stem cells versus their conditioned medium in the treatment of cisplatin-induced acute kidney injury: Evaluation of efficacy and cellular side effects.
4. Aggarwal, S., et al. (2013). "Concise Review: Stem/Progenitor Cells for Renal Tissue Repair: Current Knowledge and Perspectives." Stem Cells Transl Med **2**(12): 1011-1019.
5. Aguilar, S., et al. (2007). "Murine but not human mesenchymal stem cells generate osteosarcoma-like lesions in the lung." Stem Cells **25**(6): 1586-1594.
6. Aires, A., et al. (2016). "Multifunctionalized iron oxide nanoparticles for selective drug delivery to CD44-positive cancer cells." Nanotechnology **27**(6): 065103.
7. Alfarano, C., et al. (2012). "Intraparenchymal injection of bone marrow mesenchymal stem cells reduces kidney fibrosis after ischemia-reperfusion in cyclosporine-immunosuppressed rats." Cell Transplant **21**(9): 2009-2019.
8. Amado, L. C., et al. (2005). "Cardiac repair with intramyocardial injection of allogeneic mesenchymal stem cells after myocardial infarction." Proc Natl Acad Sci U S A **102**(32): 11474-11479.
9. Anderson, C. J. and M. J. Welch (1999). "Radiometal-labeled agents (non-technetium) for diagnostic imaging." Chem Rev **99**(9): 2219-2234.
10. Andreas, K., et al. (2012). "Highly efficient magnetic stem cell labeling with citrate-coated superparamagnetic iron oxide nanoparticles for MRI tracking." Biomaterials **33**(18): 4515-4525.
11. Angelotti, M. L., et al. (2012). "Characterization of renal progenitors committed toward tubular lineage and their regenerative potential in renal tubular injury." Stem Cells **30**(8): 1714-1725.
12. Assmus, B., et al. (2013). "Effect of shock wave-facilitated intracoronary cell therapy on LVEF in patients with chronic heart failure: the CELLWAVE randomized clinical trial." Jama **309**(15): 1622-1631.
13. Augello, A., et al. (2007). "Cell therapy using allogeneic bone marrow mesenchymal stem cells prevents tissue damage in collagen-induced arthritis." Arthritis Rheum **56**(4): 1175-1186.

14. Badar, A., et al. (2015). "Fluorescence-guided development of a tricistronic vector encoding bimodal optical and nuclear genetic reporters for in vivo cellular imaging." EJNMMI Res **5**: 18.
15. Bagó, J. R., et al. (2016). "Therapeutically engineered induced neural stem cells are tumour-homing and inhibit progression of glioblastoma." Nature Communications **7**: 10593.
16. Bakondi, B., et al. (2009). "CD133 identifies a human bone marrow stem/progenitor cell sub-population with a repertoire of secreted factors that protect against stroke." Mol Ther **17**(11): 1938-1947.
17. Balduzzi, A., et al. (2005). "Chemotherapy versus allogeneic transplantation for very-high-risk childhood acute lymphoblastic leukaemia in first complete remission: comparison by genetic randomisation in an international prospective study." Lancet **366**(9486): 635-642.
18. Balyasnikova, I. V., et al. (2014). "Intranasal Delivery of Mesenchymal Stem Cells Significantly Extends Survival of Irradiated Mice with Experimental Brain Tumors." Molecular Therapy **22**(1): 140-148.
19. Bansal, A., et al. (2015). "Novel (89)Zr cell labeling approach for PET-based cell trafficking studies." EJNMMI Research **5**: 19.
20. Barnes, C. J., et al. (2016). "Comparison of stem cell therapies for acute kidney injury." American Journal of Stem Cells **5**(1): 1-10.
21. Barrio, J. R., et al. (1989). "3-(2'-[18F]fluoroethyl)spiperone: in vivo biochemical and kinetic characterization in rodents, nonhuman primates, and humans." J Cereb Blood Flow Metab **9**(6): 830-839.
22. Ben-David, U. and N. Benvenisty (2011). "The tumorigenicity of human embryonic and induced pluripotent stem cells." Nat Rev Cancer **11**(4): 268-277.
23. Bergers, G., et al. (1999). "Effects of angiogenesis inhibitors on multistage carcinogenesis in mice." Science **284**(5415): 808-812.
24. Berndt, E. S. L., et al. (2018). Photoacoustic imaging for assessing ischemic kidney damage in vivo, SPIE.
25. Berninger, M. T., et al. (2017). "Detection of intramyocardially injected DiR-labeled mesenchymal stem cells by optical and optoacoustic tomography." Photoacoustics **6**: 37-47.

26. Berry, M. F., et al. (2006). "Mesenchymal stem cell injection after myocardial infarction improves myocardial compliance." Am J Physiol Heart Circ Physiol **290**(6): H2196-2203.
27. Betzer, O., et al. (2014). "Nanoparticle-based CT imaging technique for longitudinal and quantitative stem cell tracking within the brain: application in neuropsychiatric disorders." ACS Nano **8**(9): 9274-9285.
28. Bhattacharya, K., et al. (2014). "Enzymatic 'stripping' and degradation of PEGylated carbon nanotubes." Nanoscale **6**(24): 14686-14690.
29. Bible, E., et al. (2012). "Non-invasive imaging of transplanted human neural stem cells and ECM scaffold remodeling in the stroke-damaged rat brain by (19)F- and diffusion-MRI." Biomaterials **33**(10): 2858-2871.
30. Bobis-Wozowicz, S., et al. (2011). "Genetically modified adipose tissue-derived mesenchymal stem cells overexpressing CXCR4 display increased motility, invasiveness, and homing to bone marrow of NOD/SCID mice." Exp Hematol **39**(6): 686-696.e684.
31. Boehm-Sturm, P., et al. (2011). "In vivo tracking of human neural stem cells with 19F magnetic resonance imaging." PLoS One **6**(12): e29040.
32. Bos, C., et al. (2004). "In vivo MR imaging of intravascularly injected magnetically labeled mesenchymal stem cells in rat kidney and liver." Radiology **233**(3): 781-789.
33. Botti, C., et al. (1997). "Comparison of three different methods for radiolabelling human activated T lymphocytes." Eur J Nucl Med **24**(5): 497-504.
34. Bouffi, C., et al. (2010). "IL-6-Dependent PGE2 Secretion by Mesenchymal Stem Cells Inhibits Local Inflammation in Experimental Arthritis." PLoS One **5**(12): e14247.
35. Branchini, B. R., et al. (2010). "Red-emitting luciferases for bioluminescence reporter and imaging applications." Anal Biochem **396**(2): 290-297.
36. Breeman, W. A., et al. (2003). "Optimising conditions for radiolabelling of DOTA-peptides with 90Y, 111In and 177Lu at high specific activities." Eur J Nucl Med Mol Imaging **30**(6): 917-920.
37. Breems, D. A., et al. (2005). "Autologous bone marrow transplantation as consolidation therapy in the treatment of adult patients under 60 years with acute myeloid leukaemia in first complete remission: a prospective randomized Dutch-Belgian Haemato-Oncology Co-operative Group (HOVON) and Swiss Group for Clinical Cancer Research (SAKK) trial." Br J Haematol **128**(1): 59-65.
38. Brom, M., et al. (2012). "Improved labelling of DTPA- and DOTA-conjugated peptides and antibodies with (111)In in HEPES and MES buffer." EJNMMI Res **2**: 4.

39. Brunker, J., et al. (2017). "Photoacoustic imaging using genetically encoded reporters: a review." J Biomed Opt **22**(7).
40. Bull, E., et al. (2014). "Stem cell tracking using iron oxide nanoparticles." Int J Nanomedicine **9**: 1641-1653.
41. Burgess, R. E. and C. S. Kidwell (2011). "Use of MRI in the assessment of patients with stroke." Curr Neurol Neurosci Rep **11**(1): 28-34.
42. Cai, J., et al. (2014). "Maximum efficacy of mesenchymal stem cells in rat model of renal ischemia-reperfusion injury: renal artery administration with optimal numbers." PLoS One **9**(3): e92347.
43. Cai, X., et al. (2012). "Multi-scale molecular photoacoustic tomography of gene expression." PLoS One **7**(8): e43999.
44. Campan, M., et al. (2011). "Ferritin as a reporter gene for in vivo tracking of stem cells by 1.5-T cardiac MRI in a rat model of myocardial infarction." Am J Physiol Heart Circ Physiol **300**(6): H2238-2250.
45. Cao, F., et al. (2008). "Transcriptional and Functional Profiling of Human Embryonic Stem Cell-Derived Cardiomyocytes." PLoS One **3**(10): e3474.
46. Caplan, A. I. (2017). "Mesenchymal Stem Cells: Time to Change the Name!" Stem Cells Transl Med **6**(6): 1445-1451.
47. Castillo, S. D., et al. (2016). "Somatic activating mutations in *Pik3ca* cause sporadic venous malformations in mice and humans." Sci Transl Med **8**(332): 332ra343.
48. Charoenphun, P., et al. (2015). "[⁸⁹Zr]Oxinate(4) for long-term in vivo cell tracking by positron emission tomography." Eur J Nucl Med Mol Imaging **42**: 278-287.
49. Chen, L., et al. (2008). "Paracrine Factors of Mesenchymal Stem Cells Recruit Macrophages and Endothelial Lineage Cells and Enhance Wound Healing." PLoS One **3**(4): e1886.
50. Cheng, D., et al. (2015). "Detection of vulnerable atherosclerosis plaques with a dual-modal single-photon-emission computed tomography/magnetic resonance imaging probe targeting apoptotic macrophages." ACS Appl Mater Interfaces **7**(4): 2847-2855.
51. Cheng, S.-H., et al. (2016). "Dynamic In Vivo SPECT Imaging of Neural Stem Cells Functionalized with Radiolabeled Nanoparticles for Tracking of Glioblastoma." Journal of nuclear medicine : official publication, Society of Nuclear Medicine **57**(2): 279-284.

52. Chin, B. B., et al. (2003). "¹¹¹In oxine labelled mesenchymal stem cell SPECT after intravenous administration in myocardial infarction." Nucl Med Commun **24**(11): 1149-1154.
53. Choi, S., et al. (2009). "The role of mesenchymal stem cells in the functional improvement of chronic renal failure." Stem Cells Dev **18**(3): 521-529.
54. Clark, D. P., et al. (2013). "In vivo characterization of tumor vasculature using iodine and gold nanoparticles and dual energy micro-CT." Phys Med Biol **58**(6): 1683-1704.
55. Clifford, D. M., et al. (2012). "Stem cell treatment for acute myocardial infarction." Cochrane Database Syst Rev(2): Cd006536.
56. Comenge, J., et al. (2016). "Preventing Plasmon Coupling between Gold Nanorods Improves the Sensitivity of Photoacoustic Detection of Labeled Stem Cells in Vivo." ACS Nano **10**(7): 7106-7116.
57. Connell, J. J., et al. (2013). "Selective permeabilization of the blood-brain barrier at sites of metastasis." J Natl Cancer Inst **105**(21): 1634-1643.
58. Cores, J., et al. (2015). "Magnetically Targeted Stem Cell Delivery for Regenerative Medicine." J Funct Biomater **6**(3): 526-546.
59. Cui, L. L., et al. (2015). "The cerebral embolism evoked by intra-arterial delivery of allogeneic bone marrow mesenchymal stem cells in rats is related to cell dose and infusion velocity." Stem Cell Res Ther **6**: 11.
60. Cusso, L., et al. (2014). "Combination of single-photon emission computed tomography and magnetic resonance imaging to track ¹¹¹In-oxine-labeled human mesenchymal stem cells in neuroblastoma-bearing mice." Mol Imaging **13**.
61. Dave, M., et al. (2017). "Ultrasound-guided Intracardiac Injection of Human Mesenchymal Stem Cells to Increase Homing to the Intestine for Use in Murine Models of Experimental Inflammatory Bowel Diseases." J Vis Exp(127).
62. De, A., et al. (2003). "Noninvasive imaging of lentiviral-mediated reporter gene expression in living mice." Mol Ther **7**(5 Pt 1): 681-691.
63. De Becker, A. and I. V. Riet (2016). "Homing and migration of mesenchymal stromal cells: How to improve the efficacy of cell therapy?" World Journal of Stem Cells **8**(3): 73-87.
64. De León-Rodríguez, L. M. and Z. Kovacs (2008). "The Synthesis and Chelation Chemistry of DOTA–Peptide Conjugates." Bioconjugate Chemistry **19**(2): 391-402.

65. de Vries, I. J., et al. (2005). "Magnetic resonance tracking of dendritic cells in melanoma patients for monitoring of cellular therapy." Nat Biotechnol **23**(11): 1407-1413.
66. Detante, O., et al. (2009). "Intravenous administration of 99mTc-HMPAO-labeled human mesenchymal stem cells after stroke: in vivo imaging and biodistribution." Cell Transplant **18**(12): 1369-1379.
67. Di Rocco, G., et al. (2012). "Analysis of biodistribution and engraftment into the liver of genetically modified mesenchymal stromal cells derived from adipose tissue." Cell Transplant **21**(9): 1997-2008.
68. Dominici, M., et al. (2006). "Minimal criteria for defining multipotent mesenchymal stromal cells. The International Society for Cellular Therapy position statement." Cytotherapy **8**(4): 315-317.
69. Doyle, B., et al. (2007). "Dynamic tracking during intracoronary injection of 18F-FDG-labeled progenitor cell therapy for acute myocardial infarction." J Nucl Med **48**(10): 1708-1714.
70. Dwyer, R. M., et al. (2007). "Monocyte chemotactic protein-1 secreted by primary breast tumors stimulates migration of mesenchymal stem cells." Clin Cancer Res **13**(17): 5020-5027.
71. Eirin, A. and L. O. Lerman (2014). "Mesenchymal stem cell treatment for chronic renal failure." Stem Cell Res Ther **5**(4): 83.
72. Elvas, F., et al. (2015). "Characterization of [(99m)Tc]Duramycin as a SPECT Imaging Agent for Early Assessment of Tumor Apoptosis." Molecular Imaging and Biology **17**(6): 838-847.
73. Fang, T.-C., et al. (2004). "Adult stem cell plasticity: will engineered tissues be rejected?" International Journal of Experimental Pathology **85**(3): 115-124.
74. Fantozzi, A. and G. Christofori (2006). "Mouse models of breast cancer metastasis." Breast Cancer Res **8**(4): 212.
75. Femand, J. P., et al. (2005). "High-dose therapy and autologous blood stem-cell transplantation compared with conventional treatment in myeloma patients aged 55 to 65 years: long-term results of a randomized control trial from the Group Myelome-Autogreffe." J Clin Oncol **23**(36): 9227-9233.
76. Filonov, G. S., et al. (2012). "Deep-tissue photoacoustic tomography of a genetically encoded near-infrared fluorescent probe." Angew Chem Int Ed Engl **51**(6): 1448-1451.

77. Fischer, U. M., et al. (2009). "Pulmonary passage is a major obstacle for intravenous stem cell delivery: the pulmonary first-pass effect." Stem Cells Dev **18**(5): 683-692.
78. Fisher, S. A., et al. (2014). "Stem cell therapy for chronic ischaemic heart disease and congestive heart failure." Cochrane Database Syst Rev(4): Cd007888.
79. Freed, C. R., et al. (2001). "Transplantation of embryonic dopamine neurons for severe Parkinson's disease." N Engl J Med **344**(10): 710-719.
80. Fuente Mora, C., et al. (2012). "Differentiation of podocyte and proximal tubule-like cells from a mouse kidney-derived stem cell line." Stem Cells Dev **21**(2): 296-307.
81. Fung, M., et al. (2017). "Responsible Translation of Stem Cell Research: An Assessment of Clinical Trial Registration and Publications." Stem Cell Reports **8**(5): 1190-1201.
82. Galleu, A. and Y. Riffo-Vasquez (2017). "Apoptosis in mesenchymal stromal cells induces in vivo recipient-mediated immunomodulation." **9**(416).
83. Gao, H., et al. (2009). "Activation of signal transducers and activators of transcription 3 and focal adhesion kinase by stromal cell-derived factor 1 is required for migration of human mesenchymal stem cells in response to tumor cell-conditioned medium." Stem Cells **27**(4): 857-865.
84. Gao, J., et al. (2001). "The dynamic in vivo distribution of bone marrow-derived mesenchymal stem cells after infusion." Cells Tissues Organs **169**(1): 12-20.
85. Gaudet, J. M., et al. (2015). "Tracking the fate of stem cell implants with fluorine-19 MRI." PLoS One **10**(3): e0118544.
86. Gehmert, S., et al. (2010). "Breast cancer cells attract the migration of adipose tissue-derived stem cells via the PDGF-BB/PDGFR-beta signaling pathway." Biochem Biophys Res Commun **398**(3): 601-605.
87. Gholamrezanezhad, A., et al. (2011). "In vivo tracking of 111In-oxine labeled mesenchymal stem cells following infusion in patients with advanced cirrhosis." Nucl Med Biol **38**(7): 961-967.
88. Gilad, A. A., et al. (2007). "Developing MR reporter genes: promises and pitfalls." NMR Biomed **20**(3): 275-290.
89. Gleave, J. A., et al. (2011). "99mTc-based imaging of transplanted neural stem cells and progenitor cells." J Nucl Med Technol **39**(2): 114-120.
90. Gnecci, M., et al. (2008). "Paracrine mechanisms in adult stem cell signaling and therapy." Circulation research **103**(11): 1204-1219.

91. Gooch, A., et al. (2008). Initial report on a phase I clinical trial: Prevention and treatment of post-operative Acute Kidney Injury with allogeneic Mesenchymal Stem Cells in patients who require on-pump cardiac surgery.
92. Grange, C., et al. (2014). "Protective effect and localization by optical imaging of human renal CD133+ progenitor cells in an acute kidney injury model." Physiol Rep **2**(5): e12009.
93. Griffin, M., et al. (2014). "The Use of Adipose Stem Cells in Cranial Facial Surgery." Stem Cell Reviews and Reports **10**(5): 671-685.
94. Griffin, M., et al. (2017). "Characteristics of human adipose derived stem cells in scleroderma in comparison to sex and age matched normal controls: implications for regenerative medicine." Stem Cell Res Ther **8**(1): 23.
95. Guasti, L., et al. (2012). "High plasticity of pediatric adipose tissue-derived stem cells: too much for selective skeletogenic differentiation?" Stem Cells Transl Med **1**(5): 384-395.
96. Gyongyosi, M., et al. (2008). "Serial noninvasive in vivo positron emission tomographic tracking of percutaneously intramyocardially injected autologous porcine mesenchymal stem cells modified for transgene reporter gene expression." Circ Cardiovasc Imaging **1**(2): 94-103.
97. Haider, H., et al. (2008). "IGF-1-overexpressing mesenchymal stem cells accelerate bone marrow stem cell mobilization via paracrine activation of SDF-1alpha/CXCR4 signaling to promote myocardial repair." Circ Res **103**(11): 1300-1308.
98. Haralampieva, D., et al. (2016). "Non-invasive Imaging and Tracking of Engineered Human Muscle Precursor Cells for Skeletal Muscle Tissue Engineering Using Positron Emission Tomography." Journal of nuclear medicine : official publication, Society of Nuclear Medicine **57**(9): 1467-1473.
99. Harris, W. R., et al. (1994). "Equilibrium Constants for the Binding of Indium(III) to Human Serum Transferrin." Inorg Chem **33**(22): 4991-4998.
100. Hasenbach, K., et al. (2012). "Monitoring the glioma tropism of bone marrow-derived progenitor cells by 2-photon laser scanning microscopy and positron emission tomography." Neuro Oncol **14**(4): 471-481.
101. Hauger, O., et al. (2006). "MR evaluation of the glomerular homing of magnetically labeled mesenchymal stem cells in a rat model of nephropathy." Radiology **238**(1): 200-210.
102. He, A., et al. (2009). "The antiapoptotic effect of mesenchymal stem cell transplantation on ischemic myocardium is enhanced by anoxic preconditioning." The Canadian Journal of Cardiology **25**(6): 353-358.

103. Herrmann, R., et al. (2012). "Mesenchymal stromal cell therapy for steroid-refractory acute and chronic graft versus host disease: a phase 1 study." International Journal of Hematology **95**(2): 182-188.
104. Hoffmann, J., et al. (2010). "Angiogenic effects despite limited cell survival of bone marrow-derived mesenchymal stem cells under ischemia." Thorac Cardiovasc Surg **58**(3): 136-142.
105. Honold, J., et al. (2012). "G-CSF stimulation and coronary reinfusion of mobilized circulating mononuclear proangiogenic cells in patients with chronic ischemic heart disease: five-year results of the TOPCARE-G-CSF trial." Cell Transplant **21**(11): 2325-2337.
106. Hu, J., et al. (2013). "Mesenchymal stem cells attenuate ischemic acute kidney injury by inducing regulatory T cells through splenocyte interactions." Kidney International **84**(3): 521-531.
107. Hueper, K., et al. (2014). "Acute Kidney Injury: Arterial Spin Labeling to Monitor Renal Perfusion Impairment in Mice—Comparison with Histopathologic Results and Renal Function." Radiology **270**(1): 117-124.
108. Humphreys, B. D. (2014). "Kidney injury, stem cells and regeneration." Current opinion in nephrology and hypertension **23**(1): 25-31.
109. Humphreys, B. D., et al. (2008). "Intrinsic epithelial cells repair the kidney after injury." Cell Stem Cell **2**(3): 284-291.
110. Hung, S. C., et al. (2005). "Mesenchymal stem cell targeting of microscopic tumors and tumor stroma development monitored by noninvasive in vivo positron emission tomography imaging." Clin Cancer Res **11**(21): 7749-7756.
111. Imberti, B., et al. (2007). "Insulin-like growth factor-1 sustains stem cell mediated renal repair." J Am Soc Nephrol **18**(11): 2921-2928.
112. Inrona, M., et al. (2014). "Treatment of Graft versus Host Disease with Mesenchymal Stromal Cells: A Phase I Study on 40 Adult and Pediatric Patients." Biology of Blood and Marrow Transplantation **20**(3): 375-381.
113. Jasmin, et al. (2012). "Labeling Stem Cells with Superparamagnetic Iron Oxide Nanoparticles: Analysis of the Labeling Efficacy by Microscopy and Magnetic Resonance Imaging." Methods Mol Biol **906**: 239-252.
114. Jeevanantham, V., et al. (2012). "Adult bone marrow cell therapy improves survival and induces long-term improvement in cardiac parameters: a systematic review and meta-analysis." Circulation **126**(5): 551-568.

115. Jeon, E. S., et al. (2008). "Cancer-derived lysophosphatidic acid stimulates differentiation of human mesenchymal stem cells to myofibroblast-like cells." Stem Cells **26**(3): 789-797.
116. Ji, P., et al. (2016). "Induced Pluripotent Stem Cells: Generation Strategy and Epigenetic Mystery behind Reprogramming." Stem Cells International **2016**: 8415010.
117. Jiang, W., et al. (2008). "Nanoparticle-mediated cellular response is size-dependent." Nat Nanotechnol **3**(3): 145-150.
118. Jo, J., et al. (2018). "Photoacoustic tomography for human musculoskeletal imaging and inflammatory arthritis detection." Photoacoustics.
119. Johe, K. K., et al. (1996). "Single factors direct the differentiation of stem cells from the fetal and adult central nervous system." Genes Dev **10**(24): 3129-3140.
120. Jotzu, C., et al. (2010). "Adipose tissue-derived stem cells differentiate into carcinoma-associated fibroblast-like cells under the influence of tumor-derived factors." Anal Cell Pathol (Amst) **33**(2): 61-79.
121. Kalber, T. L., et al. (2016). "Hyperthermia treatment of tumors by mesenchymal stem cell-delivered superparamagnetic iron oxide nanoparticles." Int J Nanomedicine **11**: 1973-1983.
122. Kalimuthu, S., et al. (2017). "In Vivo Tracking of Chemokine Receptor CXCR4-Engineered Mesenchymal Stem Cell Migration by Optical Molecular Imaging." Stem Cells International **2017**: 8085637.
123. Kaneko, K., et al. (2001). "Detection of peritoneal micrometastases of gastric carcinoma with green fluorescent protein and carcinoembryonic antigen promoter." Cancer Res **61**(14): 5570-5574.
124. Karnoub, A. E., et al. (2007). "Mesenchymal stem cells within tumour stroma promote breast cancer metastasis." Nature **449**(7162): 557-563.
125. Kauer, T. M., et al. (2011). "Encapsulated therapeutic stem cells implanted in the tumor resection cavity induce cell death in gliomas." Nat Neurosci **15**(2): 197-204.
126. Khabbal, J., et al. (2015). "Differential Clearance of Rat and Human Bone Marrow-Derived Mesenchymal Stem Cells From the Brain After Intra-arterial Infusion in Rats." Cell Transplant **24**(5): 819-828.
127. Kim, D. S., et al. (2009). "Overexpression of CXC chemokine receptors is required for the superior glioma-tracking property of umbilical cord blood-derived mesenchymal stem cells." Stem Cells Dev **18**(3): 511-519.

128. Kim, J. E., et al. (2015). "In Vivo Cell Tracking with Bioluminescence Imaging." Nuclear Medicine and Molecular Imaging **49**(1): 3-10.
129. Kinnaird, T., et al. (2004). "Local delivery of marrow-derived stromal cells augments collateral perfusion through paracrine mechanisms." Circulation **109**(12): 1543-1549.
130. Kircher, M. F., et al. (2011). "Noninvasive cell-tracking methods." Nat Rev Clin Oncol **8**(11): 677-688.
131. Klingberg, H., et al. (2015). "Uptake of gold nanoparticles in primary human endothelial cells." Toxicology Research **4**(3): 655-666.
132. Klopp, A. H., et al. (2007). "Tumor irradiation increases the recruitment of circulating mesenchymal stem cells into the tumor microenvironment." Cancer Res **67**(24): 11687-11695.
133. Kondo, A., et al. (2009). "Longitudinal assessment of regional directed delivery in a rodent malignant glioma model." J Neurosurg Pediatr **4**(6): 592-598.
134. Kraitchman, D. L., et al. (2005). "Dynamic imaging of allogeneic mesenchymal stem cells trafficking to myocardial infarction." Circulation **112**(10): 1451-1461.
135. Kunter, U., et al. (2007). "Mesenchymal stem cells prevent progressive experimental renal failure but maldifferentiate into glomerular adipocytes." J Am Soc Nephrol **18**(6): 1754-1764.
136. Lassailly, F., et al. (2010). "Microenvironmental contaminations" induced by fluorescent lipophilic dyes used for noninvasive in vitro and in vivo cell tracking." Blood **115**(26): 5347-5354.
137. Lee, H., et al. (2007). "Thermally cross-linked superparamagnetic iron oxide nanoparticles: synthesis and application as a dual imaging probe for cancer in vivo." J Am Chem Soc **129**(42): 12739-12745.
138. Lee, H. Y., et al. (2008). "PET/MRI dual-modality tumor imaging using arginine-glycine-aspartic (RGD)-conjugated radiolabeled iron oxide nanoparticles." J Nucl Med **49**(8): 1371-1379.
139. Lee, K. Y. and D. J. Mooney (2012). "Alginate: properties and biomedical applications." Progress in polymer science **37**(1): 106-126.
140. Lee, S. and X. Chen (2009). "Dual-modality probes for in vivo molecular imaging." Mol Imaging **8**(2): 87-100.

141. Lee, U. Y., et al. (2014). "Y-Shaped Ligand-Driven Gold Nanoparticles for Highly Efficient Tumoral Uptake and Photothermal Ablation." ACS Nano **8**(12): 12858-12865.
142. Levy, O., et al. (2013). "mRNA-engineered mesenchymal stem cells for targeted delivery of interleukin-10 to sites of inflammation." Blood **122**(14): e23-32.
143. Lewis, C. M., et al. (2015). "⁵⁵Mn production for PET/MRI tracking of human stem cells expressing divalent metal transporter 1 (DMT1)." Theranostics **5**(3): 227-239.
144. Li, C., et al. (2006). "Dual optical and nuclear imaging in human melanoma xenografts using a single targeted imaging probe." Nucl Med Biol **33**(3): 349-358.
145. Li, L., et al. (2011). "Silica nanorattle-doxorubicin-anchored mesenchymal stem cells for tumor-tropic therapy." ACS Nano **5**(9): 7462-7470.
146. Li, L., et al. (2007). "Photoacoustic imaging of lacZ gene expression in vivo." J Biomed Opt **12**(2): 020504.
147. Li, M., et al. (2018). "Multimodality reporter gene imaging: Construction strategies and application." Theranostics **8**(11): 2954-2973.
148. Li, W. and X. Chen (2015). "Gold nanoparticles for photoacoustic imaging." Nanomedicine (London, England) **10**(2): 299-320.
149. Lin, S., et al. (2007). "Quantum dot imaging for embryonic stem cells." BMC Biotechnol **7**: 67.
150. Lindvall, O., et al. (2012). "Clinical translation of stem cells in neurodegenerative disorders." Cell Stem Cell **10**(2): 151-155.
151. Ling, X., et al. (2010). "Mesenchymal Stem Cells Overexpressing IFN-beta Inhibit Breast Cancer Growth and Metastases through Stat3 Signaling in a Syngeneic Tumor Model." Cancer Microenviron **3**(1): 83-95.
152. Liu, H., et al. (2012). "The role of SDF-1-CXCR4/CXCR7 axis in the therapeutic effects of hypoxia-preconditioned mesenchymal stem cells for renal ischemia/reperfusion injury." PLoS One **7**(4): e34608.
153. Liu, M., et al. (2013). "In vivo three dimensional dual wavelength photoacoustic tomography imaging of the far red fluorescent protein E2-Crimson expressed in adult zebrafish." Biomed Opt Express **4**(10): 1846-1855.

154. Liu, M., et al. (2018). "Using tyrosinase as a tri-modality reporter gene to monitor transplanted stem cells in acute myocardial infarction." Experimental & Molecular Medicine **50**(4): 54.
155. Lo, C. Y., et al. (2013). "The use of surface immobilization of P-selectin glycoprotein ligand-1 on mesenchymal stem cells to facilitate selectin mediated cell tethering and rolling." Biomaterials **34**(33): 8213-8222.
156. Loebinger, M. R., et al. (2009). "Mesenchymal stem cell delivery of TRAIL can eliminate metastatic cancer." Cancer Res **69**(10): 4134-4142.
157. Lourenco, S., et al. (2015). "Macrophage migration inhibitory factor-CXCR4 is the dominant chemotactic axis in human mesenchymal stem cell recruitment to tumors." J Immunol **194**(7): 3463-3474.
158. Love, Z., et al. (2007). "Imaging of mesenchymal stem cell transplant by bioluminescence and PET." J Nucl Med **48**(12): 2011-2020.
159. Lusic, H. and M. W. Grinstaff (2013). "X-ray-computed tomography contrast agents." Chem Rev **113**(3): 1641-1666.
160. Mader, E. K., et al. (2013). "Optimizing patient derived mesenchymal stem cells as virus carriers for a phase I clinical trial in ovarian cancer." J Transl Med **11**: 20.
161. Madru, R., et al. (2014). "Development of a Hybrid Nanoprobe for Triple-Modality MR/SPECT/Optical Fluorescence Imaging." Diagnostics **4**(1).
162. Madru, R., et al. (2013). "(68)Ga-labeled superparamagnetic iron oxide nanoparticles (SPIONs) for multi-modality PET/MR/Cherenkov luminescence imaging of sentinel lymph nodes." Am J Nucl Med Mol Imaging **4**(1): 60-69.
163. Makela, A. V. and P. J. Foster (2018). "Imaging macrophage distribution and density in mammary tumors and lung metastases using fluorine-19 MRI cell tracking." Magn Reson Med **80**(3): 1138-1147.
164. Mao, Z., et al. (2013). "Influence of structure and properties of colloidal biomaterials on cellular uptake and cell functions." Biomaterials Science **1**(9): 896-911.
165. Marks, P. W., et al. (2016). "Clarifying Stem-Cell Therapy's Benefits and Risks." New England Journal of Medicine **376**(11): 1007-1009.
166. Massoud, T. F. and S. S. Gambhir (2003). "Molecular imaging in living subjects: seeing fundamental biological processes in a new light." Genes Dev **17**(5): 545-580.

167. Matuszewski, L., et al. (2005). "Cell tagging with clinically approved iron oxides: feasibility and effect of lipofection, particle size, and surface coating on labeling efficiency." Radiology **235**(1): 155-161.
168. Mavligit, G. M., et al. (1991). "Regression of hepatic metastases from gastrointestinal leiomyosarcoma after hepatic arterial chemoembolization." Cancer **68**(2): 321-323.
169. McBride, J. L., et al. (2004). "Human neural stem cell transplants improve motor function in a rat model of Huntington's disease." J Comp Neurol **475**(2): 211-219.
170. McColgan, P., et al. (2011). "Stem cell tracking in human trials: a meta-regression." Stem Cell Rev **7**(4): 1031-1040.
171. Meier, R. P., et al. (2013). "Transplantation of mesenchymal stem cells for the treatment of liver diseases, is there enough evidence?" Stem Cell Res **11**(3): 1348-1364.
172. Meir, R., et al. (2015). "Nanomedicine for Cancer Immunotherapy: Tracking Cancer-Specific T-Cells in Vivo with Gold Nanoparticles and CT Imaging." ACS Nano **9**(6): 6363-6372.
173. Menk, R. H., et al. (2011). "Gold nanoparticle labeling of cells is a sensitive method to investigate cell distribution and migration in animal models of human disease." Nanomedicine **7**(5): 647-654.
174. Mercier-Letondal, P., et al. (2008). "Early immune response against retrovirally transduced herpes simplex virus thymidine kinase-expressing gene-modified T cells coinjected with a T cell-depleted marrow graft: an altered immune response?" Hum Gene Ther **19**(9): 937-950.
175. Mishra, P. J. and G. Merlino (2008). "A traitor in our midst: mesenchymal stem cells contribute to tumor progression and metastasis." Future Oncol **4**(6): 745-749.
176. Misri, R., et al. (2012). "Development and evaluation of a dual-modality (MRI/SPECT) molecular imaging bioprobe." Nanomedicine **8**(6): 1007-1016.
177. Mitchell, N., et al. (2013). "Incorporation of paramagnetic, fluorescent and PET/SPECT contrast agents into liposomes for multimodal imaging." Biomaterials **34**(4): 1179-1192.
178. Miura, M., et al. (2006). "Accumulated chromosomal instability in murine bone marrow mesenchymal stem cells leads to malignant transformation." Stem Cells **24**(4): 1095-1103.

179. Mok, P. L., et al. (2017). "Micro-Computed Tomography Detection of Gold Nanoparticle-Labelled Mesenchymal Stem Cells in the Rat Subretinal Layer." Int J Mol Sci **18**(2).
180. Moroz, M. A., et al. (2015). "Comparative Analysis of T Cell Imaging with Human Nuclear Reporter Genes." J Nucl Med **56**(7): 1055-1060.
181. Muehlberg, F. L., et al. (2009). "Tissue-resident stem cells promote breast cancer growth and metastasis." Carcinogenesis **30**(4): 589-597.
182. Muir, K. W. (2017). "Clinical trial design for stem cell therapies in stroke: What have we learned?" Neurochem Int **106**: 108-113.
183. Muller-Borer, B. J., et al. (2007). "Quantum dot labeling of mesenchymal stem cells." Journal of Nanobiotechnology **5**: 9-9.
184. Muller-Ehmsen, J., et al. (2006). "Effective engraftment but poor mid-term persistence of mononuclear and mesenchymal bone marrow cells in acute and chronic rat myocardial infarction." J Mol Cell Cardiol **41**(5): 876-884.
185. Murray, P. A. and A. S. Woolf (2014). "Using stem and progenitor cells to recapitulate kidney development and restore renal function." Curr Opin Organ Transplant **19**(2): 140-144.
186. Naderi, N., et al. (2017). "The regenerative role of adipose-derived stem cells (ADSC) in plastic and reconstructive surgery." Int Wound J **14**(1): 112-124.
187. Naderi, N., et al. (2014). "Adipogenic differentiation of adipose-derived stem cells in 3-dimensional spheroid cultures (microtissue): implications for the reconstructive surgeon." J Plast Reconstr Aesthet Surg **67**(12): 1726-1734.
188. Nagaya, N., et al. (2005). "Transplantation of mesenchymal stem cells improves cardiac function in a rat model of dilated cardiomyopathy." Circulation **112**(8): 1128-1135.
189. Nakamizo, A., et al. (2005). "Human Bone Marrow-Derived Mesenchymal Stem Cells in the Treatment of Gliomas." Cancer Research **65**(8): 3307-3318.
190. New, S. E., et al. (2015). "A matter of identity - Phenotype and differentiation potential of human somatic stem cells." Stem Cell Res **15**(1): 1-13.
191. Ng, Y. Y., et al. (2009). "Isolation of human and mouse hematopoietic stem cells." Methods Mol Biol **506**: 13-21.

192. Nguyen, P. K., et al. (2016). "Adult Stem Cell Therapy and Heart Failure, 2000 to 2016: A Systematic Review." JAMA Cardiol **1**(7): 831-841.
193. Ning, H., et al. (2008). "The correlation between cotransplantation of mesenchymal stem cells and higher recurrence rate in hematologic malignancy patients: outcome of a pilot clinical study." Leukemia **22**(3): 593-599.
194. Nitz, U. A., et al. (2005). "Comparison of rapidly cycled tandem high-dose chemotherapy plus peripheral-blood stem-cell support versus dose-dense conventional chemotherapy for adjuvant treatment of high-risk breast cancer: results of a multicentre phase III trial." Lancet **366**(9501): 1935-1944.
195. Noort, W. A., et al. (2010). "Mesenchymal stromal cells to treat cardiovascular disease: strategies to improve survival and therapeutic results." Panminerva Med **52**(1): 27-40.
196. Ogunlade, O., et al. (2018). "In vivo three-dimensional photoacoustic imaging of the renal vasculature in preclinical rodent models." Am J Physiol Renal Physiol **314**(6): F1145-f1153.
197. Oh, J. T., et al. (2006). "Three-dimensional imaging of skin melanoma in vivo by dual-wavelength photoacoustic microscopy." J Biomed Opt **11**(3): 34032.
198. Ohnishi, S., et al. (2007). "Transplantation of mesenchymal stem cells attenuates myocardial injury and dysfunction in a rat model of acute myocarditis." J Mol Cell Cardiol **42**(1): 88-97.
199. Oladipupo, S., et al. (2011). "VEGF is essential for hypoxia-inducible factor-mediated neovascularization but dispensable for endothelial sprouting." Proc Natl Acad Sci U S A **108**(32): 13264-13269.
200. Ong, H. T., et al. (2013). "Systemically delivered measles virus-infected mesenchymal stem cells can evade host immunity to inhibit liver cancer growth." J Hepatol **59**(5): 999-1006.
201. Oshima, Y., et al. (2004). "Fate of transplanted bone-marrow-derived mesenchymal cells during osteochondral repair using transgenic rats to simulate autologous transplantation." Osteoarthritis Cartilage **12**(10): 811-817.
202. Otsu, K., et al. (2009). "Concentration-dependent inhibition of angiogenesis by mesenchymal stem cells." Blood **113**(18): 4197-4205.
203. Pan, W., et al. (2018). "Non-invasive detection of the early phase of kidney injury by photoacoustic/computed tomography imaging." Nanotechnology **29**(26): 265101.

204. Paproski, R. J., et al. (2011). "Tyrosinase as a dual reporter gene for both photoacoustic and magnetic resonance imaging." Biomed Opt Express **2**(4): 771-780.
205. Patra, C. R., et al. (2008). "Targeted delivery of gemcitabine to pancreatic adenocarcinoma using cetuximab as a targeting agent." Cancer Res **68**(6): 1970-1978.
206. Patrick, P. S., et al. (2014). "Dual-modality gene reporter for in vivo imaging." Proc Natl Acad Sci U S A **111**(1): 415-420.
207. Peired, A. J. and A. Sisti (2016). "Mesenchymal Stem Cell-Based Therapy for Kidney Disease: A Review of Clinical Evidence." **2016**: 4798639.
208. Peters, W. P., et al. (2005). "Prospective, randomized comparison of high-dose chemotherapy with stem-cell support versus intermediate-dose chemotherapy after surgery and adjuvant chemotherapy in women with high-risk primary breast cancer: a report of CALGB 9082, SWOG 9114, and NCIC MA-13." J Clin Oncol **23**(10): 2191-2200.
209. Ponte, A. L., et al. (2007). "The in vitro migration capacity of human bone marrow mesenchymal stem cells: comparison of chemokine and growth factor chemotactic activities." Stem Cells **25**(7): 1737-1745.
210. Principi, M., et al. (2003). "Perfusion MRI in the evaluation of the relationship between tumour growth, necrosis and angiogenesis in glioblastomas and grade 1 meningiomas." Neuroradiology **45**(4): 205-211.
211. Progoatzky, F., et al. (2013). "From seeing to believing: labelling strategies for in vivo cell-tracking experiments." Interface Focus **3**(3): 20130001.
212. Ramkisoensing, A. A., et al. (2011). "Human embryonic and fetal mesenchymal stem cells differentiate toward three different cardiac lineages in contrast to their adult counterparts." PLoS One **6**(9): e24164.
213. Ray, P., et al. (2007). "Construction and validation of improved triple fusion reporter gene vectors for molecular imaging of living subjects." Cancer Res **67**(7): 3085-3093.
214. Rector, K., et al. (2013). "Comprehensive hematopoietic stem cell isolation methods." Methods Mol Biol **976**: 1-15.
215. Reivich, M., et al. (1979). "The [18F]fluorodeoxyglucose method for the measurement of local cerebral glucose utilization in man." Circ Res **44**(1): 127-137.

216. Rice, H. E., et al. (2007). "Superparamagnetic iron oxide labeling and transplantation of adipose-derived stem cells in middle cerebral artery occlusion-injured mice." AJR Am J Roentgenol **188**(4): 1101-1108.
217. Riemer, J., et al. (2004). "Colorimetric ferrozine-based assay for the quantitation of iron in cultured cells." Anal Biochem **331**(2): 370-375.
218. Rigotti, G., et al. (2007). "Clinical treatment of radiotherapy tissue damage by lipoaspirate transplant: a healing process mediated by adipose-derived adult stem cells." Plast Reconstr Surg **119**(5): 1409-1422; discussion 1423-1404.
219. Rippon, H. J. and A. E. Bishop (2004). "Embryonic stem cells." Cell Prolif **37**(1): 23-34.
220. Roodhart, J. M., et al. (2011). "Mesenchymal stem cells induce resistance to chemotherapy through the release of platinum-induced fatty acids." Cancer Cell **20**(3): 370-383.
221. Ruan, J., et al. (2012). "Fluorescent magnetic nanoparticle-labeled mesenchymal stem cells for targeted imaging and hyperthermia therapy of in vivo gastric cancer." Nanoscale Res Lett **7**(1): 309.
222. Rudelius, M., et al. (2003). "Highly efficient paramagnetic labelling of embryonic and neuronal stem cells." Eur J Nucl Med Mol Imaging **30**(7): 1038-1044.
223. Ruster, B., et al. (2006). "Mesenchymal stem cells display coordinated rolling and adhesion behavior on endothelial cells." Blood **108**(12): 3938-3944.
224. Ryu, M. Y., et al. (2005). "Brain Transplantation of Neural Stem Cells Cotransduced with Tyrosine Hydroxylase and GTP Cyclohydrolase 1 in Parkinsonian Rats." Cell Transplant **14**(4): 193-202.
225. Safi, M., et al. (2010). "Interactions between sub-10-nm iron and cerium oxide nanoparticles and 3T3 fibroblasts: the role of the coating and aggregation state." Nanotechnology **21**(14): 145103.
226. Sage, E. K., et al. (2014). "Systemic but not topical TRAIL-expressing mesenchymal stem cells reduce tumour growth in malignant mesothelioma." Thorax **69**(7): 638-647.
227. Sage, E. K., et al. (2016). "Genetically modified mesenchymal stromal cells in cancer therapy." Cytotherapy **18**(11): 1435-1445.
228. Santeramo, I., et al. (2017). "Human Kidney-Derived Cells Ameliorate Acute Kidney Injury Without Engrafting into Renal Tissue." Stem Cells Transl Med **6**(5): 1373-1384.

229. Sarkar, D., et al. (2011). "Engineered cell homing." Blood **118**(25): e184-e191.
230. Sasportas, L. S., et al. (2009). "Assessment of therapeutic efficacy and fate of engineered human mesenchymal stem cells for cancer therapy." Proc Natl Acad Sci U S A **106**(12): 4822-4827.
231. Scarfe, L., et al. (2015). "Measures of kidney function by minimally invasive techniques correlate with histological glomerular damage in SCID mice with adriamycin-induced nephropathy." Sci Rep **5**: 13601.
232. Schwartz, S. D., et al. (2012). "Embryonic stem cell trials for macular degeneration: a preliminary report." Lancet **379**(9817): 713-720.
233. Schwartz, S. D., et al. (2015). "Human embryonic stem cell-derived retinal pigment epithelium in patients with age-related macular degeneration and Stargardt's macular dystrophy: follow-up of two open-label phase 1/2 studies." Lancet **385**(9967): 509-516.
234. Shah, K. (2014). Genetically Engineered Mesenchymal Stem Cells: Targeted Foes of Cancer. Mesenchymal Stem Cells in Cancer Therapy. K. Shah. Boston, Academic Press: 1-36.
235. Shi, M., et al. (2007). "Regulation of CXCR4 expression in human mesenchymal stem cells by cytokine treatment: role in homing efficiency in NOD/SCID mice." Haematologica **92**(7): 897-904.
236. Shi, M., et al. (2012). "Human Mesenchymal Stem Cell Transfusion Is Safe and Improves Liver Function in Acute-on-Chronic Liver Failure Patients." Stem Cells Transl Med **1**(10): 725-731.
237. Shizuru, J. A., et al. (2005). "Hematopoietic stem and progenitor cells: clinical and preclinical regeneration of the hematolymphoid system." Annu Rev Med **56**: 509-538.
238. Singh, R., et al. (2018). "Pluripotent Stem Cells for Retinal Tissue Engineering: Current Status and Future Prospects." Stem Cell Rev **14**(4): 463-483.
239. Siphanto, R. I., et al. (2005). "Serial noninvasive photoacoustic imaging of neovascularization in tumor angiogenesis." Opt Express **13**(1): 89-95.
240. Srinivas, M., et al. (2010). "(19)F MRI for quantitative in vivo cell tracking." Trends in biotechnology **28**(7): 363-370.

241. Stojanov, K., et al. (2012). "[18F]FDG labeling of neural stem cells for in vivo cell tracking with positron emission tomography: inhibition of tracer release by phloretin." Mol Imaging **11**(1): 1-12.
242. Stuckey, D. J., et al. (2006). "Iron particles for noninvasive monitoring of bone marrow stromal cell engraftment into, and isolation of viable engrafted donor cells from, the heart." Stem Cells **24**(8): 1968-1975.
243. Stuckey, D. W. and K. Shah (2013). "TRAIL on trial: preclinical advances in cancer therapy." Trends Mol Med **19**(11): 685-694.
244. Studeny, M., et al. (2002). "Bone marrow-derived mesenchymal stem cells as vehicles for interferon-beta delivery into tumors." Cancer Res **62**(13): 3603-3608.
245. Sun, J. H., et al. (2008). "In vivo monitoring of magnetically labeled mesenchymal stem cells administered intravascularly in rat acute renal failure." Swiss Med Wkly **138**(27-28): 404-412.
246. Sutton, E. J., et al. (2008). "Cell tracking with optical imaging." Eur Radiol **18**(10): 2021-2032.
247. Takeda, N. and M. Diksic (1999). "Relationship between drug delivery and the intra-arterial infusion rate of SarCNU in C6 rat brain tumor model." J Neurooncol **41**(3): 235-246.
248. Tang, Y., et al. (2015). "MRI/SPECT/Fluorescent Tri-Modal Probe for Evaluating the Homing and Therapeutic Efficacy of Transplanted Mesenchymal Stem Cells in a Rat Ischemic Stroke Model." Adv Funct Mater **25**(7): 1024-1034.
249. Tavera-Mendoza, L. E. and M. Brown (2017). "A less invasive method for orthotopic injection of breast cancer cells into the mouse mammary gland." Lab Anim **51**(1): 85-88.
250. Terrovitis, J., et al. (2008). "Ectopic expression of the sodium-iodide symporter enables imaging of transplanted cardiac stem cells in vivo by single-photon emission computed tomography or positron emission tomography." J Am Coll Cardiol **52**(20): 1652-1660.
251. Thakur, M. L., et al. (1977). "Indium-111-labeled cellular blood components: mechanism of labeling and intracellular location in human neutrophils." J Nucl Med **18**(10): 1022-1026.
252. Thomas, E. D., et al. (1957). "Intravenous infusion of bone marrow in patients receiving radiation and chemotherapy." N Engl J Med **257**(11): 491-496.
253. Thomson, J. A., et al. (1998). "Embryonic stem cell lines derived from human blastocysts." Science **282**(5391): 1145-1147.

254. Thorne, N., et al. (2010). "Illuminating insights into firefly luciferase and other bioluminescent reporters used in chemical biology." Chem Biol **17**(6): 646-657.
255. Tiffen, J. C., et al. (2010). "Luciferase expression and bioluminescence does not affect tumor cell growth in vitro or in vivo." Molecular Cancer **9**: 299-299.
256. Togel, F., et al. (2005). "Administered mesenchymal stem cells protect against ischemic acute renal failure through differentiation-independent mechanisms." Am J Physiol Renal Physiol **289**(1): F31-42.
257. Togel, F., et al. (2008). "Bioluminescence imaging to monitor the in vivo distribution of administered mesenchymal stem cells in acute kidney injury." Am J Physiol Renal Physiol **295**(1): F315-321.
258. Tyler, J. L., et al. (1986). "Pharmacokinetics of superselective intra-arterial and intravenous [¹¹C]BCNU evaluated by PET." J Nucl Med **27**(6): 775-780.
259. Unsal, I. O., et al. (2015). "Comparison of therapeutic characteristics of islet cell transplantation simultaneous with pancreatic mesenchymal stem cell transplantation in rats with Type 1 diabetes mellitus." Stem Cell Rev **11**(3): 526-532.
260. Urabe, K., et al. (1994). "The inherent cytotoxicity of melanin precursors: a revision." Biochim Biophys Acta **1221**(3): 272-278.
261. Vallabhajosula, S. (2009). Molecular imaging: radiopharmaceuticals for PET and SPECT.
262. Varghese, J., et al. (2017). "Systematic review of patient factors affecting adipose stem cell viability and function: implications for regenerative therapy." Stem Cell Res Ther **8**(1): 45.
263. Vexler, A. M., et al. (1995). "Reduction of the systemic toxicity of cisplatin by intra-arterial hepatic route administration for liver malignancies." International Journal of Cancer **60**(5): 611-615.
264. Vilalta, M., et al. (2008). "Biodistribution, long-term survival, and safety of human adipose tissue-derived mesenchymal stem cells transplanted in nude mice by high sensitivity non-invasive bioluminescence imaging." Stem Cells Dev **17**(5): 993-1003.
265. Vilquin, J. T. and P. Rosset (2006). "Mesenchymal stem cells in bone and cartilage repair: current status." Regen Med **1**(4): 589-604.
266. Waerzeggers, Y., et al. (2008). "Multimodal imaging of neural progenitor cell fate in rodents." Mol Imaging **7**(2): 77-91.

267. Walczak, P., et al. (2008). "Dual-modality monitoring of targeted intraarterial delivery of mesenchymal stem cells after transient ischemia." Stroke **39**(5): 1569-1574.
268. Wathen, C. A., et al. (2013). "In vivo X-ray computed tomographic imaging of soft tissue with native, intravenous, or oral contrast." Sensors (Basel) **13**(6): 6957-6980.
269. Weiner, M. M., et al. (2013). "Ultrasound-guided vascular access: a comprehensive review." J Cardiothorac Vasc Anesth **27**(2): 345-360.
270. Wheatley, M. A., et al. (1990). "Contrast agents for diagnostic ultrasound: development and evaluation of polymer-coated microbubbles." Biomaterials **11**(9): 713-717.
271. Woods, M., et al. (2004). "Solution dynamics and stability of lanthanide(III) (S)-2-(p-nitrobenzyl)DOTA complexes." Inorg Chem **43**(9): 2845-2851.
272. Xinaris, C., et al. (2013). "A novel strategy to enhance mesenchymal stem cell migration capacity and promote tissue repair in an injury specific fashion." Cell Transplant **22**(3): 423-436.
273. Xu, D., et al. (2016). "Noninvasive and high-resolving photoacoustic dermoscopy of human skin." Biomed Opt Express **7**(6): 2095-2102.
274. Xu, Z., et al. (2017). "(18)F-Fluoromisonidazole in tumor hypoxia imaging." Oncotarget **8**(55): 94969-94979.
275. Xue, S., et al. (2015). "99mTc-Labeled Iron Oxide Nanoparticles for Dual-Contrast (T1/T2) Magnetic Resonance and Dual-Modality Imaging of Tumor Angiogenesis." J Biomed Nanotechnol **11**(6): 1027-1037.
276. Yaghoubi, S. S., et al. (2009). "Noninvasive detection of therapeutic cytolytic T cells with 18F-FHBG PET in a patient with glioma." Nat Clin Pract Oncol **6**(1): 53-58.
277. Yao, S., et al. (2017). "Maximized nanodrug-loaded mesenchymal stem cells by a dual drug-loaded mode for the systemic treatment of metastatic lung cancer." Drug Deliv **24**(1): 1372-1383.
278. Yi, T. and S. U. Song (2012). "Immunomodulatory properties of mesenchymal stem cells and their therapeutic applications." Arch Pharm Res **35**(2): 213-221.
279. Yuan, L., et al. (2011). "VEGF-modified human embryonic mesenchymal stem cell implantation enhances protection against cisplatin-induced acute kidney injury." Am J Physiol Renal Physiol **300**(1): F207-218.

280. Yukawa, H., et al. (2012). "Monitoring transplanted adipose tissue-derived stem cells combined with heparin in the liver by fluorescence imaging using quantum dots." Biomaterials **33**(7): 2177-2186.
281. Zhang, S., et al. (2015). "Corticosterone mediates the inhibitory effect of restraint stress on the migration of mesenchymal stem cell to carbon tetrachloride-induced fibrotic liver by downregulating CXCR4/7 expression." Stem Cells Dev **24**(5): 587-596.
282. Zhang, Y., et al. (2018). "Establishment of a murine breast tumor model by subcutaneous or orthotopic implantation." Oncol Lett **15**(5): 6233-6240.
283. Zheng, Y., et al. (2017). "Stem Cell Tracking Technologies for Neurological Regenerative Medicine Purposes." Stem Cells International **2017**: 9.
284. Zhu, J., et al. (2006). "Tracking neural stem cells in patients with brain trauma." N Engl J Med **355**(22): 2376-2378.
285. <https://www.statnews.com/2018/10/14/harvard-brigham-retractions-stem-cell/>
286. <https://www.nature.com/articles/d41586-018-06756-9>

Appendix 1 – Staining solution

Oil Red O staining solution

The stock solution was prepared by mixing 300 mg of Oil Red O powder with 100 ml of 99% isopropanol. The working solution was prepared by mixing 3 parts of stock solution with 2 parts of deionised water and was allowed to sit at room temperature for 10 minutes and then filtered using 0.2 µm syringe filter to remove large particles.

Alizarin Red staining solution

1% Alizarin red staining solution was freshly prepared by mixing 1 g of Alizarin red powder with 100 ml deionised water and adjusted to pH 4.1 – 4.3 using 1 M HCl and then filtered using 0.2 µm syringe filter to remove large particles.

Perl's Prussian blue staining

20% potassium ferrocyanide ($K_4Fe(CN)_6 \cdot 3H_2O$) was prepared by mixing 0.2 g of potassium ferrocyanide to 1 ml of deionised water. 20% HCl was prepared by mixing 625 µl of 32% HCl to 375 µl of deionised water.

Perl's solution was freshly prepared by mixing the equal part of both 20% potassium ferrocyanide and 20% HCl together and covered the tube with aluminium foil to protect it from the light.

Appendix 2 – *In vivo* stability assessment of ¹¹¹In-DOTA-SPION

Table A2.1 *In vivo* 3D ROI quantification of SPECT signal (%ID/mm³) in liver of ¹¹¹InCl₃, ¹¹¹In-SPION and ¹¹¹In-DOTA-SPION at 1 hour, days 1, 3 & 7 after injection (n = 3 in each group).

liver	¹¹¹ InCl ₃		¹¹¹ In-SPION		¹¹¹ In-DOTA-SPION	
	Mean	SD	Mean	SD	Mean	SD
1 hour	0.006	0.0009	0.02	0.006	0.037	0.001
Day 1	0.005	0.0009	0.019	0.007	0.039	0.001
Day 3	0.006	0.0008	0.021	0.008	0.036	0.004
Day 7	0.005	0.0001	0.015	0.005	0.036	0.007

Table A2.2 *In vivo* 3D ROI quantification of SPECT signal (%ID/mm³) in kidney of ¹¹¹InCl₃, ¹¹¹In-SPION and ¹¹¹In-DOTA-SPION at 1 hour, days 1, 3 & 7 after injection (n = 3 in each group).

kidney	¹¹¹ InCl ₃		¹¹¹ In-SPION		¹¹¹ In-DOTA-SPION	
	Mean	SD	Mean	SD	Mean	SD
1 hour	0.012	0.003	0.005	0.005	0.002	0.00007
Day 1	0.011	0.002	0.006	0.006	0.003	0.00056
Day 3	0.009	0.002	0.004	0.004	0.003	0.00096
Day 7	0.005	0.001	0.003	0.001	0.003	0.00046

Appendix 3 – ¹¹¹In-DOTA-SPION labelled cell distribution in healthy animals after systemic injections

Table A3.1 *Ex vivo* quantification of radioactivity distribution (%ID/g) in all organs at 1 hour, days 1, 3 & 7 after IV and IC injection (n = 3 in each group).

1 hour	IV		IC	
	Mean	SD	Mean	SD
brain	0.0791	0.015	10.881	3.857
lungs	192.442	22.592	36.705	1.007
liver	26.405	7.035	34.848	4.377
kidney	4.744	0.507	22.205	10.738
spleen	4.722	0.923	11.828	2.993
blood	3.758	0.348	3.905	0.357
thyroid & salivary	0.778	0.092	1.301	0.540
heart	0.974	0.204	35.006	2.302
lymph nodes	0.597	0.259	0.732	0.471
stomach	0.703	0.041	3.132	1.230
small intestine	0.976	0.282	10.188	2.521
caecum	0.709	0.287	16.788	2.990
large intestine	0.646	0.09	5.316	0.588
muscle	0.32	0.078	1.526	1.092
bone	2.217	0.561	2.517	0.438
tail	4.466	4.129	0.629	0.077

Day 1	IV		IC	
	Mean	SD	Mean	SD
brain	0.139	0.034	5.030	3.341
lungs	86.851	12.696	31.206	7.064
liver	34.867	3.085	51.179	9.559
kidney	11.181	3.685	17.005	2.950
spleen	33.504	2.537	36.354	13.972
blood	1.238	0.399	1.315	0.601
thyroid & salivary	1.497	0.767	2.145	0.809
heart	1.396	0.282	21.261	13.078
lymph nodes	0.700	0.163	1.975	1.117
stomach	0.947	0.170	2.093	0.532
small intestine	2.570	0.761	4.032	1.093
caecum	1.849	0.439	3.526	0.982
large intestine	1.090	0.234	2.724	0.617
muscle	0.429	0.054	0.589	0.116
bone	4.061	0.648	3.898	0.865

tail	2.902	1.617	0.605	0.255
-------------	-------	-------	-------	-------

Day 3	IV		IC	
	Mean	SD	Mean	SD
brain	0.137	0.020	2.611	2.751
lungs	72.118	9.054	4.468	2.452
liver	45.085	10.601	48.321	6.582
kidney	11.120	0.915	8.678	3.986
spleen	43.785	5.682	29.099	6.343
blood	0.491	0.070	0.433	0.112
thyroid & salivary	1.433	0.734	2.325	0.961
heart	1.325	0.061	9.468	9.189
lymph nodes	0.877	0.544	2.540	2.169
stomach	1.285	0.126	1.498	0.671
small intestine	1.539	0.148	2.314	0.956
caecum	1.343	0.385	2.149	1.162
large intestine	1.046	0.134	1.359	0.548
muscle	0.446	0.074	0.489	0.232
bone	5.908	0.263	2.544	0.617
tail	2.355	1.321	0.342	0.160

Day 7	IV		IC	
	Mean	SD	Mean	SD
brain	0.050	0.005	1.472	0.259
lungs	24.000	11.129	4.047	1.477
liver	41.945	7.600	41.755	2.057
kidney	3.016	0.264	5.156	0.285
spleen	18.779	5.541	19.850	2.132
blood	0.149	0.024	0.128	0.025
thyroid & salivary	0.585	0.156	0.852	0.270
heart	0.518	0.106	5.868	2.144
lymph nodes	1.536	0.423	1.330	0.119
stomach	0.404	0.082	0.787	0.254
small intestine	0.353	0.121	1.212	0.371
caecum	0.496	0.280	1.184	0.282
large intestine	0.449	0.207	0.878	0.212
muscle	0.181	0.015	0.267	0.015
bone	2.019	0.044	2.151	0.332
tail	1.421	0.931	0.297	0.044

Appendix 4 – ¹¹¹In-DOTA-SPION labelled cell distribution in tumour bearing animals after systemic injections

Table A4.1 *Ex vivo* quantification of radioactivity distribution (%ID/g) in all organs at 1 hour and day 3 after IV and IC injection in tumour bearing mice (n = 3 in each group).

1 hour	IV-ADSCs		IC-ADSCs		IV-Particles		IC-Particles	
	Mean	SD	Mean	SD	Mean	SD	Mean	SD
tumour	0.308	0.087	1.402	0.124	0.331	0.088	0.308	0.059
brain	0.112	0.021	12.768	0.550	0.167	0.035	1.826	0.263
lungs	142.731	41.312	46.972	1.724	40.637	10.798	16.561	4.169
liver	42.766	2.975	59.109	5.819	70.121	24.175	67.820	41.900
kidney	6.263	1.623	18.435	3.753	11.537	2.942	12.880	7.836
spleen	16.991	3.755	38.536	17.299	85.383	64.437	96.834	70.162
blood	3.101	0.643	4.204	0.118	3.638	2.136	3.441	2.248
heart	1.764	0.854	52.754	10.414	1.955	0.693	10.462	1.064
stomach	0.788	0.148	2.716	0.682	1.175	0.370	1.130	0.587
small intestine	0.978	0.257	7.096	1.630	1.398	0.302	1.791	0.473
caecum	0.979	0.285	15.599	2.058	1.405	0.262	2.160	0.543
large intestine	0.565	0.139	5.820	3.834	0.430	0.388	1.135	0.351
muscle	0.285	0.033	0.380	0.048	0.659	0.297	0.536	0.416
bone	2.182	0.409	1.841	0.335	3.852	0.554	3.515	0.355
tail	9.219	11.190	0.445	0.031	5.227	5.060	0.636	0.327

Day 3	IV-ADSCs		IC-ADSCs		IV-Particles		IC-Particles	
	Mean	SD	Mean	SD	Mean	SD	Mean	SD
tumour	3.465	0.700	4.308	1.290	3.452	0.947	3.106	0.485
brain	0.116	0.008	6.911	2.431	0.149	0.032	1.436	0.637
lungs	96.489	17.429	9.484	3.315	19.550	15.091	6.739	2.425
liver	50.203	6.941	65.658	18.605	64.503	5.983	59.334	10.363
kidney	12.228	1.375	21.902	5.396	13.397	3.078	14.182	1.517
spleen	50.969	13.372	89.647	7.309	55.780	8.052	141.885	125.890
blood	0.529	0.062	0.499	0.097	0.494	0.091	0.477	0.137
heart	1.278	0.395	15.872	12.457	1.367	0.170	6.468	1.224
stomach	1.049	0.175	2.276	0.525	1.262	0.162	1.243	0.326
small intestine	1.540	0.175	5.800	1.173	1.923	0.244	2.126	0.123
caecum	1.374	0.149	4.388	1.621	1.571	0.068	1.809	0.204
large intestine	1.080	0.015	2.514	0.555	1.144	0.185	1.384	0.366
muscle	0.649	0.197	0.944	0.514	0.851	0.343	0.551	0.229
bone	4.146	1.020	6.146	1.307	4.448	0.694	3.781	1.253
tail	5.278	7.294	0.886	0.180	6.818	8.704	0.586	0.223

